Development of Optical Sensor Platforms based on Evanescent Wave Interactions

By

Aidan Doyle B.Sc. (Hons)

A thesis presented

to

Dublin City University

For the degree of Doctor of Philosophy

June 1999

School of Physical Sciences

Dublin City University

Ireland

I hereby certify that this material, which I now submit for assessment on the programme of study leading to the award of Doctor of Philosophy is entirely my own work and has not been taken from the work of others save and to the extent that such work has been cited and acknowledged within the text of my work.

Signed:____________________ Date: 5/11/99__________

Dedication

There are three very special people to whom this thesis is dedicated. Firstly, my parents Larry and Mary who have always been there when I needed them most. Mom, Dad this is for you as well as for me This thesis is also dedicated to my special friend Marleine who has sacrificed so much for me over the years. Marleine, I thank you so much for just being you.

Acknowledgements

I would like to thank all the past and present members of the optical sensors group; in particular Colm, Paud, Mick and the honorary lads Sarah-Jane, Antoinette and Penny for providing an enjoyable four years at DCU. I must also say a word of thanks to Marian and Katriona for somehow putting up with my constant demands about the status of orders, without resorting to violent means.

I would like to thank all the physics technicians, especially Des Lavelle and his various partners in crime in the workshop for sneaking so many of my jobs up the queue. Des, the brown envelope is on the way. Thanks are also due to Dr Colette McDonagh and Dr Brian Lawless for their enthusiasm and valuable input.

Finally, I would also like to thank Professor Brian MacCraith for allowing me this excellent opportunity. Brian, thank you ever so much.

Abstract

A study of the principles, fabrication and behaviour of a range of optical sensor platforms based on evanescent wave interactions is presented. The platforms utilise a range of sensing techniques including absorption, fluorescence quenching and surface plasmon resonance. The absorbance-based platforms employ sol-gel-derived planar waveguides and grating couplers to launch light into guided modes, the evanescent fields of which can interrogate a sensing layer. A detailed characterisation of these integrated optic devices is presented. Two platforms employing few-mode and multi-mode waveguides, respectively, are described and applied to the detection of gaseous ammonia and carbon dioxide.

A fluorescence-based sensor platform which utilises the anisotropy of fluorescence emitted near an interface is also presented. The platform consists of a planar waveguide coated with a sol-gel-derived fluorescent layer. A substantial amount of the analyte-sensitive fluorescence is captured by guided modes in the planar waveguide. This configuration is described in detail and is applied to the detection of gaseous oxygen as a proof of principle. Finally, work leading to the development of a fibre optic probe biosensor based on surface plasmon resonance is presented together with its application to the detection of red blood cells.

In summary, this work highlights the feasibility of combining evanescent wave interactions and sol-gel technology to fabricate miniature sensor platforms which may be applied to the detection of a wide range of target analytes in a reliable and cost effective manner.

Table of Contents

Page

Chapter 1 Introduction

1.1 Introduction

The word 'sensor', which is derived from the word *sentire* meaning to perceive, describes a device that is capable of continuously measuring the value of a physical parameter, or the concentration of a chemical or biochemical species. There are many different types of sensors[1] ranging from mechanical, electrical, thermal, electrochemical to optical devices, which is the type investigated in this thesis

Integrated optics is a relatively new technology that is concerned with the fabrication of miniature optical components that can perform a variety of optical functions[2,3]. Integrated optic components such as planar waveguides, grating couplers and diffractive optic elements may all be used to redirect, propagate and shape an optical beam as required by an application. It is expected that integrated optic components, due to their relative ease of fabrication, low cost and high performance, will with time, replace a large proportion of electronic components in many applications ranging from the ever-expanding field of telecommunications to areas such as sensing and process control.

In this thesis, attempts are made to integrate these two diverse technologies using the sol-gel process and thus produce a range of integrated optic sensor platforms which may be applied to the detection of chemical entities using the well understood optical phenomena of analyte-sensitive absorption and fluorescence. The aim of this chapter is to briefly introduce all topics dealt with in this work. More detailed discussions are provided in the relevant chapters.

1.2 Optical Sensors

Optical sensors are devices which use light and changes in light to detect certain physical, chemical or biological parameters[4,5] Optical sensors may employ a wide range of optical phenomena as sensing mechanisms. Two of the most important techniques for chemical and biological parameters are absorption and fluorescence Typically, in absorption-based chemical sensors the target analyte either directly absorbs incident radiation or alters the absorption properties of an indicator compound in proportion to its concentration. In a typical fluorescence-based sensing technique, the target analyte induces or quenches fluorescence of an indicator compound in proportion to its concentration.

The main competition to optical gas sensors comes from both semiconductor and electrochemical sensors. However, both of these families of devices suffer in terms of specificity, poisoning and long-term stability. With appropriate design optical sensors can overcome some of these problems.

Optical Chemical sensors offer a number of advantages over other sensor types:

1. The primary signal is optical, and therefore is not subject to electrical interference.

2. Optical sensing processes are generally reversible and thus the analyte is not used up in the detection mechanism.

3. Optical sensors do not present a significant risk of sparking, and are therefore suitable for use in potentially explosive areas e.g. mining and petroleum industries.

4. Analysis may be performed in real-time

5 Optical sensors are generally smaller in size and simpler in configuration than amperometric cells and hence facilitate the development of small, portable devices.

However, optical sensors are not without their limitations such as:

1. Ambient light can interfere with the detected signal. Therefore, optical sensors must either be used in dark conditions, covered with an optical isolation layer or use lock-in detection techniques.

2. There is a lack of suitable light sources particularly in the UV and IR regions of the spectrum.

3. There is a lack of selective indicators for many analytes of interest.

4. Sensors with indicator phases may have limited long-term stability due to photobleaching or washout.

However, despite these limitations, optical sensors are becoming an increasingly attractive means of sensing for a wide range of properties

1.3 Evanescent Wave Sensing

As radiation propagates along a waveguide, an amount extends a short distance beyond the guiding medium and into the surrounding media of lower refractive index, as shown in figure 1.1. This radiation is referred to as the evanescent field[6,9], and decays exponentially with distance from the waveguide boundaries. Evanescent fields are characterised by a parameter known as the *penetration depth* that is defined as the distance into the surrounding media that the power has dropped by a factor of e^{-1}.

The evanescent field may be employed as an optical sensing mechanism, and can be used in two distinct approaches. Firstly, the evanescent wave can interact directly with the analyte if the interrogating wavelength coincides with an absorption band of the species. Such direct spectroscopic evanescent wave sensors are of particular interest in the infrared spectral region, where many species absorb strongly Alternatively, an intermediate reagent, which responds optically, e.g. by fluorescence or absorption change, to the analyte, may be attached to the waveguide and thus be interrogated by the evanescent field of a guided wave. In general, reagent-mediated evanescent wave sensors are the more common because they provide greater sensitivity than direct spectroscopic devices.

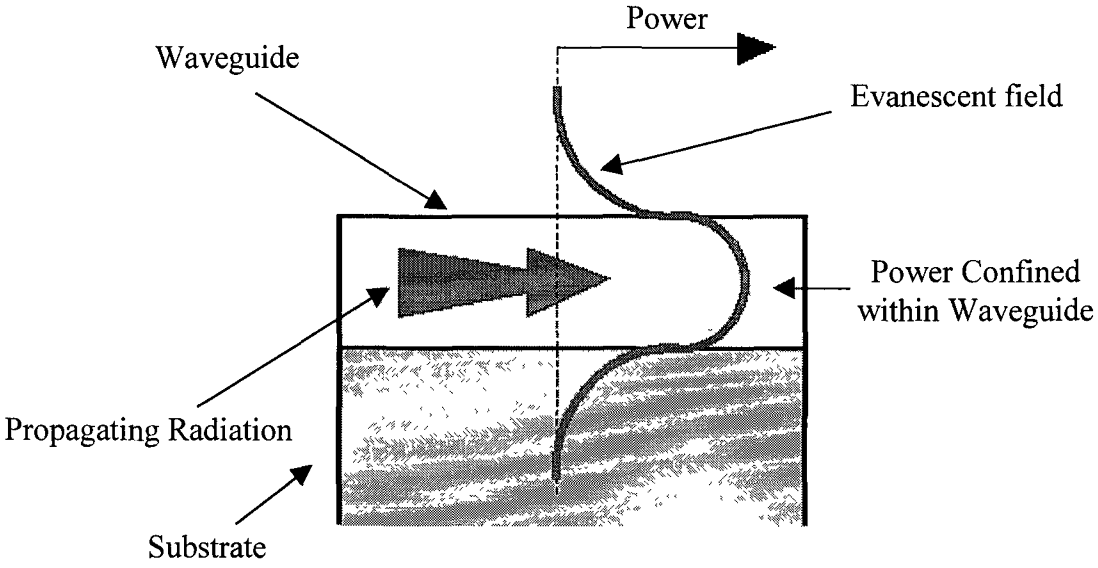

Figure 1.1 *Evanescent Fields of Guided Modes*

Optical waveguide-based sensors which employ evanescent wave sensing techniques exhibit a number of favourable properties, some of which are listed below:

1. No coupling optics is required in the sensing region, because the interrogating light remains guided.

2. It is possible to control the penetration depth of the evanescent field into the sensing media and thereby optimise device performance to suit a particular application.

3. The technique can provide enhanced sensitivity over conventional bulk-optic approaches For example, waveguide-based evanescent wave absorption devices

are more sensitive than bulk-optic attenuated total reflection (ATR) crystals by virtue of the greater number of reflections per unit length.

4 By coating discrete areas of the waveguide, there is the possibility of carrying out fully- or quasi-distributed sensing.

5. Greater control over interaction parameters such as interaction length, sensing volume and response time is possible.

However, they also have a number of associated disadvantages including the following:

1. In coated optical waveguide sensors fouling of the sensor may be a problem if the evanescent field is not fully contained within the coating

2. The relative sensitivity compared to bulk absorption is lower due to the small fraction of power typically carried in the evanescent field.

It is also possible to employ direct absorption waveguide-based sensors in which the sensing reagent is immobilised directly into the waveguide core thus facilitating direct interrogation of the sensing reagent by the propagating mode. This technique ideally provides higher sensitivity than its evanescent wave counterpart due to increased interaction lengths. However, in reality such a configuration is not feasible due to the high densification temperatures required to produce waveguides (500 C) and the lower temperatures at which pyrolysis of the sensing reagents occur.

1.4 Optical Waveguides

An optical waveguide[7] is a dielectric structure that transports energy at wavelengths in the visible or infrared portions of the electromagnetic spectrum. There are generally considered to be two main types of optical waveguide. The first and most commonly used is the well-known optical fibre[8] An optical fibre generally consists of three regions as shown in figure 1.2. The central region, which is known as the core, is surrounded by the cladding, which in turn is surrounded by a protective jacket.

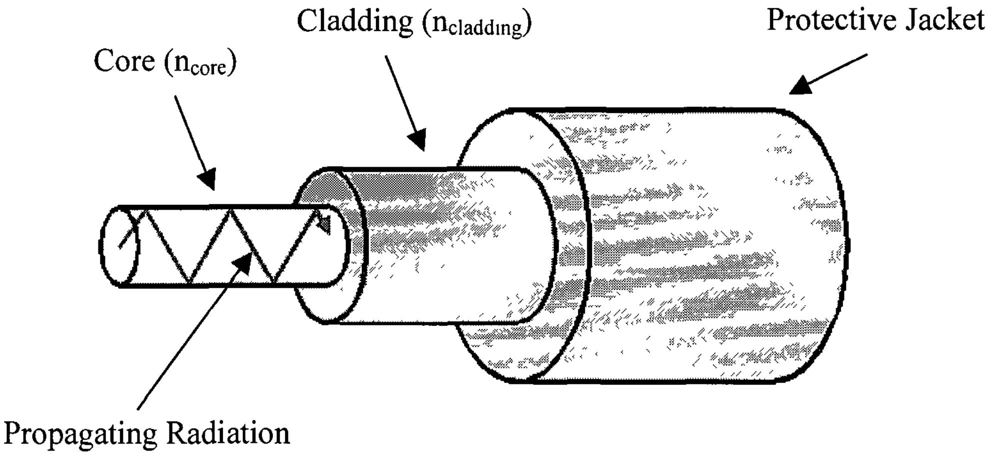

Figure 1.2 *Optical Fibre*

In order to allow the fibre to support propagating modes of radiation it is necessary for the core to have a higher refractive index than that of the surrounding cladding. Total internal reflection of the light at the core - cladding interface may then occur provided that the beam propagation angle is greater than the critical angle θ_c such that

$$\sin\theta_c = \frac{n_{cladding}}{n_{core}} \qquad [1.1]$$

Fibre optics are extremely useful in a wide range of applications due to their flexible nature and their low propagation losses (dB/km)

The second type of dielectric waveguide is commonly referred to as the planar waveguide[9,10]. This device, which has a planar geometry as illustrated in figure 1.3, consists of a thin (0.25μm → 10μm) dielectric film of high refractive index (1.51 → 1.7) which is deposited on a lower refractive index substrate (1.43 → 1.51). A superstrate layer is optional depending on the application. As with the optical fibre, light propagation occurs by total internal reflection at the boundaries of the thin guiding layer. A more detailed description of the operation of a planar waveguide is provided in chapter three.

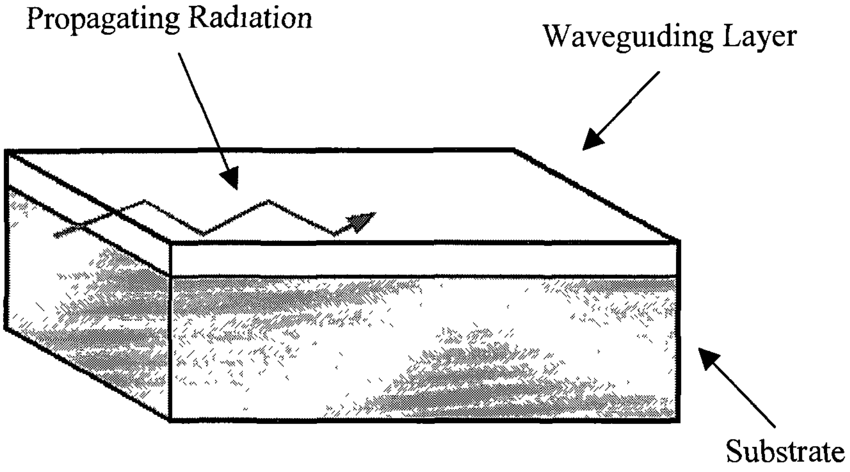

Figure 1.3 *Planar Dielectric Waveguide*

The losses in planar dielectric waveguides are usually much higher than those of an optical fibre but are typically < 1 dB/cm. Such high propagation losses restrict the use of planar waveguides to operations where guiding only occurs over a short distance. However, the planar waveguide also exhibits many favourable characteristics. Its planar geometry ensures compatibility with the planar technology of integrated circuits (IC's), allowing for the production hybrid opto-electronic devices. Other advantages of the planar waveguide are its small dimensions, ease of production and ease of handling

1.5 Waveguide Input Couplers

Efficient coupling of a light source into a thin-film optical waveguide is a problem for many integrated-optic designs. The difficulty is to maintain efficient coupling of the light into the waveguide with minimal alignment difficulties. Many different coupling techniques[11] have been utilised to this end. In this section the three main coupling techniques for launching light into planar waveguides are presented.

1.5.1 End-face Couplers

The most basic technique employed to launch light into a guided mode in a waveguide is end-fire coupling which, as shown in figure 1 4, typically involves focusing the incident radiation onto the end-face of the waveguide. For efficient coupling the width of the beam must be comparable to the waveguide thickness. In principle, this method is almost 100% efficient. However, in reality this is not the case because normally the end-face of the waveguide is not ideal. Moreover, many waveguides are of the order of microns and lower in thickness and therefore require critical alignment of the incident radiation and the lens. Due to these highly restrictive conditions, end-fire couplers have been rarely employed for general integrated-optics applications.

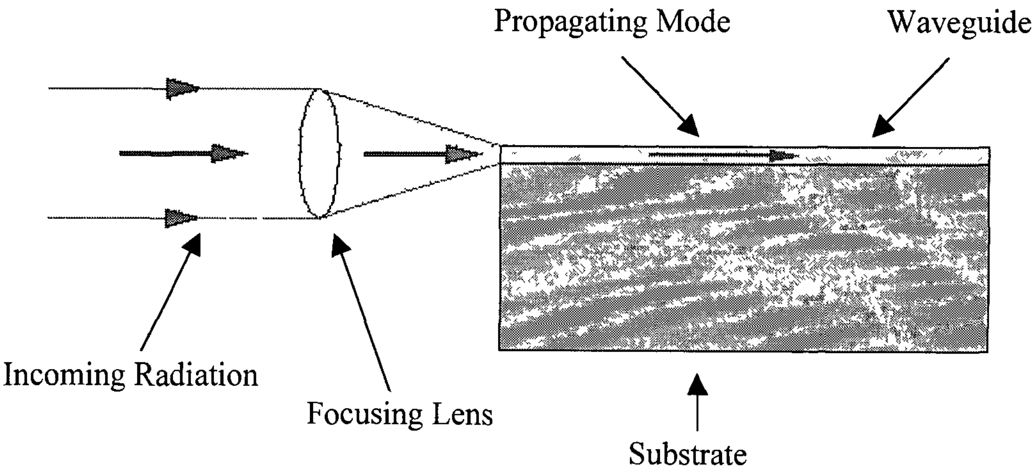

Figure 1.4 *End-fire Coupling into a Planar Waveguide*

1.5.2 Prism Couplers

Prism couplers are a popular laboratory choice for the launching of light into thin film waveguides. The principle of operation is as follows: a plane wave is incident upon the face of the prism as shown in figure 1 5. The beam enters the prism and is totally internally reflected. Upon total internal reflection, an evanescent wave is set up in the air gap below the prism Below the air gap is the waveguide into which coupling is desired. The waveguide can typically support one or more propagating modes which have corresponding evanescent fields that extend upwards into the air gap. These evanescent fields can interact with each other and thus energy from the prism mode can be transferred to the waveguide mode by optical tunnelling.

Prism coupling is a very efficient technique (80% for input coupling). However, it has a number of drawbacks First, the width of the air gap between the prism and the waveguide is critical, and any shift in this dimension alters the coupling efficiency. Second, since the prism is detachable, reproducibility from experiment to experiment is a problem. Finally, the prism needs to have a high refractive index to facilitate total internal reflection, and also needs to be of high optical quality. Therefore, they are usually quite expensive. Due to such drawbacks prism coupling is rarely employed outside of laboratory situations and is certainly not compatible with integrated optic applications.

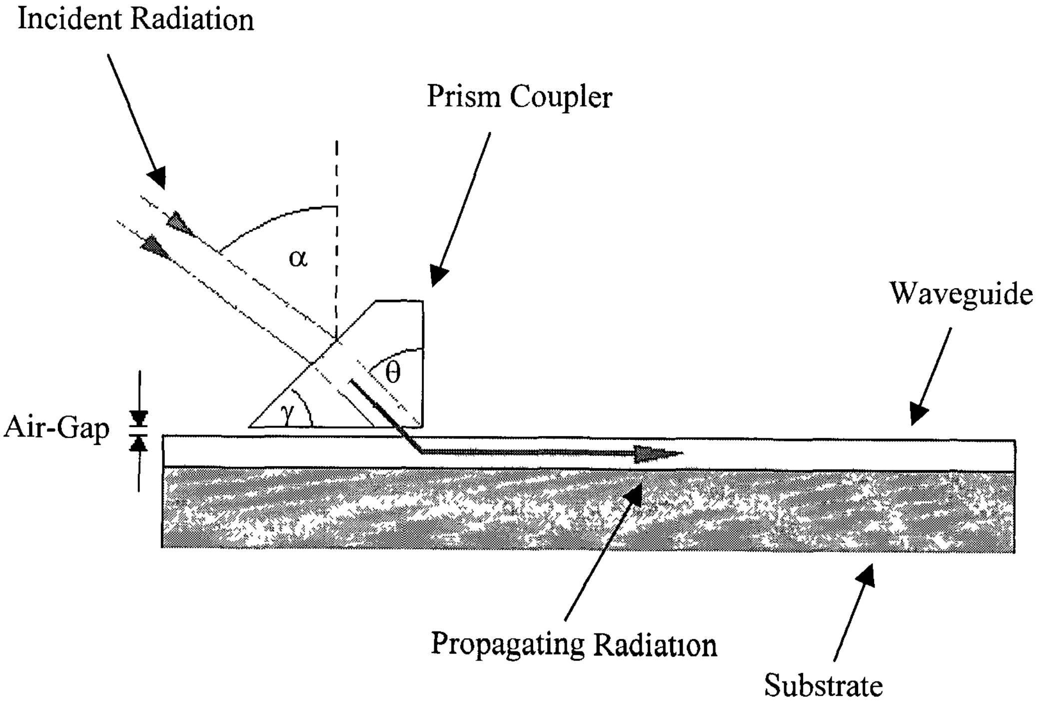

Figure 1.5 *Prism Coupling into a Planar Waveguide*

1.5.3 Grating Couplers

There exists an alternative coupling technique to the two methods described previously. The technique can provide relatively high efficiency, easy alignment and a high level of repeatability. The method in question is grating coupling.

Grating couplers are simply perturbations on the surface of a waveguide, as shown in figure 1.6, which can relax the phase match condition required for coupling between an incident beam and a waveguide mode. They may be fabricated by a variety of methods which range from the highly accurate but expensive technique of reactive ion etching to the low cost technique of embossing a negative image of a surface relief master grating onto the surface of the waveguide.

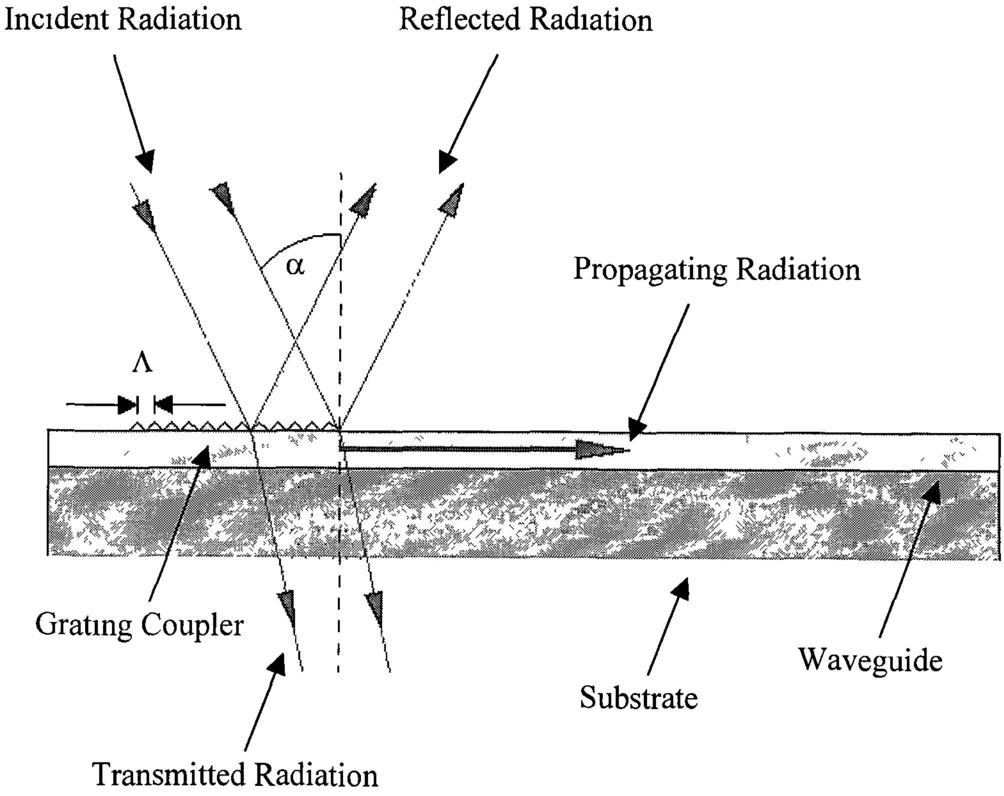

Figure 1.6 *Grating Coupling into a Planar Waveguide*

Radiation incident upon the grating is diffracted and at a certain angle of incidence of the incident beam, the propagation constant of one of the diffracted orders in the waveguide region matches the propagation constant of a guided mode and energy transfer to the guided mode occurs. The coupling conditions for launching light into a guided mode of effective index neff are described by the well-known grating equation

$$n_{eff} - n_a \sin\alpha = \frac{m\lambda}{\Lambda} \qquad [1.2]$$

where n_{eff} is the effective index of the guided mode, n_a is the refractive index of the medium through which the radiation is incident, α is the angle of incidence, m is the diffraction order, λ is the wavelength of the incident radiation and Λ is the grating period

The main advantages of grating couplers are that they are compact and stable in nature. In addition, due to their planar nature, they are easily integrated into many different geometries with which prism and end-face couplers are not compatible. The main drawback of grating couplers is that they are not as efficient as prism couplers due to the large fraction of incident energy transmitted through the structure. Furthermore, due the multiple diffraction orders generated by gratings there can be substantial loss of power to higher non-coupling diffraction orders. However, it is possible to increase grating coupler efficiency by employing asymmetric (blazed) gratings which can be design to increase the power in coupling diffraction orders.

Finally, an alternative technique to coupling radiation into waveguides is to deposit a thin high index overlayer waveguide onto a polished optical fibre and to evanescently couple radiation from the fibre modes to waveguide modes[12].

1.6 The Sol-Gel Process

The sol-gel process[13,14] is a technique which may be applied to the production of glasses and ceramics at low temperatures by the hydrolysis and condensation of organic precursors. The technique can be used to fabricate optical fibres, thin films and bulk monoliths. The preparation of such materials using the sol-gel technique generally involves the use of a metal alkoxide precursor, water, a solvent and a catalyst. These basic ingredients are mixed thoroughly to achieve homogeneity on a molecular scale. Hydrolysis and condensation reactions lead to the formation of a viscous gel, which is an amorphous porous material containing liquid solvent in the pores. From this gel one can produce thin films which can be either porous or densified in structure. The former are produced by curing a thin sol-gel-derived film at low temperatures (typically < 100°C), while the latter are fabricated by curing at elevated temperatures (typically > 400°C). This indicates that the sol-gel process has great flexibility and could be used for a variety of applications. Porous sol-gel derived thin films can be used as sensing layers by physically entrapping an analyte-sensitive reagent in the pores. It is also possible to fabricate sol-gel-derived planar waveguides by densifying thin films produced from a sol-gel with an appropriately high index of refraction at high temperatures. Integrated optic components such as grating couplers, which are used to launch light into guided modes of a waveguide, may also be produced using the sol-gel method, by embossing a thin film. In this thesis the application of the sol-gel process to the production of waveguide based sensor devices will be discussed.

1.7 Surface Plasmon Resonance

Surface Plasmon Resonance (SPR)[15,16] is an optical-electrical effect that may be used as a refractometric-based sensing mechanism to detect for a broad range of chemical and biological species. The principle of operation of SPR is the transfer of energy carried by photons of light to electrons in a thin metal layer (~ 50 nm), as shown in figure 1.7. This results in a decrease in the intensity of the guided signal. The wavelength (or incident angle) of light at which energy transfer occurs is dependent on the type of metal employed and the refractive indices of the surrounding media.

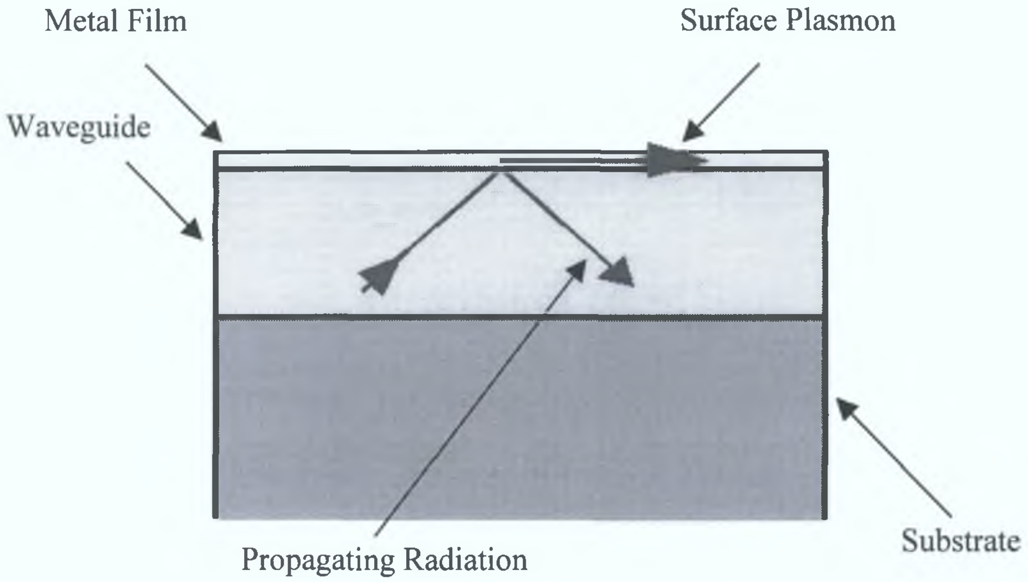

Figure 1.7 *Surface Plasmon Resonance.*

Surface plasmon resonance is a non-specific sensing technique. However, it is possible to use advanced chemical and biological techniques to make the mechanism specific. For example, by attaching to the sensor a molecule that exhibits an affinity only to the target analyte it is possible to detect the target analyte by the mass change undergone at the metal film interface upon binding. These molecules may be an antigen and antibody, a DNA probe and complementary DNA strand or an enzyme and its substrate. The change in mass at the metal surface which manifests itself as a refractive index change produces a shift in the resonant wavelength (or angle) of the incident light. The size of the shift is proportional to the quantity of the analyte in the sample. Because of the specificity of the binding mechanism between the target and immobilised molecules, no other molecules in the sample can be mistakenly measured by the sensor.

There exists a wide range of metals that may be employed to produce SPR such as gold, silver, indium, sodium, copper and aluminium. The main requirement is that the metal must have conduction band electrons capable of resonating with light of the appropriate wavelength. However, some of the metals that may be employed to produce SPR are impractical due to price (indium), reactivity (sodium), broad SPR response (copper, aluminium) and tendency to oxidise (silver). Therefore, gold is usually the metal of choice.

Some areas of application of the surface plasmon resonance sensing technique include medical diagnostics, environmental monitoring, antibiotic monitoring and real time chemical and biological production process monitoring.

1.8 State of the Art

There is increasing interest in the field of integrated-optic (bio)chemical sensors. A great deal of research has been carried out into the production of low-loss waveguides for use in these devices. Ion exchange has been a widely employed technique to produce waveguides for sensor applications for many years[17]. Najafi et al.[18, 19] proposed a novel sol-gel technique for the production of planar, ridge and channel waveguides. A thin film (microns) of a photosensitive sol is deposited on a substrate and selectively cured using UV radiation to produce low-loss waveguide structures. Saavedra et al. reported a method for the production of sol-gel-derived planar waveguides[20] which they later employed in a pH sensor configuration[21]. The waveguides were fabricated by depositing a sol-gel-derived thin film on an appropriate substrate followed by desification at high temperatures (500°C) The waveguides were low-mode in nature and exhibited low propagation losses. The pH sensor configuration employed prism coupling to launch light into guided modes whose evanescent fields interrogated a pH sensitive layer coated on the waveguide surface. The device exhibited good response to pH within the range 4 to 9. Further work by this group reports a grating-coupled waveguide-based device for the detection of gaseous iodine[22]. The device exhibited excellent response to gaseous iodine with a limit of detection of 100 ppb. However, the grating couplers employed to couple light into and out of the waveguides were fabricated using reactive ion etching, which is both a complicated and expensive technique. Many other less complex techniques for the production of grating couplers have been reported in the literature. For example, in 1986 Lukosz et al.[23] described a simple technique for imprinting (embossing) a negative image of a surface relief grating in a sol-gel-derived waveguide using a pneumatically operated piston. The resultant couplers were of a high quality and exhibited high coupling efficiencies. Choquette et al.[24] also employed the embossing technique to produce high quality grating couplers for planar waveguide optical sensors. In this work a small drop of UV curable epoxy was placed onto the waveguide surface and pressed against a master grating and cured by exposure to UV radiation. The gratings produced exhibited coupling efficiencies of the order of 18%. Roncone et al.[25] also described a low cost embossing technique which produced high quality grating couplers on planar waveguides. Saavedra et al.[26] reported a novel configuration of waveguide coupler capable of launching a 70 nm bandwidth of incident radiation into a planar waveguide. The coupler comprised a double-parallel grating assembly and a prism.

Much theoretical research into the optimisation of grating coupling to waveguides has been reported in the literature. Parriaux et al.[27] analysed a silicon-based step-index waveguide with a corrugation at its surface and established the conditions for maximum coupling. Li et al.[28,29] studied planar waveguide-grating couplers to determine the effect of grating length, incident beam size, beam focusing and coupling length on the input coupling efficiency.

Many integrated optic sensors based on the aforementioned techniques have been reported in the literature. Choquette et al.[30] employed a planar waveguide ion-selective sensor. The device employed embossed grating couplers to efficiently couple light to and from guided modes. A potassium-sensitive layer deposited on the waveguide surface was interrogated by the evanescent fields of the modes The device showed excellent response to potassium ions with a limit of detection of 0.05 mM K^+ observed. Burgess et al [31] also developed a planar waveguide sensor for liquid phase absorption measurements The waveguide comprised a thin film of tantalum pentoxide deposited on a glass substrate with a pair of diffraction gratings etched into the substrate surface Finally, Wolfbeis et al [32] presented a study on the detection of gas phase ammonia by means of integrated optical components. Light was launched into guided modes of an ion-exchange waveguide using the end-face coupling technique described in section 1.5.1. The sensing layers consisted of Bromocresol Green or Bromophenol Blue indicators immobilised in silicone. Limits of detection of less than 1 ppm were observed with a dynamic range of 1 to 200 ppm.

1.9 Objectives and Structure of Thesis

The main objective of the work presented in this thesis was the development of generic integrated optic sensor platforms that may be applied to the detection of chemical or biological analytes. The sensors, which were to be fabricated using state of the art sol-gel technology, were to employ guided wave technology and utilise well-known absorption- and fluorescence-based sensing techniques. Finally, the devices had to be miniature, compatible with mass production and possibly disposable in nature. The development of an optimised technology to fabricate both sol-gel-derived waveguides and grating couplers will be presented. These integrated optic components then will be incorporated into a series of sensor platforms which may be applied to the absorbance and fluorescence-based detection of a range of target analytes. Finally, a surface plasmon-based sensor employing optical fibres will be demonstrated and applied to the detection of biological entities.

The structure of the thesis is described in the following paragraphs.

Background information on all the important concepts addressed in the thesis is provided in chapter one. The sol-gel process and its application to the production of a wide range of components from reagent-doped sensing layers to photosensitive materials which may be used to produce integrated optic devices is discussed in chapter two.

Chapters three to six describe the theory, fabrication and characterisation of sol-gel-derived planar waveguides and grating couplers, which are key components in the proposed sensor platforms The application of commercially available software to provide valuable information on device operation and optimisation is also described.

The absorption- and fluorescence-based sensor platform configurations investigated are presented in chapters seven and eight. Application of the various configurations to the detection of gaseous ammonia, carbon dioxide and oxygen is also described in this section of the thesis. It should be noted at this point that sensors response curves are plotted in arbitrary units In reality, sensor output signals of the order of volts with changes due to the presence of a target analyte from hundreds of millivolts to volts being observed.

A separate, unrelated project is also presented in this thesis in chapter nine. The project involved the development of a probe-type biosensor that employed surface plasmon resonance technology. The device configuration and principle of operation is described in detail. The sensor is then applied to the detection of antibodies and red blood cells.

Finally, in chapter ten the presented work is summarised and possible future work and developments are discussed.

References

1. Janata J , Josowicz M., DeVaney D. M.: '**Chemical Sensors**', Analytical Chemistry, 1994, Vol. 66, No. 12, pp. 207R-228R

2. Tamir T.: '**Integrated Optics**', 1979, Vol. 7, Springer - Verlag, New York

3. Najafi S. I.: '**Introduction to Glass Integrated Optics**', 1992, Artech House, London

4. Wolfbeis O. S.. '**Fibre Optic Sensors and Biosensors**', 1991, Vols. I and II, Boca Raton, CRC Press

5. Boisdé G., Harmer A.: '**Chemical and Biochemical Sensing with Optical Fibers and Waveguides**', 1996, Artech House, London

6. MacCraith B. D.: '**Enhanced Evanescent Wave Sensors based on Sol-Gel-Derived Porous Glass Coatings**', Sensors and Actuators B, 1993, Vol. 11, pp. 29-34

7. Snyder A. W., Love J. D.: '**Optical Waveguide Theory**', 1983, Chapman and Hall, London

8. Hecht E.: '**Optics**', 1989, 2nd Ed., Addison - Wesley, Wokingham

9. Lee D. L.: '**Electromagnetic Principles of Integrated Optics**', 1986, Wiley, New York

10. Nishihara H., Haruna M., Suhara T.: '**Optical Integrated Circuits**', 1989, McGraw - Hill, New York

11. Hunsperger R. G : '**Integrated Optics: Theory and Technology**', 1991, 3rd Ed , Springer - Verlag, New York

12. Flannery D., James S. W., Tatam R. P., Ashwell G. J.: '**Fiber Optic pH Sensors Using Thin-Film Langmuir-Blodgett Overlay Waveguides On Single-Mode Optical Fibers**', Proc SPIE Vol. 3133, 264-272

13. Brinker C. J., Scherer G. W : '**Sol-Gel Science**', 1990, Academic Press, New York

14. Klein L. '**Sol-Gel Optics: Processing and Applications**', 1994, Kluwer, London

15. Raether H.. '**Surface Plasmons on Smooth and Rough Surfaces and on Gratings**', 1988, Springer - Verlag, New York

16. Liedberg B., Nylander C., Lundström I.: '**Surface Plasmon Resonance for Gas Detection**', Sensors and Actuators, 1983, Vol. 4, pp. 299-304

17. Anzaria Z. A., Karekar R. N., Aiyer R. C.: '**Humidity Sensor Using Planar Optical Waveguides With Claddings of Various Oxide Materials**', Thin Solid Films, 1997, Vol. 305, No. 1-2, pp. 330-335

18. Fardad A , Andrews M., Milova G , Malek-Tabrizi A , Najafi I.: '**Fabrication of Ridge Waveguides: A New Sol-Gel Route**', Applied Optics, 1998, Vol. 37, No. 12, pp. 2429-2434

19 Coudray P., Etienne P., Moreau Y., Porque J., Najafi S. I : '**Sol-Gel Channel Waveguide on Silicon: Fast Direct Imprinting and Low Cost Fabrication**', Optics Communications, 1997, Vol. 143, pp 199-202

20. Yang L., Saavedra S. S., Armstrong N. R., Hayes J.: **'Fabrication and Characterisation of Low-Loss, Sol-Gel Planar Waveguides'**, Analytical Chemistry, 1994, Vol. 66, No 8, pp. 1254-1263

21 Yang L., Saavedra S. S.: **'Chemical Sensing Using Sol-Gel-Derived Planar Waveguides and Indicator Phases'**, Analytical Chemistry, 1995, Vol. 67, No. 8, pp. 1307-1314

22. Yang L., Saavedra S. S., Armstrong N. R.: **'Sol-Gel-Based Planar Waveguide Sensors for Gaseous Iodine'**, Analytical Chemistry, 1996, Vol. 68, No. 11, pp. 1834-1841

23 Heuberger K., Lukosz W.· **'Embossing Technique for Fabricating Surface Relief Gratings on Hard Oxide Waveguides'**, Applied Optics, 1986, Vol. 25, No. 9, pp. 1499-1504

24. Ramos B. L., Choquette S. J., Fell N. F.: **'Embossable Grating Couplers for Planar Waveguide Optical Sensors'**, Analytical Chemistry, 1996, Vol. 68, No. 7, pp. 1245-1249

25. Roncone R. L., Weller-Brophy L. A., Weisenbach L., Zelinski B. J. J.: **'Embossed Gratings in Sol-Gel Waveguides: Pre-Emboss Heat Treatment Effects'**, Journal of Non-Crystalline Solids, 1991, Vol. 128, pp. 111-117

26 Mendes S B., Li L , Burke J. J , Lee J E , Saavedra S S.: **'70-nm-Bandwidth Achromatic Waveguide Coupler'**, Applied Optics, 1995, Vol. 34, No 27, pp. 6180-6186

27 Sychugov V A., Tishchenko A. V., Usievich B. A., Parriaux O.: **'Optimisation and Control of Grating Coupling to or from a Silicon-Based Optical Waveguide'**, Optical Engineering, 1996, Vol. 35, No. 11, pp. 3092-3100

28. Brazas J. C., Li L.: **'Analysis of Input-Grating Couplers having Finite Lengths'**, Applied Optics, 1995, Vol. 34, No. 19, pp. 3786-3792

29. Li L., Gupta M. C : 'Effects of Beam Focusing on the Efficiency of Planar Waveguide Grating Couplers', Applied Optics, 1990, Vol. 29, No. 36, pp. 5320-5325

30 Toth K., Nagy G., Lan B.T.T., Jeney J , Choquette S.J.: **'Planar Waveguide Ion-Selective sensors'**, Analytica Chimica Acta, 1997, Vol. 353, pp. 1-10

31. DeGrandpre M. D., Burgess L. W., White P L., Goldman D. S.: **'Thin Film Planar Waveguide Sensors for Liquid Phase Absorbance Measurements'**, Analytical Chemistry, 1990, Vol. 62, pp. 2012-2017

32. Brandenburg A., Edelhauser R., Werner T., He H., Wolfbeis O.S.: **'Ammonia Detection via Integrated Optical Waveguide Sensors'**, Mikrochimica Acta, 1995, Vol 121, pp. 95-105

Chapter 2 The Sol-Gel Process

2.1 Introduction

The sol-gel process is a material fabrication technique, first reported in 1846 by a French chemist M. Ebelman[1], which may be applied to the production of high purity, homogenous gels, glasses and ceramics[2]. The preparation of such materials by the sol-gel process generally involves the use of metal alkoxides, which undergo hydrolysis and condensation polymerisation reactions to produce three-dimensional structures consisting of Si-O-Si molecules.

One of the primary advantages of the sol-gel technique is that it enables the production of glasses at temperatures, which are significantly lower than those used by conventional melting techniques. Such low temperatures facilitate the production of materials whose compositions may otherwise not be obtained by conventional means due to volatilisation, high melting temperatures or crystallisation problems. The versatility of the sol-gel process also facilitates the production of a wide variety of optical materials such as glass, fibres, monoliths and thin films, which can be both porous and densified in structure, and which may be used to fabricate numerous optical components[3].

In this chapter the basics of the sol-gel processes used in the Optical Sensors Laboratory at Dublin City University will be discussed. The effect on the sol-gel structure of important parameters such as sol pH and ratio of water to alkoxide precursor will also be addressed. This section will also describe how it is possible to control the sol-gel structure by using organically modified precursors, to fabricate structures known as organically modified silicates (ORMOSILS). Fabrication of sol-gel-derived sensing layers by physically entrapping sensing reagents into the sol-gel structure will be addressed. Modification of the refractive index of the sol-gel by the addition of metal alkoxides other than the traditional silicon based precursors and the fabrication of photosensitive sols will also be discussed briefly. Finally, deposition of sol-gel-derived thin films onto substrates using the dip-coating technique will be presented.

2.2 The Basic Sol-Gel Process

A sol is a colloidal suspension of solid particles in a liquid. A gel is an interconnected rigid network with pores of submicrometer dimensions and polymeric chains whose average length is greater than one micron[4]. In a typical sol-gel process the main ingredients required to produce these materials are a metal alkoxide, water, a solvent and a catalyst. The metal alkoxide is also known as a precursor and typically consists of a metal element surrounded by various ligands One of the most common precursors employed in the sol-gel process[5] is tetraethoxysilane (TEOS, $Si(OC_2H_5)_4$). This simply consists of a central silicon atom surrounded by four ethoxy groups. Other types of precursors known as organoalkoxysilanes, which contain one or more organic ligands may also be used. An example of such a precursor is methyltriethoxysilane (MTES, $CH_3(C_2H_5O)_3Si$). One of the primary functions of the solvent is to act as a homogenising agent because water and alkoxysilanes are immiscible It is possible to avoid the use of such an agent if sonication is employed

The basic ingredients of the sol-gel process are mixed together and hydrolysis and polycondensation of the metal alkoxide precursor occurs resulting in the formation of an interconnected rigid network known as a gel This gel may then be subjected to a temperature programme, which controls the densification process and thus the physical characteristics of the resultant material. If the liquid within the gel is removed by simple evaporation then the produced structure is known as a xerogel, while if the liquid is removed above its critical temperature and pressure then it is known as an aerogel[6]. It is possible to fabricate either sol-gel-derived thin films by coating the gel onto substrates or monoliths by casting it in a mould.

2.2.1 Hydrolysis and Condensation

A typical sol-gel is fabricated by the hydrolysis and polycondensation of organometallic compounds[7-9]. The first step in the sol-gel process is hydrolysis and is shown in equation 2.1. The hydrolysis reaction replaces alkoxide groups (OR) on the precursor with hydroxyl groups (OH) by the nucleophilic attack on silicon atoms by oxygen.

$$\equiv \mathrm{Si-OR} + \mathrm{H_2O} \Leftrightarrow \equiv \mathrm{Si-OH} + \mathrm{ROH} \qquad [2.1]$$

The condensation reactions, which are shown in equations 2.2 and 2.3 occur via a nucleophilic condensation reaction and produce siloxane bonds, Si–O–Si, along with by-products of alcohol (ROH), or water.

$$\equiv \mathrm{Si-OR} + \mathrm{HO-Si} \equiv \Leftrightarrow \equiv \mathrm{Si-O-Si} \equiv + \mathrm{ROH} \qquad [2.2]$$

$$\equiv \mathrm{Si-OH} + \mathrm{HO-Si} \equiv \Leftrightarrow \equiv \mathrm{Si-O-Si} \equiv + \mathrm{H_2O} \qquad [2.3]$$

The alcohol itself is an important component in the sol-gel process because it participates in the reverse reactions shown in equations 2.1 and 2.2. In the sol-gel process the condensation reactions continue to build up long polymeric chains of Si-O-Si molecules which with time interlink to become a three-dimensional network which is known as a gel. The physical characteristics of this gel network depend upon the size of particles and extent of cross-linking prior to gelation. The gelation time t_g is defined as the point in time at which the sol can support a stress elastically. Experimentally, the point of gelation is marked by a sharp increase in the viscosity of the sample due to an increased number of interconnected particles.

2.2.2 Ageing and Drying

Ageing is the term used to describe the process whereby after the ingredients have been mixed the sol is left at elevated temperature so as to accelerate the hydrolysis and condensation process. The ageing process serves a number of purposes. Aging for sols used to produce monoliths is different to that of a sol being used for deposition of thin films A monolithic sol may be aged before or after gelation and the main aim to is produce a gel which is strong enough to withstand the stresses encountered during the drying stage For coating sols, the main function of aging is to increase the viscosity of the solution by accelerating cross-linking of polymers to ensure that dip-coating is possible.

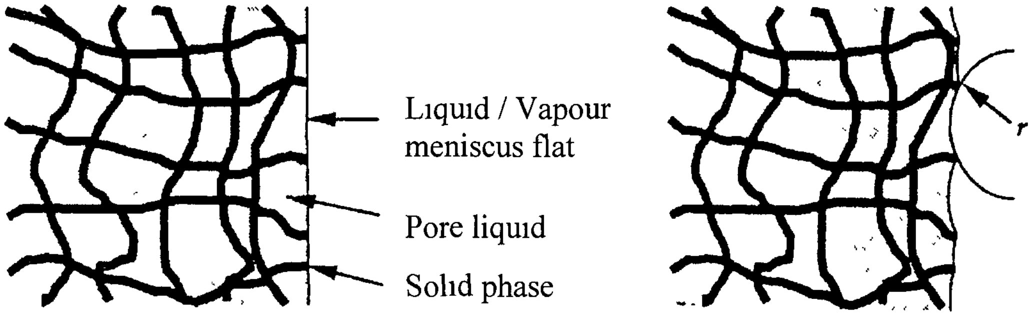

a) Initial condition

b) Constant rate period

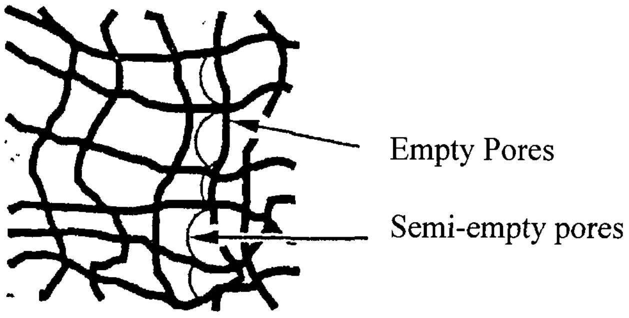

c) Falling rate period

Figure 2.1 *Drying stages of the sol-gel process*[6]

A drying process is essential for the removal of excess liquid from the interconnected pore network. The drying process may be divided into distinct stages[6]. The first stage is known as the constant rate drying period since the rate of evaporation per unit area is independent of time. In this stage the fabricated gel network is deformed by the large capillary forces and the structure shrinks by an amount equal to the volume of liquid that evaporates and the liquid – vapour interface remains on the outside surface of the structure as can be seen in figure 2.1b. The second stage which is referred to as the falling rate period occurs when the gel network stiffens due to shrinkage and the evaporating liquid moves the menisci into the interior of the structure and leaves air-filled pores near the surface of the structure. The falling rate period is illustrated in figure 2.1c.

One of the major disadvantages of sol-gels is that they are liable to crack during the second drying period due to some pores emptying before their neighbours. Such a scenario may be prevented by employing a number of different techniques. Ageing a gel before drying has the effect of strengthening the network and thus reducing the possibility of cracking. Also surfactants or drying control chemical additives (DCCA) may be included in the recipe to prevent cracking occurring. Surfactants reduce the interfacial energy and thereby decrease the capillary stress while DCCA's produce gels that are harder and have a larger and more uniform pore size which helps to reduce cracking

2.3 Factors Affecting the Sol-Gel Process

2.3.1 Influence of pH of Sol

The pH value of the starting solution is one of the more important parameters in the sol-gel process because it determines whether the process is acid or base catalysed Acid catalysis is usually associated with fast hydrolysis and relatively long gel times Acid catalysis produces structures with a fine network structure of linear chains with pore sizes < 2 nm. On the other hand, base catalysis gives slow hydrolysis but the gel times are faster due to faster condensation rates[2]. Under basic conditions more dense colloidal particles are formed with larger pores. For silica, starting solutions of pH < 2 are acid catalysed while solutions of pH > 2 are base catalysed, due to the fact that the isoelectric point of silica (the point at which the electron mobility and surface charge is zero) occurs at approximately pH = 2. This pH value then defines the boundary between acid and based catalysis in silica sol-gel processes

The dependence of the gel time of sols catalysed by HCl on the starting solutions pH value[10] is clearly illustrated in figure 2.2, where the gel time is equal to 1 / average condensation rate. It can be seen from this plot that the overall condensation rate is minimised between pH values of 1.5 – 2.0 and maximised approximately at a pH value of 4.

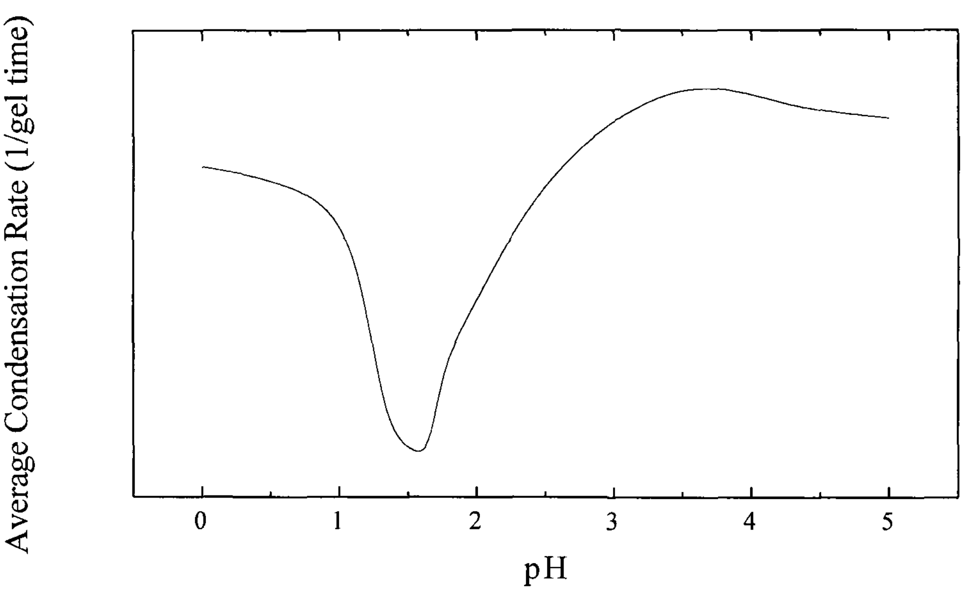

Figure 2.2 *Condensation rates for TEOS as a function of pH*[10]

2.3.2 Influence of the Ratio of Water to Precursor (R Value)

The R value of a sol is defined as the molar ratio of water to silicon alkoxide precursor. This is another very important parameter of the sol-gel process because water is used in the hydrolysis reaction and evolved in the condensation reaction Therefore, the amount added to the initial solution can strongly influence the structure of the resultant gel. Theoretically an R value of 2 is sufficient for complete hydrolysis and condensation to occur[2]. However, as a direct consequence of the formation of intermediate species and reverse reactions in the sol-gel process, the hydrolysis and condensation reactions generally do not go to completion under these conditions. Therefore, R values greater than 2 are commonly utilised to ensure that hydrolysis is completed before condensation and drying occur. For acid catalysis an initial increase in the R value of a sol will result in a decrease in the gel time at a given pH up to a certain point beyond which the increasing water concentration starts to dilute the sol resulting in increased gel times. Such a phenomenon is illustrated in figure 2.3.

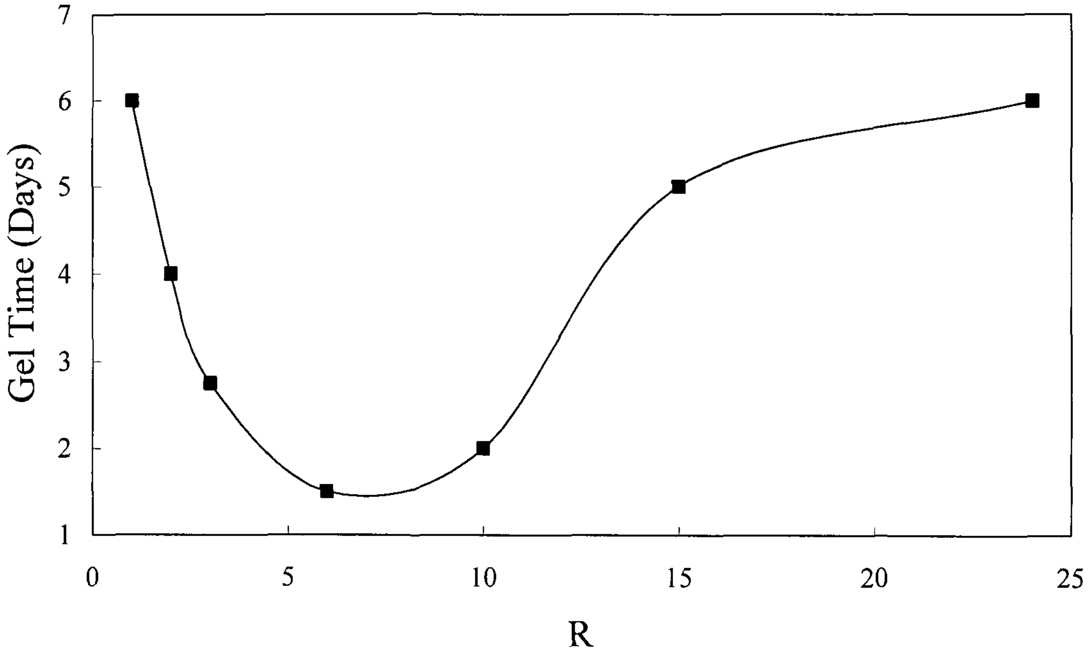

Figure 2.3 *Gelation Time as a function of R value*[2]

2.4 Ormosils

Standard alkoxide (such as TEOS) based sol-gels have hydrophilic surfaces, which are covered with hydroxyl groups, which allow the adsorption of water molecules. This however is not always a desired characteristic and certain applications require the surface of a sol-gel material to be hydrophobic. This requirement necessitates the removal of the hydroxyl groups from the surface of the structure. Many techniques for the removal of hydroxyl groups have been investigated, the most important ones being thermal dehydration and chemical modification. For thin films thermal dehydration is not a feasible option due to cracking of the structure at elevated temperatures and hence chemical modification is the more commonly employed technique Chemical modification involves the combination of organic and inorganic precursors resulting in the formation of materials, which have properties intermediate between those of glasses and polymers. Such materials are referred to as organically modified silicates or ORMOSILS[11].

The use of a modified precursor, which has one or more non-hydrolysable organic groups attached to the silicon atom allows organic components to be incorporated into a sol-gel material. A typical example of a modified silicon alkoxide precursor is methyltriethoxysilane (MTES, $CH_3(C_2H_5O)_3Si$), in which a methyl group replaces one of the ethoxy groups This methyl group is bonded to the silicon atom through a non-hydrolysable covalent bond and has a substantial effect on the surface properties of the sol-gel structure. The use of ORMOSILS results in the replacement of surface hydroxoyls with methyl groups which gives rise to hydrophobic surfaces.

Ormosils also have some very interesting properties, which distinguish them from standard inorganic materials. The addition of an organic component to a sol-gel structure enables the fabrication of crack-free sol-gel derived thin films of up to 2 μm in thickness. This is substantially greater than the maximum crack-free thickness of 0.5 μm obtained for films prepared using standard silicon alkoxide precursors such as TEOS[28]. It is also possible to control the porosity of sol-gel derived material by carefully controlling the type and concentration of the organic groups[12]. Typically, the hybrid organic-inorganic gels are less porous and more dense in nature than the standard inorganic gels[13]

2.5 Entrapment of Sensing Reagents

Sol-gel technology offers a wide range of advantages as an immobilisation technique for chemical reagents in optical sensor applications[14]. One of the primary advantages is that it is a low temperature process. Consequently, organic and biological molecules with poor thermal stability, which otherwise may not be immobilised into glass, may now be encapsulated. The impregnated reagents are accessible to gases and liquids for sensing applications due to the struture porosity. Among the other advantages is the fact that the fabrication process for the production of sol-gel-derived glass and doped sol-gel derived glasses is simple, versatile and inexpensive and the fabricated glass matrix is transparent down to wavelengths of 250 nm making it suitable for use in spectrophotometric and spectrofluorimetric applications. Another advantage of the sol-gel encapsulation technique is that it is quite easy to immobilise polar organic analyte-sensitive reagents into conventional hydrophilic sol-gels. However, the solubility of these reagents is limited on encapsulation into sol-gel environments of a reduced polarity In a hydrophilic sol-gel fabricated using a standard silicon alkoxide precursor, hydrogen bonding between the dye and the surface hydroxyl groups is high. Upon reducing the silanol group population (as in case for ormosils) the alkyl groups which reside on the surface do not interact with the polar dyes. Additionally it is often desirable to control the protonated / deprotonated dye population. For the detection of acid species, the dyestuff has to have a large deprotonated population, which may interact with environmental protic species to effect a sensor reaction. In the acid environment of micro-porous sol-gel fabrication the deprotonated dye population is reduced by dye – silanol group interactions. This problem has been overcome by the use of phase transfer reagents co-extracted with the dye. Such reagents facilitate the incorporation of the deprotonated polar dye into an ormosil matrix.

The application of doped sol-gel-derived thin films for the detection of a range of analytes such as metal ions, gases such as oxygen, ammonia and carbon dioxide and pH change has been demonstrated by many research groups world-wide[15-18]. One of the sole drawbacks of the immobilisation technique is that there is a certain amount of leaching out of the entrapped reagent from the matrix[19]. However, it is possible to overcome such problems by covalently binding the reagent to the matrix or employing matrices with extremely small pore dimensions

2.6 Refractive Index Modification

There are many applications in optical technology, which require control of component refractive index. One such area of interest is the fabrication of thin films, which may function as planar waveguides for transmission of information or sensing applications The sol-gel process is ideally suited to the production of high quality defect free thin films. However, completely densified silica thin films only have refractive indices of about 1.46. Such a thin film while of high enough quality usually has too low a refractive index to be considered for the application of planar waveguides since the majority of substrates used in planar waveguide structures have indices of refraction of greater than 1.46. Thus the sol-gel derived thin film could not function as a planar waveguide when coated on such substrates. However, it is possible to fabricate high refractive index sol-gel derived thin films by incorporating different metal alkoxide precursors into the traditional silicon based sol-gel recipe[20].

Titania (TiO_2) has a much higher refractive index than silica (SiO_2). Incorporation of titania into a sol-gel matrix would result in an increase in the refractive index of the structure. This may be realised by incorporating titanium metal alkoxide precursors into silicon based sol-gel recipes[21,22]. It is important to maintain anhydrous conditions during the sol-gel process when using titanium alkoxide precursors. This is due to vastly different hydrolysis rates for silicon alkoxide and titanium alkoxide precursors. If an abundance of water were present, it would result in titania and silica rich sites throughout an inhomogeneous glass. The amount of titanium precursor added will determine the refractive index of the resultant sol-gel and of any thin films fabricated. Thin films of a high refractive index sol may be deposited on substrates, densified at elevated temperatures and used for a variety of applications, such as planar dielectric waveguides for light transportation and chemical sensing[23].

2.7 Photosensitive Sols

Photosensitive sol-gel-derived hybrid glasses are rapidly becoming popular for the production of integrated optical components[24-26] Upon exposure to ultraviolet radiation these novel materials densify as a result of photoinitiated polymerisation of monomeric species entrapped within the matrix. Photo-mask technology allows for selective exposure of regions of the material and may be used to produce integrated optic components such as ridge waveguides, splitters and gratings.

The typical photosensitive sol ingredients are a silicon alkoxide with a vinyl moiety, a vinyl monomer, a solvent, a catalyst and a photoinitiator, which promotes polymerisation of the vinyl monomer For fabrication of integrated optical devices, a thin film of the photosensitive material is deposited onto a substrate. The film may be prebaked at elevated temperatures prior to UV exposure to harden the films sufficiently to prevent adhesion to the photomask during photoimprinting. Samples are then placed in contact with a mask of the desired profile and exposed to ultraviolet radiation. This initiates polymerisation of the vinyl groups contained within the thin film as well as forming long chain polymers from the vinyl pendant groups on the silicon alkoxide sol-gel precursor. Therefore, covalent bonds are formed between the glass and polymer species in the bulk material resulting in the formation of a coherent hybrid network. Subsequent washing with alcohol removes any monomeric species from the unexposed areas leaving only UV photopolymerised regions of the film. The devices are then postbaked at elevated temperatures to promote hardening.

2.8 Dip-Coating Process

Thin films may be deposited on planar substrates by a number of different deposition techniques. However, by far the two most popular are dip-coating and spin-coating. Both of these techniques have the ability to deposit thin layers of very precise thicknesses. Dip-coating is primarily the technique used in this work for the deposition of thin films for sensing and waveguiding applications, and this technique will now be discussed in more detail.

The dip-coating technique may operate in two distinct modes· firstly, by maintaining the sample at a fixed position and drawing the liquid away at a constant rate and secondly by maintaining the liquid at a constant position and removing the sample. The former is the technique employed in this work.

The dip-coating process[27-29] may be divided into five separate stages immersion, start-up, deposition, drainage and evaporation. With volatile solvents such as alcohol, evaporation normally accompanies the start-up, deposition and drainage steps The entire dip-coating process is illustrated in figure 2 4.

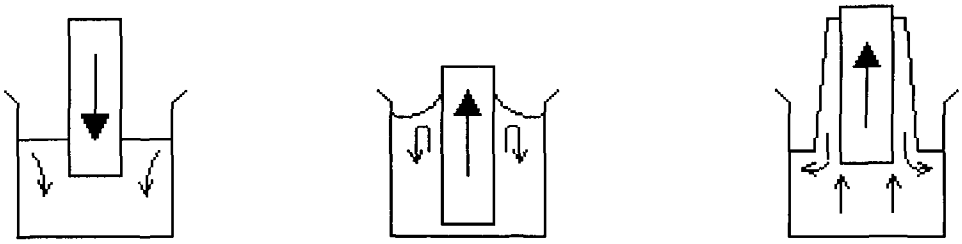

Immersion Start-up Deposition & Drainage

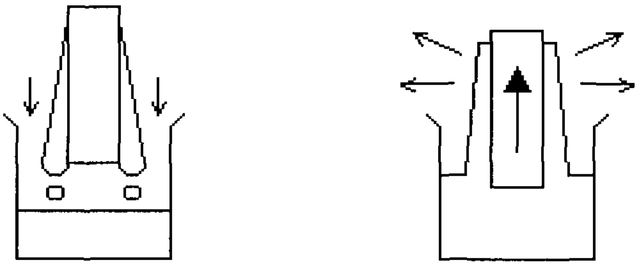

Drainage Evaporation (Constantly occurring)

Figure 2.4 *Example of Stages in Dip-coating process*

As the sample is immersed in the liquid and withdrawn, the inner layer of deposited liquid moves in tandem with the substrate while the outer layer returns to the container The film thickness is related to the position of the dividing border between the upward moving and the downward moving layers. In the dip-coating technique there are a number of forces, each in competition with one another which determine the position of the streamline and hence the film thickness. They are: (1) viscous drag upward on the liquid due to the relative movement of the substrate and the liquid container; (2) force due to gravity; (3) surface tension; (4) inertial force of the boundary layer liquid arriving at the deposition region, (5) the disjoining or conjoining pressure.

The relationship between film thickness and dip speed for Newtonian fluids is shown in the following equation[27]

$$t = 0.944(N_{ca})^{1/6}\left(\frac{\eta U}{\rho g}\right)^{1/2} \qquad [2.4]$$

where t is the film thickness, U is the dip speed, η is the liquid viscosity, N_{ca} is the capillary number, ρ is the density of the solution and g is the acceleration due to gravity. If, as is the case with the sol-gel derived materials, the viscosity and density of the sample remain constant then the film thickness is proportional to the square root of the withdrawal speed

The dip-coating apparatus used throughout this research was computer controlled and is illustrated in figure 2.5. The substrate is held rigidly above a moveable platform supporting the sol container The mechanism employed to move the platform is a threaded bar rotated by a computer controlled DC motor. When the substrate is immersed in the liquid, the platform is lowered at a constant speed thus depositing a thin film on the substrate.

The quality of the resultant thin films is very much dependent on the smooth removal of the liquid container and as a result the entire dip-coating apparatus is housed in a draught free chamber. It is also crucial to minimise vibrations during the dip-coating procedure by ensuring no contact is made with the apparatus

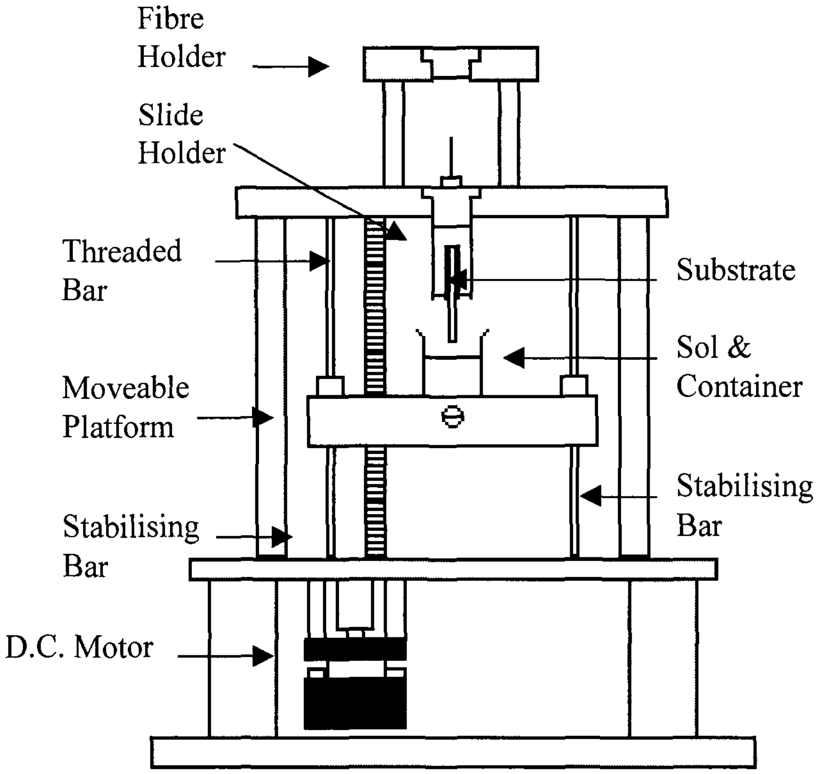

Figure 2.5 *Dip-coating apparatus*

Another commonly used thin film deposition technique is spin coating[30,31]. This technique involves the deposition of thin films by centrifugal draining and evaporation. The liquid to be deposited is placed at the centre of the substrate and the entire device is rotated at the required rate resulting in the uniform spreading out of the deposited liquid into a thin uniform film. However, this technique was not employed during the course of this work.

2.9 Conclusion

In conclusion, the sol-gel process, a technique for the production of gels, glasses and ceramics has been described in detail. The technique offers a number of advantages over conventional fabrication techniques when applied towards the production of optical components, some of which are discussed below

(1) The sol-gel process is a low temperature application with operating temperatures for the production of sol-gel-derived glasses in the range 25°C (for porous glass) to 500 °C (for densified glass). Such relatively low temperatures compare extremely favourably with the high temperatures required for the production of glasses by conventional melting techniques.

(2) The basic ingredients in the sol-gel process are commercially available low grade, low cost chemicals.

(3) The sol-gel process is extremely versatility and may be used to produce a wide range of optical devices, which may be porous or densified in structure and bulk or thin-film in nature. Sensor materials for the detection of a range of chemicals and biomolecules may be fabricated by immobilising an analyte-sensitive reagent in a porous sol-gel-derived material. It has also been shown that it is possible to produce high refractive index and photosensitive glasses using the sol-gel technique. These glasses may be used in the fabrication of integrated optic components such as waveguides and grating couplers

In summary, the sol-gel technique offers a low cost and versatile route for the production of glass components for a number of applications. The process is reliable, reproducible and compatible with mass production techniques. In the course of this thesis the sol-gel process will be applied to the production of densified planar waveguides, grating couplers and porous sensing layers for use in sensor platforms.

References

1. Ebelman M.: '**Annales de Chemie et de Physique**', 1846, No. 3, Vol. 57, pp. 319-355

2. Brinker C.J., Scherer G.W.: '**Sol-gel Science**', 1990, Academic Press, New York

3. MacKenzie J.D.: '**Sol-Gel Optics**', Journal of the Ceramic Society of Japan, 1993, Vol. 101, No. 1, pp. 1-10

4. Hench L.L., West J.K.: '**The Sol-Gel Process**', Chem. Rev., 1990, Vol. 90, pp. 33-72

5. Pope E.J.A., MacKenzie J.D.: '**Sol-Gel Processing of Silica**', Journal of Non-Crystalline Solids, 1986, Vol. 87, pp. 185-198

6. Klein L.C.: '**Sol-gel Optics - Processing and applications**', 1994, Kluwer Academic Publishers

7. Buckley A.M., Greenblatt M.: '**The Sol-Gel Preparation of Silica Gels**', Journal of Chemical Education, 1994, Vol. 71, No. 7, pp. 599-602

8. Sakka S., Kozuka H., Kim S.H.: '**Various Factors Affecting the Conversion of Silicon Alkoxide Solutions to Gels**', Ultrastructure Processing of Advanced Ceramics, 1988, Wiley, New York, pp. 159-171

9. Unger B., Janke H., Hahnert M., Stade H.: '**The Early Stages of the Sol-Gel Processing of TEOS**', Journal of Sol-gel Science and Technology, 1994, Vol. 2, pp. 51-56

10. Coltrain B.K., Melpolder S.M., Salva J.M.: '**Effect of hydrogen ion concentration on Gelation of Tetrafunctional Silicate Sol-Gel Systems**',

Ultrastructure Processing of Advanced Materials, 1992, Wiley, New York, pp 69-76

11 Hoshino Y , MacKenzie J.D.: '**Viscosity and Structure of Ormosil Solutions**', Journal of Sol-gel Science and Technology, 1995, Vol. 5, pp. 83-92

12 Sakka S.: '**The Current State of Sol-Gel Technology**', Journal of Sol-gel Science and Technology, 1994, Vol. 3, pp. 69-81

13. Innocenzi P., Abdirashid M.O., Guglielmi M.: '**Structure and Properties of Sol-Gel Coatings from Methyltriethoxysilane and Tetraethoxysilane**', Journal of Sol-gel Science and Technology, 1994, Vol 3, pp. 47-55

14. Badini G.E., Grattan K.T.V., Tseung A.C., Palmer A.W.: '**Characteristics of Dye-Impregnated Tetraethylorthosilicate (TEOS) Derived Sol-Gel Coatings**', Journal of Sol-gel Science and Technology, 1996, Vol. 6, pp. 269-272

15 Yeatman E.M., Dawnay E.J.C.: '**Doped Sol-Gel Films for Silica-on-Silicon Photonic Components**', Journal of Sol-gel Science and Technology, 1997, Vol. 8, pp. 1007-1011

16. MacCraith B D.. '**Enhanced Evanescent Wave Sensors based on Sol-Gel-Derived Porous Glass Coatings**', Sensors and Actuators B, 1993, Vol. 11, pp. 29-34

17 Kraus S.C., Czolk R., Reichert J., Ache H J.. '**Optimization of the Sol-Gel Process for the Development of Optochemical Sensors**', Sensors and Actuators B, 1993, Vol. 15-16, pp. 199-202

18. MacCraith B.D., McDonagh C.M., O'Keeffe G., McEvoy A.K., Butler T, Sheridan F.R.: '**Sol-Gel Coatings for Optical Chemical Sensors and Biosensors**', Sensors and Actuators B, Vol. 29, pp. 51-57

19. Butler T M., MacCraith B.D., McDonagh C.· '**Leaching in Sol-Gel-Derived Silica Films for Optical pH Sensing**', Journal of Non-Crystalline Solids, 1998, Vol 224, pp. 249-258

20. Vorotilov K.A., Orlova E.V., Petrovsky V.I : '**Sol-Gel TiO2 Films on Silicon Substrates**', Thin Solid Films, 1992, Vol. 207, pp. 180-184

21. McCulloch S., Stewart G., Guppy R.M., Norris J.O.W.: '**Characterisation of TiO_2-SiO_2 Sol-Gel Films for Optical Chemical Sensor Applications**', International Journal of Optoelectronics, 1994, Vol. 9, No. 3, pp. 235-241

22. Orignac X., Vasconcelos H.C., Du X M., Almeida R.M.· '**Influence of Solvent Concentration on the Microstructure of SiO_2-TiO_2 Sol-Gel Films**', Journal of Sol-gel Science and Technology, 1997, Vol. 8, pp. 243-248

23. Yang L., Saavedra S.S., Armstrong N.R., Hayes J.: '**Fabrication and Characterisation of Low-Loss, Sol-Gel Planar Waveguides**', Analytical Chemistry, 1994, Vol. 66, pp. 1254-1263

24. Etienne P , Coudray P., Moreau Y., Porque J.: '**Photocurable Sol-Gel Coatings: Channel Waveguides for Use at 1.55 μm**', Journal of Sol-gel Science and Technology, 1998, Vol. 13, pp 523-527

25. Coudray P., Etienne P., Moreau Y , Porque J., Najafi S.I.: '**Sol-Gel Channel Waveguide on Silicon: Fast Direct Imprinting and Low Cost Fabrication**', Optics Communications, 1997, Vol 143, 199-202

26. Coudray P., Chisham J., Andrews M.P., Najafi S.I.: '**Ultraviolet Light Imprinted Sol-Gel Silica Glass Low-Loss Waveguides for use at 1.55 μm**', Optical Engineering, 1997, Vol 36, No 4, pp 1234-1240

27 Brinker C J., Hurd A.J.: '**Fundamentals of Sol-Gel Dip-Coating**', 1994, J. Phys. III France, pp. 1231-1242

28. Strawbridge I., James P F.: '**The Factors Affecting the Thickness of Sol-Gel-Derived Silica Coatings Prepared by Dipping**', Journal of Non-Crystalline Solids, 1986, Vol. 86, pp. 381-393

29. Brinker C.J., Hurd A.J., Schunk P.R., Frye G.C., Asheley C.S.: '**Review of Sol-Gel Thin Film Formation**', Journal of Non-Crystalline Solids, 1992, Vol. 147-148, pp. 424-436

30. Scriven L E.: '**Physics and Applications of Dip-Coating and Spin-Coating**', Better Ceramics through Chemistry III, 1998, Mat. Res. Soc., Pittsburgh, pp 717-729

31 Meyerhofer D.. '**Characteristics of Resist Films Produced by Spinning**', Journal of Applied Physics, 1978, Vol. 49, No 7, pp 3993-3997

Chapter 3 Waveguide and Grating Coupler Theory

3.1 Introduction

A waveguide is a material medium that confines and supports a propagating electromagnetic wave. It may consist of a hollow metallic conductor, a solid cylindrical glass fibre that has a refractive index greater than that of its surrounding media or it may be a thin dielectric film surrounded by lower refractive index media. The latter type of waveguide is known as a slab-dielectric waveguide and usually has a rectangular cross section, the dimensions of which determine the operating wavelength and the modes the guide will support. Planar waveguides are currently attracting substantial interest in both the telecommunications and sensing industries due to ease of fabrication, low cost and geometrically convenient configurations. In this chapter the underlying theory of the planar waveguide will be described in detail[1-7].

The use of periodic structures with extremely small dimensions (microns) as a technique for launching light into planar waveguides was first proposed by Dakss et al in 1970[8]. Since then, research into the use of grating couplers for both telecommunications[9] and sensing applications[10-13] has gained considerable interest. The main reasons for such continued interest over the past three decades are the ease of fabrication of such grating couplers and their compatibility with current planar fabrication technology, enabling the fabrication of extremely low cost integrated optical devices.

The most basic principle of operation for a grating coupler is the conversion of a specific diffracted order of incident radiation into a guided mode that propagates along the waveguide structure. It is possible to design grating couplers which can couple light into forward or backward propagating modes. However, only forward coupling grating theory will be discussed and presented in this thesis.

3.2 Waveguide Theory

The theory of slab waveguides may be analysed from two different points of view Firstly, one may use the classical ray optic technique, which provides a very simple physical description of waveguide modes and secondly, one may use the more advanced technique of wave optics in which Maxwell's equations may be used to obtain expressions for the guidance condition of modes within a waveguide[1-7]. It is these guidance conditions which fully describe the characteristics of a waveguide mode, and hence are of vital importance in all integrated optics applications and device optimisation. This section will discuss the theory of planar waveguides using both of these approaches.

3.2.1 Ray Optics

A planar waveguide consists of a substrate of refractive index n_s which is assumed to be infinite in thickness, upon which a thin waveguiding layer (thickness = d) of higher refractive index n_f is deposited. The cover layer, which is above the thin waveguide layer is usually air (but not always) and its refractive index is n_c. Such a configuration is illustrated in figure 3.1.

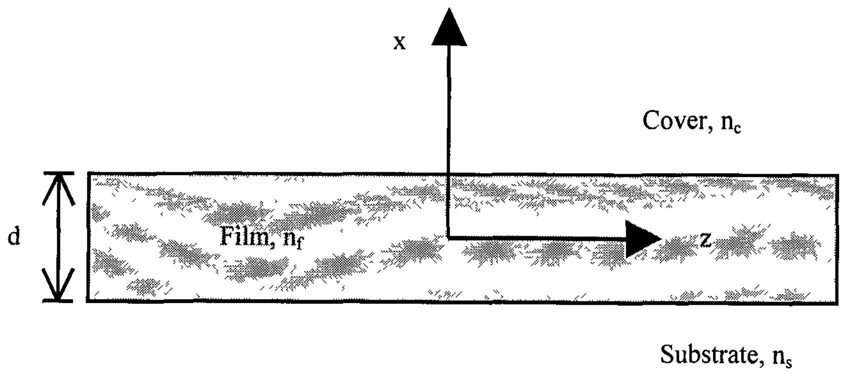

Figure 3.1 *Planar Waveguide*

Consider a beam of light incident at an angle θ with respect to the normal of a step-index slab waveguide, as shown in figure 3.2.

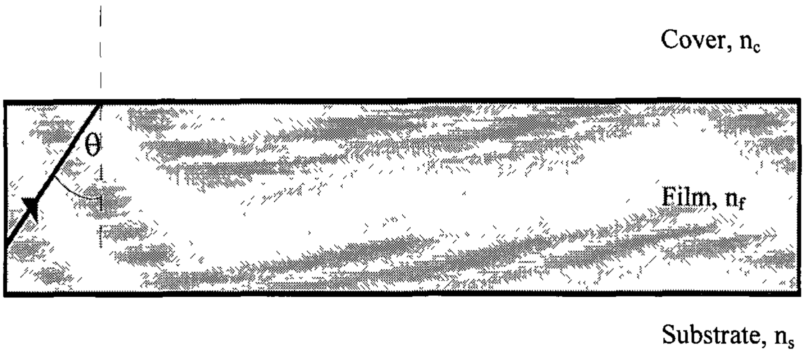

Figure 3.2 *Light beam incident on waveguide interface*

The critical angles at both the upper and lower interfaces are

$$\theta_c^c = \sin^{-1}\left(\frac{n_c}{n_f}\right) \qquad [3.1]$$

and

$$\theta_c^s = \sin^{-1}\left(\frac{n_s}{n_f}\right) \qquad [3.2]$$

Since $n_s > n_c$ in general, it follows that $\theta_c^s > \theta_c^c$. Therefore, three possible ranges of incident angle θ exist: (1) $\theta_c^s < \theta < 90°$, (2) $\theta_c^c < \theta < \theta_c^s$, and (3) $\theta < \theta_c^c$.

(1) $\theta_c^s < \theta < 90°$: here the light is confined in the guiding layer by the total internal reflections at both the upper and lower interfaces and propagates along the zigzag path as shown in figure 3.3. This case corresponds to a guided mode, which is the situation of most interest in this work.

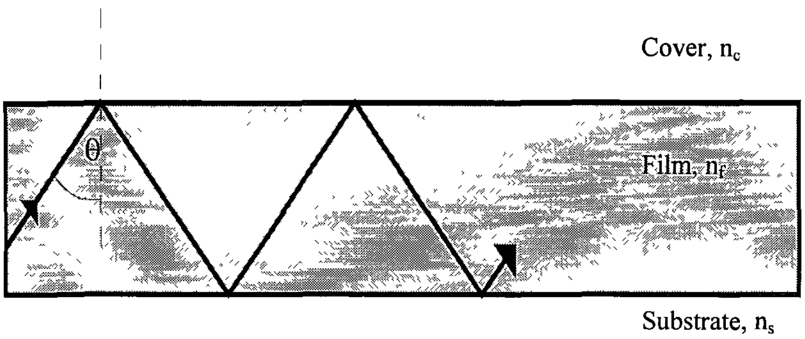

Figure 3.3 *Guided mode,* $\theta_c^s < \theta < 90^\circ$

(2) $\theta_c^c < \theta < \theta_c^s$. This situation is shown in figure 3.4. The incident radiation is totally internally reflected at the film - cover interface but not at the waveguide - substrate interface. Light escapes through the substrate layer according to Snell's law because $\theta < \theta_c^s$. This light is a substrate radiation mode whose amplitude decreases significantly along the propagation direction.

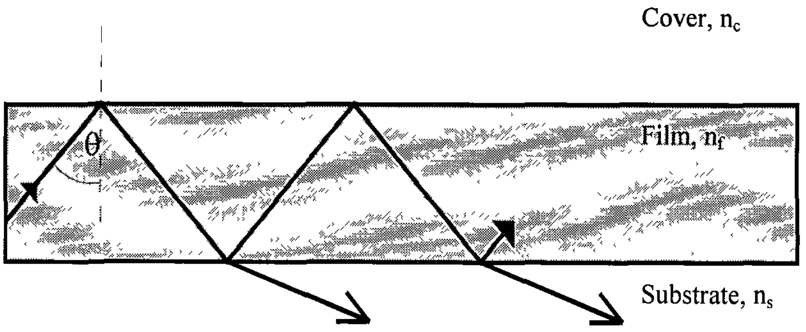

Figure 3.4 *Substrate radiation mode,* $\theta_c^c < \theta < \theta_c^s$

(3) $\theta < \theta_c^c$. this case also leads to a substrate-clad radiation mode that radiates to both the cover and the substrate as shown in figure 3.5

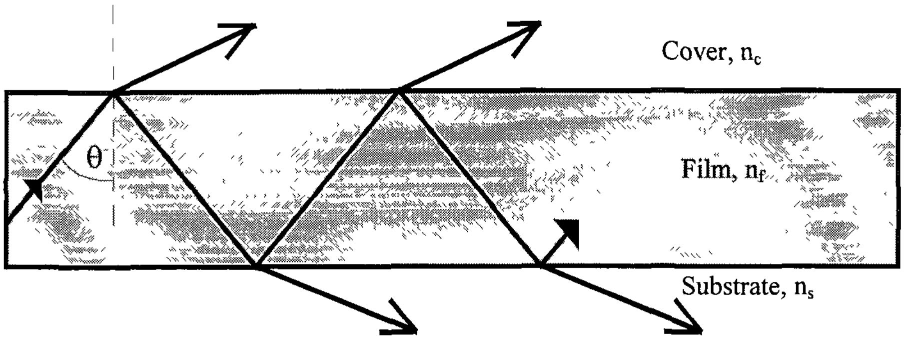

Figure 3.5 *Substrate-clad radiation mode,* $\theta < \theta_c^c$

Modes can be classified easily based on the ray-optical picture. However, we shall concentrate on analysis using the wave optics approach in this work.

3.2.2 Wave Optics

Two of Maxwell's equations in isotropic, lossless dielectric medium are

$$\nabla \times \tilde{E} = -\mu_0 \frac{\partial \tilde{H}}{\partial t} \qquad [3.3]$$

and

$$\nabla \times \tilde{H} = \varepsilon_0 n^2 \frac{\partial \tilde{E}}{\partial t} \qquad [3.4]$$

where ε_0 and μ_0 are the dielectric permittivity and magnetic permeability of free space, respectively, and n is the refractive index. As is shown in appendix 1, it is possible to use these equations to derive an expression for the dispersion relation of an asymmetric planar waveguide as shown in equation 3.5 for the case of TE modes:

$$V\sqrt{1-b} = p\pi + \tan^{-1}\left(\sqrt{\frac{b+a^{TE}}{1-b}}\right) + \tan^{-1}\left(\sqrt{\frac{b}{1-b}}\right) \qquad [3.5]$$

where V, the normalised frequency parameter, is given by

$$V = k_0 d \sqrt{\frac{\varepsilon_f - \varepsilon_s}{\varepsilon_0}} \qquad [3.6]$$

b, the normalised waveguide index is expressed as

$$b = \frac{\varepsilon_{eff} - \varepsilon_s}{\varepsilon_f - \varepsilon_s} \qquad [3.7]$$

and a^{TE}, a measure of the asymmetry of the waveguide (in this case for TE modes) is given by

$$a^{TE} = \frac{\varepsilon_s - \varepsilon_c}{\varepsilon_f - \varepsilon_s} \qquad [3.8]$$

This equation fully describes the properties of any guided mode propagating in a planar waveguide. Figure 3 6 is the dispersion plot for equation 3.5. Such a plot enables rapid determination of the properties of any specific guided mode It is clear from the dispersion plot that for the fundamental mode of an asymmetric planar waveguide ($a \neq 0$), and for all higher order modes in both symmetric and asymmetric waveguides there exists a critical value of the normalised frequency (V number) below which the waveguide can not support the guided mode. This frequency is usually referred to as the cut-off frequency (V_m) of the guided mode and is given by equation 3.9

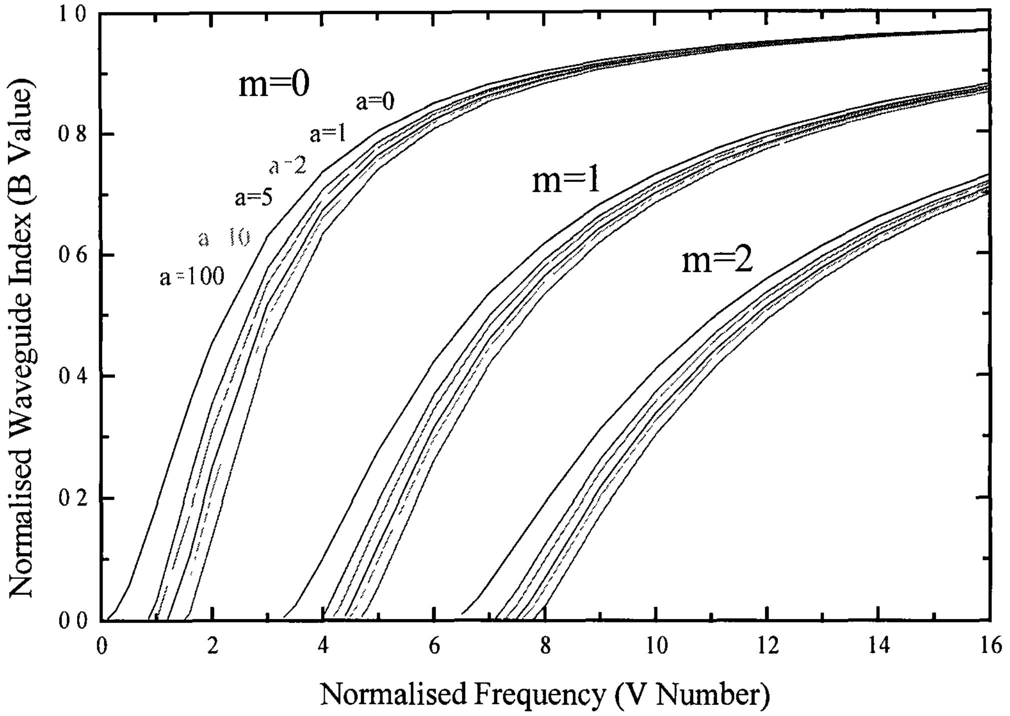

Figure 3.6 *Dispersion curve for TE modes in a slab waveguide (a = a^{TE})*

$$V_m = V_0 + m\pi \qquad [3.9]$$

where $V_0 = \tan^{-1}\sqrt{a}$ is the cut-off value for the fundamental mode and m is the mode number. Such a cut-off situation occurs when the effective index of the guided mode n_{eff} is equal to or less than the refractive index of the substrate n_s.

If one numerically evaluates the guidance equation for a given waveguide of known thickness and refractive index profile, a value for the normalised waveguide index (b) is returned. The normalised index for a given guided mode may then be used to determine the modal effective refractive index in accordance with equation 3.7.

3.2.2.1 Penetration Depth

A guided mode in a waveguide of thickness d is essentially confined to a thickness d_{eff} (the effective waveguide thickness) because its evanescent fields extend somewhat into the substrate and cover layers. Such a situation is illustrated in figure 3.8.

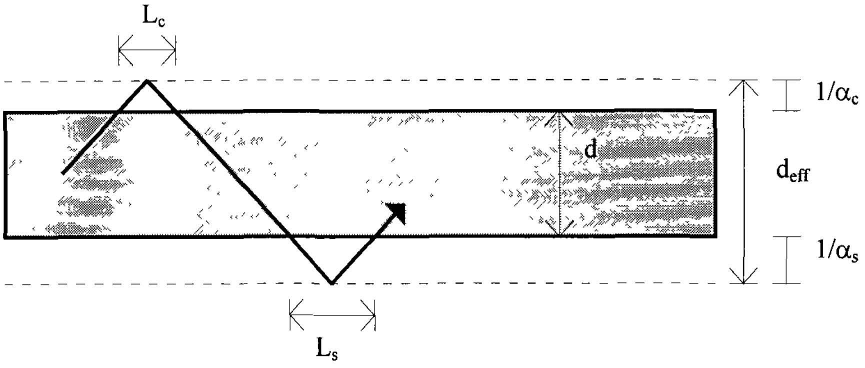

Figure 3.7 *Effective waveguide thickness*

The evanescent fields of the propagating mode extend into the substrate and cover regions, the distances of which are given by $1/\alpha_s$ and $1/\alpha_c$ respectively. Thus, the effective thickness of a waveguide is given by

$$d_{eff} = d + \frac{1}{\alpha_s} + \frac{1}{\alpha_c} \qquad [3.10]$$

The determination of the effective index of a guided mode also allows for calculation of the evanescent field penetration depths into the surrounding media. Shown in figure 3 8 is the dependence of the penetration depth on guided mode effective index.

It is important to realise that the guided mode is actually totally internally reflected at the real interfaces. Consequently, the light undergoes lateral shifts L_s and L_c at the respective interfaces. These lateral shifts due to the total internal reflection are known as *Goos-Haenchen shifts*, and are given by

$$L_c = \frac{2n_{eff}}{k_0\sqrt{n_{eff}^2 - n_c^2} \times \sqrt{n_f^2 - n_{eff}^2}} \qquad [3.11]$$

$$L_s = \frac{2n_{eff}}{k_0\sqrt{n_{eff}^2 - n_s^2} \times \sqrt{n_f^2 - n_{eff}^2}} \qquad [3.12]$$

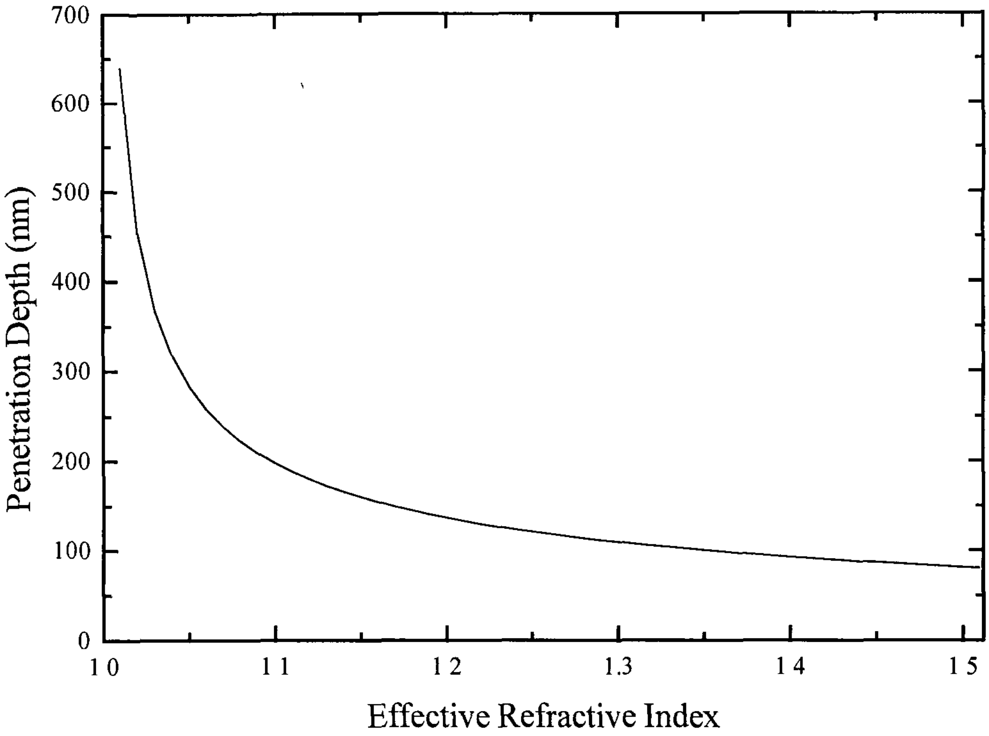

Figure 3.8 *Dependence of penetration depth of evanescent field on modal effective index*

If one wishes to employ planar waveguides as a platform for evanescent-absorbance based sensing then knowledge of the penetration depth of the evanescent field into the cover (or sensing layer) is crucial. This penetration depth is one of the major factors which determines the sensitivity of a waveguide-based sensor. The larger the penetration depth of the evanescent field the more power there is in the sensing layer for absorbance Thus in simple terms the larger the penetration depth the more sensitive the sensor. However this is not always the case. Sometimes the evanescent field can extend beyond the sensing layer, such a situation is more difficult to explain. Figure 3.8 clearly shows the dependence of the penetration depth of the evanescent field of a mode on the effective index of the guided mode.

3.3 Grating Coupler Theory

Perturbations, or periodic structures on the surface of a waveguide, have been shown to possess the ability to couple light from an incident light beam into a thin film waveguide mode[3,4,14-16]. Such devices are commonly referred to as grating couplers. In this section the principle of operation for such grating couplers is discussed in detail.

Let us first consider the case illustrated in figure 3.9 where there is no grating present on the waveguide surface. Radiation from an external source is incident from a medium of refractive index n_a onto the surface of a planar waveguide. The waveguide has a refractive index of n_f and the substrate has a refractive index of n_s, where $n_a < n_s \leq n_f$.

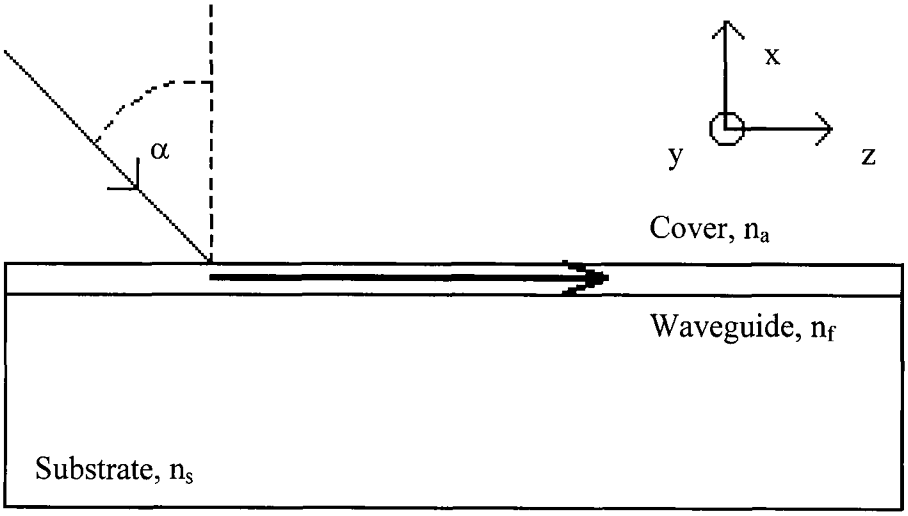

Figure 3.9 *Light beam incident obliquely onto surface of a planar waveguide*

The propagation constant β_{inc} of the incident radiation in the z-direction is given by

$$\beta_{inc} = k_0 n_a \sin\alpha \qquad [3.13]$$

where k_0 is the free-space wavenumber, n_a is the refractive index of the incident medium and α is the angle of incidence

The propagation constant β_{mode} for a guided mode in the planar waveguide is given by

$$\beta_{mode} = k_0 n_{eff} \qquad [3.14]$$

where n_{eff} is the guided mode effective refractive index and $n_s \leq n_{eff} \leq n_f$.

Coupling of power from the incident radiation into the guided mode will only occur if the propagation constants in the z-direction are equal. Thus, a phase-match condition, which requires

$$\beta_{inc} = \beta_{mode} \qquad [3.15]$$

must be satisfied. This equation may be rewritten as

$$k_0 n_a \sin\alpha = k_0 n_{eff} \qquad [3.16]$$

If coupling were to occur in this situation it would require $\sin\alpha > 1$, since $n_a < n_s \leq n_f$ and $n_s \leq n_{eff} \leq n_f$ This is of course impossible and therefore, if light is incident upon the surface of an unperturbed planar waveguide, coupling of power into a waveguide mode is not physically possible.

It is possible, however, to couple into a waveguide mode if one can somehow achieve the phase match condition. Phase matching conditions may be attained by utilising a grating coupler as shown in figure 3.10.

The coupler consists of a grating on or in the surface of a waveguide. Due to its periodic nature the grating perturbs the waveguide modes in the region underneath it, causing each mode to have a set of spatial harmonics propagation constants β_m^{pert} given by

$$\beta_m^{pert} = \beta_0 + \frac{2m\pi}{\Lambda} \qquad [3.17]$$

where m = 0, ± 1, ± 2,. .. , Λ is the spatial periodicity of the grating coupler and β_0 is the fundamental mode in the perturbed region

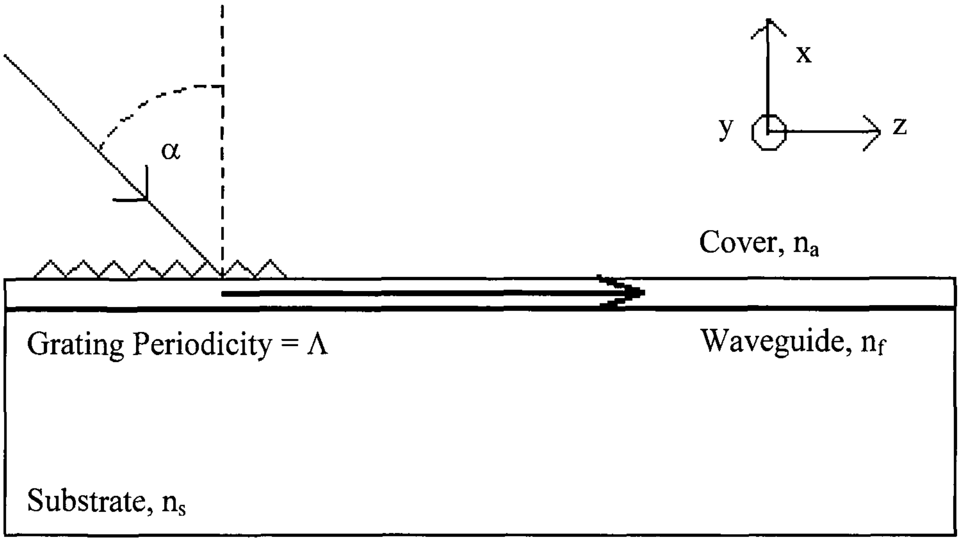

Figure 3.10 *Schematic diagram of a grating coupler*

However, all the spatial harmonics of each mode are coupled together to form the complete surface wave field in the grating region. Therefore, energy coupled from the incident beam into any one of these harmonics is coupled into the fundamental (m=0) harmonic. This fundamental harmonic β_0 is very close in value to the propagation constant of the m^{th} mode β_m outside of the grating region and thus can transfer its energy to the specific mode in the unperturbed waveguide region and hence equation 3.21 may be rewritten as

$$k_0 n_{eff} = k_0 n_a \sin\alpha + \frac{2m\pi}{\Lambda} \qquad [3.18]$$

It can be seen that for some incident angle α the phase match condition can be satisfied since m may be positive or negative. Hence at some incident angle α for external radiation, phase matching is achieved and light can be coupled into a guided mode by radiation from the mth diffraction order of the incident radiation. Equation 3.18 may then be expressed in the more common form of the grating equation.

$$n_{eff} - n_a \sin\alpha = \frac{m\lambda}{\Lambda} \qquad [3.19]$$

The efficiency of the grating coupler for converting radiation from obliquely incident radiation into guided modes is determined by a number of factors including grating depth, grating periodicity, grating layer refractive index, waveguide device properties and input beam focusing, and is discussed extensively elsewhere[17-24]. Due to the complex relationship between the coupling efficiency and the parameters mentioned above, advanced programming which is beyond the scope of the research presented in this thesis, is required to determine theoretical coupling efficiencies.

Coupling efficiencies of above 30% to planar waveguides are rarely observed. This is due in part to the generation of both reflected and transmitted diffracted beams, only one of which may couple to a propagating mode and also to the fact that only one diffracted order can couple to a waveguide mode For single and low mode waveguides, the coupling conditions required to launch a guided mode are extremely angular intolerant (see chapter 7 for further details). This coupling intolerance can lead to configurational problems with low-mode based waveguide sensors (see chapter 7). It is possible to overcome this problem by employing waveguides which have quasi-infinite number of possible modes. This then facilitates the use of a broadband source focused onto the grating coupler, resulting in a number of grating coupling conditions being satisfied This approach is described in chapter 7 in the context of LED-based sensor platforms.

It is also possible to use the same grating as an output coupler, because, by reciprocity, energy from waveguide modes will be coupled out at specific angles α, corresponding to a particular mode.

3.4 Conclusion

The theory of planar waveguides has been addressed from both a ray optic and a wave optic viewpoint. A derivation of the dispersion equation for transverse electric (TE) waveguide modes, and how this equation may be used to determine all the required parameters of the guided modes such as effective index, penetration depth into surrounding media has been presented.

The underlying theory of converting energy from radiation incident on a waveguide device into a guided mode using grating coupling has also been explained in detail and the grating equation was derived.

References

1. Snyder A. W., Love J D · '**Optical Waveguide Theory**', 1983, Chapman and Hall, London

2. Lee D. L.: '**Electromagnetic Principles of Integrated Optics**', 1986, Wiley, New York

3. Nishihara H., Haruna M , Suhara T.· '**Optical Integrated Circuits**', 1989, McGraw - Hill, New York

4. Hunsperger R. G.: '**Integrated Optics: Theory and Technology**', 1991, 3rd Ed., Springer - Verlag, New York

5. Wilson J., Hawkes J. F. B.: '**Optoelectronics: An Introduction**', 1983, Prentice - Hall, London

6. Lit J W. Y., Li Y. F., Hewak D W.: '**Guiding Properties of Multilayer Dielectric Planar Waveguides**', Canadian Journal of Physics, 1988, Vol. 66, pp. 914-940

7. Tamir T.· '**Integrated Optics**', 1979, Vol. 7, Springer - Verlag, New York

8. Dakss M.L., Kuhm L., Heidrich P.F., Scott B.A.: '**Grating coupler for efficient excitation of optical guided waves in thin films**', Applied Physics Letters, 1970, Vol. 16, pp. 523-525

9. Strasser T.A., Gupta M.C : '**Grating coupler dispersion compensation with a surface-relief reflection grating**', Applied Optics, 1994, Vol. 33, No. 15, pp. 3220-3226

10. Kunz R.E., Kempen L.U.: '**Miniature Integrated Optical Sensors**', Chemical, Biochemical and Environmental Fiber Sensors V, Proc. SPIE, 1994, Vol. 2068

11. Lukosz W., Nellen P M., Stamm C., Weiss P '**Output grating couplers on planar waveguides as integrated optical chemical sensors**', Sensors and Actuators B, 1990, Vol. 1, pp. 585-588

12. Tiefenthaler K., Lukosz W.: '**Integrated optical switches and gas sensors**', Optics Letters, 1984, Vol. 9, pp. 137-139

13. Nellen P.M., Lukosz W.: '**Model experiments with integrated optical input grating couplers as direct immunosensors**', Biosensors & Bioelectronics, 1991, Vol. 6, pp. 517-525

14. Najafi S. I.: '**Introduction to Glass Integrated Optics**', 1992, Artech House, London

15. Tamir T.: '**Beam and Waveguide Couplers**', Integrated Optics, Topics in Applied Physics, 1985, Vol 7, 2nd Edition, Springer-Verlag

16. Avrutsky I.A., Svakhin A.S., Sychugov V.A., Parriaux O.: '**High efficiency single order waveguide grating coupler**', Optics Letters, 1990, Vol. 15, pp. 1446-1448

17 Tamir T., Peng S.T : '**Analysis and design of grating couplers**', Applied Physics, 1977 Vol. 14, pp 235-254

18. Touam T., Najafi S.I.: '**Accurate analysis of reflective and diffractive gratings for integrated optics**', SPIE Proc, Vol. 2695, pp. 57-70

19. Kunz R.E., Dubendorfer J., Morf R H.: '**Finite grating depth effects for integrated optical sensors with high sensitivity**', Biosensors & Bioelectronics, 1996, Vol. 11, No. 6/7, pp. 653-667

20. Sychugov V.A , Tishchenko A.V., Usievich B.A., Parriaux O.: '**Optimization and control of grating coupling to or from a silicon-based optical waveguide**', Optical Engineering, 1996, Vol. 35, No. 11, pp. 3092-3100

21. Li L., Brazas J C.: '**Analysis of input-grating couplers having finite lengths**', Applied Optics, 1995, Vol. 34, No. 19, pp. 3786-3792

22. Chang K C., Tamir T : '**Simplified approach to surface-wave scattering by blazed dielectric gratings**', Applied Optics, 1980, Vol. 19, No. 2, pp. 282-288

23. Li L., Gupta M.C.: '**Effects of beam focusing on the efficiency of planar waveguide grating couplers**', Applied Optics, 1990, Vol. 29, pp. 5320-5325

24. Pascal D , Orobtchouk R., Layadi A., Koster A., Laval S.: '**Optimized coupling of a Gaussian beam into an optical waveguide with a grating coupler: comparison of experimental and theoretical results**', Applied Optics, 1997, Vol. 36, No. 12, pp. 2443-2447

Chapter 4 Waveguide Fabrication and Characterisation

4.1 Introduction

In this chapter the sol-gel fabrication technique employed for the production of low-loss asymmetric low mode planar waveguides, along with the effect of varying such parameters as sol composition, annealing temperature, annealing time and dip speed on thickness and refractive index are discussed. These studies are used to identify optimum fabrication conditions and parameters required to produce sol-gel-derived waveguides with the appropriate properties for the sensing applications discussed in chapter 7. These properties are a refractive index higher than both the substrate (1.515) and superstrate (1.43) refractive indices and a corresponding thickness which produces low mode guiding structures

Finally, the characterisation procedures utilised to determine the physical and chemical properties of the waveguides such as propagation losses, surface roughness and chemical structure are presented in detail.

4.2 Waveguide Fabrication

This section discusses the fabrication process utilised for the production of sol-gel derived planar waveguides for use in integrated optic sensor platforms. The sol preparation routine used to produce a high refractive index material will be discussed along with the procedure used to prepare substrate for coating with sol-gel derived materials. Finally, the thin film fabrication routine will be discussed.

4.2.1 Sol Preparation

Thin films may only function effectively as waveguides when the refractive index of the film is higher than the refractive indices of both substrate and superstrate[1-5]. In the work presented here the substrates utilised were glass microscope slides of refractive index 1.512. Thin films with refractive indices higher than 1.512 were obtained by adding a titania based refractive index modifier to the silica-based sol.

The sol was prepared by mixing controlled quantities of methyltriethoxysilane ($CH_3(C_2H_5O)_3Si$, MTES), titanium(IV) tetrabutoxide ($Ti(OBu)_4$), and a precatalyst silicon tetrachloride ($SiCl_4$), in ethanol[6]. Hydrolysis and condensation reactions were allowed to proceed as discussed in chapter 2 and the resultant sol was homogeneous, transparent and light yellow in colour The sol was then passed through a 0.45 μm disposable syringe filter to remove any large particles that could reduce thin film quality, stirred for 2 hours and aged for 10-24 hours at room temperature prior to use.

4.2.2 Substrate Preparation

Soda lime glass microscope slides (Chance Propper, n = 1.512) and low grade undoped silicon wafers were used as waveguide substrates Substrates were prepared for use by rigorously cleaning the slide sequentially with de-ionised water, methanol and acetone. The cleaned substrates were then stored in de-ionised water at 70°C for 24 hours prior to use.

4.2.3 Thin-Film Fabrication

Thin films of sol-gel-derived materials were deposited on preconditioned substrates by immersing the substrates in the sol and withdrawing them at a constant speed using a computer controlled dip-coating apparatus as discussed in chapter 2. This technique produced a thin film of uniform thickness on the substrate. After dip-coating the samples were left to dry in air for a short period of time following which they were annealed at elevated temperatures to produce densified thin films which could function as planar waveguides.

The entire sol / waveguide fabrication procedure is illustrated in the flow chart of figure 4.1.

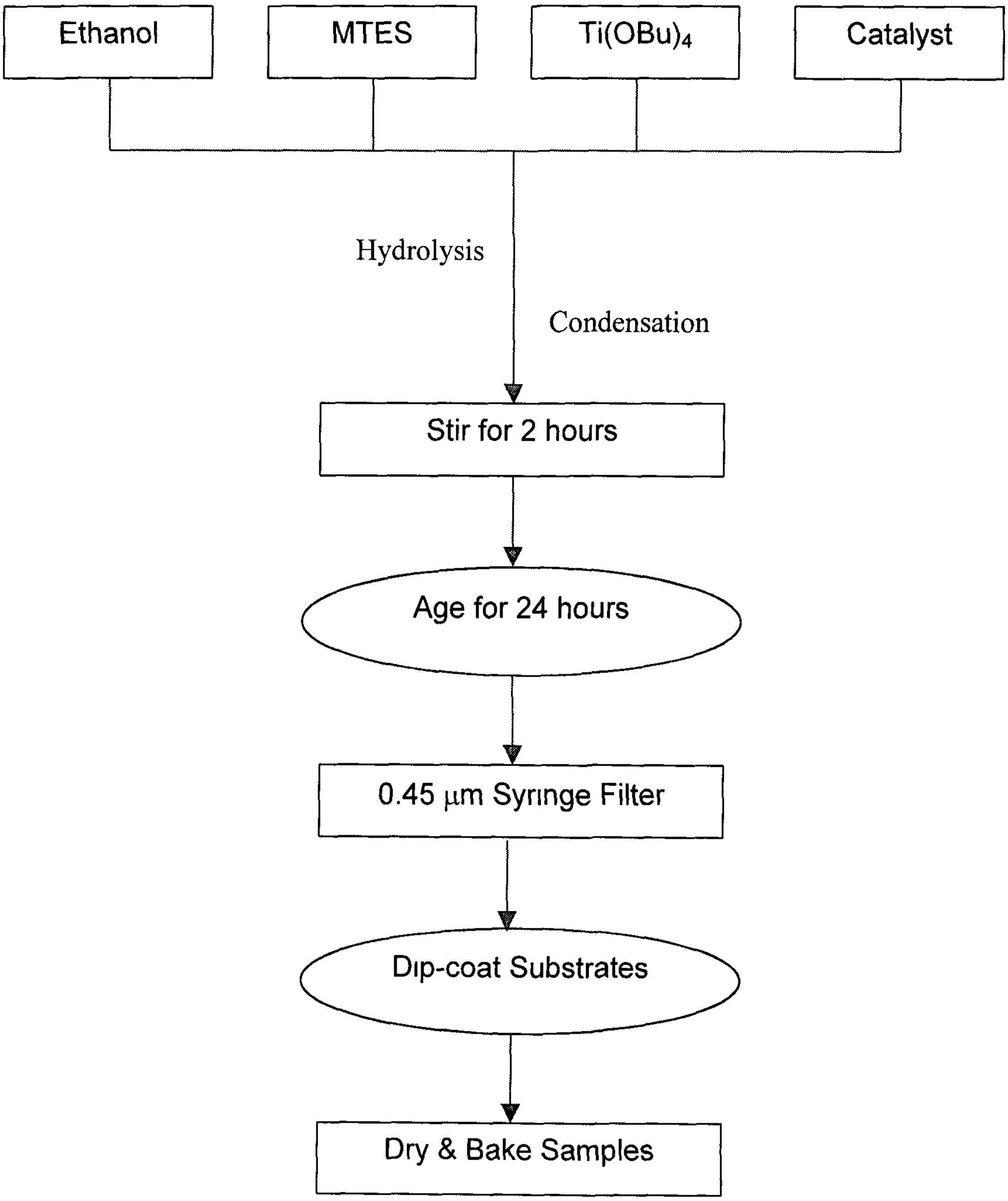

Figure 4.1 *Flow chart of sol preparation procedure*

4.3 Waveguide Characterisation

Once a procedure for the fabrication of sol-gel derived planar waveguides had been identified it was then necessary to characterise the fabricated samples both physically and chemically. Such characterisation provides a route to efficient waveguide fabrication and hence sensors device optimisation. In this section the techniques used to characterise the physical and chemical properties of sol-gel-derived waveguides are presented and the results are discussed.

4.3.1 Physical Characterisation

In this section characterisation of the physical properties of the sol-gel-derived thin films is presented. The effect of fabrication parameters such as dip speed, annealing temperature, annealing time and sol composition on the thin film refractive index and thickness are discussed. This study was used to identify optimum conditions for the fabrication of waveguides. The characterisation of the propagation losses and surface roughness of the resultant waveguides is also reported.

4.3.1.1 Effect of Fabrication Parameters

If the V number of a sol-gel-derived layer is below a certain cut-off value then the thin film can not support guided modes and hence will not function as a waveguide. The V number is determined by the thickness and refractive index profile of the thin film structure, both of which may be controlled by carefully controlling the fabrication procedure. This section deals with the effect of varying processing parameters such as sol composition, annealing temperature, annealing time, dip speed and application of multiple coatings on the refractive index and thickness of the fabricated thin films. This study was then used to identify conditions for the production of optimised waveguide structures that support the desired number of modes and that may be used in sensor applications. It should be noted that all graphical data points presented in this section represent average values of thickness and refractive index measurements at a number of positions along the samples. Typical errors in thickness are ± 10 nm while the errors in the refractive index values are approximately 0.005.

4.3.1.1.1 Sol Composition

The refractive index and thickness of a sol-gel derived thin film are dependent on sol composition. The addition of different amounts of titania precursor (titanium tetrabutoxide) to a silica-based sol mixture enables one to fabricate sols that produce films with a range of refractive indices above that of pure silica.

Sols with a titanium tetrabutoxide content from 0% (v/v) to 30% (v/v) were fabricated using the procedure outlined earlier. Sol-gel derived thin films were fabricated by dip-coating onto silicon substrates at a dip speed of 2.8 mm sec^{-1}. The resultant thin films were then annealed at 500°C for 20 minutes. Ellipsometry was used to determine the refractive index and thickness of the samples. Figure 4.2 shows the effect of sol composition on thickness. It is evident that film thickness increased with increasing titania content. In fact it was possible to produce a large range of film thicknesses (250 nm – 600 nm) by simply varying sol composition and keeping all other parameters constant. It is also evident in figure 4.2 that thin films produced from pure silica sols were slightly thicker than films produced by sols with a low titania content. This anomaly is not understood but is possibly due to different behaviour of pure silica and silica - titania sols

The titania precursor acts principally as a refractive index modifier. It can be seen in figure 4.3 that as concentration of titania precursor in the sol increases, the resultant refractive index of the sol-gel derived thin films increases almost linearly. The only deviation from this behaviour is when there is no titania precursor present in the sol. Here the refractive index is substantially lower than with low titania concentrations.

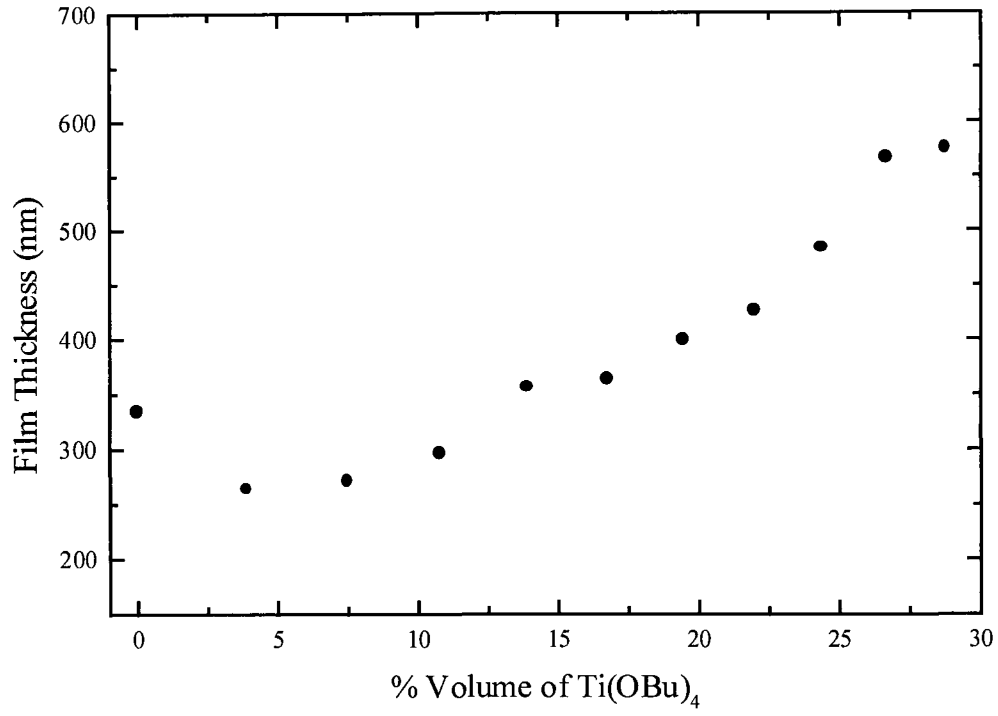

Figure 4.2 *Dependence of film thickness on sol composition*

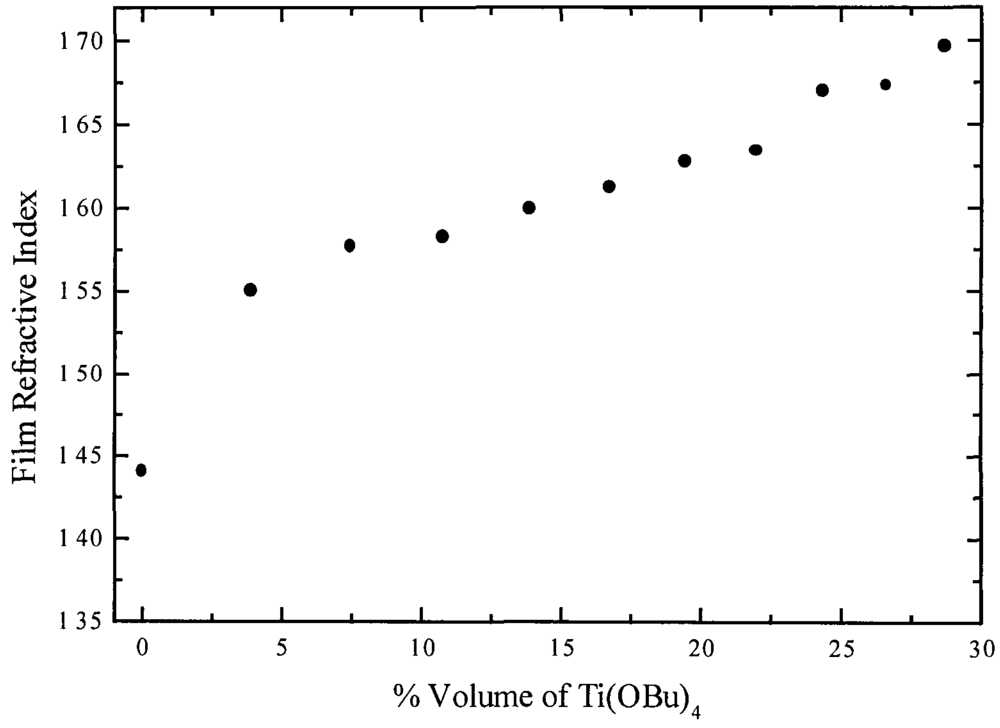

Figure 4.3 *Dependence of film refractive index on sol composition.*

It is clear from these data that varying sol composition enables close control of the thickness and refractive index of sol-gel derived thin films. Thickness ranging from 250 nm to 600 nm and refractive indices of between 1.44 and 1.7 can be produced under identical conditions simply by control of the titania content of the sol.

4.3.1.1.2 Annealing Temperature

After the dip-coating procedure it is necessary to anneal the thin film at elevated temperatures for a period of time. This serves to both harden and densify the layer, resulting in changes in refractive index and thickness while also decreasing propagation losses for guided modes by decreasing film porosity. If sufficient densification does not occur then the refractive index / thickness profile of the thin film may not provide a sufficiently high V number to support guided modes. Hence, it is very necessary to be able to determine an annealing temperature, which will produce a thin film capable of supporting guided modes.

Thin films were produced by dip-coating silica – titania sol-gels onto silicon substrates at a constant withdrawal speed of 0.988 $mm.sec^{-1}$. The samples were then annealed at temperatures ranging from room temperature to 600°C and the resultant thickness and refractive indices were measured using ellipsometry. The choice of temperatures investigated was determined by previous reports on the effect of annealing temperature on waveguide properties[6]. Figure 4.4 shows the effect of annealing temperature on film thickness. It is evident that as annealing temperature increases, there is a transition temperature of approx. 400°C above which the thickness of the fabricated thin film decreases more rapidly with temperature. It is not fully understood why this occurs. However, it may be related to thermal instability of the Si-C bond at such elevated temperatures. The details of this phenomenon will be discussed later in the chapter.

The annealing temperature also has a substantial effect on the film refractive index. It can be seen in figure 4.5 that as the annealing temperature is increased the refractive index increases also. An increase in refractive index of up to 0.053 is obtained when the annealing temperature is increased from room temperature to 600°C. Such increases are thought to be due to densification of the films. During this process the film decreases in thickness but becomes more optically dense by reducing pore size and pore population within the film. Reducing pore population within the thin film also serves to reduce propagation losses of guided modes.

In conclusion it can be stated that the annealing temperature has a strong influence on the thickness and refractive index of a sol-gel derived thin film. However, one of the main drawbacks of using this technique as a thickness and refractive index controller is that low annealing temperatures produce waveguides with high pore populations which consequentially exhibit high propagation losses.

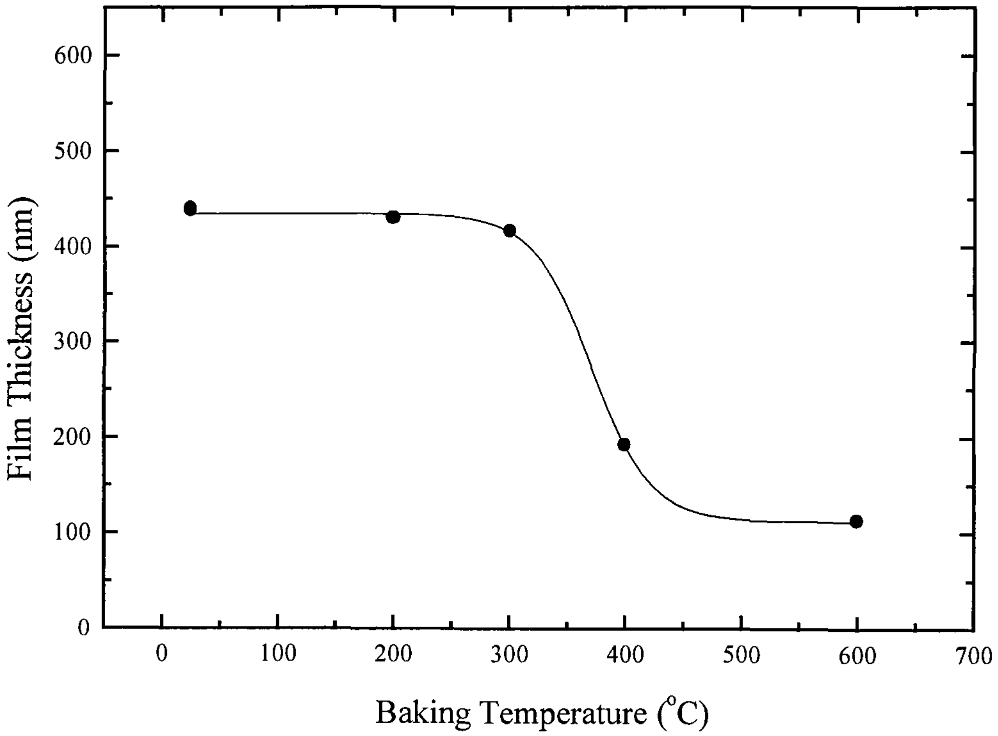

Figure 4.4 *Dependence of film thickness on annealing temperature.*

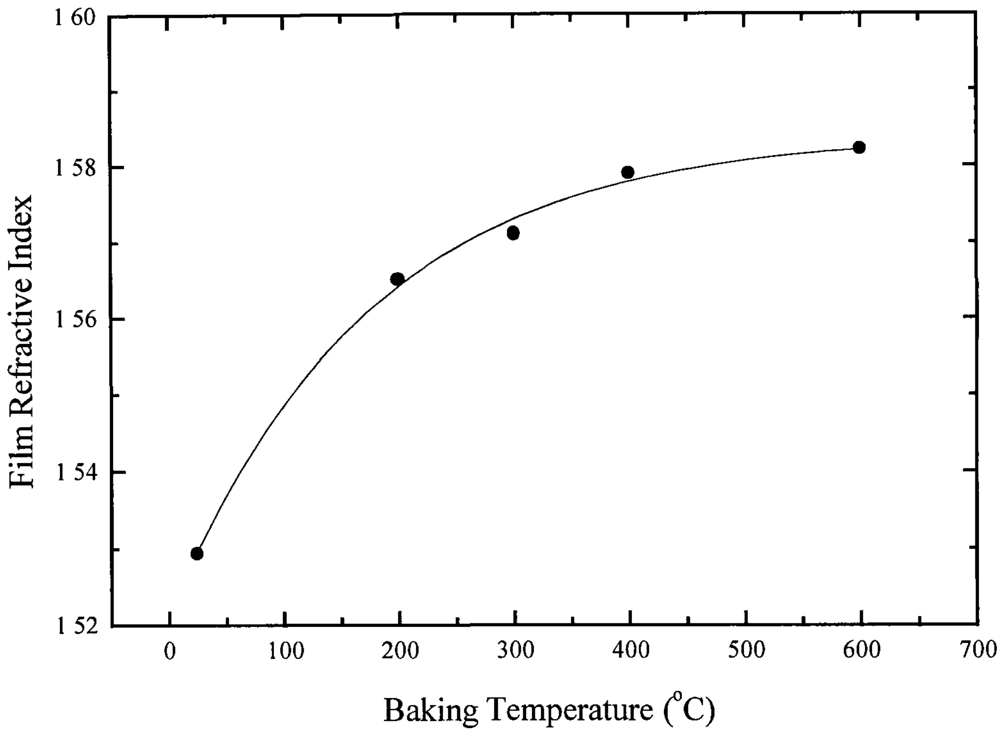

Figure 4.5 *Dependence of film refractive index on annealing temperature*

4.3.1.1.3 Annealing Time

It was expected that the annealing time would have a large influence on the properties of the thin films produced. As the anneal time increases the layer thickness should decrease and refractive index increase, due to increased time available for densification.

As with previous experiments sol-gel derived thin films were deposited onto silicon substrates. In this instance the withdrawal speed was 2 8 mm.sec^{-1}. The layers were then annealed at 500°C for periods of time ranging from 10 minutes up to 17 hours. As can be seen from figures 4.6 and 4.7, an increase in annealing time results in a decrease in film thickness and an increase in refractive index. Such an observation is consistent with the densification process.

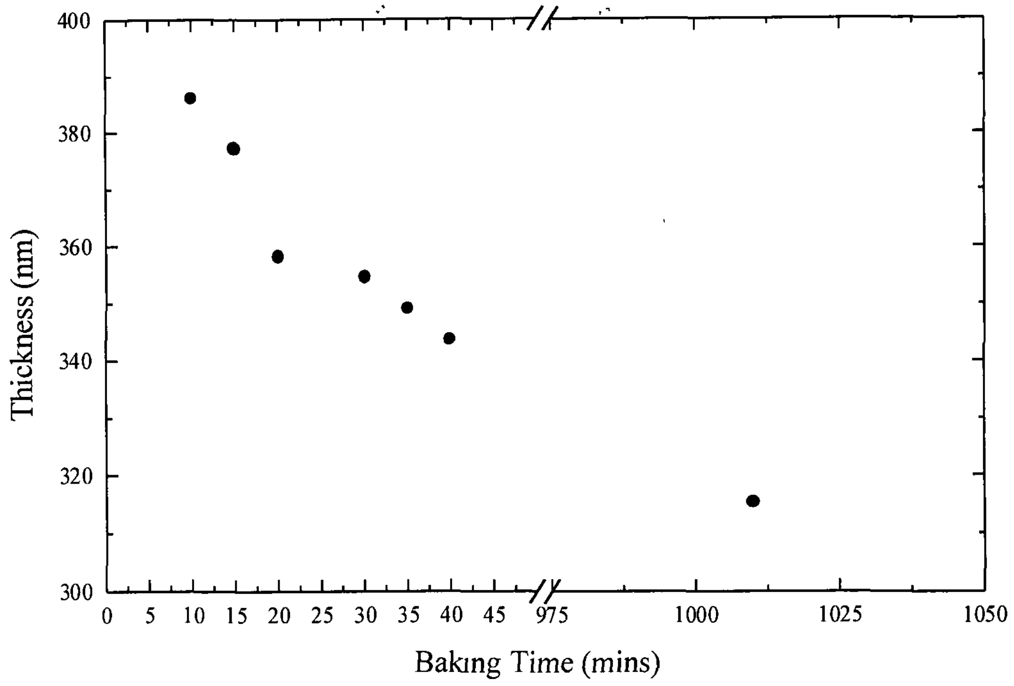

Figure 4.6 *Dependence of film thickness on annealing time*

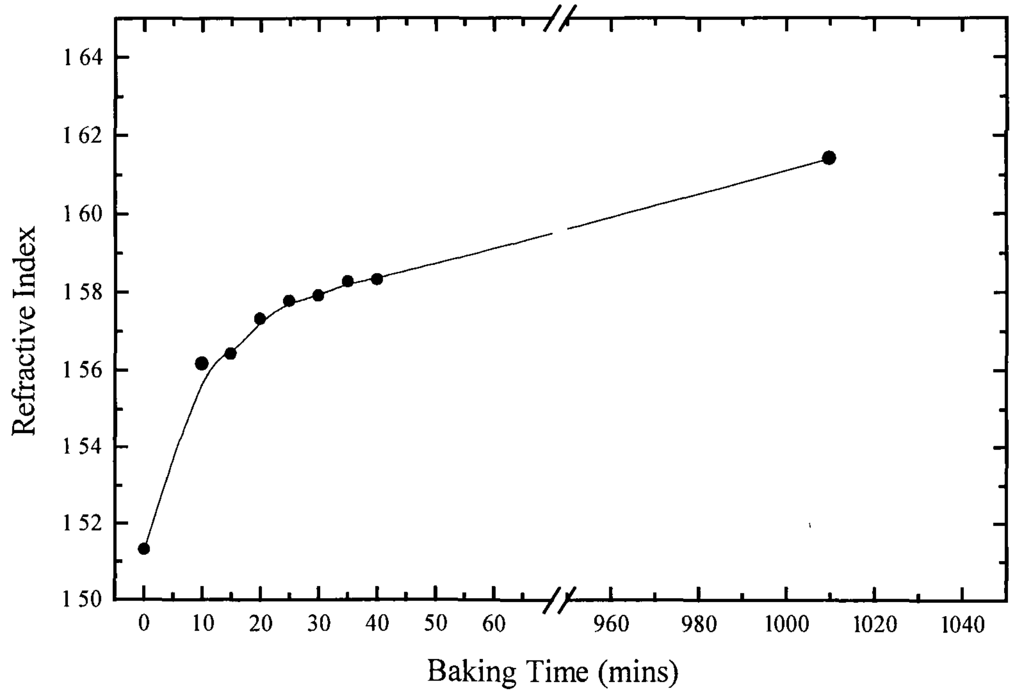

Figure 4.7 *Dependence of film refractive index on annealing time*

It is evident from figure 4 6 that most of the film shrinkage occurs in the first hour of the annealing process Indeed for the samples analysed it was found that overall shrinkage for samples annealed for 17 hours was approximately 71 nm (18 %). Almost 50 % of this shrinkage occurred in the first 40 minutes. Hence it may be concluded that large annealing times (17 hours) are not really necessary. Similarly, figure 4.7 illustrates that the highest rate of change in film refractive index also occurs in the first hour of the annealing process.

It may concluded from this study that excessive annealing times are not particularly advantageous because the biggest changes in thickness and refractive index occur early in the annealing process. Moreover, since waveguiding operation will always be at temperatures close to ambient, it was expected that films annealed for less than 40 minutes would be stable for operation at these low temperatures (see section on film stability with time 4.3.1.1.5).

4.3.1.1.4 Dip Speed

The theory of dip coating has been previously explained in chapter 2. It was expected that an increase in dip speed would result in an increase in film thickness. The effect of increased dip speed on film refractive index was not known.

Sol-gel-derived thin films were deposited on silicon substrates at dip speeds ranging from 0.482 mm sec^{-1} to 2.8 mm sec^{-1}. The resultant thin films were then annealed at 500 °C for 20 minutes. Figure 4 8 shows that film thickness increases with increasing dip speed. It is also evident that for dip speeds lower than 1.5 mm.sec^{-1} there is little change in film thickness possibly due to complete densification being achieved. However, at faster dip speeds film thickness increases in an exponential manner.

Figure 4.9 illustrates that the refractive index remains approximately constant as the dip speed increases.

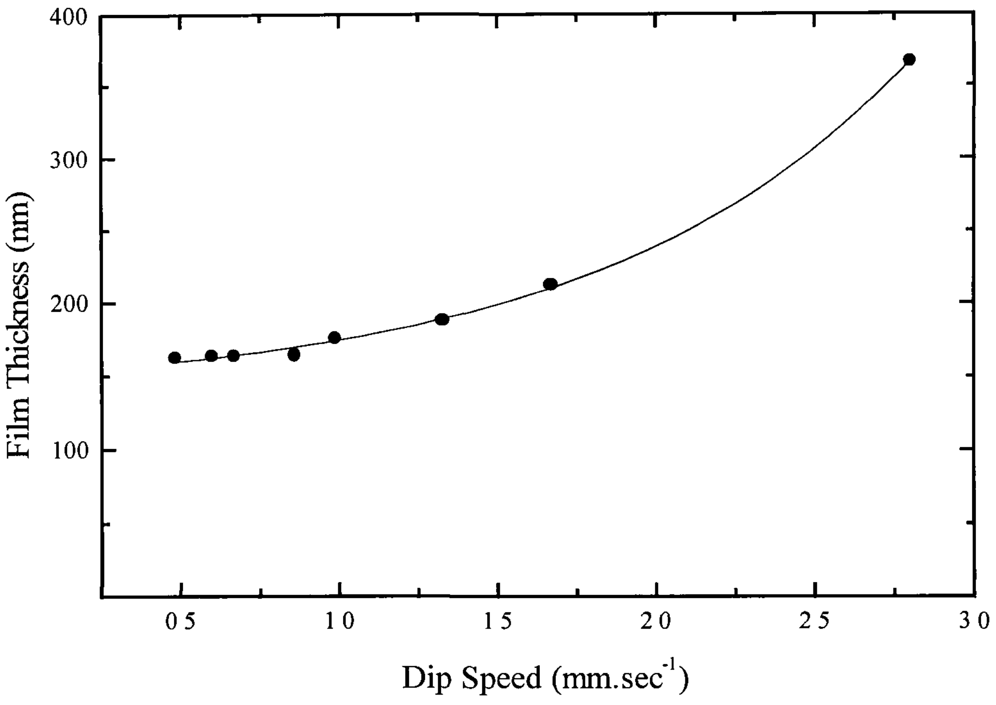

Figure 4.8 *Dependence of thickness of annealed waveguide on dip speed*

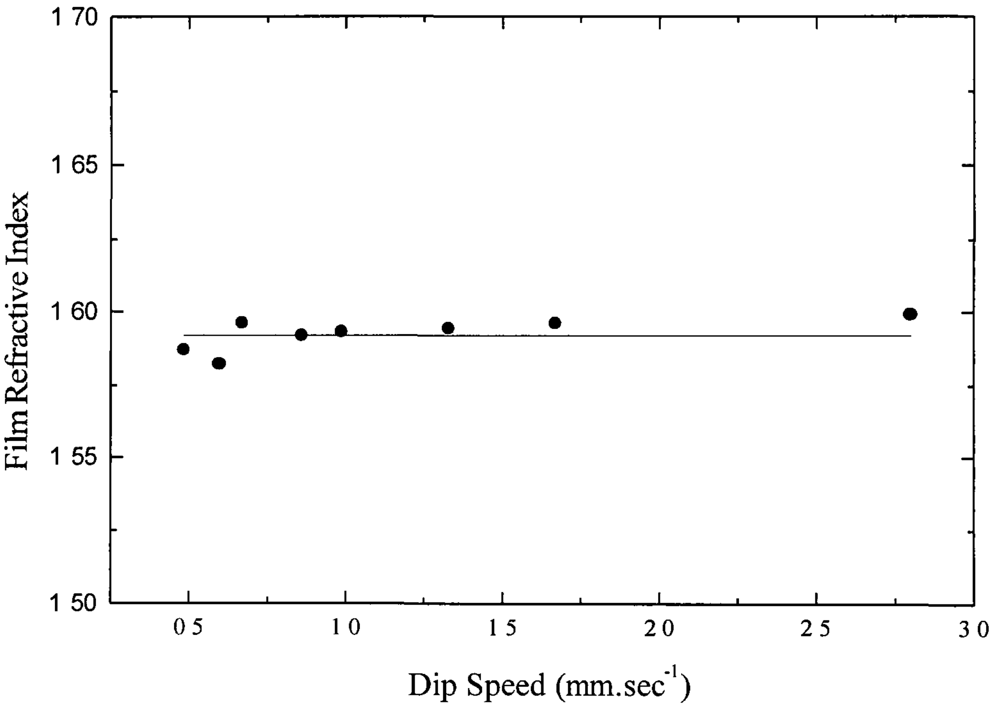

Figure 4.9 *Dependence of refractive index of annealed waveguide on dip speed*

4.3.1.1.5 Temporal Stability

The long term stability at ambient temperatures of the sol-gel derived thin films was determined by measuring film thickness and refractive index at regular intervals over an extended period of time. The films investigated were dip-coated onto silicon substrates at 2.8 mm sec^{-1} and annealed at 500°C for twenty minutes. Ellipsometry was used to measure any variations in thickness and refractive index with time.

Figure 4.10 shows the measured variation of film thickness with time. It can be clearly seen that the thickness of the deposited layers does not change over time when used at ambient temperatures. A similar trend is observed in figure 4.11 where it can be seen that refractive index is constant over time.

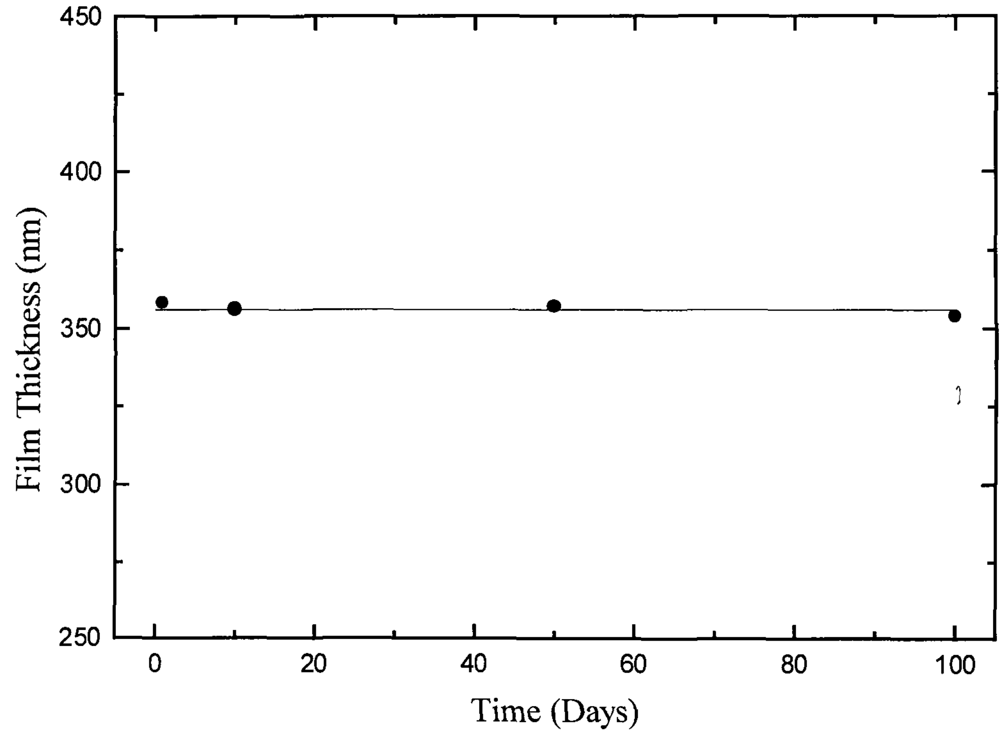

Figure 4.10 *Temporal stability of film thickness*

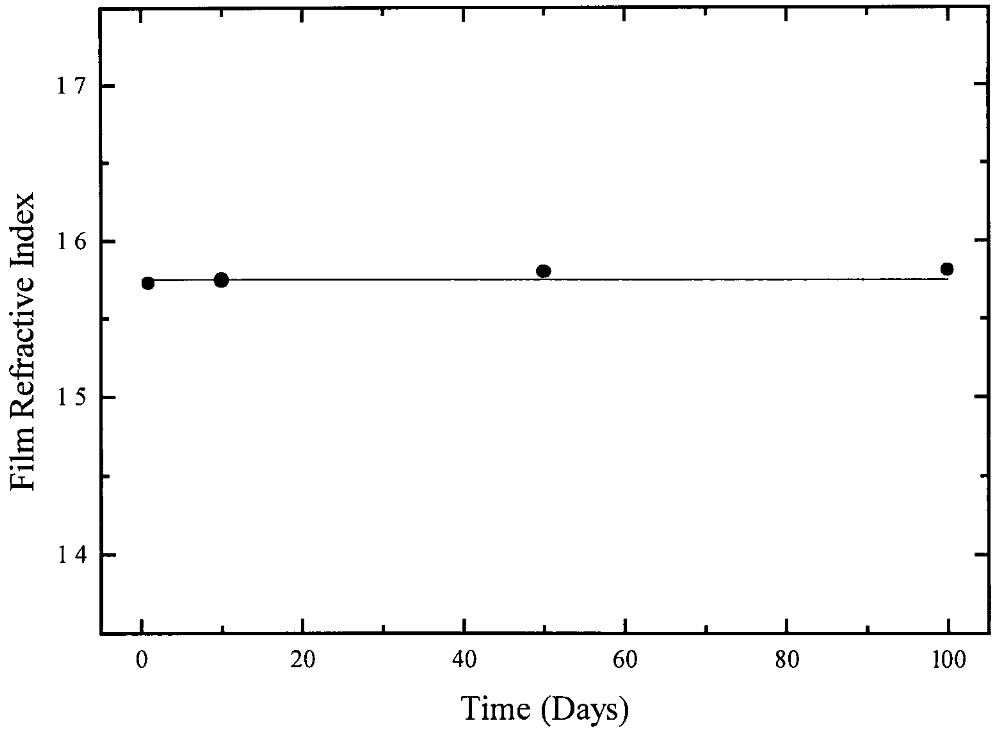

Figure 4.11 *Temporal stability of film refractive index*

Such observations indicate that sol-gel derived thin films annealed for short periods of time undergo sufficient densification to ensure that the films are temporally stable.

4.3.1.1.6 Multiple Layer Waveguides

For the sol employed in this work, a single dip-coating application produces waveguide of a maximum thickness of about 600 nm. Such waveguides are normally only single or double mode in nature. Fabrication of sol-gel derived multimode waveguides using a single dip-coating application at increased speed is not suitable, as they tend to crack very easily and exhibit increased propagation losses. Fabrication of thicker multimode waveguides, however, may be achieved by applying multiple coatings of the sol to the substrate prior to annealing. The fabrication technique is similar to that reported in section 4.2. The film is deposited on either a glass or silicon substrate at a constant dip-speed of 2 8 mm.sec^{-1} producing a layer of thickness 350 nm. The sample is then dried in air for approximately 5 minutes and then another coating is applied. The process in repeated until the required number of layers has been applied. Up to 5 coatings can be applied to a single substrate, depending on dip speed. The samples are then annealed at 500°C for 20 minutes Multimode waveguides up to 1.5 microns in thickness can be fabricated by this procedure.

Figure 4.12 illustrates how the thickness of the densified waveguide increases linearly with increased coating applications. While, figure 4.13 shows that the refractive index of the waveguide also changes with the number of applied layers. The reason for this observation is not understood at present.

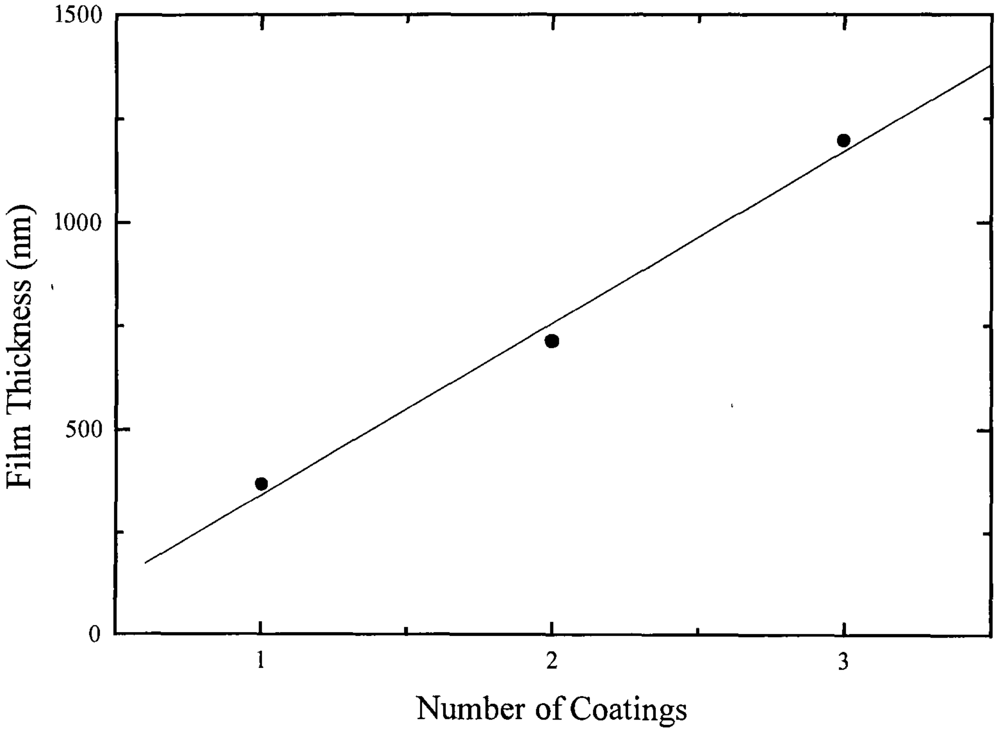

Figure 4.12 *Dependence of film thickness on number of layers*

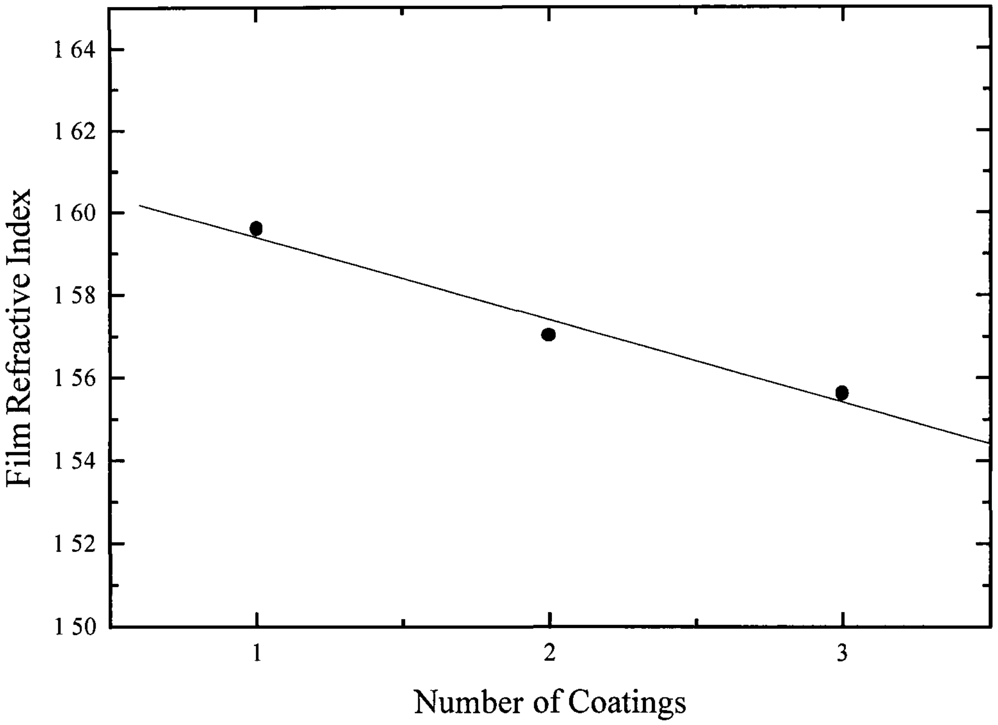

Figure 4.13 *Dependence of film refractive index on number of layers*

4.3.1.1.7 Summary

It is evident from the studies presented in this section that it is possible to fabricate temporally stable sol-gel derived thin films with selected thickness / refractive index values within certain limits. Such films may be used as planar waveguides. The waveguides may be single or multimodal in nature, with thicknesses of up to 1500 nm and refractive indices of up to 1.7. Production of such customised waveguides is possible by tailoring fabrication parameters such as dip speed, annealing temperature, annealing time, sol composition and number of coatings applied. For the purpose of this research it was determined that a sol which contained 13.8 % (v/v) titania precursor would produce single-mode waveguides of refractive index values (1.6) sufficiently larger than the substrate (1.515) and superstrate (1.43) index values to ensure strong guiding. The waveguides were fabricated at a dip speed of 2 8 mm sec^{-1} with an annealing temperature of 500°C for 20 minutes. Such a fabrication technique produced single mode waveguides of thickness 350nm Fabrication of multimode waveguides was achieved by the application of multiple coatings.

4.3.1.2 Waveguide Attenuation

One of the most important parameters to take into account when one is fabricating waveguides for both telecommunications and sensing applications is the attenuation. Guided modes must be able to propagate along the waveguide without substantial loss of power due to scattering at impurity sites and uneven interfaces. Due to the trade off between high propagation losses and the requirement for long interaction lengths of the evanescent field typical, waveguide-based sensors have propagation distances of approximately 2 centimetres.

The main contribution to propagation loss in the waveguides produced here is scattering losses. Preparation of the sol is fabricated in anhydrous conditions can reduce such propagation losses. This is necessary because the rates of hydrolysis of the two precursors used in the fabrication of waveguide sols (titania and organically modified silica) are different. Addition of water to the sol will result in faster hydrolysis of the titania precursor and thus the formation of separate titania and silica rich sites in the sol. This leads to inhomogeneity in the waveguide layer and increases in guided mode scattering[6,7]. The use of silicon tetrachloride as the catalyst, instead of the usual acidified water approach ensures anhydrous reaction conditions. In this scenario ambient water promotes hydrolysis, and fabrication of homogenous low-loss sol-gel derived planar waveguides is possible. Losses may be further reduced by ensuring that the preparation procedure is carried out with extreme care.

The experimental configuration employed for the determination of propagation losses in sol-gel derived planar waveguides is illustrated in figure 4.14. A sol-gel derived planar waveguide with an embossed sol-gel grating coupler (see chapter 5 for further information) is mounted on a high-resolution rotary stage. Light from a helium neon laser (632.8 nm) is incident on the grating coupler and at a specific incident input angle a proportion of this light is coupled into the TE_0 waveguide mode in accordance with equation 4.1

$$n_{eff} - n_a \sin\alpha = \frac{m\lambda}{\Lambda} \qquad [4.1]$$

n_{eff} is the effective index of the waveguide mode, n_a is the refractive index of the medium through which the laser light is incident, α is the angle of incidence, m is the diffraction order which excites the guided mode, λ is the wavelength of the incident light and Λ is the grating coupler periodicity.

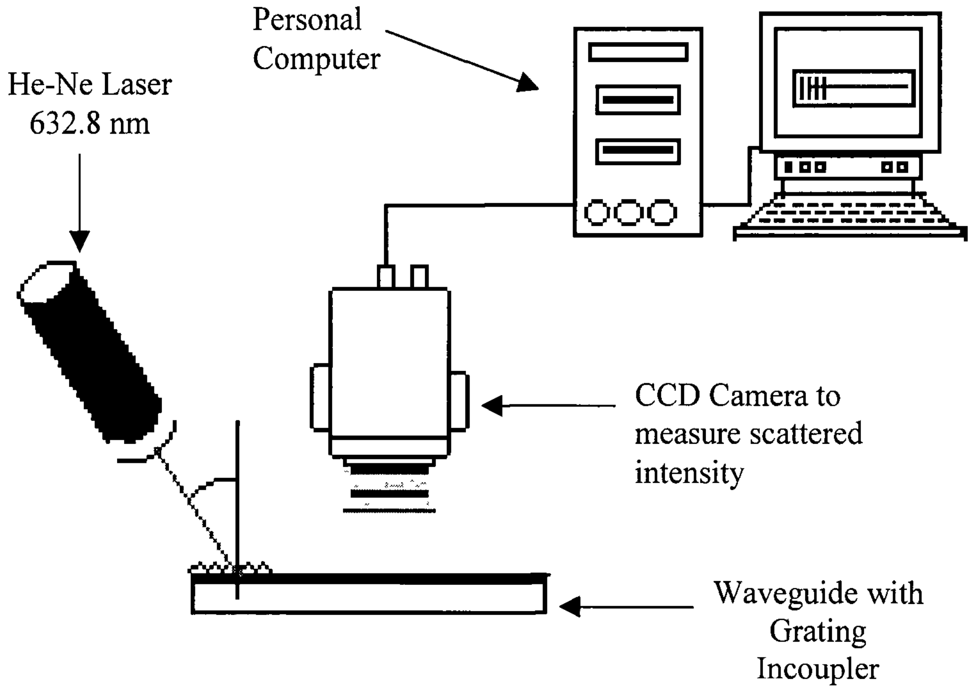

Figure 4.14 *Experimental configuration for measurement of attenuation*

A charge-coupled device (CCD) camera controlled by a personal computer via an interface card is used to obtain a single shot image of the guided mode as it propagates along the length of the waveguide. A typical propagation image is shown in figure 4.15.

The observed noise on the image could be removed by averaging multiple images of the guided mode.

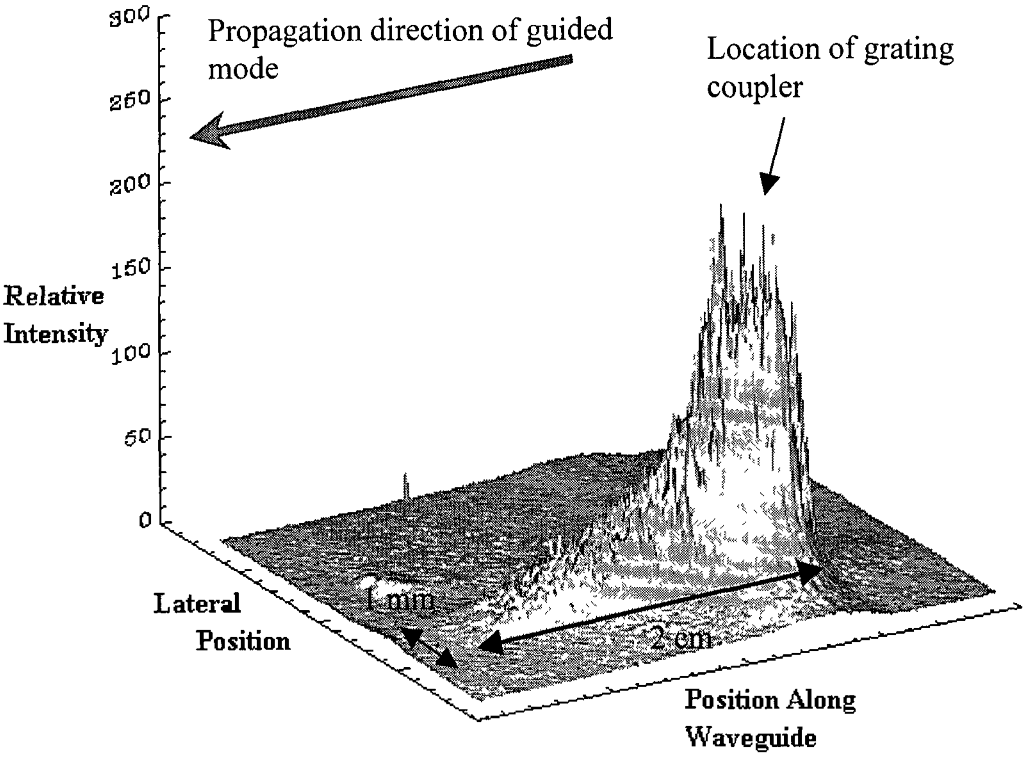

Figure 4.15 *Intensity profile of a mode propagating in a planar waveguide*

The images are saved as bitmap files and attenuation curves are generated, in which the logarithm of the scattered intensity from the waveguide mode is plotted against the propagation distance A typical attenuation curve is shown in figure 4.16 and is fitted with a straight line.

Using this linear fit and the equation shown below it is possible to determine the propagation losses for sol-gel-derived planar waveguides.

$$\alpha = -\frac{10}{L}\mathrm{Log}_{10}\left(\frac{P_{out}}{P_{in}}\right) \qquad [4\ 2]$$

where L is the propagation distance of the mode in centimetres. P_{in}, P_{out} are the initial and final powers, and α is the attenuation coefficient (propagation losses) in decibels per centimetre

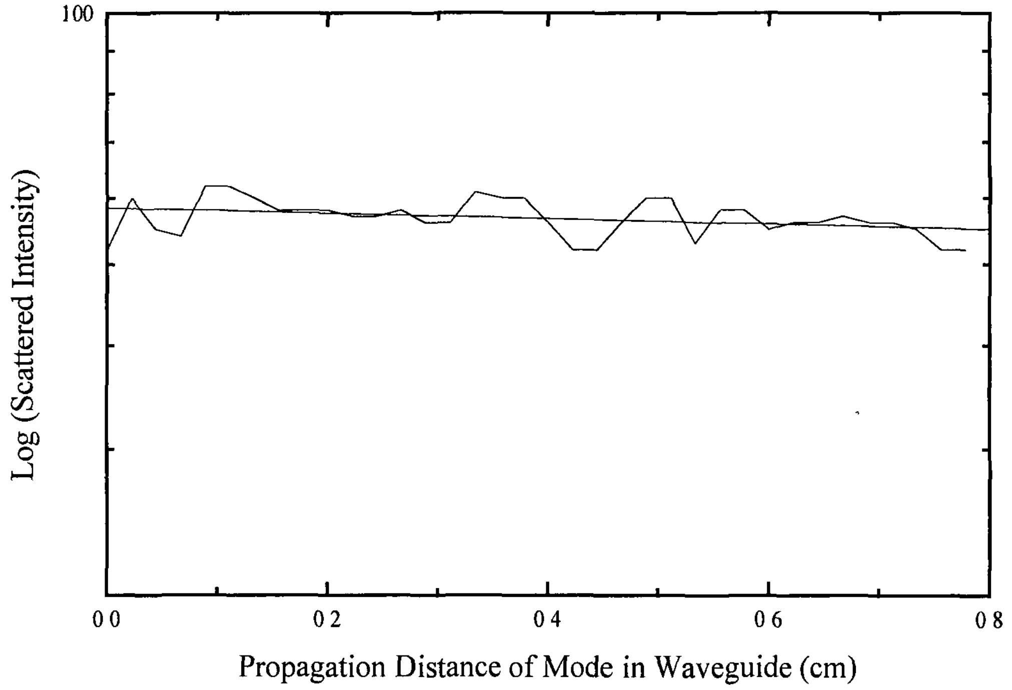

Figure 4.16 *Attenuation profile for a mode propagating in a planar waveguide*

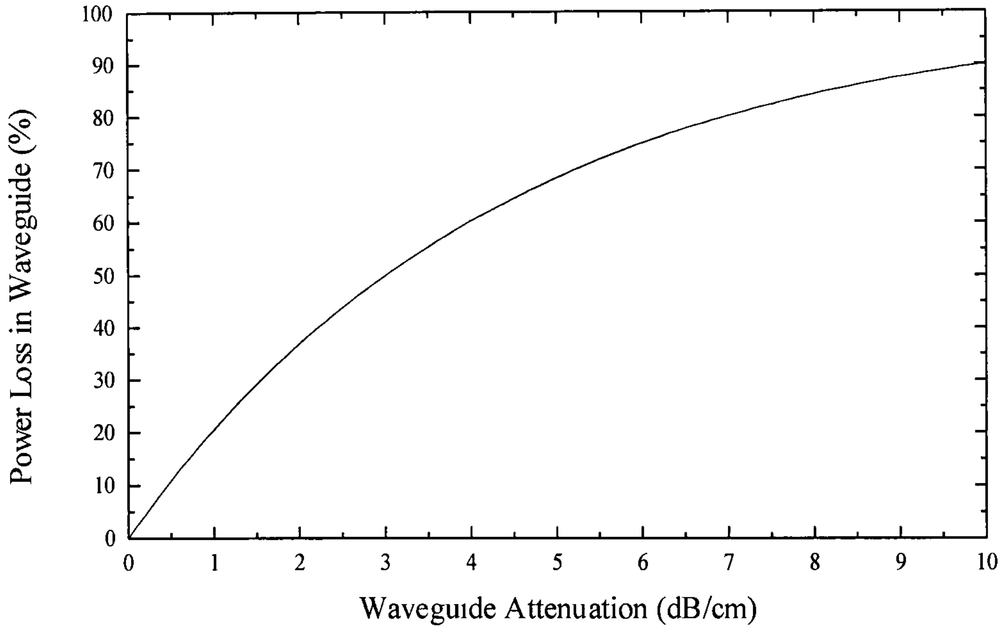

Figure 4.17 *Relationship between attenuation coefficient and % power loss*

The relationship between the attenuation coefficient which is expressed in dB/cm and actual percentage of power lost as the guided mode propagates along a unit length of the waveguide is clearly illustrated in figure 4.17. It can be seen from this plot that an attenuation coefficient of 3 dB/cm indicates that a guided mode loses 50 % of its power for a propagation distance of one centimetre in a waveguide.

Figure 4 18 shows a histogram of attenuation coefficients measured for a number of sol-gel-derived planar waveguide samples fabricated from identical sol recipes and under similar conditions.

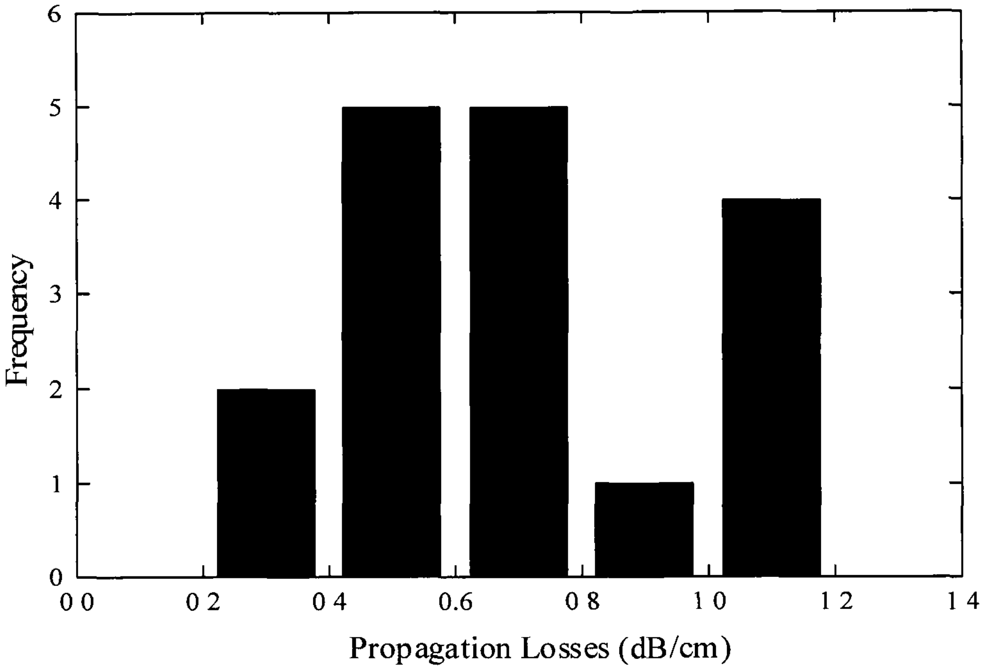

Figure 4.18 *Histogram of propagation losses for sol-gel derived planar waveguides*

It can be seen from the histogram that the typical attenuation coefficient for a waveguide is 0 6 dB / cm which corresponds to a loss in power of 13 % per cm of propagation in the waveguide. Such waveguide power losses are sufficiently small and acceptable for applications in integrated optic components. There is however, one major drawback envisaged for the future development of such devices, namely the variation in propagation losses between waveguide despite identical laboratory fabrication techniques. If commercialisation of such waveguides were to be realised such irregularities must be erased.

4.3.1.3 Surface Roughness

A guided mode propagating in a planar waveguide suffers from attenuation all along the waveguide. One of the major contributors to such attenuation is scattering at the waveguide cladding boundaries due to imperfect or rough surfaces[8]. Surface roughness of the sol-gel derived planar waveguides was determined using atomic force microscopy.

The atomic force microscope (AFM), or scanning force microscope (SFM) is a surface profile analysis technique which utilises an atomically sharp probe moving over the surface of a sample in a raster scan. The probe, a tip which typically is fabricated from silicon nitride, is brought very close to the surface and will experience a force from the surface and as a result will move up or down on its supporting cantilever. The tip movement is usually monitored by using a laser beam, which is reflected or diffracted by the tip or cantilever. Up or down movement of the tip is then detected by changes in the laser beam position. Thus rastering the tip across the surface produces a topographic map of the surface with extremely high resolution.

Waveguide samples were fabricated on glass substrates using the fabrication procedure outlined in section 4.2 and surface roughness values for a number of samples and sample areas were determined using atomic force microscopy (AFM). The surfaces of the sol-gel-derived waveguides typically exhibited a root mean square (rms) surface roughness of 10 nm, which was approximately 3% of the overall thickness.

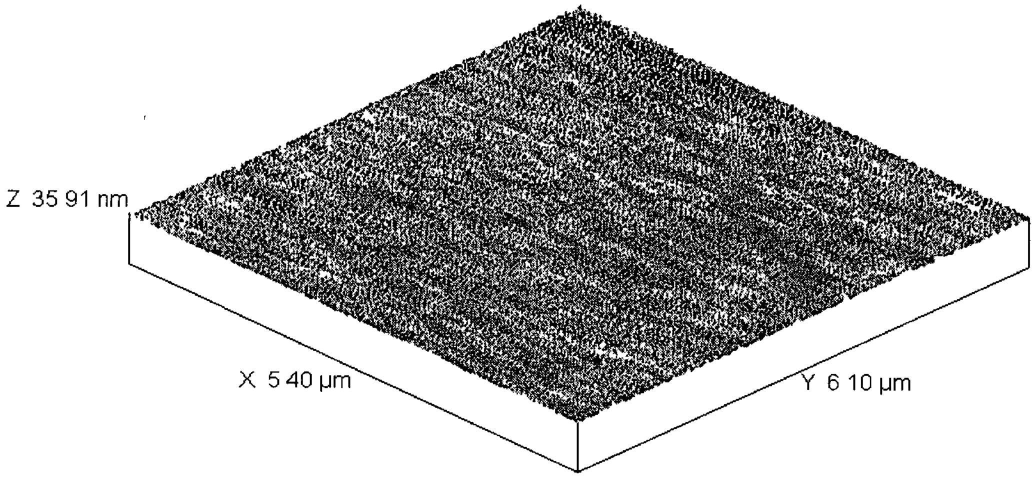

Figure 4.19 *AFM image of waveguide surface*

Figure 4 20 is an AFM scan which clearly shows the roughness of the surface It can be seen that there are very few anomalies in the portion of the waveguide illustrated.

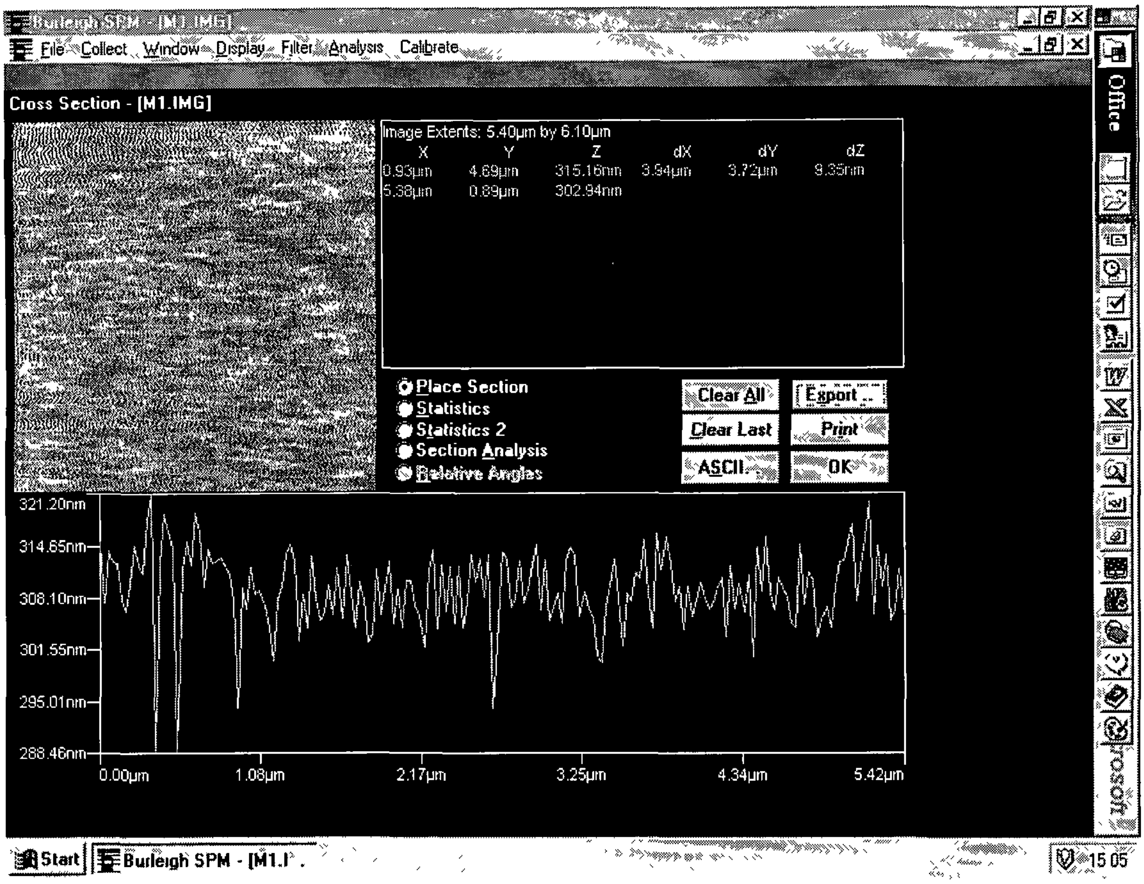

Image Extents: 5.40µm by 6.10µm

X	Y	Z	dX	dY	dZ
0.93µm	4.69µm	315.16nm	3.94µm	3.72µm	9.35nm
5.38µm	0.89µm	302.94nm			

Figure 4.20 *Screen printout of data from AFM scan of waveguide surface*

4.3.2 Chemical Characterisation

4.3.2.1 Fourier Transform Infrared Spectroscopy (FT-IR)

Fourier transform infrared spectroscopy (FTIR) is an extremely powerful analytical tool that may be used to characterise and identify organic molecules. The infrared spectrum of an organic compound serves as its fingerprint and provides information about the chemical bonding and molecular structure of the sample. FTIR spectroscopy was used in this work to analyse the bonding in a sol-gel derived planar waveguide and subsequent changes as a function of annealing temperature. The resultant data could provide valuable information about the stability of waveguides fabricated via the sol-gel process.

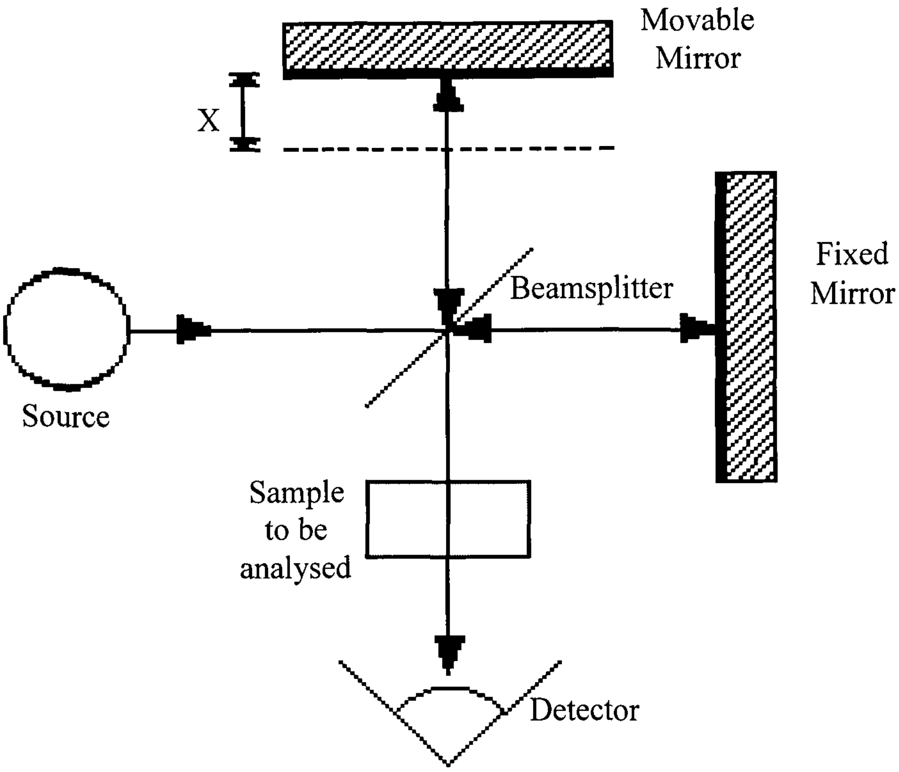

Figure 4.21 *Principle of Fourier transform infrared spectroscopy*

The basic set-up for Fourier transform infrared spectroscopy is illustrated in figure 4.21. Fourier transform infrared spectroscopy employs the technique of Michelson interferometry whereby a beam of light from a broadband infrared source is split into two. One of the beams is transmitted to a fixed mirror, while the second beam is reflected to a moving mirror. The beams are reflected from the mirrors, recombined at the beam-splitter and sent to a detector. Recombination of the two beams will result in constructive and destructive interference for different wavelengths of light, depending on the relative distances of the two mirrors from the beamsplitter. The intensity variation with optical path difference is the Fourier transform of the incident radiation. The IR absorption spectrum for a sample is then obtained by measuring the intensity variations with and without a sample and transforming the data into spectra.

A Bomem MB 120 FTIR spectrometer was used to generate all results presented in this thesis. Spectra for sol-gel derived planar waveguides which were deposited on silicon substrates and annealed at temperatures ranging from room temperature to 660 °C, (from 1800 cm^{-1} to 600 cm^{-1} with a resolution of 4 cm^{-1}) are presented in figure 4.22. It can be clearly seen that there is a large temperature dependence of the spectra. In order to be able to comment on the sources of temperature dependence it was first necessary to identify the bond(s) that resulted in the formation of each feature observed.

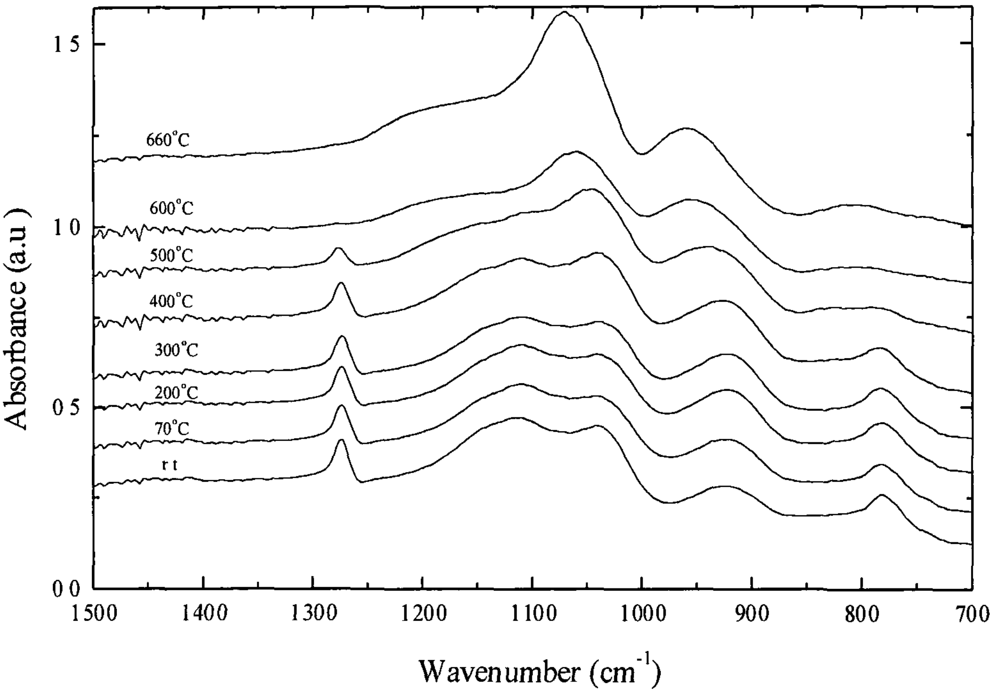

Figure 4.22 *FT-IR Spectra of waveguides annealed at various temperatures*

The first major feature encountered was at ~ 1273 cm^{-1} and has been assigned in the literature to a symmetric deformation of the Si-CH_3 group[6,9]. Moving across the spectrum the next features encountered are broad unresolved bands in the 1200 cm^{-1} – 1000 cm^{-1} region. These bands have previously been attributed to asymmetric stretching vibrations of Si-O-Si bridging sequences. The broad band observed at ~ 920 cm^{-1} is thought to be due to two bonds, a Si-O-Ti vibrational mode and a mode due to the thermal oxidation of Si-CH_3 to Si-OH. Finally, a peak is observed in the spectra at ~ 780

cm^{-1}. Again, this feature has been attributed in the literature to two overlapping bands: the Si-CH_3 and the Si-O-Si modes.

Once the features of interest had been identified, it was then necessary to determine the effect of annealing temperature. The first point of interest to be noted is that the changes in the spectra in the region of interest only occurred for annealing temperatures above 300 °C. However, such sol-gel derived thin films would not function practically as waveguides because such thin films are still quite porous due to incomplete densification of the sol-gel and as a result have large guided mode propagation losses.

At temperatures above 300 °C there were substantial changes observed in the spectra. The Si-CH_3 peak at ~ 1273 cm^{-1} maintained a constant intensity up to annealing temperature of 400 °C. Between 400 °C and 500 °C the intensity of the peak decreased by half, and at 600 °C it had completely disappeared. Such observations indicate that the Si-C bond is thermally stable up to 400 °C. However, above this temperature the bond is quite unstable. It was also observed that substantial changes occurred in the 1200 cm^{-1} – 1000 cm^{-1} band as temperature increased. The features in this region of the spectra were inverted in relative intensity and broadened to the high frequency side as the annealing temperature increased. Such spectral changes in the Si-O-Si features are attributed to densification of the gel. The band at ~ 920 cm^{-1} which was attributed to both the Si-O-Ti and Si-CH_3 bonds was observed to shift to higher frequencies (~ 958 cm^{-1} at 660 °C). Most of this change occurred between 400 °C and 500 °C. It was noted that this was the same temperature range in which the Si-CH_3 feature at ~ 1273 cm^{-1} was sharply attenuated due to conversion to Si-OH. Hence, it was concluded that the Si-CH_3 bond was also responsible for the majority of the change observed at ~ 920 cm^{-1}. Finally, the lowest frequency band at ~ 780 cm^{-1} was observed to be sharply attenuated above 400 °C and shifted in position to ~ 804 cm^{-1} at 660 °C. It is thought that this change is due to both gel densification and thermal instability of the Si-C bond.

Table 4.1 summarises all the information on the observed features and their dependence on annealing temperature. It is very apparent that annealing temperature strongly influences the film structure. The majority of structural changes are observed between 300 °C and 500 °C. It was decided that an annealing temperature of 500 °C would be used in the fabrication of sol-gel derived planar waveguides because it was high enough to have low propagation losses, but also because at this annealing temperature there was little carbon present resulting increased thermal stability.

Feature	Bond	Temperature Effect	Reason
1273 cm^{-1}	Si-CH_3	Attenuated above 400 °C, completely disappeared at 600 °C.	Thermal instability of Si-C bond.
1200 - 1000 cm^{-1}	Si-O-Si	Shift to higher frequencies, inverted in relative intensity, and broadened to high frequency side	Gel densification
920 cm^{-1}	Si-O-Ti, Si-OH	High frequency shift and broadened.	Thermal oxidation of Si-CH3 to Si-OH.
780 cm^{-1}	Si-CH_3, Si-O-Si	Attenuated at temperatures above 400 °C and shifted to higher frequencies.	Thermal instability of Si-C bond and Gel densification.

Table 4.1 *Main features on FT-IR spectra of waveguide layers*

4.4 Conclusion

The processes involved in the fabrication of sol-gel derived thin films for use as planar waveguides, such as sol preparation and substrate preparation have been discussed. Investigations on the effect of varying film preparation parameters such as sol composition, annealing temperature, annealing time and dip speed on both the thickness and refractive index of the thin films have also been presented Fabrication of thicker waveguide layers using the multiple coating technique was also discussed.

Physical and chemical characterisation of the sol-gel derived planar waveguides were then discussed in detail. A range of technologies such as CCD imaging, atomic force microscopy (AFM) and Fourier transform infrared spectroscopy (FTIR) were used to determine such parameters as waveguide propagation losses, surface roughness and chemical structure. Table 4.2 below provides summary information about the sol-gel-derived planar waveguides that are employed in the sensing configuration reported in chapter 7 of this thesis

Fabrication Conditions			
Sol	**Dip Speed**	**Annealing Temp**	**Annealing Time**
13.8% (v/v) Titania Precursor:	2 8 mm.sec^{-1}	500° C	20 Minutes

Waveguide Properties				
Structural Dimensions	**Waveguide Thickness**	**Refractive Index**	**Propagation Losses**	**Surface Roughness**
40 mm x 10 mm x 1mm	350 nm	1.6	< 1 dB/cm	< 10 nm (rms)

Table 4.2 *Summary table of waveguide fabrication conditions and properties*

In conclusion, it has been demonstrated in this chapter that the sol-gel technique provides a feasible route for the fabrication of low cost, low loss planar waveguides for sensing purposes. The flexibility of the sol-gel process enables control of the thickness and refractive index of the derived thin films through a number of techniques, thus providing a route to the fabrication of customised devices.

References

1 Snyder A W., Love J. D.: '**Optical Waveguide Theory**', 1983, Chapman and Hall, London

2. Lee D. L.. '**Electromagnetic Principles of Integrated Optics**', 1986, Wiley, New York

3. Nishihara H., Haruna M., Suhara T.: '**Optical Integrated Circuits**', 1989, McGraw - Hill, New York

4. Hunsperger R. G.: '**Integrated Optics: Theory and Technology**', 1991, 3rd Ed., Springer - Verlag, New York

5. Wilson J., Hawkes J. F. B.: '**Optoelectronics: An Introduction**', 1983, Prentice - Hall, London

6. Yang L., Saavedra S. S., Armstrong N. R., Hayes J.: '**Fabrication and Characterisation of Low-Loss, Sol-Gel Planar Waveguides**', Analytical Chemistry, 1994, Vol 66, pp. 1254-1263

7. Najafi S. I.: '**Introduction to Glass Integrated Optics**', 1992, Artech House, London

8 Unger H. G.· '**Planar Optical waveguides and Fibers**', 1977, Clarendon, Oxford

9 Silverstein R. M., Bassler G. C., Morrill T. C.: '**Spectrometric Identification of Organic Compounds**', 1974, 3rd Ed., Wiley, New York

Chapter 5 Grating Coupler Fabrication and Characterisation

5.1 Introduction

Grating couplers may be fabricated using a variety of techniques, which range from the very expensive; reactive ion etching (RIE)[1], to the low cost; wet-chemical etching[2], photolithography[3] and embossing[4,5]. The procedures may be utilised to produce gratings of any desired profile[6-8] for a variety of applications. In this section an embossing procedure which allows for the production of sol-gel-derived grating couplers is presented. The technique is simple, rapid and low cost and produces embossed sol-gel-derived grating couplers of extremely high quality. Due to restrictions on the type of commercially available gratings only linear periodic gratings were employed as master gratings, however, the technique is extendable to all grating profiles.

5.2 Grating Coupler Fabrication

5.2.1 Master Gratings

The master gratings used to produce embossed sol-gel-derived gratings couplers are commercially available aluminium coated surface relief gratings (Ealing Electro-optics, Watford, UK). The properties of the master gratings employed for the experiments reported in this thesis are detailed in table 5.1.

The ruled diffraction gratings are produced using an interferometrically controlled diamond tip cutting tool. Such a device allows for the production of closely spaced, straight parallel grooves into an optically flat aluminium coated substrate. Sinusoidal holographic gratings are formed by interfering two laser beams, and exposing a polished substrate coated with photo resist to the interference fringe field. In both situations the surface contour is transferred to an epoxy coated glass flat in a process known as replication and coated with a thin layer of aluminium. It is these replicated gratings which are used as the master gratings for the embossing procedure, and thus will be referred to as master gratings throughout this thesis. Schematic diagrams for both types of grating are illustrated in figure 5.1.

Grating Type	**Dimensions (mm)**	**Grooves per mm**	**Depth (nm)**	**Wavelength (nm)**	**Blaze Angle (Degrees)**
Ruled (Sawtooth)	12 7 x 12.7 x 6.0	600	253	500	8° 37'
Holographic (Sinusoidal)	12.7 x 12.7 x 6.0	1200	41	Visible	N/A
Holographic (Sinusoidal)	12 7 x 12 7 x 6.0	2400	41	Visible	N/A

Table 5.1 *Master grating specifications.*

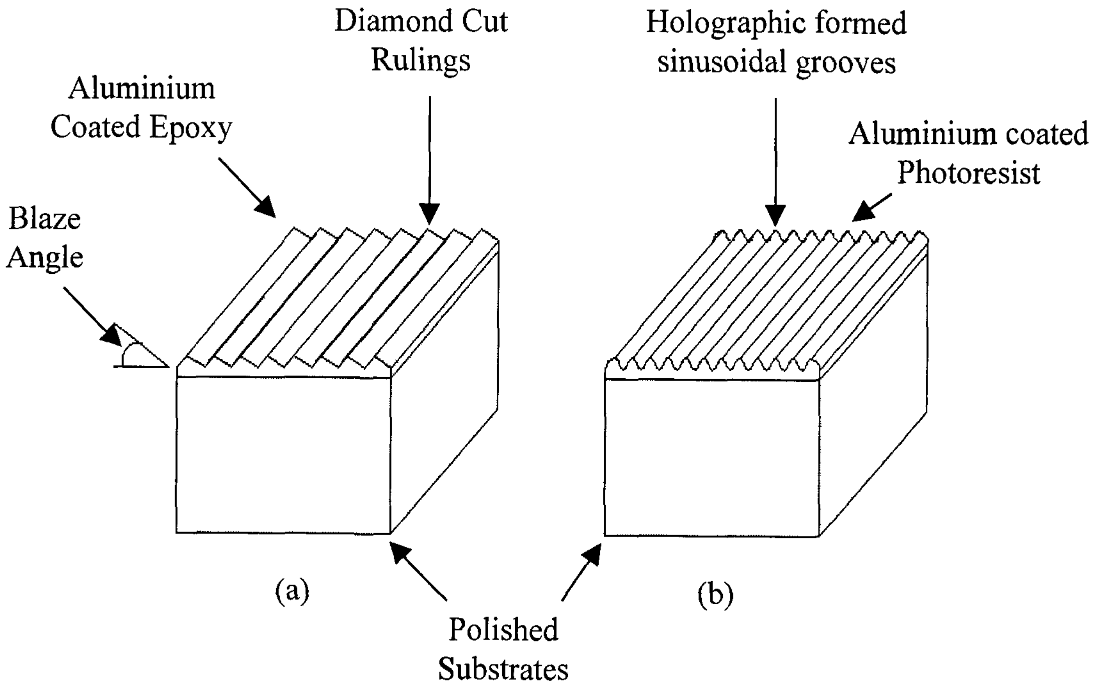

Figure 5.1 *Master Gratings (a) Ruled, (b) Holographic*

Atomic force microscopy (AFM) can be used to provide information on the surface profile of the gratings. An AFM image of a 10 μm x 10 μm area of a typical master grating is shown in figure 5.2. It can be clearly seen from this image that the initial quality of the commercially available master gratings is extremely high, with very little defects visible on the surface.

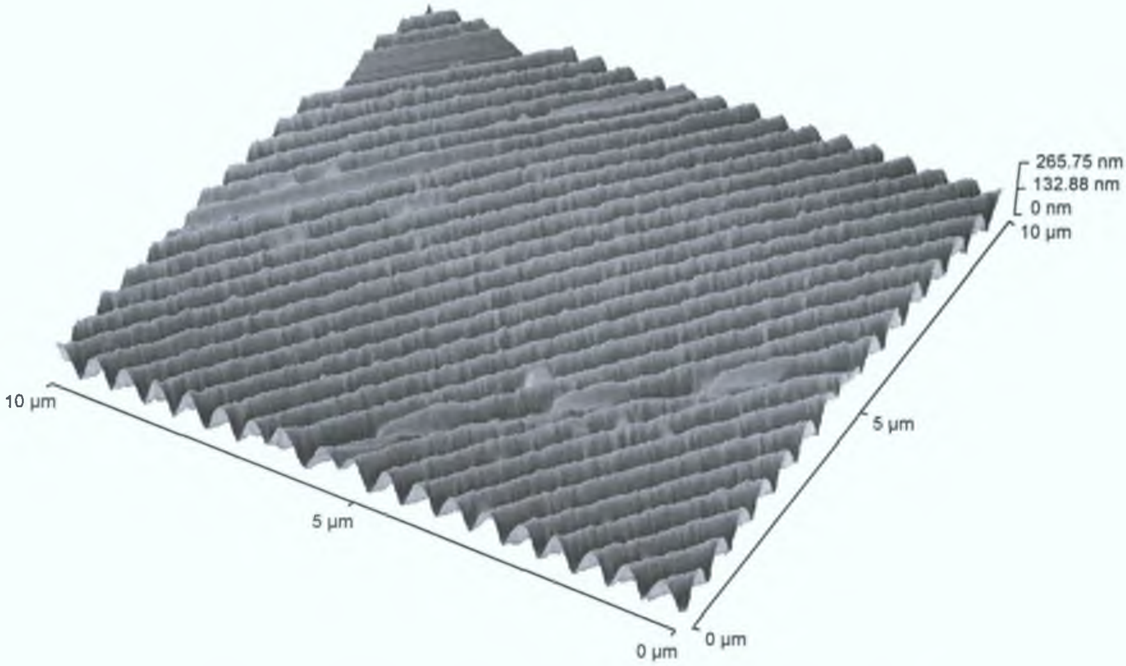

Figure 5.2 *AFM image of master grating (holographic, 2400 line mm^{-1}).*

The periodicity of the master gratings may also be determined using atomic force microscopy, however, it is not possible to carry out accurate grating depth determination due to the large dimension of the imaging tip (4 μm). Such a tip can not fit into the smaller (< 2 μm) grooves and rulings of the master gratings thus rendering depth measurements useless.

5.2.2 Embossing Procedure

Prefabricated planar waveguides are allowed to stabilise for 1 month prior to grating fabrication. A thin film of the titania - silica sol used to produce planar waveguides is deposited over a length of approximately 1 centimetre on the surface of the sol-gel-derived planar waveguides via the dip-coat technique at a dip speed of approximately 1.0 mm sec^{-1} The coated waveguide is then immediately placed in a dedicated embossing apparatus as shown in figure 5.3 where a master surface relief grating is pressed against the coated waveguide surface for a pre-determined period of time. It was found that an embossing time of less than 30 seconds produced only partial gratings while an embossing time of over 60 seconds resulted in adherence of the waveguide device to the master grating. Therefore, an optimum embossing time of 45 seconds was chosen. After this time the master grating is withdrawn from the coated waveguide and a negative imprint of the surface relief grating is observed in the sol-gel layer on the surface of the waveguide.

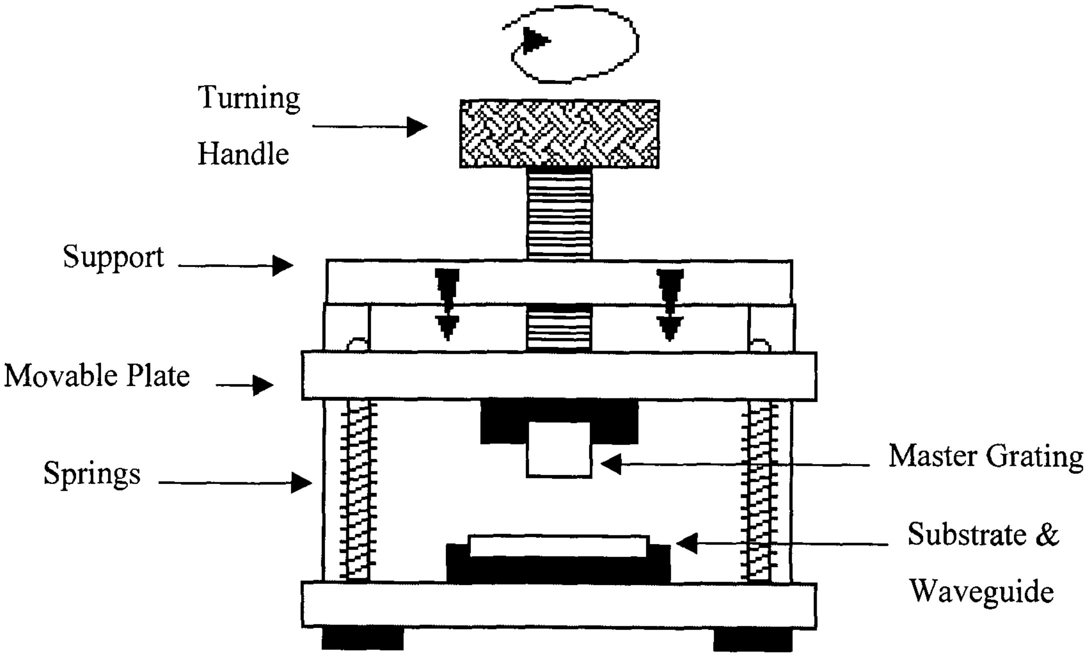

Figure 5.3 *Embossing Apparatus*

All excess sol-gel not imprinted by the grating may be removed using methanol. The sol-gel-derived grating couplers are then left to dry for three days at room temperature prior to use. The complete embossing procedure is illustrated in figure 5.4.

After embossing the master gratings are cleaned using lens tissue and methanol to remove any sol which may have remained in the grooves.

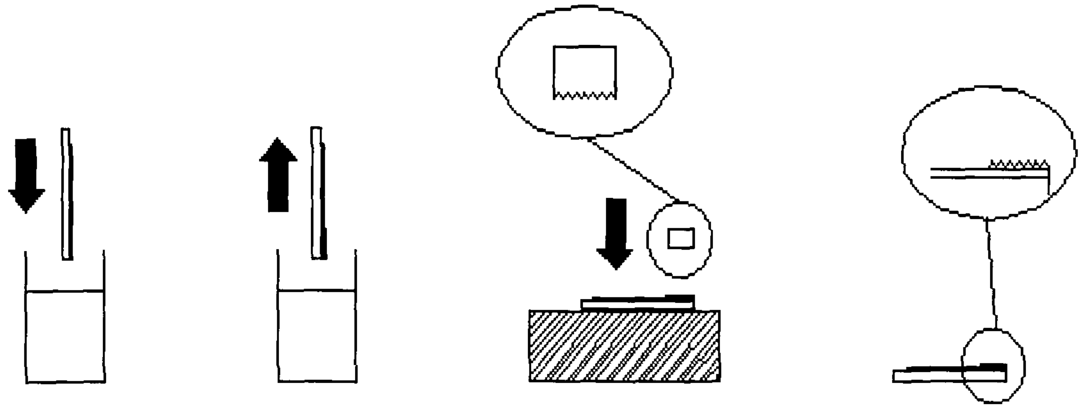

(1) Dip (2) Withdrawal (3) Emboss (4) Product

Figure 5.4 *Embossing Procedure*

5.3 Embossed Grating Characterisation

This section describes the characterisation of the embossed sol-gel derived grating couplers. Important parameters include similarity of embossed and master gratings, grating periodicity, temporal stability of sol-gel-derived gratings and coupling efficiency of embossed gratings. Atomic force microscopy and Scanning tunnelling microscopy may be used to compare the master and embossed gratings and provide information on grating periodicities. Diffraction studies are used to determine grating periodicity and stability with time. Finally, grating coupling efficiency is determined by coupling into guided modes of sol-gel-derived planar waveguides.

5.3.1 AFM Study of Embossed Sol-Gel-Derived Gratings

Atomic force microscopy is used to image embossed sol-gel-derived gratings fabricated from both ruled and holographic master gratings. This aim of this study is to determine whether the sol-gel embossing procedure allows for the complete replication of master grating characteristics.

A three dimensional image of 20 µm x 20 µm area of an embossed grating coupler is illustrated in figure 5.5. The grating was fabricated from a 600 line mm^{-1} blazed master and it is immediately apparent from this image that the sol-gel grating strongly retains the blaze of the master Such high quality replication of the blazed profile of the grating using an extremely simple embossing procedure suggest that the sol-gel embossing process may provide an ideal route for the low cost fabrication of optical devices with elaborate surface profiles such as diffractive optic elements (DOE's)[9].

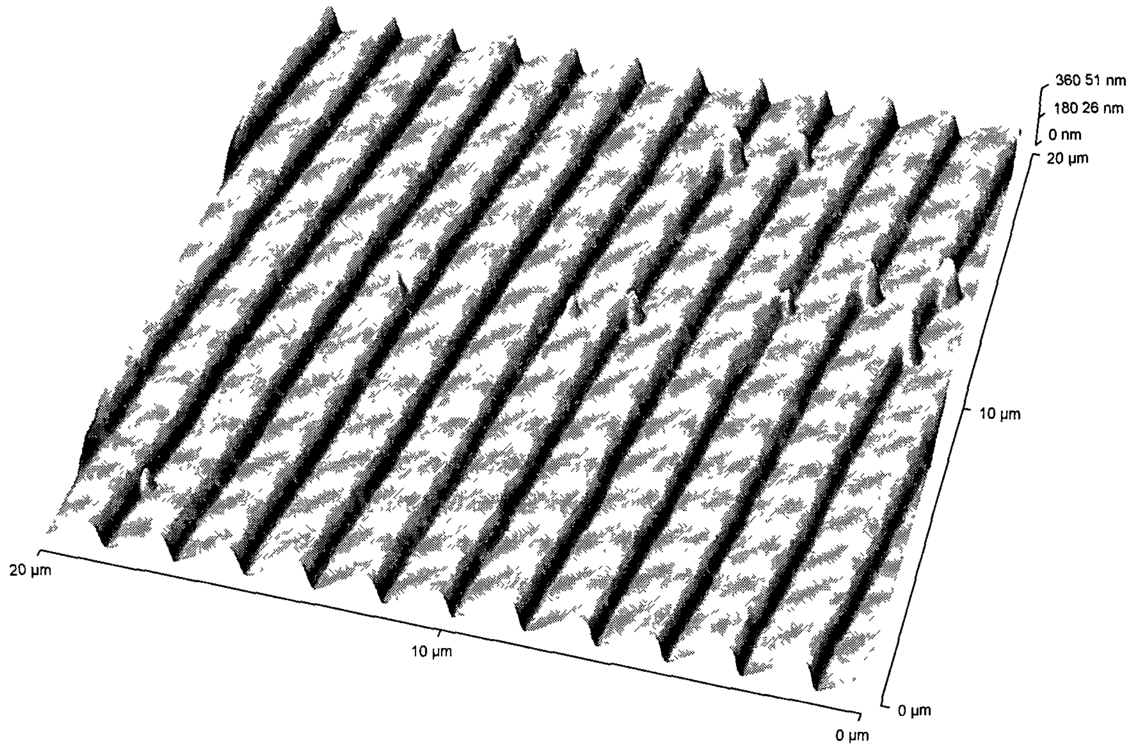

Figure 5.5 *AFM image of embossed grating coupler (blazed, 600 lines mm^{-1})*

The periodicity of the imaged area of the embossed sol-gel-derived grating is determined to be 1.705 µm which corresponds to 587 lines.mm^{-1} Such a periodicity, is extremely close to the quoted master grating value of 600 lines.mm^{-1}.

There are a small number of defects observed on the surface of the embossed sol-gel derived grating. Such defects may simply be due to dust accumulation on the surface during the embossing procedure However, the somewhat periodic nature and profile of the defects tends to suggest that they may arise from defects which were present on the surface of the master grating at the time of use.

Atomic force microscopy is also be used to investigate embossed gratings derived from a holographic master Shown in figure 5.6 is a three dimensional image of a 10 µm x 10 µm section of an embossed sol-gel-derived grating fabricated using a 2400 line.mm^{-1} sinusoidal holographic master grating. As with the ruled gratings, the quality of embossed grating is extremely high with very little visible defects. The slight curvature observed in figure 5.6 is not in fact a characteristic of the embossed device it is the result of a small error in the graphics software accompanying the AFM machine, which occasionally causes slight bending of the stored image, and thus may be ignored.

The periodicity of the imaged area of the embossed holographic grating is determined to be 0.4229 µm which corresponds to 2365 lines.mm^{-1}. Such a measurement is favourable when compared with a quoted master value of 2400 lines.mm^{-1}.

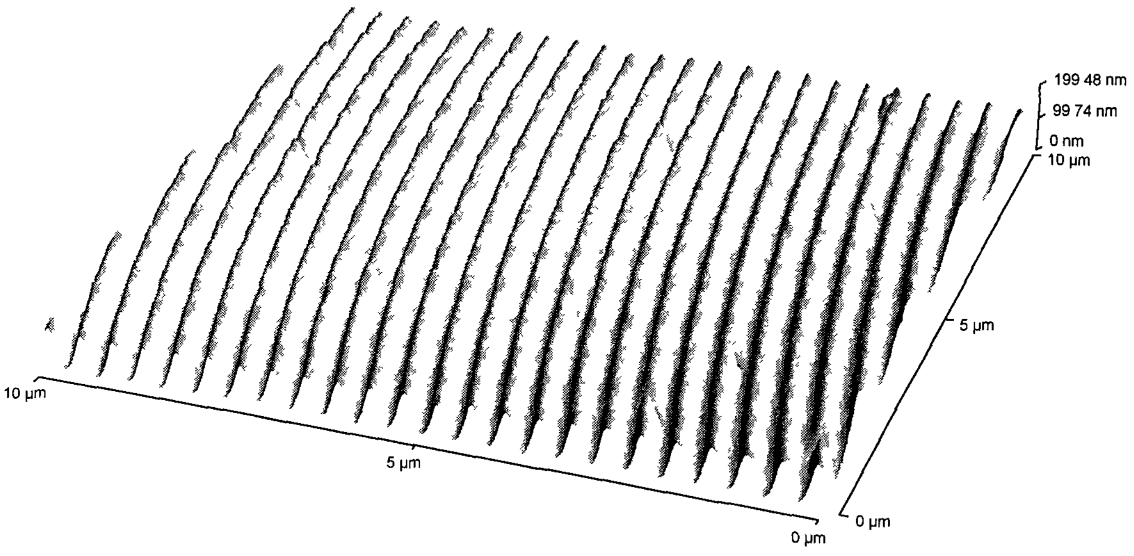

Figure 5.6 *AFM image of embossed grating coupler (holographic, 2400 lines mm^{-1})*

In conclusion, atomic force microscopy has been used to emphatically demonstrate that the embossing procedure utilised to produce sol-gel-derived gratings has the ability to replicate the very fine surface relief details. Sol-gel-derived embossed gratings fabricated from both ruled and holographic masters were found to closely match the masters, with periodicities very close to the quoted master values. However, it is not possible to unequivocally state that the embossed gratings are exact replicas because, tolerances for master grating production are not provided by the manufacturers.

As with the master gratings it was not possible to determine the embossed grating depths due to unfavourable tip dimensions.

5.3.2 STM Study of Embossed Sol-Gel-Derived Gratings

Scanning-tunnelling microscopy (STM) may be used to image surfaces of conducting materials with atomic-scale resolution and is used in this thesis as a complimentary imaging technique to atomic force microscopy for determination of grating quality.

STM uses an atomically-sharp metal tip that is brought very close to the surface. When the tip and sample are connected with a voltage source, a small tunnelling current flows between the tip and sample surface. This current can be measured, and the magnitude depends on the distance between the tip and the surface. As the tip is moved laterally across the surface, a feedback mechanism moves the tip up and down to maintain a constant tunnelling current. Rastering the tip across the surface therefore produces a topographic map of the surface.

A thin layer of gold (45 nm) is evaporated onto the embossed sol-gel-derived grating couplers, the purpose of which is to produce a conducting grating sample. Gold is chosen because when coated onto samples it tends to adapt the same surface relief profile as the sample. As with the atomic force microscopy study, embossed gratings fabricated from both ruled and holographically generated masters are investigated. Figure 5.7 is a screen dump of the STM output for a gold-coated sol-gel-derived embossed grating coupler fabricated from a 600 line.mm^{-1} blazed master grating It can be immediately seen that the gold layer has removed the blaze effect from the embossed grating however, the determined periodicity of 1 804 μm indicates 555 lines mm^{-1}, which is comparable to the quoted master value

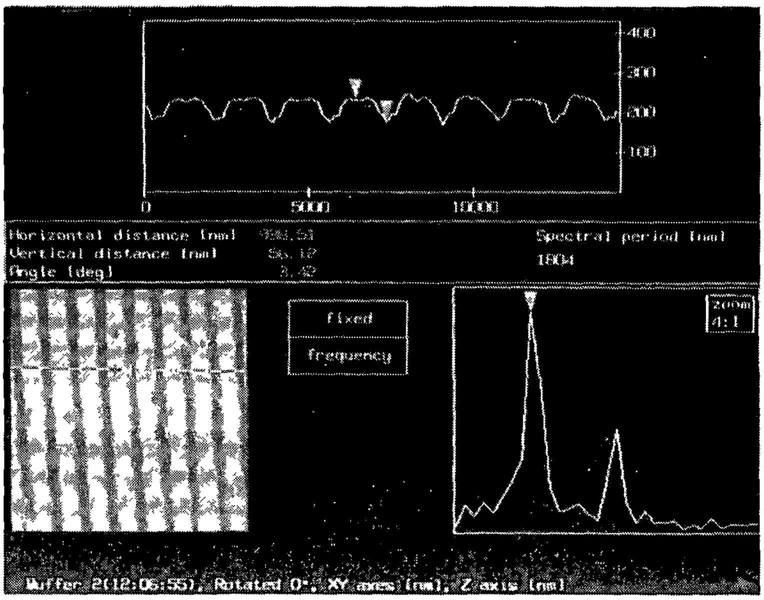

Horizontal distance [nm] [illegible]
Vertical distance [nm] 56.12
Angle [deg] 3.42
Spectral period [nm] 1804
Buffer 2(12:06:55), Rotated 0°, XY axes [nm], Z axis [nm]

Figure 5.7 *STM image of embossed grating coupler (blazed, 600 lines.mm^{-1})*

A three-dimensional image of the gold-coated sol-gel-derived embossed grating coupler is shown in figure 5.8.

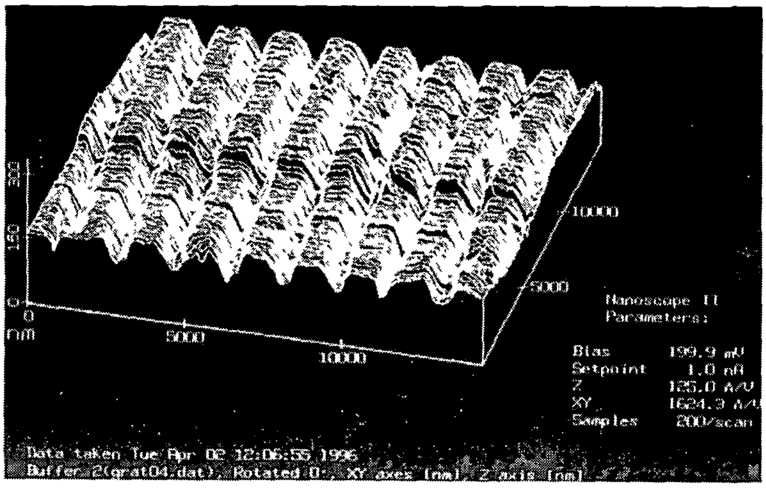

Nanoscope II
Parameters:
Bias 199.9 mV
Setpoint 1.0 nA
Z 125.0 A/V
XY 1624.3 A/V
Samples 200/scan
Data taken Tue Apr 02 12:06:55 1996
Buffer 2(grat04.dat) Rotated 0°, XY axes [nm], Z axis [nm]

Figure 5.8 *3D STM image of embossed grating coupler (blazed, 600 lines mm^{-1})*

Embossed sol-gel-derived grating couplers fabricated using holographic sinusoidal 1200 line.mm^{-1} master gratings were also analysed using scanning tunnelling microscopy. Shown in figure 5 9 is a screen dump of the STM output for such a grating.

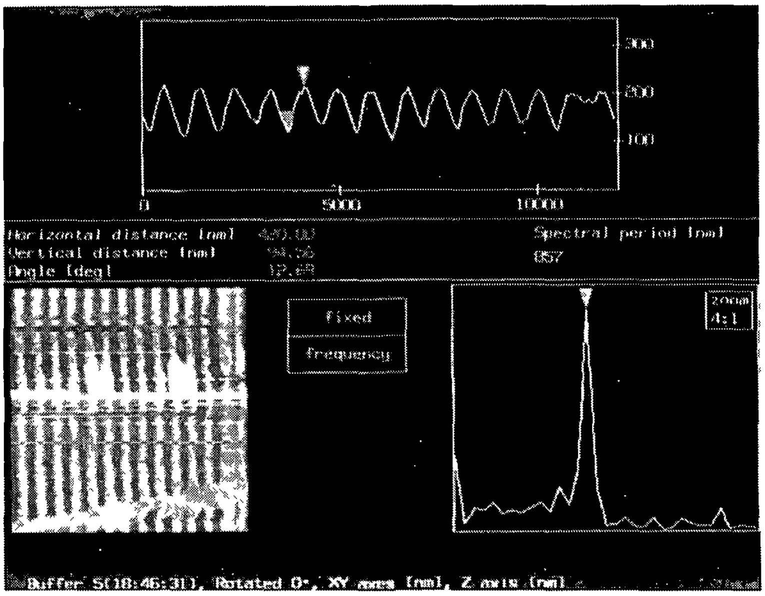

Horizontal distance [nm]
Vertical distance [nm]
Angle [deg]
Spectral period [nm] 857

Figure 5.9 *STM image of embossed grating coupler (holographic, 1200 lines mm^{-1})*

It can be seen that the quality of the gold-coated sinusoidal gratings is excellent and, as with the blazed sample, there are no defects visible. The periodicity of the imaged area is 857 nm which corresponds to 1166 lines.mm^{-1}, which is very close to the quoted master value and the AFM results presented previously.

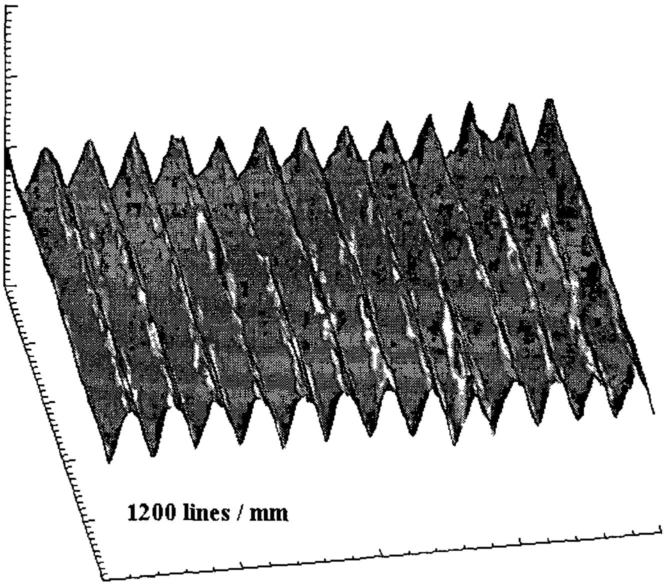

Figure 5.10 *3D image of embossed grating coupler (holographic, 1200 lines mm^{-1}).*

Figure 5.10 shows a three-dimensional image of such an embossed sol-gel-derived replica grating. It is evident from this image that the quality of the coated gratings is high with few defects visible. This in itself is not conclusive evidence of high quality gratings because the gold layer may be masking any defects, however, when considered in conjunction with the atomic force microscopy study, there is strong evidence suggesting that the sol-gel process and the embossing technique produce high quality surface relief devices.

In summary, the scanning tunnelling microscopy study has further illustrated that the embossing procedure utilised produces high quality sol-gel-derived grating couplers, the periodicities of which were in close agreement with the AFM and diffraction studies (see section 5.3.3) and quoted master values However, it was observed that the gold coating tends to mask out the blaze characteristic of some devices and as with AFM it was not possible to determine accurate grating depth values because the tips employed in this study were not calibrated for use on gold samples.

5.3.3 Temporal Stability of Embossed Sol-Gel-Derived Gratings

An important property of embossed sol-gel-derived gratings is temporal stability of the periodicity. High temporal stability of grating periodicity would enhance the possibility of incorporation of sol-gel-derived embossed grating couplers into commercial instruments since the coupling conditions would remain constant. However, a low temporal stability would tend to indicate that commercialisation of such components would not be feasible since the coupling conditions for the embossed sol-gel-derived grating would vary with time.

Grating stability with time was determined using diffraction studies and the experimental set-up is shown in figure 5.11

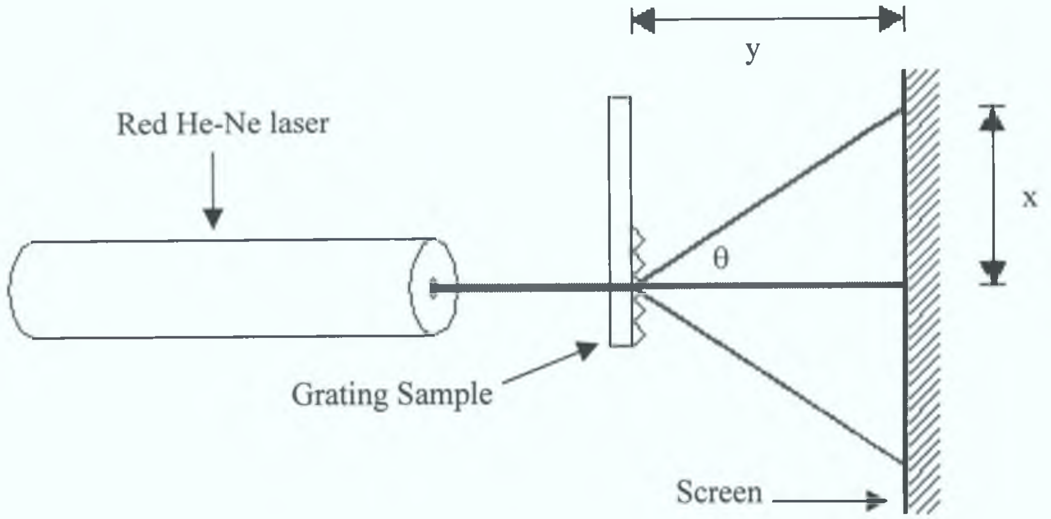

Figure 5.11 *Experimental configuration for determination of grating periodicity.*

Light from a helium-neon laser (λ = 632.8 nm) is directed normally onto the sol-gel derived grating couplers. A diffraction pattern can be observed on the viewing screen to the right of the sample. The dimensions of this pattern are used to determine the periodicity of the gratings in accordance with the diffraction equation shown below.

$$n\lambda = d\mathrm{Sin}\theta \qquad [5.1]$$

where n is the diffraction order, d is the grating periodicity and $\tan\theta = x/y$.

Temporal stability was determined only for the 600 and 1200 line.mm^{-1} samples because at normal incidence 2400 line.mm^{-1} gratings tend to couple into either a glass substrate or a sol-gel derived waveguide thus rendering it difficult to determine periodicities using diffraction. However, due to identical fabrication procedures the results derived are applicable to all gratings. All gratings analysed were stored in sealed petri dishes in ambient conditions in the absence of UV light.

It can clearly be seen from figure 5.12 that over the course of 1 year the periodicity of the embossed sol-gel derived gratings remains extremely stable. For sol-gel derived embossed gratings fabricated from a 1200 line.mm^{-1} master grating the initial periodicity measured when the grating was fabricated was 1201.45 ± 6 line.mm^{-1} while

364 days later the periodicity was determined to be 1200.25 ± 6 line.mm^{-1}. For gratings produced from a 600 line mm^{-1} master, initial measurements indicated a periodicity of 600 25 line mm^{-1} The periodicity after 364 days was determined to be 600.74 line.mm^{-1}. It is apparent that the differences between the experimentally obtained periodicities over the course of one year are substantially lower than the error of the experiment (± 6 lines / mm) and thus the conclusion can be drawn that the gratings are completely stable with time.

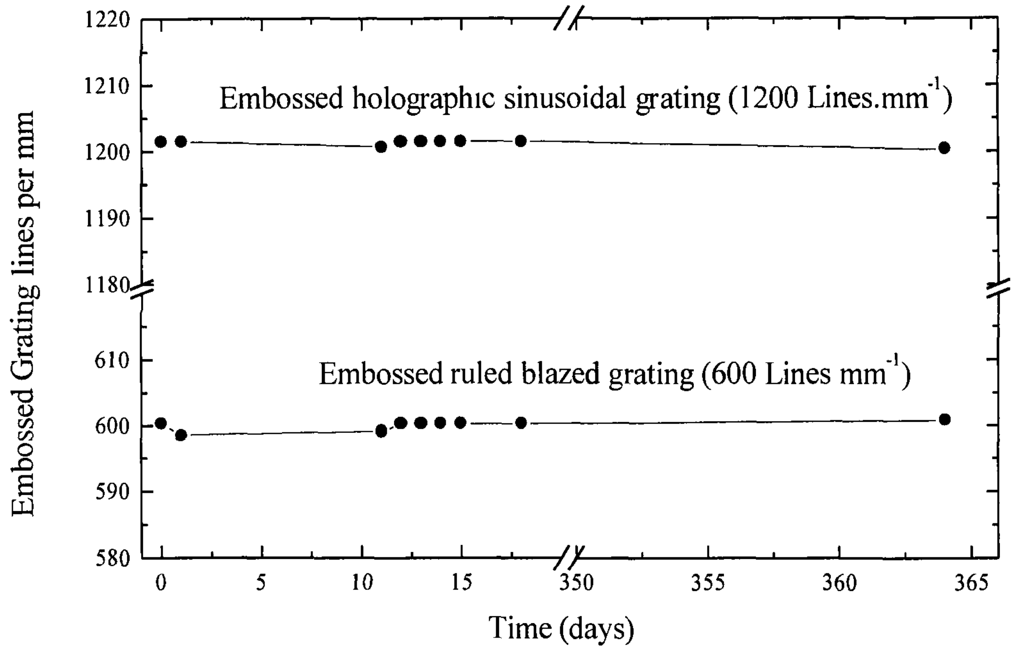

Figure 5.12 *Variation in embossed grating coupler periodicity with time*

5.3.4 Embossed Grating Coupling Efficiency

The efficiency with which a grating coupler converts energy from an incident beam of radiation into a guided mode in a waveguide is a very important parameter. Too low a coupling efficiency and the grating will not be couple in enough of the incident energy into a guided mode, thus rendering a device inefficient. Grating coupling efficiency is directly related to the dimensions of the coupler and the profile of the incident radiation

The coupling efficiencies of the sol-gel derived embossed grating couplers may be determined by measuring the fraction of power incident on a grating which is coupled into a sol-gel derived planar waveguide. The experimental configuration is shown in figure 5.13. Light from a helium-neon laser (632 8 nm) is incident on an embossed sol-gel derived grating coupler on the surface of a planar waveguide also fabricated using the sol-gel technique The waveguide / grating coupler configuration is mounted on a high-resolution rotary stage. The entire configuration is rotated with respect to the laser until coupling conditions had been reached and a mode was visible. At this point the power transmitted through the device and the power reflected at the grating are measured. The coupling efficiency, η, is then calculated using the equation[10]

$$\eta = \frac{I_i - I_r - T_r}{I_i} \qquad [5.2]$$

where I_i is the incident power of the laser on the grating, T_r is the transmitted power through the sample (including all diffraction orders) and I_r is the power reflected from the grating (including all diffraction orders).

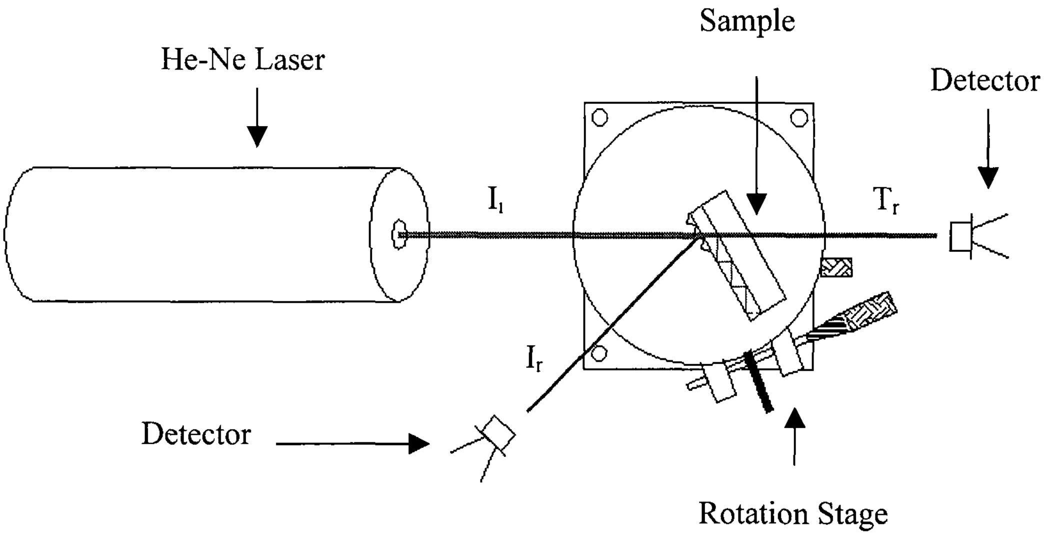

Figure 5.13 *Configuration for determination of grating coupler efficiency*

Coupling efficiencies for a number of waveguide / grating coupler samples were determined and the results are presented in the form of a histogram in figure 5 14.

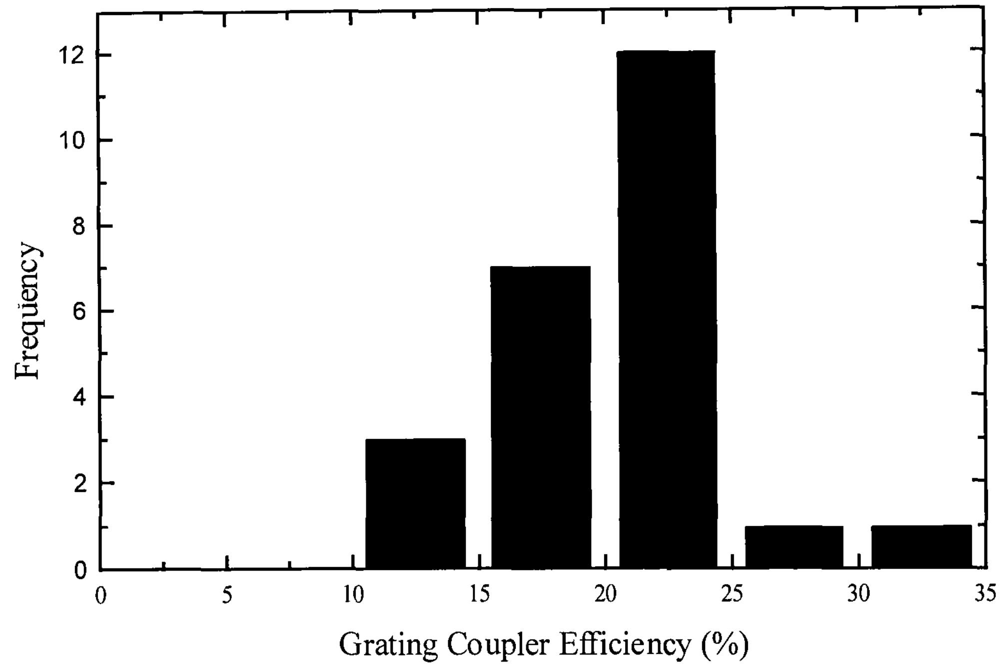

Figure 5.14 *Histogram of embossed sol-gel-derived grating coupler efficiency*

It was found that the majority of sol-gel derived embossed grating couplers had coupling efficiencies between 20 and 25 %. It is possible to increase efficiency by optimising grating coupler profile, since grating layer refractive index, grating depth and grating periodicity all affect the coupling efficiency. However, due to the limited range of cheap commercially available surface relief gratings which could be used as masters it was decided that such coupling efficiencies were adequate for use in laser and light emitting diode-based integrated optic gas sensors.

5.4 Limitations of Embossing Technique

The embossing technique, while able to produce high quality replicas of master gratings, is not without its drawbacks. The main problem associated with the technique is the degradation of master gratings due to cleaning.

After use, it is necessary to clean the master grating to remove excess sol-gel from the grooves which, if not removed will dry and harden within the grooves and alter the surface relief profile of the master. In the cleaning procedure a master grating is immersed in methanol and lens tissue is used to remove the excess material. This is then followed by a short drying period.

The cleaning procedure has the desired effect in that it removes all the excess sol-gel material from the grooves However, due to the delicacy of the surface relief structure and the severity of the cleaning technique, master degradation is common The more times a master is exposed to the cleaning process the larger the extent of degradation.

Shown in figure 5 15 is a blazed master grating of quoted periodicty; 600 lines.mm^{-1}. This sample has been exposed to the abrasive cleaning procedure numerous times and it may be clearly seen that there are a number of defects visible on the sample surface. A similar effect was observed for the holographic sinusoidal master gratings, an image of a damaged 1200 lines mm^{-1} holographic master grating is illustrated in figure 5.16.

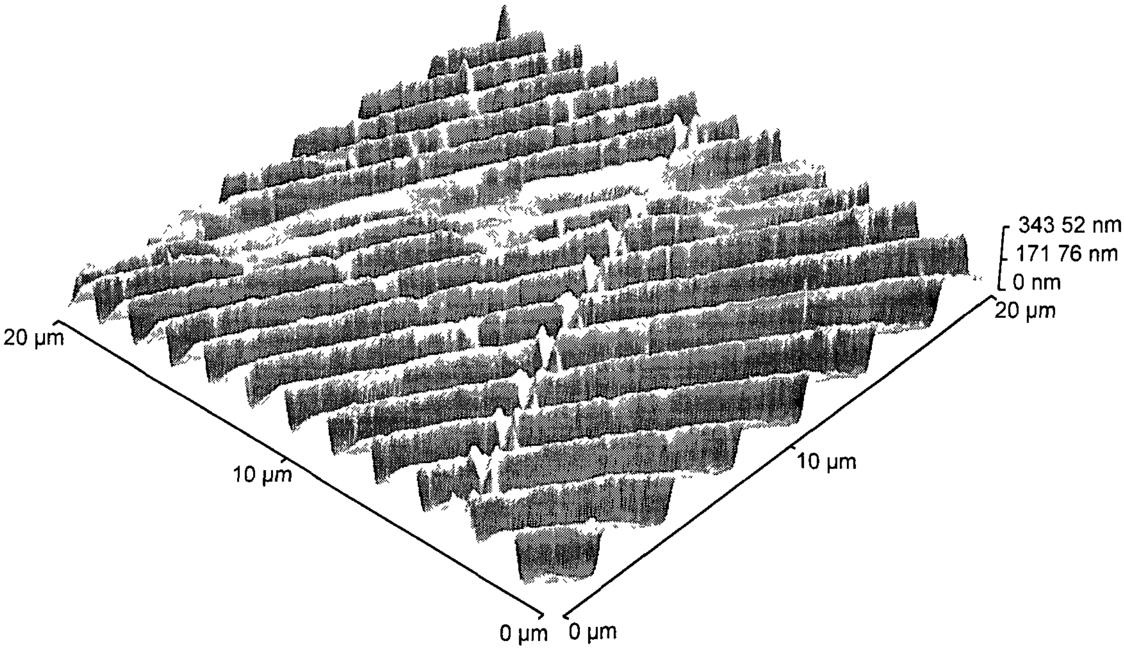

Figure 5.15 *AFM image of master grating (600 lines mm^{-1})*

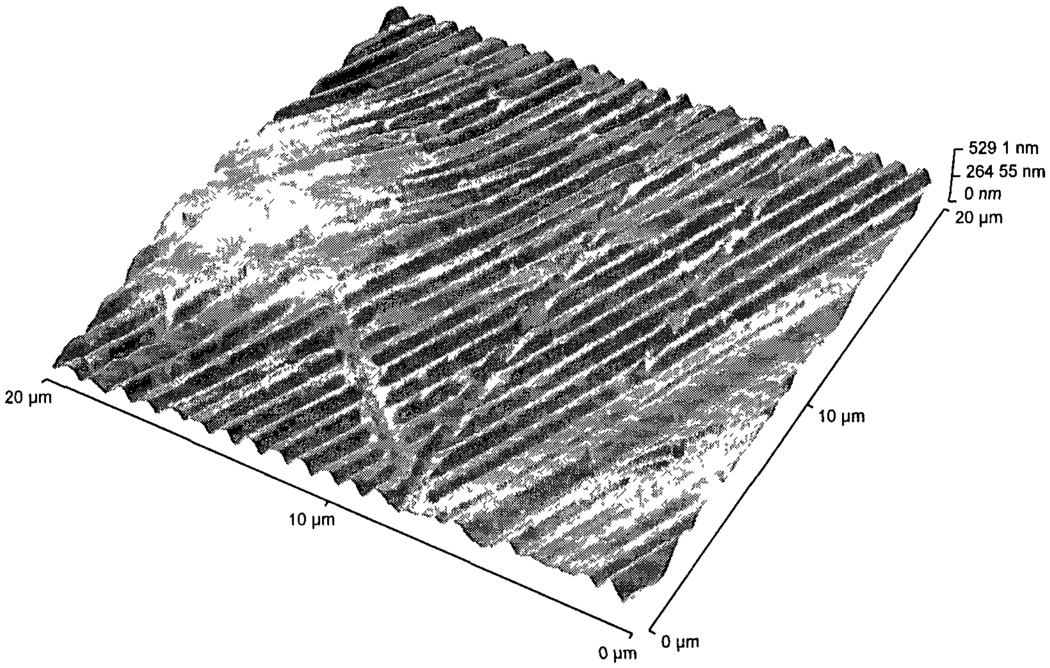

Figure 5.16 *AFM image of master grating (1200 lines mm^{-1}).*

Due to the high replication nature of the embossing procedure, if a master grating contains defects then so will any embossed sol-gel-derived grating couplers fabricated from the damaged master. Such a situation is clearly illustrated in figure 5.17 where it can be seen that the grating produced via the embossing technique contains a high number of defects. These defects are the result of master grating defects as opposed to embossing procedure-induced defects.

A solution to such problems would be to develop a new less abrasive cleaning procedure, which, while removing the excess sol from the grooves would not interfere with the master grating quality. However, since the master gratings used throughout this research are cheap and readily available, and since the cleaning-induced damage only occurs after substantial master usage (typically > 10 routines), such a procedure was not investigated.

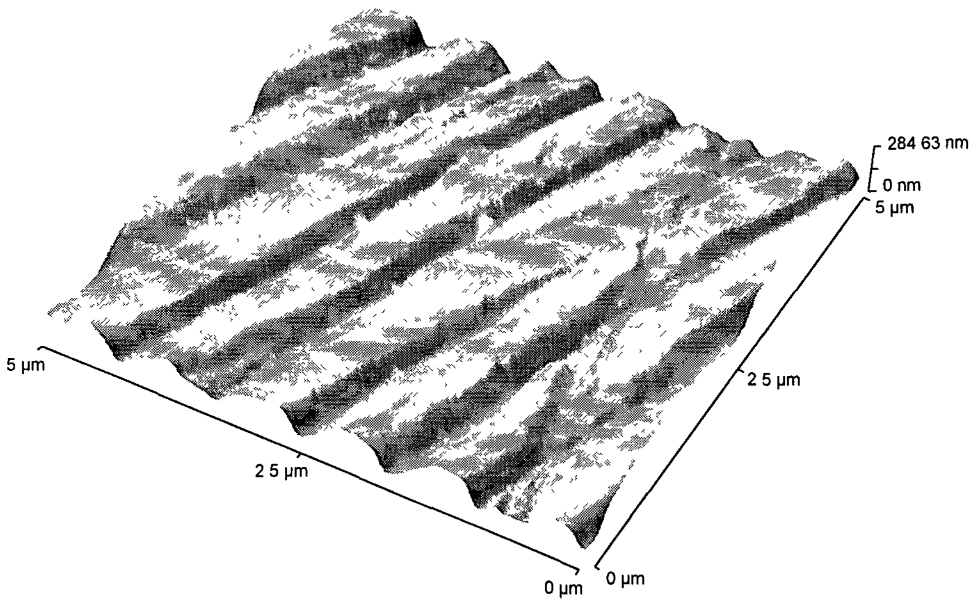

Figure 5.17 *AFM image of embossed sol-gel-derived grating (1200 lines mm^{-1})*

Another problem associated with the current embossing procedure, is the lack of regulation of the pressure applied to the sample during embossing. This is not possible because the embossing device is a mechanical device which utilises a screw type effect to increase the pressure on the sample. A possible improvement to this routine would be use of a pneumatic device as illustrated in figure 5.18.

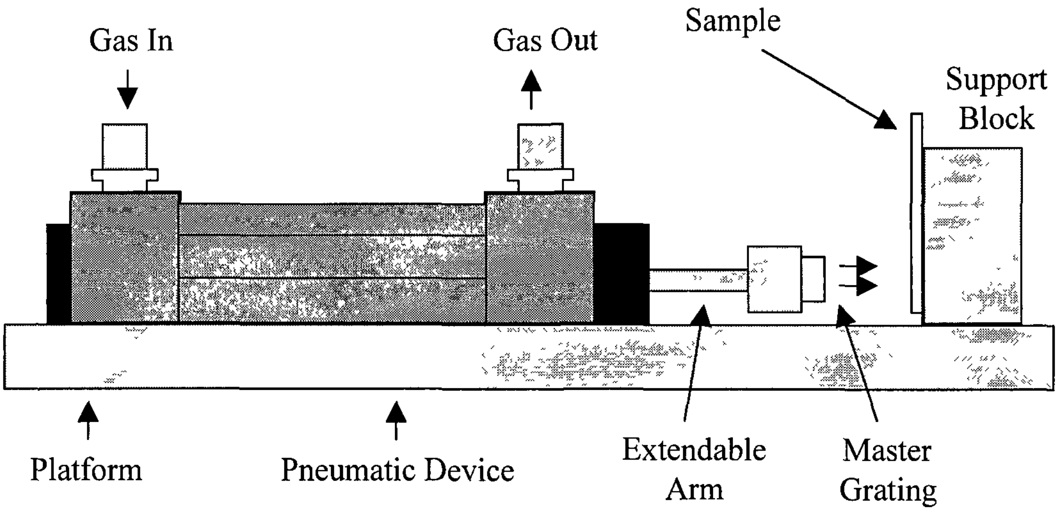

Figure 5.18 *Pneumatic Embossing Apparatus*

Initial investigations into the use of such a device were carried out with very limited success. However, it is expected that increased development of such a technique could produce a pneumatic embossing device which would allow for pressure control, and optimisation of the technique resulting in the production of high quality embossed grating couplers.

5.5 Conclusion

The embossing procedure utilised for the fabrication of sol-gel-derived grating couplers from commercially available master gratings was explained clearly and atomic force microscopy (AFM) was used to analyse the structures of the master gratings. The resultant embossed gratings were then physically characterised in terms of quality, similarity to master, periodicity, temporal stability and coupling efficiency using a wide range of experimental techniques including atomic force microscopy (AFM), scanning tunnelling microscopy (STM), diffraction studies and laser coupling into thin film sol-gel-derived waveguides. Limitations of and possible improvements to the embossing technique were discussed.

In conclusion, it has been demonstrated in this chapter that the sol-gel technique provides a feasible route for the fabrication of high quality, low cost replica grating couplers that exhibit high coupling efficiencies and excellent temporal stability. Such observations imply that the embossing procedure reported in this thesis could provide an extremely low cost, yet highly reproducible route for the fabrication of elaborate diffractive optic elements (DOE's), such applications were not investigated in the course of work for this thesis.

References

1. Mendes S.B., Li L., Burke J J., Lee J.E., Saavedra S.S.. '**70-nm-bandwidth achromatic waveguide coupler**', Applied Optics, 1995, Vol. 34, No. 27, pp. 6180-6186

2. Weısenbach L., Zelınsı B J.J , Roncone R.L., Burke J.J.: '**Wet-chemical fabrication of a single leakage-channel grating coupler**', Optics Letters, 1995, Vol. 20, No. 7, pp. 707-709

3. Moreau Y., Arguel P., Coudray P. Etienne P., Porque J., Sıgnoret P.: '**Direct printing of gratings on sol-gel layers**', Optical Engıneering, 1998, Vol. 37, No. 4, pp. 1130-1135

4. Heuberger K., Lukosz W.· '**Embossing technique for fabricating surface relief gratings on hard oxide waveguides**', Applied Optics, 1986, Vol. 25, No. 9, pp. 1499-1504

5. Roncone R L., Weller-Brophy L.A., Wıesenbach L., Zelinski B.J.J.: '**Embossed gratings in sol-gel waveguides: pre-emboss heat treatment effects**', Journal of Non-Crystalline Solids, 1991, Vol. 128, pp. 111-117

6. Kunz R.E., Edlinger J., Sixt P., Gale M.T.: '**Replicated chirped waveguide gratings for optical sensing applications**', Sensors and Actuators A, 1995, Vol. 46-47, pp. 482-486

7. Li M., Sheard S.J.: '**Experimental study of waveguide grating couplers with parallelogramic tooth profiles**', Optical Engineering, 1996, Vol. 35, No. 11, pp. 3101-3106

8. Nishiwaki S., Ascada J., Ohshima K., Kitagawa T.: '**Fabrication of a concentric-circular focusing grating coupler by a conic-wave-front**

interference method and light-convergence experiments using the coupler', Applied Optics, 1995, Vol. 34, No. 31, pp 7372-7382

9. Kipfer P , Collischon M., Haidner H., Schwider J.· '**Subwavelength structures and their use in diffractive optics**', Optical Engineering, 1996, Vol. 35, No. 3, pp. 726-731

10. Gong Q., Assanto G., Zanoni R., Stegeman G.I., Burzynski R., Prasad P.N.· '**Efficient grating coupling to poly-4BCMU optical waveguides**', Applied Optics, 1990, Vol 29, pp. 3887-3890

Chapter 6 Modelling of Platform

6.1 Introduction

Grating for windows is a commercially available CAD tool (BBV Software, The Netherlands) which may be used for the design of integrated optical grating couplers. It allows the user to find the resonance condition between incident radiation and a waveguide mode. It also allows the user to optimise the coupler geometry and can deal with different profiles for waveguides, beam inputs and grating grooves.

In this chapter, an introduction to operating the software is presented. The software predictions for two distinct purposes are presented. First, the effect of various parameters (waveguide refractive index, waveguide thickness, grating groove depth etc.) on guided-mode coupling efficiency was investigated. The aim of this modelling was to provide information on optimisation of device performance within the constraints imposed by the fabrication procedures. Secondly, the software was employed to verify that the experimentally obtained results for parameters such as grating coupling efficiency and resonance angle, complied with predicted theory. The aim was to obtain information about the accuracy of fabrication and characterisation techniques.

6.2 Using the Software

In this section, the operation of the *Grating* software is described and the procedure for the determination of the peak coupling efficiency and coupling efficiency profile for a given waveguide / grating configuration is presented.

The program is activated and information about the structure to be analysed is entered in the **Waveguide, Grating, Geometrical and Beam parameters** dialog boxes as shown in figure 6.1.

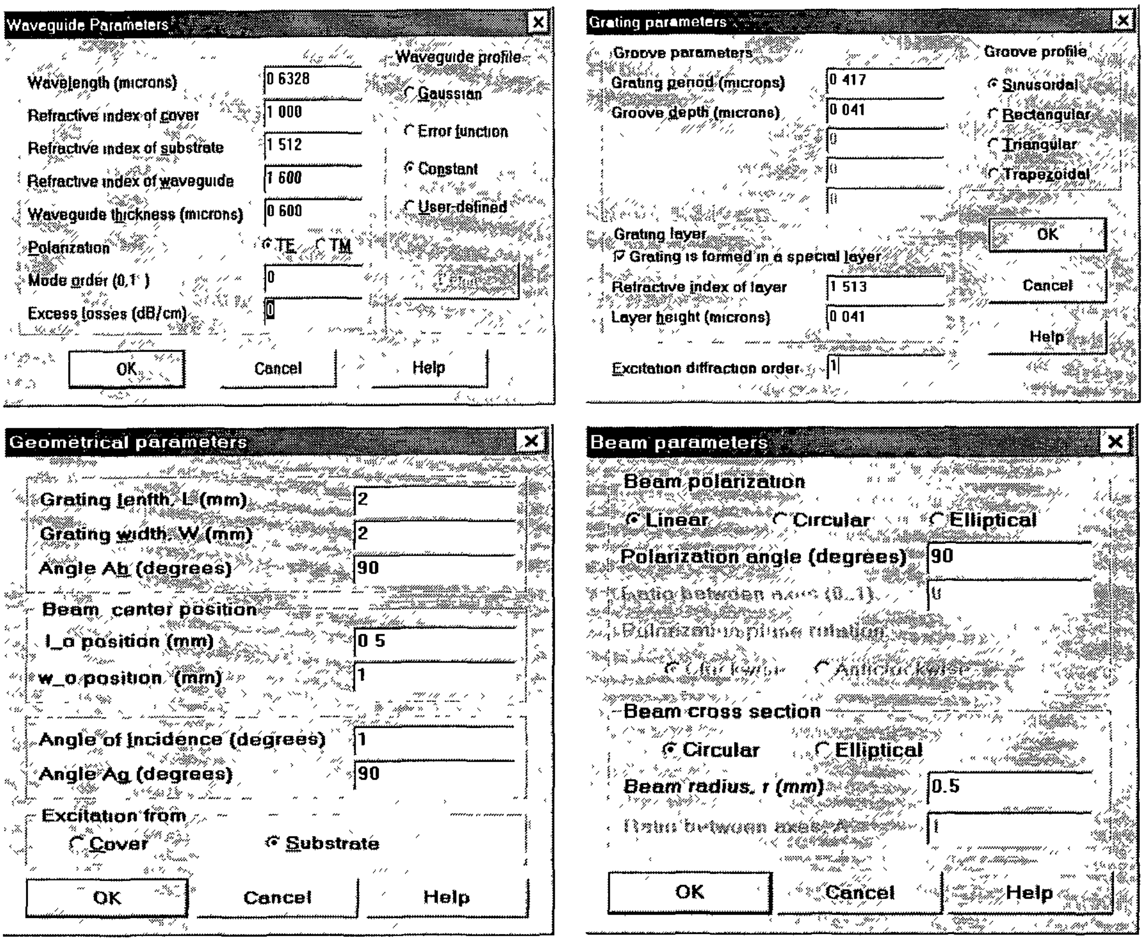

Wavelength (microns) 0 6328
Refractive index of cover 1 000
Refractive index of substrate 1 512
Refractive index of waveguide 1 600
Waveguide thickness (microns) 0 600
Polarization ● TE ○ TM
Mode order (0,1) 0
Excess losses (dB/cm) 0
Waveguide profile
○ Gaussian
○ Error function
● Constant
○ User-defined

Groove parameters
Grating period (microns) 0 417
Groove depth (microns) 0 041
0
0
0
Groove profile
● Sinusoidal
○ Rectangular
○ Triangular
○ Trapezoidal
Grating layer
☑ Grating is formed in a special layer
Refractive index of layer 1 513
Layer height (microns) 0 041
Excitation diffraction order 1

Grating lenfth, L (mm) 2
Grating width, W (mm) 2
Angle Ab (degrees) 90
Beam center position
l_o position (mm) 0 5
w_o position (mm) 1
Angle of Incidence (degrees) 1
Angle Ag (degrees) 90
Excitation from
○ Cover ● Substrate

Beam polarization
● Linear ○ Circular ○ Elliptical
Polarization angle (degrees) 90
Ratio between axes (0..1) 0
Polarization plane rotation
● Clockwise ○ Anticlockwise
Beam cross section
● Circular ○ Elliptical
Beam radius, r (mm) 0.5
Ratio between axes, A 1

Figure 6.1 *Waveguide, Grating, Geometrical and Beam Parameters Dialog Boxes*

Once all information pertaining to the structure has been inputted, the software determines if the structure produces resonance between the incident radiation and a guided mode and the user may determine the excitation angle and coupling efficiency by accessing the **Find Efficiency** dialog box as shown in figure 6.2.

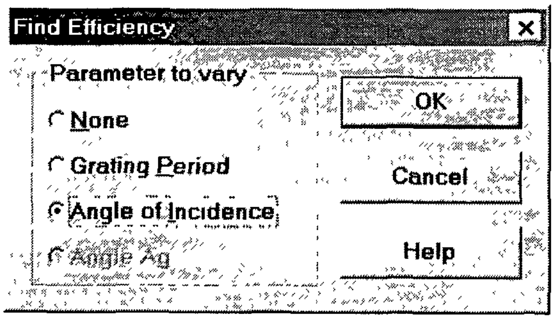

Parameter to vary
○ None
○ Grating Period
● Angle of Incidence
○ Angle Ag

Figure 6.2 *Determination of Angular Efficiency*

The user defines the parameter to vary and a dialog box as shown below appears. In this dialog box, information about the resonance condition is presented. In the example discussed here, the angle of incidence was varied and resonance occurred at a launch angle of 1.742° with a full width at half maximum of 0.0048°. The coupling efficiency value by defining a range of incident angles as shown in figure 6.3.

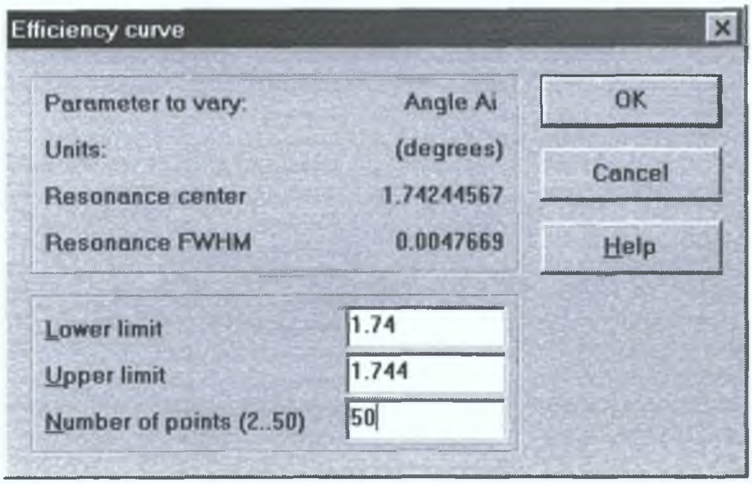

Parameter to vary: Angle Ai
Units: (degrees)
Resonance center 1.74244567
Resonance FWHM 0.0047669
Lower limit 1.74
Upper limit 1.744
Number of points (2..50) 50

Figure 6.3 *Setting Angular Range.*

Coupling efficiency data for the defined range of incidence angles is generated and may be viewed in graphical form as illustrated in figure 6.4, or in tabulated form. The actual peak efficiency value may then be extracted from the generated data.

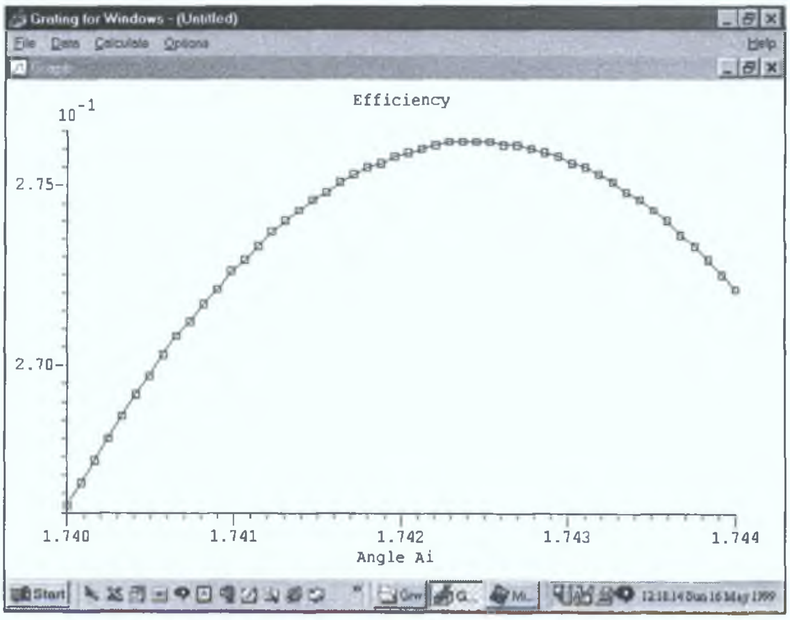

Figure 6.4 *Generated Efficiency Curve.*

6.3 Effect of Parameters on Coupling Efficiency

In this section, the effect of device parameters on the coupling efficiency is investigated. A schematic diagram of the structure to be analysed is shown in figure 6.5.

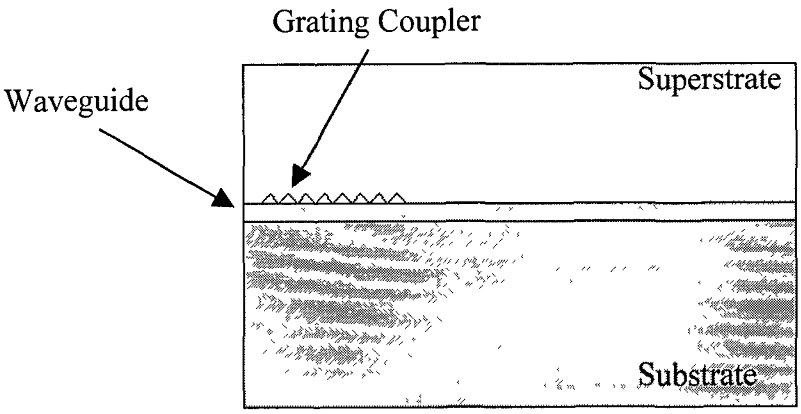

Figure 6.5 *Device Structure*

The main parameters investigated are listed in the left-hand column of table 6.1. The effect of each parameters on the coupling efficiency was determined by varying its value whilst maintaining all other parameters constant. The constant values maintained in all situations are listed in the right hand column of table 6.1. In all cases the incident radiation was of wavelength 632.8 nm and the grating periodicity was 417 nm.

Parameter	Value
Substrate Refractive Index	1.512
Waveguide Refractive Index	1 600
Superstrate Refractive Index	1.000
Waveguide Thickness	600 nm
Grating Groove Depth	41 nm
Grating Layer Thickness	41 nm
Grating Layer Refractive Index	1.513

Table 6.1 *Standard Values Employed for Modelling*

6.3.1 Substrate Refractive Index

The effect of the substrate refractive index was investigated. Typical substrate refractive indices can vary from about 1 4 → 1 56. Therefore, in the software modelling the substrate refractive index was varied over this range in increments of 0 02. The resultant effect upon the coupling efficiency to a guided mode is illustrated in figure 6.6. It was found that the coupling efficiency decreased as the refractive index increased.

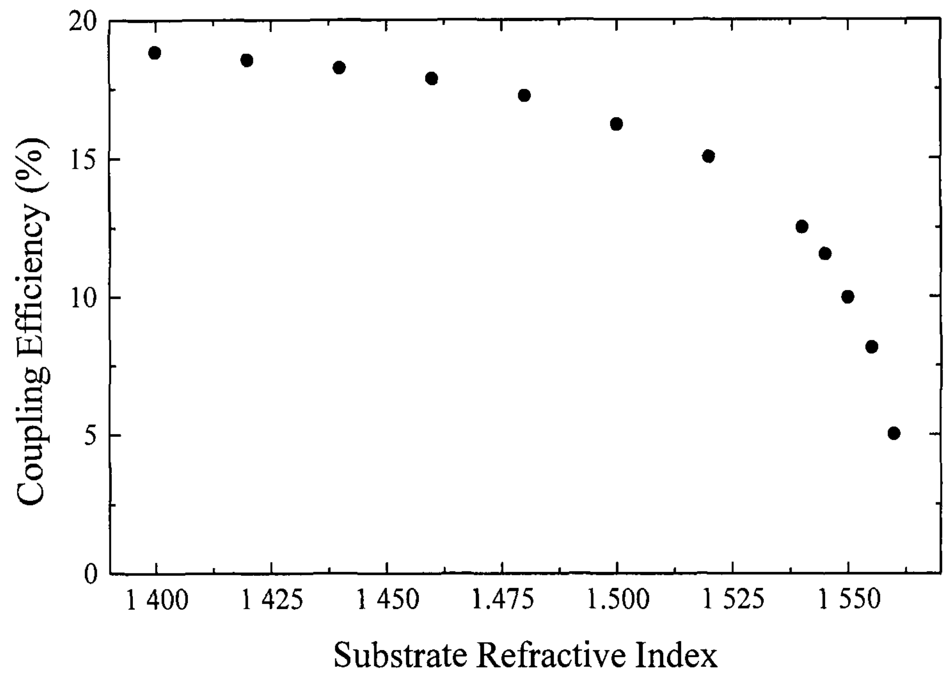

Figure 6.6 *Effect of substrate refractive index on coupling efficiency*

Such an observation is consistent with the theory, which implies that the closer the refractive index of the substrate is to the waveguide refractive index, the less tightly bound the excited modes, and the lower the coupling efficiency. Figure 6.6 indicates that the lower the substrate refractive index the better, indicating that a plexiglass substrate would provide better coupling performance. However, in practise due to the high temperatures required in the waveguide farication procedure, it was not possible to employ such substrates because they would melt. Hence, it was necessary to employ more thermally robust substrates such as glass microscope slides (refractive index

1.512) which, while providing a slightly lower coupling efficiency, also provided a more thermally stable device.

6.3.2 Waveguide Refractive Index

The effect of the waveguide refractive index upon coupling efficiency was investigated. Coupling efficiencies of waveguides with refractive indices in the range 1.53 → 1.65 were examined and the results of this study are presented in figure 6.7. It may be seen that as the waveguide refractive index increases the coupling efficiency increases. Initially, the rise is quite sharp. However, above a waveguide refractive index of 1.58 for the defined configuration, the coupling efficiency does not increase further. Therefore, it is evident that a waveguide refractive index of approximately 1.58 will give near optimal coupling.

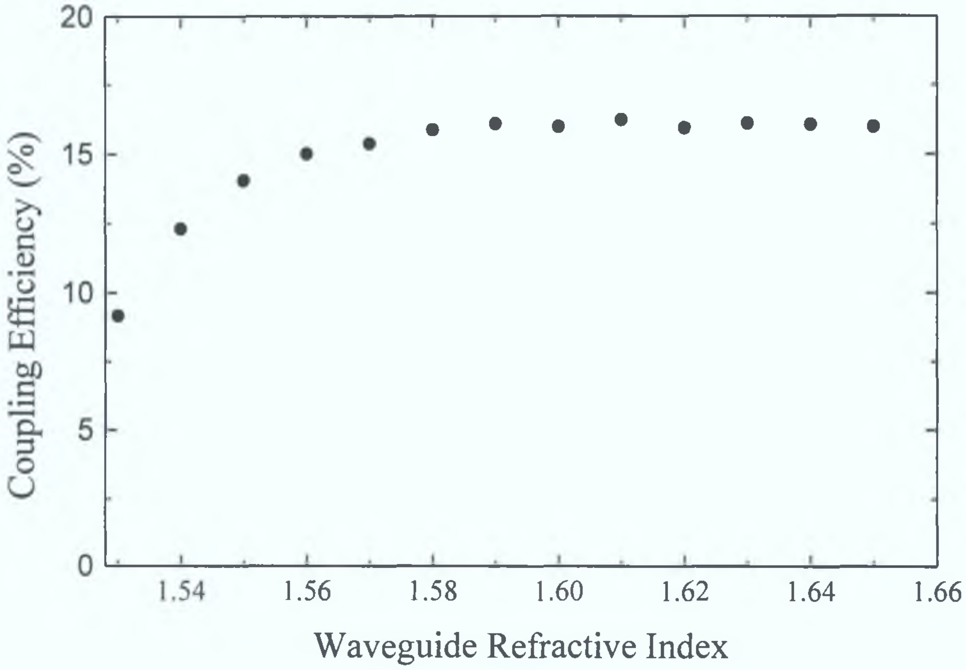

Figure 6.7 *Effect of Waveguide Refractive Index on Coupling Efficiency.*

The sol-gel technique, described in chapter 4, can be used to fabricate waveguides with a refractive index in the range 1.44 → 1.7. The computational results indicated that no improvement in coupling efficiency would be observed with a refractive index higher than 1.58. Therefore, a sol-gel recipe which produced waveguides with refractive indices of 1.58 → 1.6 was employed for all sensor platforms.

6.3.3 Superstrate Refractive Index

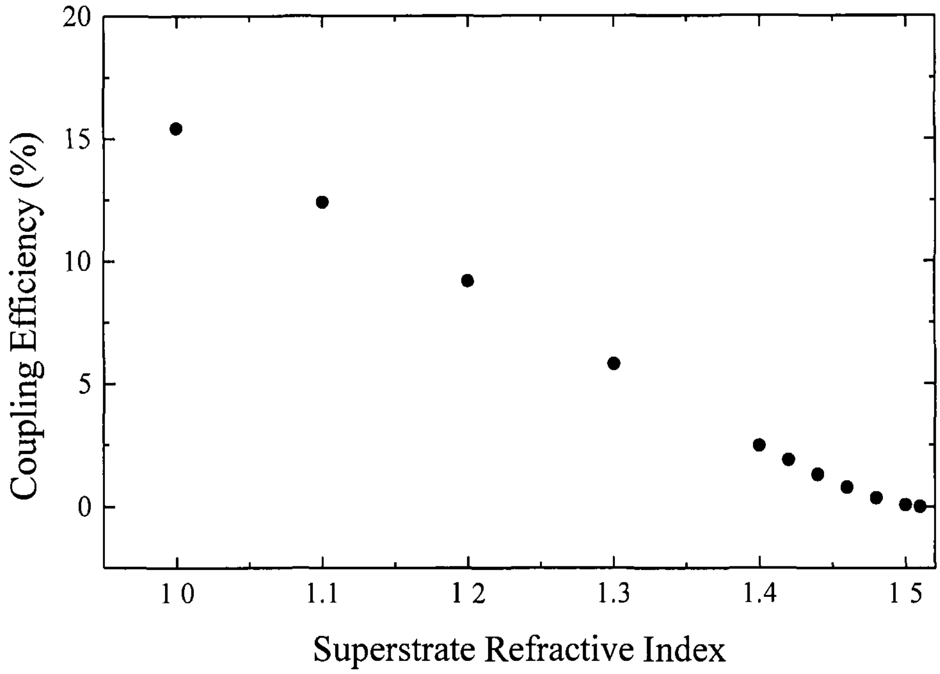

Figure 6.8 *Effect of Superstrate refractive index on coupling efficiency*

It is clear from figure 6.8 that as the superstrate refractive index increases, the coupling efficiency decreases. For the cover materials of interest for this research (e.g. sol-gel-derived sensing layers) the typical refractive index value of 1.43 (porous silica) is of importance. It can be seen that at this cover refractive index, the coupling efficiency is extremely low (< 3%). In order to counterbalance this extremely low efficiency, it was decided that for the sensing platforms presented in the following chapter, air should be the only material covering the grating surface, and the sensing layers should be deposited on the waveguide but not on the grating coupler. The importance of software modelling is highlighted here, and leads to the conclusion that an alternative approach to coating the grating with a high refractive index cover layer had to be employed.

6.3.4 Waveguide Thickness

The *Grating* software indicated that there exists an optimal thickness of approximately 340 nm at which the waveguide exhibits maximum coupling efficiency, as is illustrated in figure 6.9. Above this thickness the coupling efficiency of the structure decreases in an exponential manner. The reasons for such an observation are not understood at present. Below this optimal thickness, the waveguide does not support guided modes and the coupling efficiency correspondingly decreases.

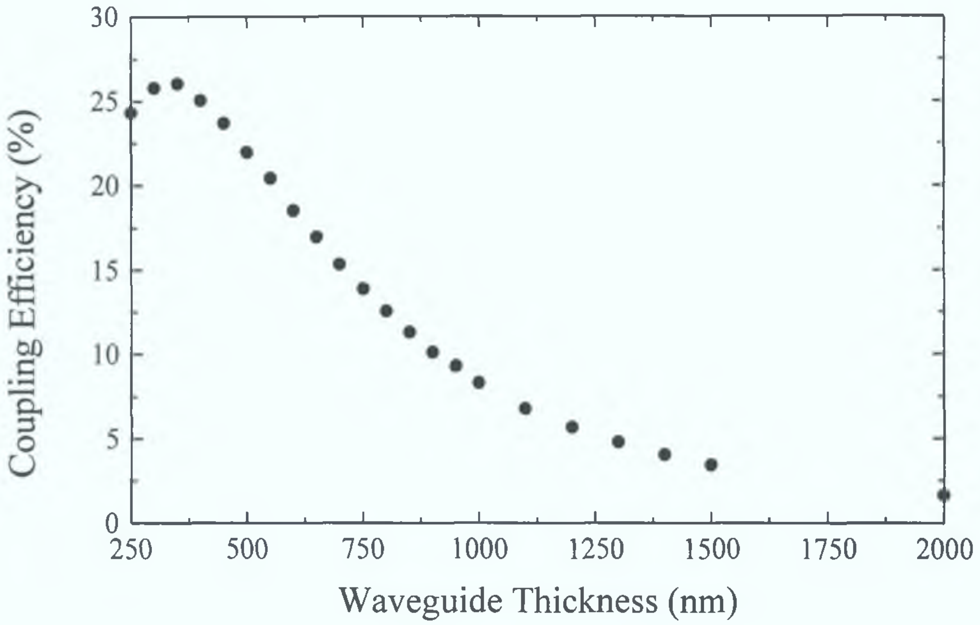

Figure 6.9 *Effect of Waveguide Thickness on Coupling Efficiency.*

This study implies that a sol-gel-derived planar waveguide with a thickness close to this optimal value would provide high coupling efficiency. It was previously determined in chapter 4, that the sol-gel process could produce waveguides close to 340 nm in thickness by employing a deposition speed of 2.8 mm.sec^{-1}. Therefore, the waveguides employed in the sensing platfrom presented in the following chapter were fabricated in accordance with the results presented in this section.

6.3.5 Grating Groove Height

The effect of the grating groove height upon coupling efficiency is presented in figure 6.10. It may be clearly seen that there exists an optimal groove height at which coupling efficiency is a maximum. For the given profile, this groove height was determined to be 84 nm. However, the results of this theoretical study could not be implemented in practise because the master gratings employed in this research were commercially available structures of fixed depth (see chapter 5) and it was decided that the expense of fabricating optimal gratings far outweighed the slightly enhanced efficiency.

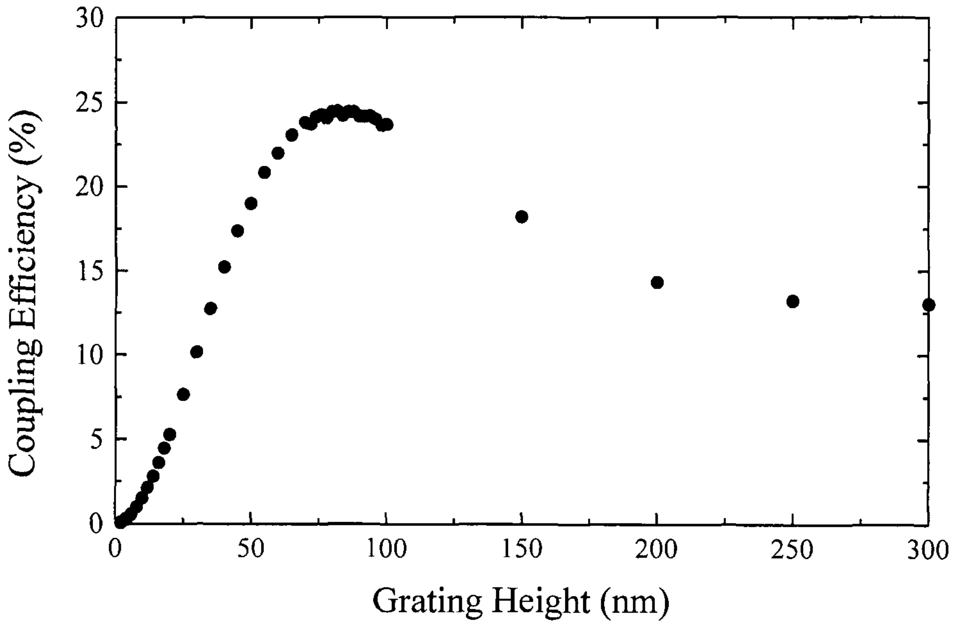

Figure 6.10 *Effect of Grating Height on Coupling Efficiency*

6.3.6 Grating Layer Thickness

The grating coupler fabrication technique employed in this research involved the deposition of a thin layer of high refractive index sol upon the waveguide surface. A negative image of a master grating was then embossed into this layer. A theoretical study of the effect of the layer thickness is presented in figure 6.11 where it can be seen that for a given groove height that the coupling efficiency decreases as the layer thickness increases. Indeed, it can be seen that optimal coupling efficiency exists when the layer thickness exactly matches the groove height. This stands to reason, since the further away the perturbations are from the waveguide surface the lower the coupling efficiency. It is thought that this condition is satisfied in the grating fabrication technique employed in this research since the embossing technique involves pressing the master grating into the thin layer at high pressures which would tend to indicate that excess deposited sol would be pushed out from within the grating area yielding only a layer as thick as the groove height.

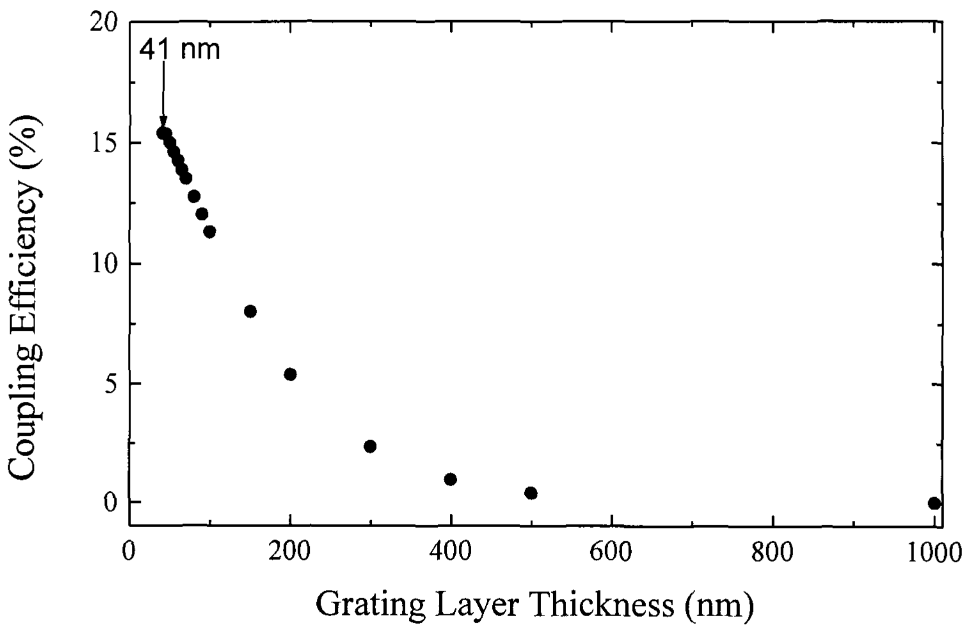

Figure 6.11 *Effect of Grating Layer Thickness on Coupling Efficiency*

6.3.7 Grating Layer Refractive Index

It can be seen from figure 6.12 that the grating coupler layer refractive index has quite a substantial effect upon the coupling efficiency of the grating / waveguide structure In fact, for an increase in layer refractive index of 0.2 the coupling efficency doubles These data indicate that the higher the layer refractive index the better. However, the layer refractive index was confined to values below 1.53 because sols fabricated to have a room-temperature refractive index above this value contain a high concentration of titania, which precipitates out of the sol causing it to become cloudy and therefore rendering it useless.

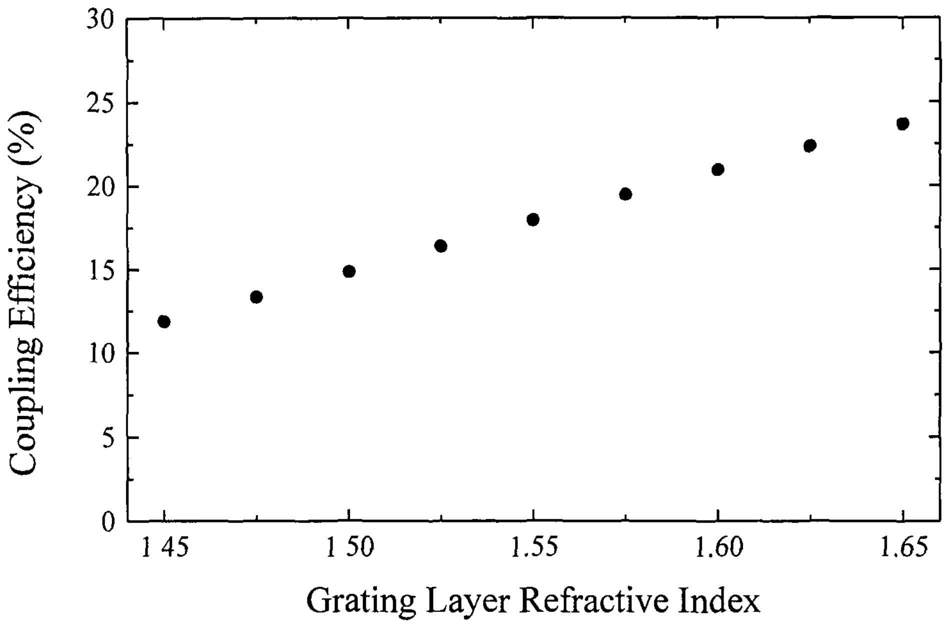

Figure 6.12 *Effect of Grating Layer Refractive Index on Coupling Efficiency*

6.3.8 Summary

It has been clearly illustrated, using the commercially available *Grating* software that each of the variable parameters within a waveguide / grating device has a substantial effect upon the coupling efficiency of the device. The optimal values for each parameter for the given structure were determined and where possible were employed in the device fabrication thus leading to a near optimal device configuration.

6.4 Comparison of Experimental and Theoretical Results

In this section experimentally obtained results for the optimum coupling angle and efficiency for a range of waveguides are compared to theoretically results The purpose of this study is to illustrate that the fabricated devices behaved as predicted by theory.

6.4.1 Resonance Angle

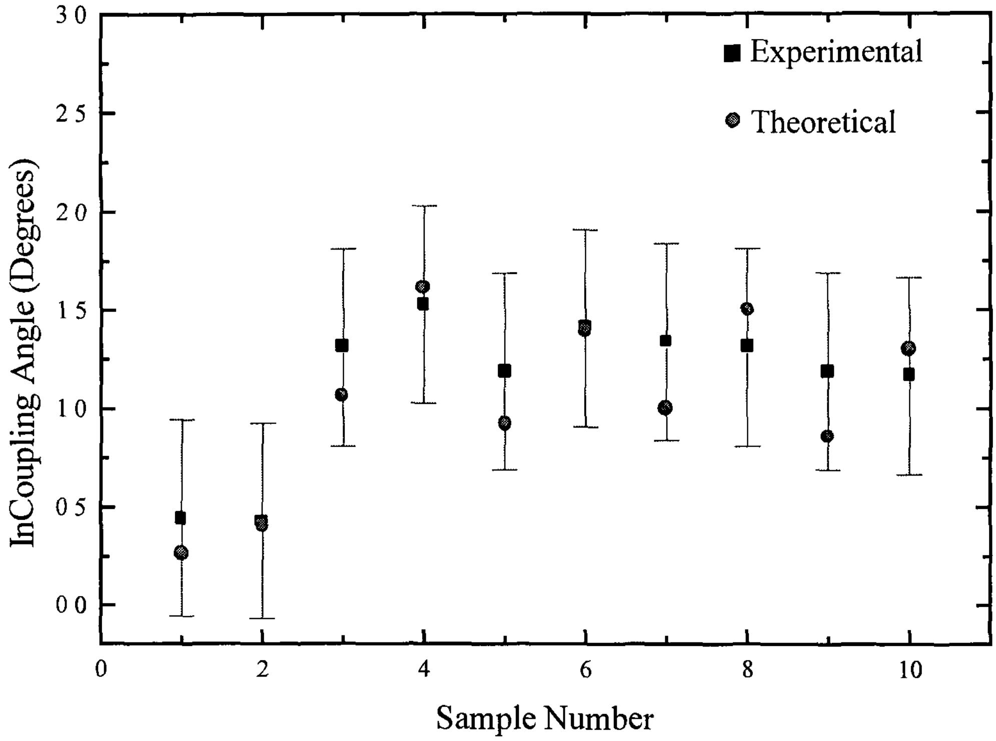

Figure 6.13 *Comparison of Experimental and Theoretical Results for Determination of Resonance Angle*

The theoretically predicted launch angles for a range of samples were compared with the experimentally observed coupling angles and the results are presented in figure 6.13. It can be seen there is a close agreement between the two, with any differential contained within the error bars of the experimental results. This tends to indicate that the fabrication techniques used to produce sol-gel-derived planar waveguide / grating coupler configurations are reproducible and reliable in nature. The results also indicate that the characterisation techniques, such as ellipsometry, spectrophotometry, diffraction studies and atomic force microscopy, which are employed to determine device parameters also provide accurate information about the fabricated grating coupler devices.

6.4.2 Coupling Efficiency

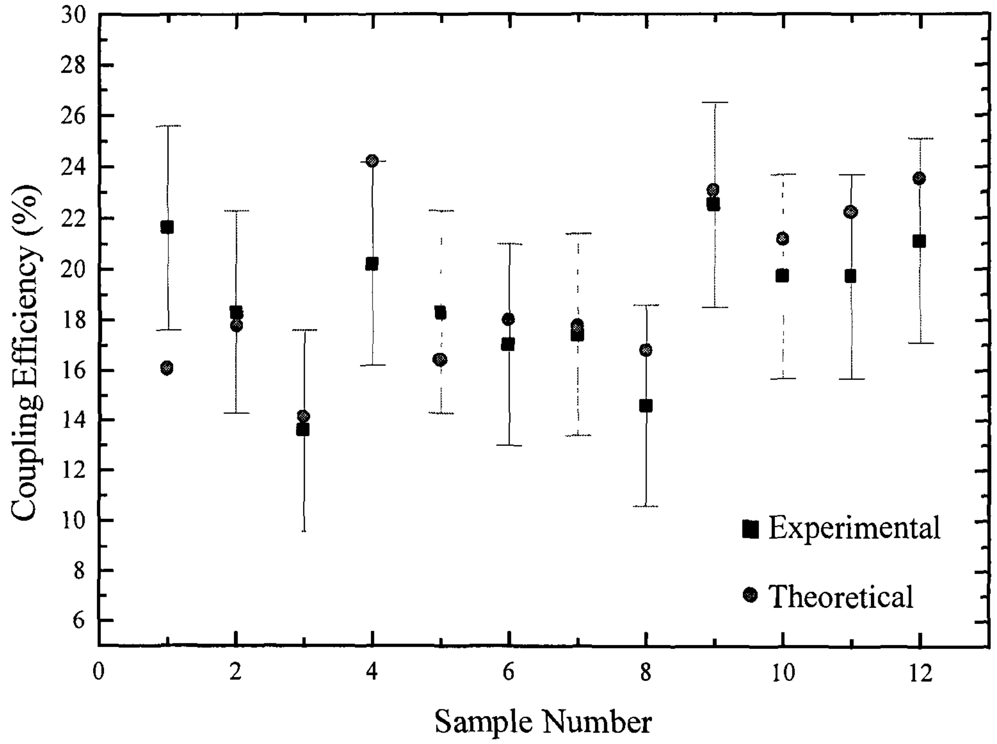

Figure 6.14 *Comparison of Experimental and Theoretical Results Peak Coupling Efficiency*

A comparison of the theoretically obtained coupling efficiencies and the experimentally obtained values was carried out. The experimentally obtained results were determined as outlined in section 5.3.4 The results are presented in figure 6.14 where it can be seen that there is close agreement between the theoretical and experimental for the majority of samples analysed. This study tends to indicate that the fabricated grating couplers behave as theoretically predicted by the *Grating* software for the given configuration.

6.5 Conclusion

In conclusion, commercially available software was used to analyse and determine the effect of a range of waveguide / grating structure properties upon the coupling efficiency to a guided mode. This study yielded optimal values for each parameter and, where possible, these values were implemented into the fabricated devices Experimental data was then used to verify that the fabricated devices behaved as theoretically predicted. It was found that there existed close agreement between the experimentally obtained and theoretically predicted results for parameters such as angular profile of resonance, peak resonance angle and peak coupling efficiency.

Chapter 7 Waveguide Sensor Platforms for Absorbance

7.1 Introduction

Many optical sensors employing optical fibres[1-6] or planar sensor membranes[7,8] have been proposed for the detection of chemical entities over the past few years with considerable success. Fibre optic-based sensors have many positive attributes including availability and low cost of raw materials, low attenuation, ease of coupling and the feasibility of probe type configurations which are suitable for either dip-stick or inline measurements. However, more recently, integrated optic (IO) sensor configurations based on planar waveguide technology have been gaining popularity due to their compatibility with the mainly planar semiconductor fabrication technologies, possibility of incorporation into integrated circuits, simplicity of their planar geometry and large interaction lengths. IO sensors have been successfully applied to the colorimetric detection of a range of analytes such as pH, lead, ammonia and even biomolecules[9-15].

The most common planar waveguide sensors are 3-layer structures consisting of a dielectric substrate upon which a waveguiding layer and an analyte-sensitive absorbing layer are deposited. The principle of operation for such sensor devices is extremely straightforward. The evanescent field of a guided mode propagating in the waveguide layer interrogates the sensing layer and is modified depending upon the surrounding environment, manifesting itself in a change in the power of the guided mode. This change in guided mode intensity may be detected using a standard silicon photodiode upon emergence from the waveguide.

Guided wave sensor configurations such as fibre-optic and planar waveguide-based devices offer increased sensitivity over other configurations, due to longer optical path lengths within the sensing layer. However, the planar-waveguide sensors also offer a number of advantages over their fibre-optics counterparts including, mechanical robustness, potential for integration with other optoelectronic components for compactness, relative ease in applying specific coatings on the waveguide surface due to the planar geometry and significant potential for low cost, mass produced sensors

In this chapter absorbance based sensor platforms fabricated using state of the art sol-gel technology employing optical waveguides and grating coupling are described. In particular, two sensing configurations are discussed. Firstly, an optical sensor platform employing a single or low mode sol-gel derived planar waveguide as the light guiding medium is presented and applied towards the detection of gaseous ammonia. The limitations of such a configuration are discussed and possible solutions proposed. The second platform configuration presented is an LED compatible device employing a multimode planar waveguide. The operation of this platform is discussed in detail and applied to the detection of gas phase ammonia and carbon dioxide.

7.2 Low-mode Sensor Platform

7.2.1 Principle of Operation

The generic configuration for the low mode absorbance-based sensor is illustrated in figure 7.1. The device consists of three main components, the waveguide, grating coupler(s) and the sensing layer, all of which may be fabricated using sol-gel technology. The planar waveguides, which have been described in detail in chapter three, are low-loss asymmetric structures with the capability to support one or two guided modes. While the grating couplers, employed to launch light into (and in some situations remove light from) the guided modes, are sol-gel-derived components fabricated as per the procedure outlined in chapter four. The sensing layers employed in this research are typically reagent-doped sol-gel or polymer thin films.

Light from a laser or laser diode source is grating-coupled into a guided mode of the sol-gel-derived planar waveguide in accordance with the grating coupler equation shown below

$$n_{eff} - n_a \sin\alpha = \frac{m\lambda}{\Lambda} \qquad [7.1]$$

where n_{eff} is the effective refractive index of the guided mode, n_a is the refractive index of the medium through which the radiation is incident on the grating, α is the angle of incidence, λ is the wavelength of the incident grating, m is the diffraction order which couples into the waveguide mode and Λ is the grating coupler periodicity.

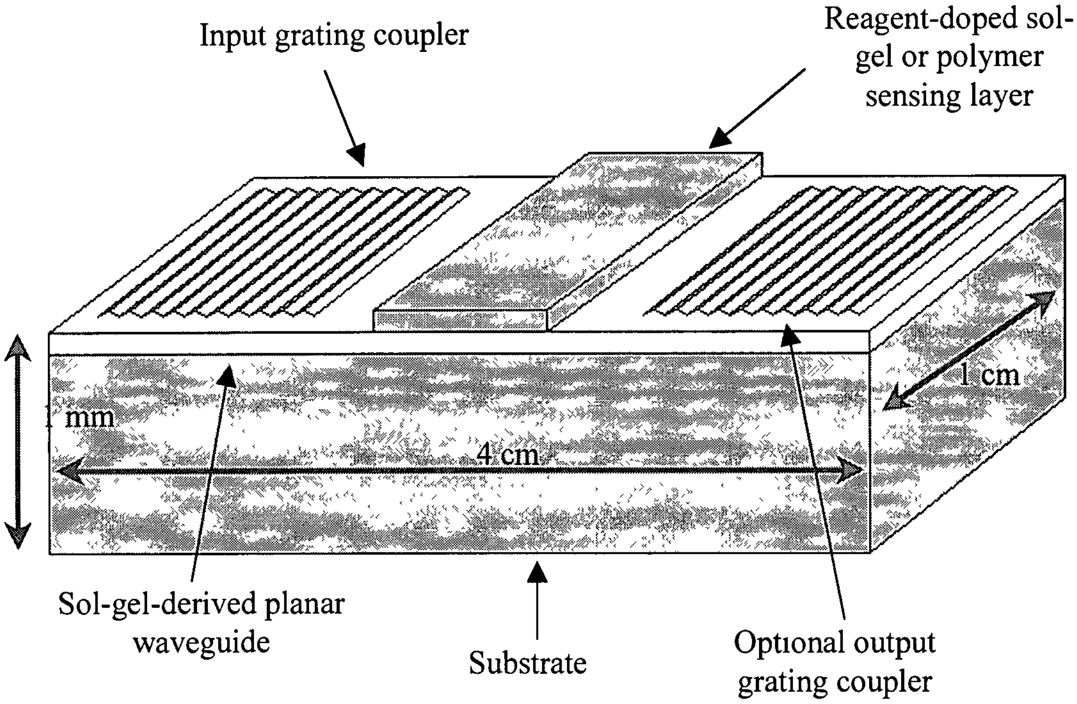

Figure 7.1 *Configuration of Generic Sensor Platform*

At a specific angle of incidence α, a fraction of the incident radiation is coupled into a guided mode which, propagates along the waveguide by total internal reflection at the boundaries. A quantity of the guided power, referred to as the evanescent field, which has been described in detail in chapter three, resides in the surrounding media as shown in figure 7.2. The sensor platforms employed in this research exhibited penetration depths of approximately 160 nm into the sensing layer, where the penetration depth, d_p, is described by the equation below

$$d_p = \left(\frac{2\pi\sqrt{n_{eff}^2 - n_{cl}^2}}{\lambda} \right)^{-1} \qquad [7.2]$$

where n_{eff} is the effective refractive index of the guided mode, n_{cl} is the cladding index and is the wavelength of the radiation.

As the guided mode propagates along the length of the sol-gel-derived waveguide, its evanescent field extends into and thus interrogates the sensing layer residing upon the waveguide surface. The sensing layer is fabricated such that its absorbance is analyte-sensitive and reversible with a sensing mechanism as illustrated in figure 7.3.

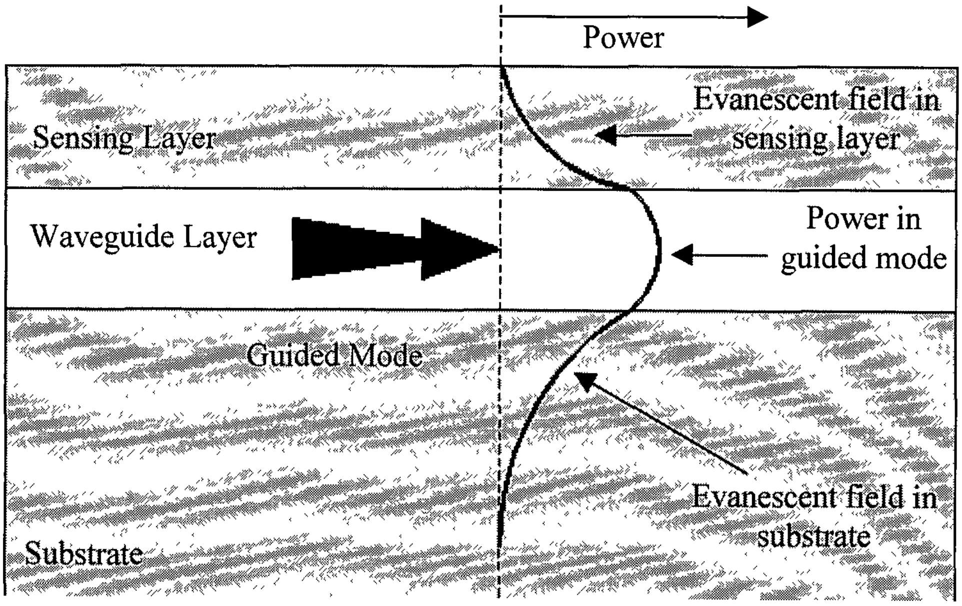

Figure 7.2 *Evanescent Fields and Penetration Depth*

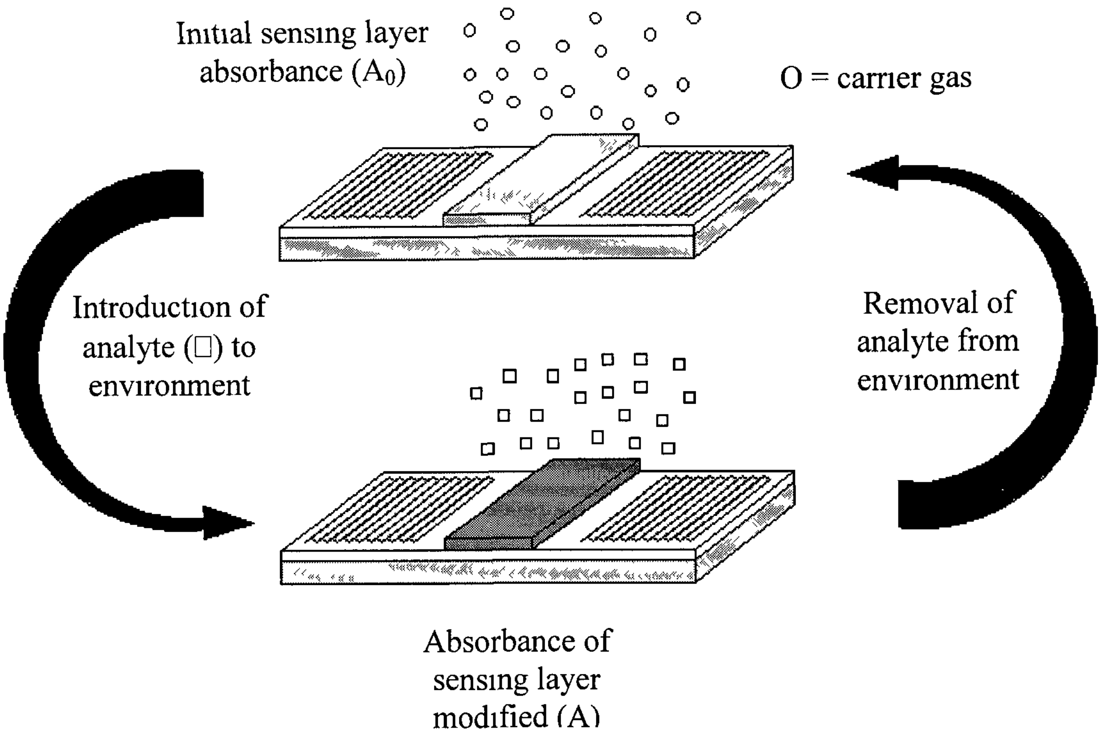

Figure 7.3 *Generic Sensing Mechanism*

Careful matching of the wavelength of the radiation source to the absorption band of the sensing layer ensures that as the guided mode propagates past the sensing layer region its evanescent field is partially absorbed, the extent of this absorption is dependent upon analyte concentration The removal of power from the evanescent field results in a change in the power of guided mode which is then out-coupled from the waveguide using either a second grating coupler as illustrated in figure 7 1 or by capturing the signal emerging from the end-face of the waveguide The intensity of the emerging signal is therefore analyte dependent and a typical response curve would have a similar profile to that shown in figure 7 4 Intensity referencing was not employed in the course of this work however it is apparent that for future work there is a need to remove the effect of fluctuations in source intensity This may be done in a number of ways one of which involves the tapping off of a fraction of the incident intensity and using it as a reference signal

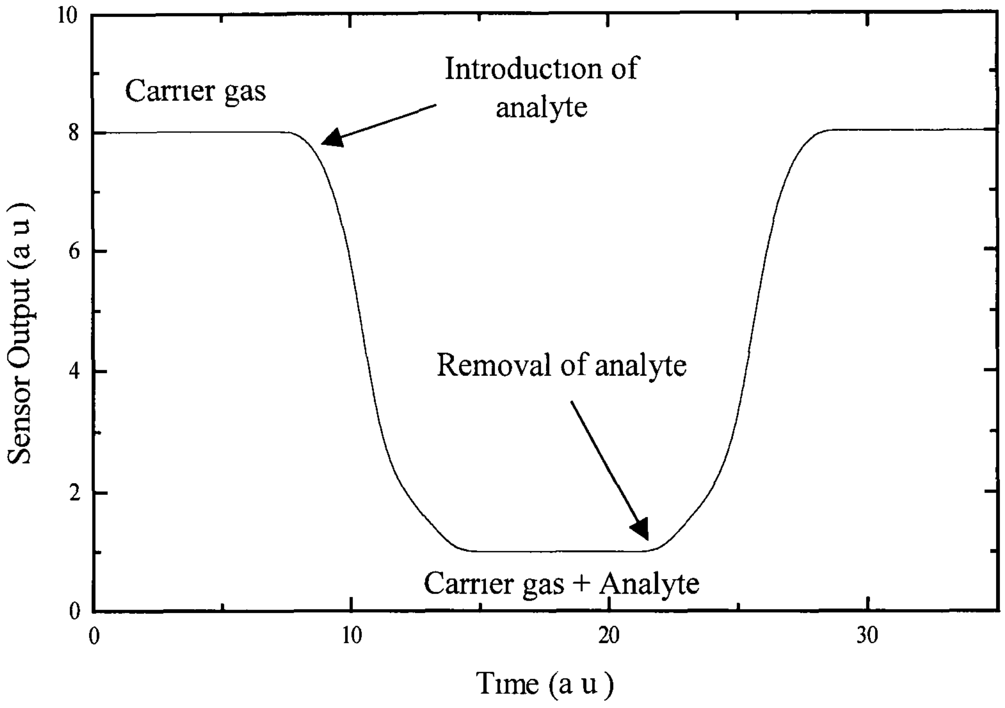

Figure 7.4 *Typical Sensing Response Curve Profile*

Careful choice of the immobilised reagent within the sensing layer allows for the fabrication of sensor devices which possess the ability to sense for a large range of analytes such as ammonia, carbon dioxide, heavy metals etc

7.2.2 Detection of Gaseous Ammonia

Ammonia is a corrosive, flammable and highly toxic gas used in a wide range of industrial applications ranging from manufacture of fertilisers and plastics to refrigeration techniques Due to its adverse properties, the ability to detect small quantities of ammonia gas is an important safety requirement Indeed, the current long-term occupational exposure standard is 25 ppm (maximum exposure in 8 hour period in 40 hour week) Typically, ammonia sensors designed to provide an alarm signal when the concentration exceeds a threshold limit require a rapid response time (< 150 seconds) However, they do not normally need to have a range capability far in excess of the legal exposure limit (25 ppm) This alarm style of sensor is typically employed in environments where humans could be exposed to large concentrations of ammonia and where leaks could prove fatal Alternatively, for dosimeter type applications the response time is not a critical issue Instead accurate determination of the ammonia exposure level is the critical property In such a scenario the sensor must be capable of detecting ammonia concentrations in the sub ppm range

The principal technique used for the optical detection of gaseous ammonia is to immobilise a colourimetric or fluorimetric indicator in a sol-gel or polymer support network[16-18] Ammonia gas induces deprotonation of the indicator dye resulting in a change of the absorbance or emission characteristics of the sensing material

In this section the previously presented low mode sensor platform is applied to the detection of gaseous ammonia The experimental sensing configuration is illustrated in figure 7 5 Light from a laser source, which is modulated at 1 KHz using a mechanical chopper, is coupled into a guided mode of the sol-gel-derived planar waveguide The guided radiation propagates along the waveguide, whilst all the time its evanescent field interacts with the sensing layer deposited at the waveguide boundary Ammonia and nitrogen mass flow controllers (Unit Instruments, Ireland) allow careful regulation of the ammonia concentration within the gas flow cell (internal volume 7×10^{-8} m^3, material = mild steel) As the guided mode emerges from the end face of the waveguide (or grating outcoupler) the signal level is monitored using a silicon photodiode (Hamamatsu, UK) and an analog lock-in amplifier (Stanford Research, USA) A data acquisition card (Bytronics) is then used to transport the data to a computer for further analysis

The versatility of the device is illustrated by employing two separate sensing layers, each with a different response profile to ammonia The first sensing layer consists of methyl red, a sulfonephtalein pH indicator[19], immobilised in a sol-gel matrix, while the second employs a more ammonia specific indicator, calixarene[20], in a polymer structure The response of each structure to the presence of ammonia and device limits of detection are presented.

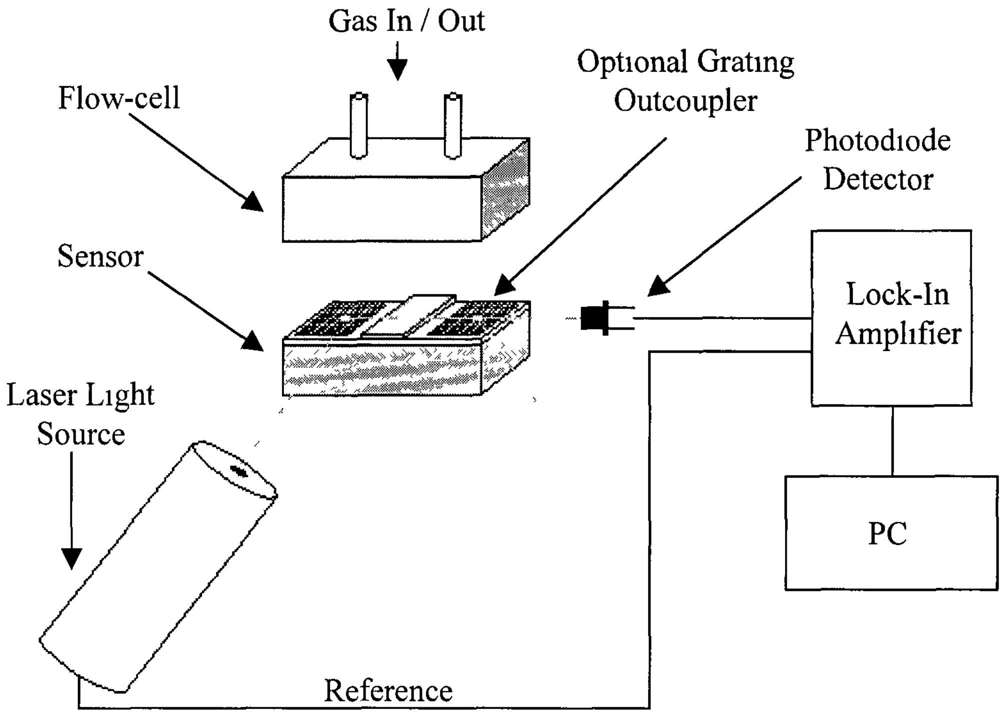

Figure 7.5 *Experimental Configuration for Ammonia Detection*

7.2.2.1 Sulfonephtalein Indicator

The sulfonephtalein family of pH sensitive acid-base indicators are commonly used for ammonia detection They are extremely stable dyes that are compatible with a wide range of support matrices An environment containing ammonia proportionally increases the pH around the indicator This can be measured as a change in absorbance of the sensing layer The absorption band of the base form of the indicator is usually employed for sensing since its peak absorption is generally greater than that of the acid form, and hence provides a better sensitivity to ammonia concentration changes

The typical sulfonephtalein-induced reversible ammonia detection mechanism consists of three steps Initially, the gaseous ammonia diffuses into the pores of the sensing layer and reacts with water to form ammonium hydroxide

$$\mathrm{NH_3(gas) + H_2O \leftrightarrow NH_4^+OH^-} \qquad [7\ 3]$$

This is followed by the deprotonation of the indicator dye by ammonium hydroxide as described by equation 7 4 This reaction produces a modified form of the indicator dye with water as a by-product

$$\mathrm{NH_4^+OH^- + H^+Dye^- \leftrightarrow NH_4^+Dye^- + H_2O} \qquad [7\ 4]$$

Finally, this sensing mechanism is reversible and the modified dye compound regenerates the primary dye and ammonia

$$\mathrm{NH_4^+Dye^- \leftrightarrow H^+Dye^- + NH_3(gas)} \qquad [7\ 5]$$

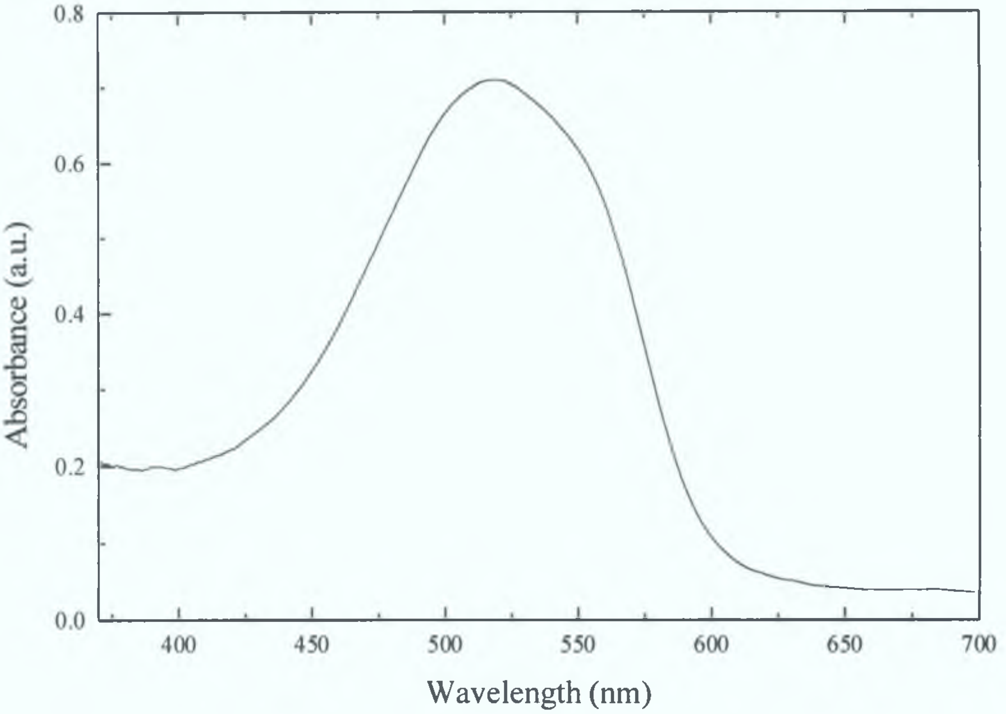

Figure 7.6 *Ammonia Sensitive Absorption Spectrum of Methyl Red-Doped Sol-Gel.*

The sulfonephtalein pH sensitive indicator employed in this section is methyl red, an anionic compound. Methyl red, when immobilised in a sol-gel matrix exhibits an absorbance spectrum as is shown in figure 7.6. Peak absorbance occurs at 519 nm, this facilitates the use of the 514 nm line of an argon ion laser as the radiation source.

Sensing layers were fabricated by dissolving the indicator in ethanol and mixing the resultant solution with pH1 water. The metal alkoxide precursor (tetraethylorthosilicate, $Si(OC_2H_5)_4$,TEOS) was then introduced and the entire mixture stirred for 1 hour and aged at 70°C for 17 hours. Sensing layers were then deposited on the waveguides by dip-coating and dried at 70°C for 17 hours followed by 1 months stabilisation.

The sensor device was exposed to various ammonia concentrations, and shown in figure 7.7 below is a normalised calibration response curve. It can be seen that the sensor output increases as ammonia concentration is increased, indicating a decrease in absorbance. Such behaviour is attributed to the anionic nature of the indicator.

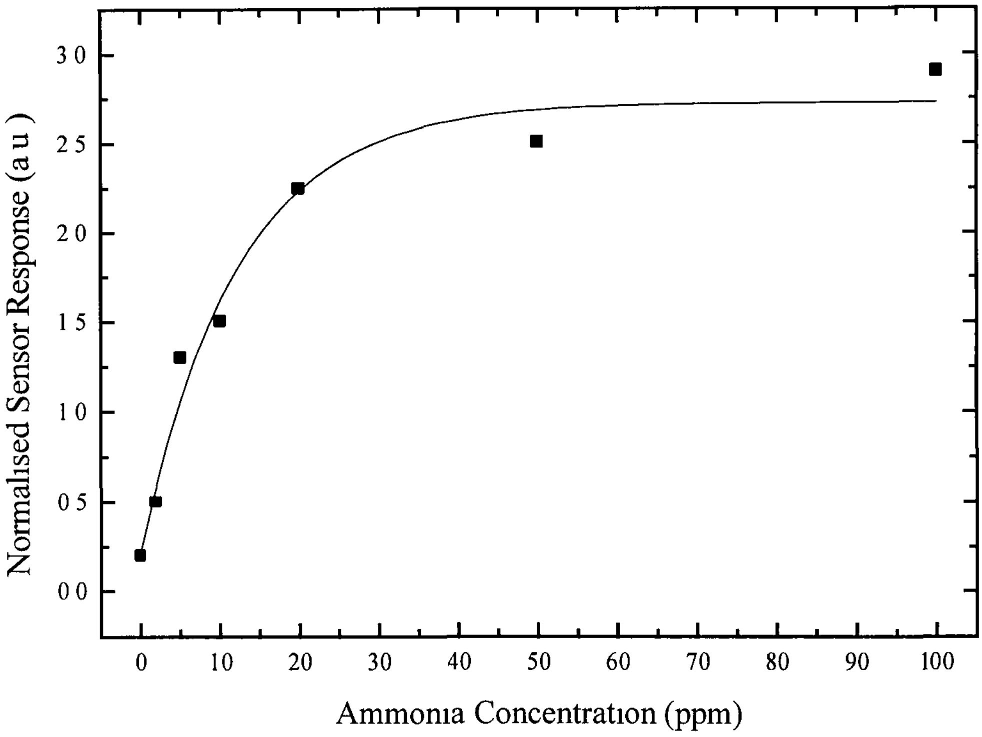

Figure 7.7 *Sensor Calibration Curve*

The device is sensitive to low levels of ammonia (< 20ppm) with large changes in output observed However, as ammonia concentration increases the device becomes less and less responsive

The sensor limit of detection may be determined by calculating the concentration equivalent to 3 times the standard deviation (σ) of the output signal on exposure to zero concentration This is the minimum detectable signal (3σ) for the device A limit of detection of 0 34 ppm ammonia in nitrogen gas may be extracted from the presented data

7.2.2.2 Calixarene Indicator

Sensing layers employing sulfonephtalein indicators have the disadvantage of being cross-sensitive to other acidic and basic gases such as carbon dioxide and sulphur dioxide In this section a more ammonia specific compound, calixarene, is immobilised in the sensing layer The calixarene compound, nitrophenylazophenol calix[4]arene was fabricated in the School of Chemical Sciences, Dublin City University, where a family of these compounds were developed for the detection of metal ions such as lithium or amine gases such as ammonia and trimethylamine The compound has a cavity or cup like structure, which is thought to produce the specificity The sensing mechanism is similar to the previous indicator in that it is colorimetric in nature The presence of a ammonia causes deprotonation of the calixarene compound and producing a colour change The sensing mechanism is described by the following equation

$$\mathrm{L-COH + NH_3 \leftrightarrow L-CO^- + NH_4} \qquad [7\ 6]$$

The calixarene compound may not be immobilised in sol-gel-derived thin films due to its insolubility in ethanol, and inability to survive low pH Therefore, a polymer-based sensing layer (PVC) is employed In a typical polymer preparation 16 mg of calixarene ligand was mixed with PVC (100 mg), a plasticiser (200 mg) and tetrahydrofuran (THF), the common solvent The plasticiser dissolved the ligand in the PVC A metal cation ($LiClO_4$, lithium perchlorate) was added to the cocktail This increases the acidity of the ionisable chromophore, thereby lowering the pK and facilitating proton uptake by the ammonia thus increasing sensitivity and shifting peak absorbance

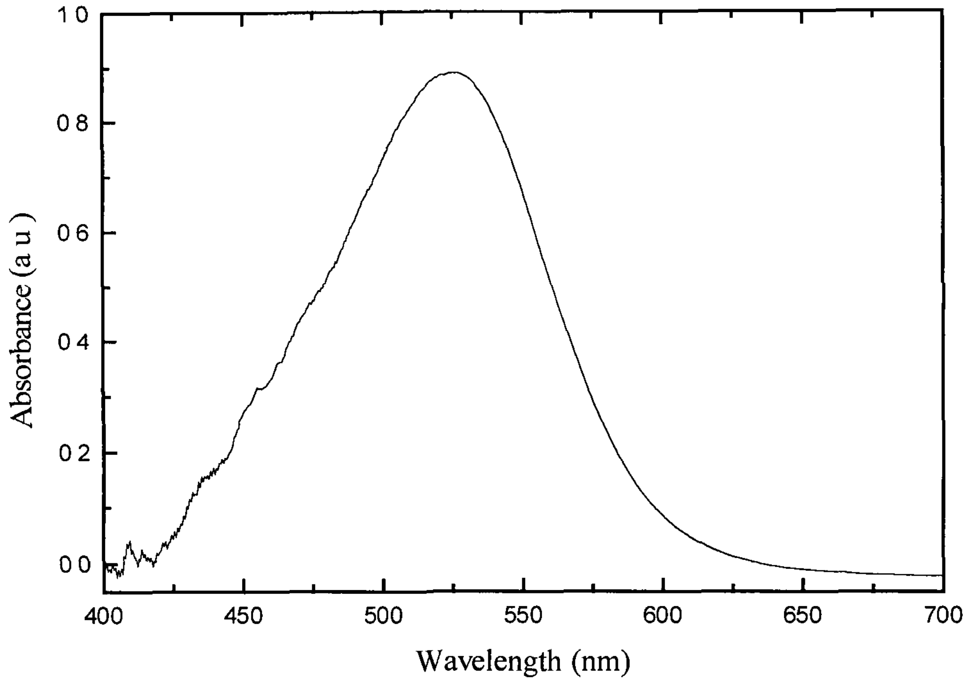

Figure 7.8 *Ammonia Sensitive Absorption Spectra of Calixarene-Doped Sol-Gel*

Shown in figure 7 8 is the absorbance spectrum of the calixarene-doped polymer layer It can be seen that the peak absorbance occurs at approximately 525 nm allowing for the use of the 514 nm line of the argon-ion laser as the interrogating radiation

The experimental sensing configuration is as shown in figure 7 5 Upon achievement of the resonance condition as defined by equation 7 1 the incident laser light is coupled into a guided mode The evanescent field of the confined mode interrogates the sensing layer and is absorbed Shown in figure 7 9 is a typical response curve for the device upon exposure to 250 ppm ammonia in nitrogen gas It can be seen from this response curve that the sensor responds in a manner which is the opposite to that observed for the sulfonephtalein dye discussed earlier, the absorbance increases with increasing ammonia concentration This is due to the cationic nature of the indicator It is also evident from figure 7 9 that the device response to the presence of ammonia is quite slow (> 10 minutes) This is due to the diffusion times required for ammonia to enter the PVC-based sensing layer

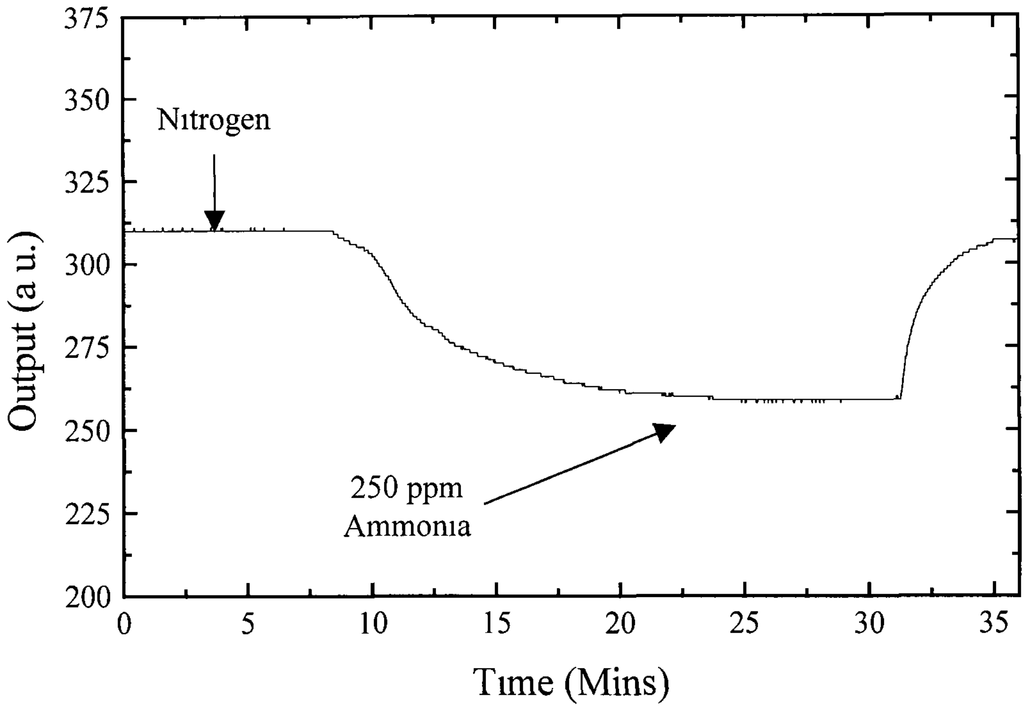

Figure 7.9 *Sensor Response to 250 ppm Ammonia in Nitrogen*

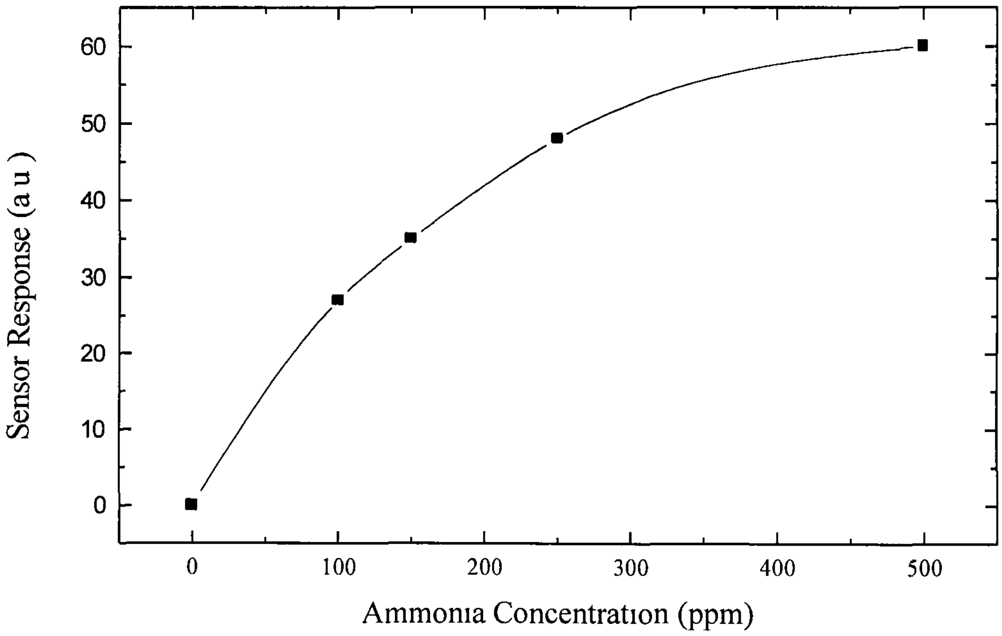

Figure 7.10 *Sensor Calibration Curve*

The device was then exposed to a range of ammonia concentrations up to 250 ppm in nitrogen and a calibration curve was obtained. It may be seen from this curve which is illustrated in figure 7.10 that the calixarene-based ammonia sensor shows a lower sensitivity to the sulfonephtalein-based system. Indeed, a limit of detection of 3.7 ppm ammonia in nitrogen was derived for the calixarene-based device, which is almost 10 times less sensitive than the methyl red-based configuration. The sensitivity of the device may be altered by varying the concentration of the indicator dye, and also by employing an alternative sensor matrix to PVC, which is more favourable to diffusion. However, as a proof of principle and device versatility, it is suffice to illustrate sensing results for two unoptimised sensing layers.

7.2.3 Device Limitations

Coupling to a guided mode in a low-mode waveguide structure using a linear periodic grating coupler is extremely angular dependent as illustrated in figure 7.11. The grating coupling equation 7.1 indicates that any variation in parameters such as wavelength of incident radiation or angle of incidence will result in a shift in the coupling condition.

It was observed during the course of ammonia sensitivity measurements that there was substantial drift over time of the guided mode coupling efficiency which led to a certain amount of unreliability in the sensor results over extended periods of time. The cause of such drift is thought to be twofold. Firstly, it may be partly attributed to instability in the emitted wavelength from the radiation source. Such a problem is easily overcome by employing highly stable radiation sources with low spectral drift. However, the second and probably more important cause of the drift in coupling efficiency with time was more difficult to counteract. The problem observed was drift of the incident angle with respect to the grating normal on application of flowing gas to the flow cell. Upon attachment of a gas flow-cell and flowing of gaseous samples through the cell the output signal of the sensor device decreased gradually over time due to minute pressure-induced movements of the sensing arrangement with respect to the incident radiation resulting in non-optimal coupling conditions and therefore a decrease in the detected signal

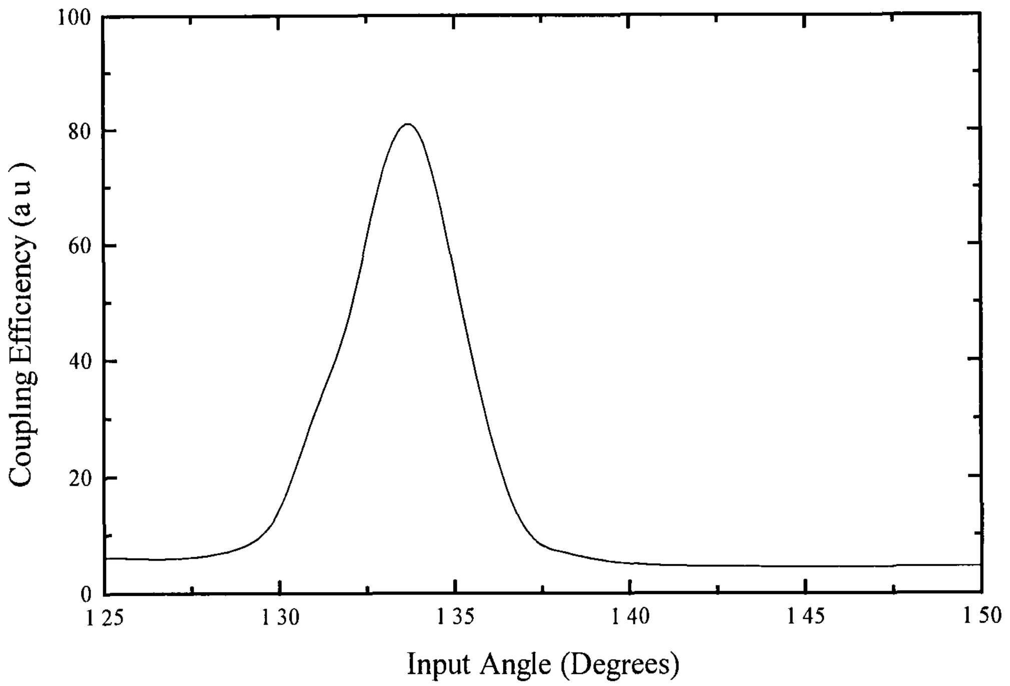

Figure 7.11 *Dependency of Coupling Efficiency on Launch Angle*

Efforts were made to improve the mechanical stability of the device by redesigning a more mechanically stable device however signal drift over time was still observed upon application of flowing gas

The linear nature of the grating coupler and the low-mode nature of the waveguide, present difficulties also Due to the extreme angular dependence of the coupling condition as illustrated in figure 7 11 efficient coupling can only be achieved using a laser or laser diode source (i e high power at a signal wavelength or small wavelength band) Such sources are available only at a limited number of operating wavelengths, and therefore it is often found that for a particular sensing reagent a laser source with the desired operating wavelength is not available

Finally, a more elementary problem is that each sol-gel-derived planar waveguide fabricated using the dip-coating technique differs slightly from all others in terms of thickness and refractive index despite identical fabrication conditions This may be attributed to the lack of process control techniques in place to ensure identical fabricated components Such minor differences in samples leads to different coupling conditions from device to device, resulting in lack of compatibility from waveguide to waveguide and possibly removing the possibility of disposable type sensors which may be used with one fixed interrogating system

7.2.4 Summary

A waveguide based sensor platform based on evanescent wave absorption was demonstrated The device was applied to the detection of ammonia gas and exhibited sub parts-per-million limits of detection Two different indicators were employed to illustrate the generic nature and versatility of the device The structure is not, however, without its difficulties and drawbacks These include movement of the structure under gas flow, discrepancies amongst supposedly identical samples and the necessity for laser or laser diode sources due to the precise coupling conditions As a result of such problems an alternative device which employed LED sources and multimode waveguide structures was investigated and is presented in the following section

7.3 Multi-mode Sensor Platform

7.3.1 Principle of Operation

The generic configuration for the multi-mode absorbance-based sensor is illustrated in figure 7 12 The device consists of four main components, a multi-mode waveguide (typically a glass microscope slide, $n_{guide} = 1\ 515$), grating input and output couplers and the sol-gel-derived sensing layer

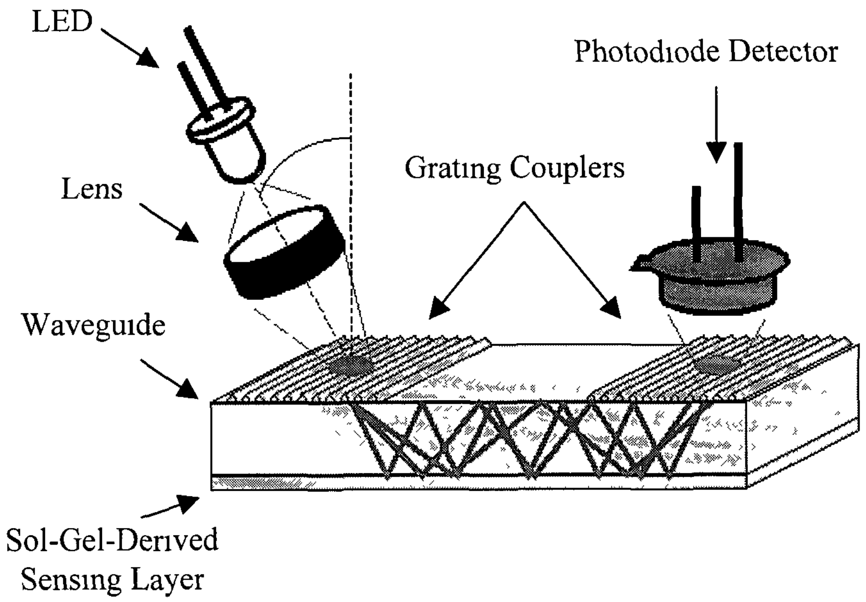

Figure 7.12 *Multimode Platform Configuration*

Light emerging from an LED is focused onto the grating input coupler resulting in a spread of incident wavelengths at a spread of incident angles Therefore, multiple coupling conditions are satisfied in accordance with equation 7 1, resulting in the launching of a large number of guided modes, with possible effective refractive indices ranging from 1 → 1 515 These guided modes are then outcoupled using a second grating coupler, where their intensity is determined using a photodiode

Guided modes with an effective refractive index greater than the refractive index of the sensing layer (typically 1 43 for a sol-gel-derived layer), are confined solely to the waveguide The evanescent field of these guided modes may then be used to interrogate the absorbance of the sensing layer and thus provide information on the target analyte concentration as illustrated in figure 7 13 Hence, the sensing technique employed by these modes is evanescent wave absorption

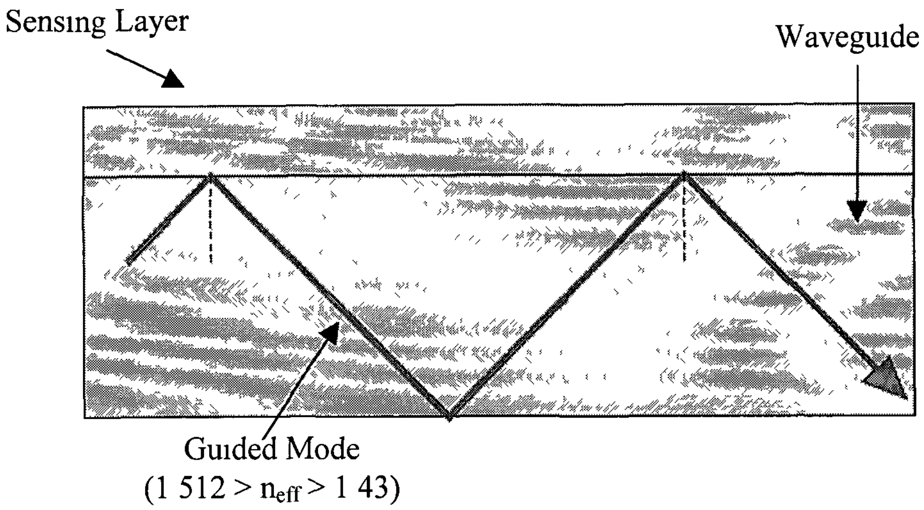

Figure 7.13 *High Effective Index Modes*

On the other hand, guided modes with an effective refractive index lower than the refractive index of the sensing layer are not confined solely to the waveguide, rather they are guided in a two layer structure which comprises of the waveguide and the sensing layer as shown in figure 7 14 These guided modes propagate within the sensing layer and therefore directly interrogate the sensing layer In this situation the sensing technique employed is direct wave absorption

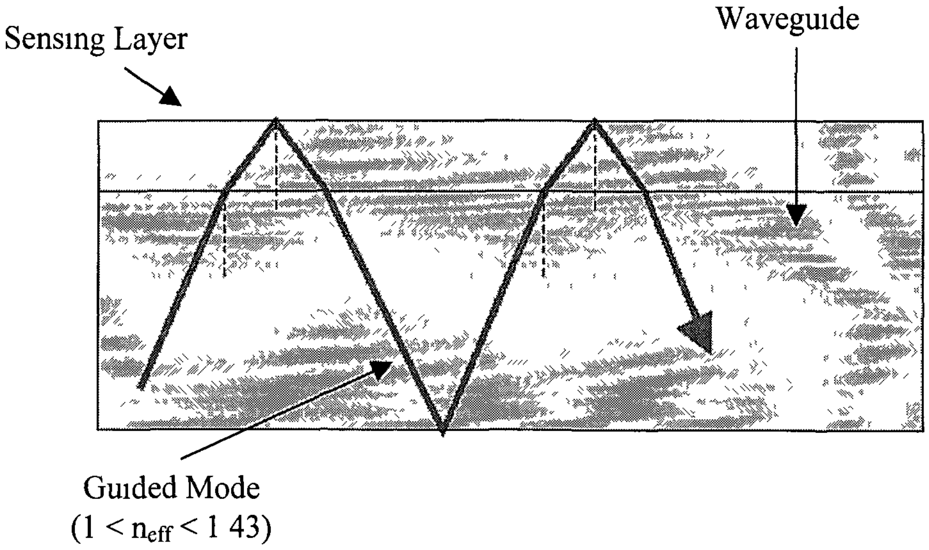

Figure 7.14 *Low Effective Index Modes*

Focusing of the LED light onto the grating coupler creates a spread of input wavelengths at a range of input angles (in the platform presented here a 30 mm focusing lens is employed which produces a 44° wide range of input angles). Therefore, for a given configuration there is usually a large number of guided modes with a large range of effective indices, thus resulting in the simultaneous deployment of both sensing techniques. There also exists a discrete combination of these two sensing techniques at which the device exhibits optimum sensitivity. This can be seen in figure 7.15 where it is evident that for a green LED (λ_{max} = 563 nm, bandwidth = nm, intensity 250 mcd, RS Components, Ireland) focused onto a sensor platform containing a sol-gel-derived sensing layer of refractive index 1.43 and thickness 400 nm the peak sensitivity for the device occurs at a central launch angle of 20°. Therefore, for all sensing experiments presented in the following sections, a central launch angle of 20° is employed. The position of optimum sensitivity is dependent on a number of factors including grating coupler period, waveguide refractive index, sensing layer refractive index and wavelength of incident radiation.

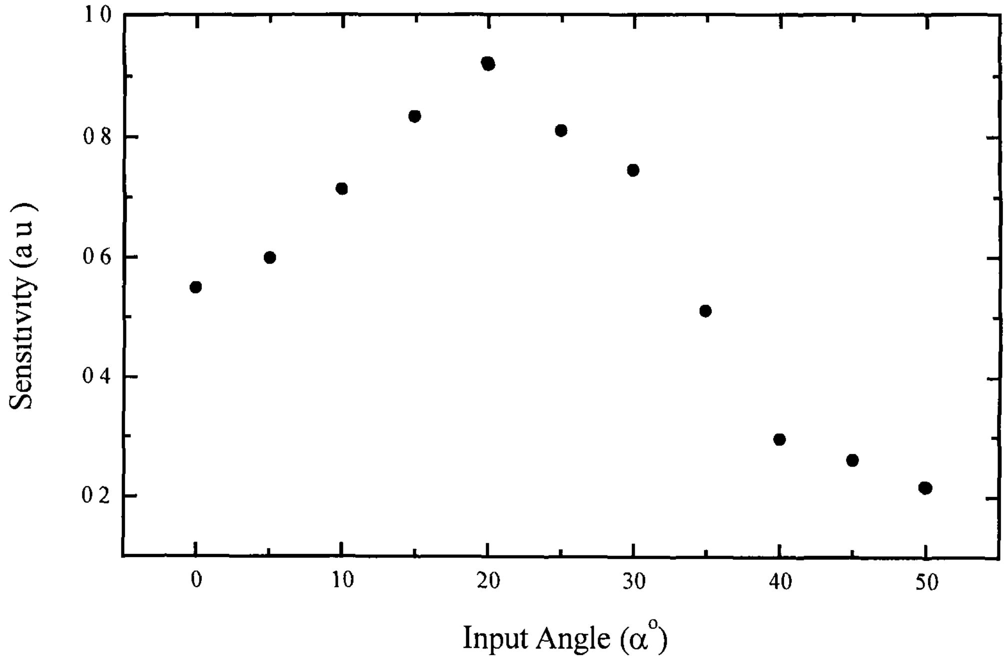

Figure 7.15 *Device Sensitivity as a Function of Launch Angle*

A full mathematical treatment of this configuration is beyond the scope of the work presented in this thesis However, there is a substantial amount of research being carried out by the theoretical section of the Optical Sensors Group at Dublin City University towards producing a mathematical model which fully describes and allows for the theoretical optimisation of this structure

7.3.2 Detection of Gaseous Ammonia

As with the previous absorbance-based sensor platform, the multimode device was applied to the detection of gaseous ammonia as a proof of principle Again, two different indicator dyes were employed to emphasise device versatility These indicators were, bromocresol purple[19], a cationic sufonephtalein pH sensitive indicator, and 1,1,3-methyl-2-[{1,1,3-methyl-2(1H,3H)-indolylidene-1-propenyl}]-5-oxo-2-furfurylidene-(3H)-indolium perchlorate[21,22], a polymethine dye, hereafter referred to as PM In both situations the indicators were immobilised in a sol-gel-derived structure

The ammonia detection configuration is illustrated in figure 7 16 Light from a high power green LED, (λ_{max} = 563 nm, bandwidth = 35 nm, intensity 250 mcd, RS Components, Ireland) the spectrum of which is shown in figure 7 17, is focused onto the grating in-coupler with a central angle of 20° This facilitates the launch of multiple guided modes into the planar waveguide which propagate along the waveguide and are out-coupled via a second embossed sol-gel-derived grating coupler A silicon photodiode detector (Hamamatsu, UK) positioned above the grating detects the emerging light intensity Along the length of the waveguide, both the evanescent fields of a portion of the guided modes, and the actual guided mode interrogate the absorption spectrum of the ammonia sensitive reagent immobilised in the sensing layer Any changes in the absorbance of the sensing layer in the bandwidth covered by the light source will result in a change in the intensity of the out-coupled light

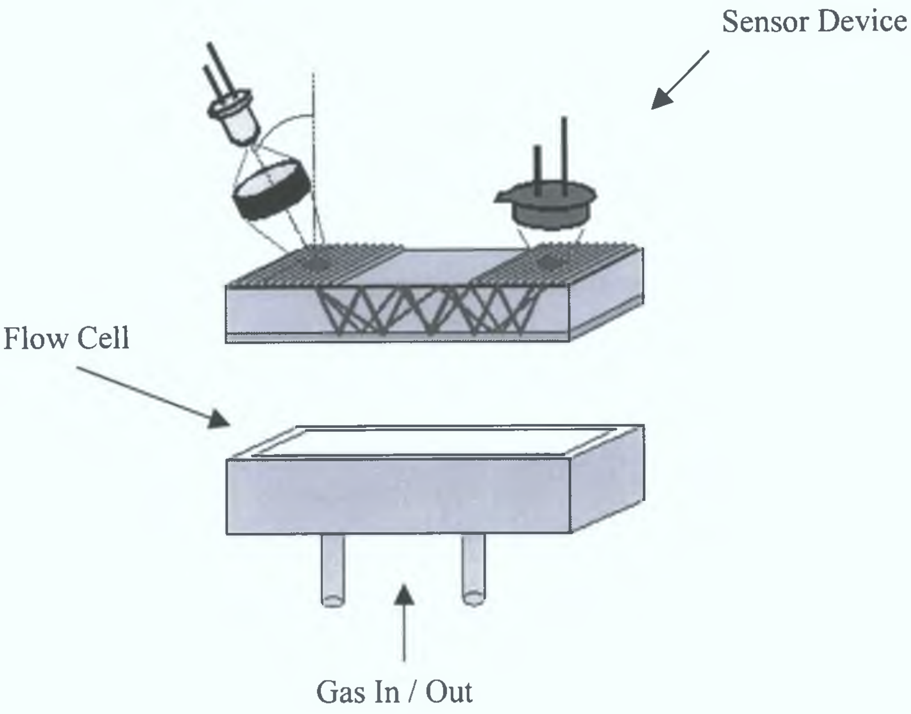

Figure 7.16 *Sensing Configuration.*

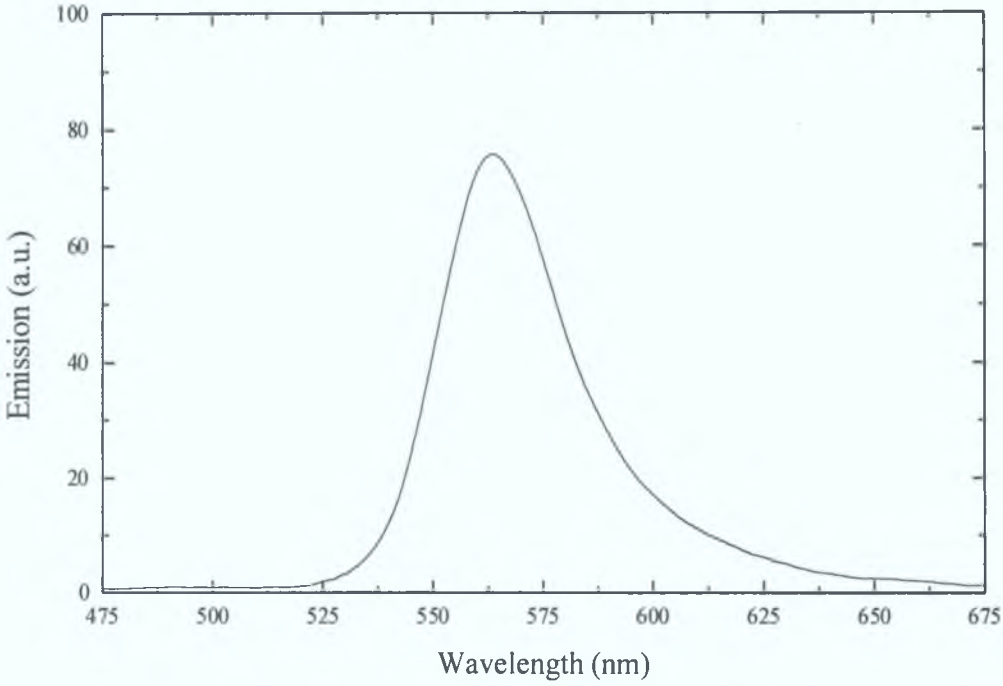

Figure 7.17 *Green LED Spectrum.*

Dedicated lock-in circuitry was used to detect the light from a green LED modulated at 1 kHz coupled out of the sensor device Lower modulation frequencies would yield greater 1/f noise A small flow cell was attached to the waveguide to allow exposure of the sensing layer to gaseous samples Gas flow was regulated using mass flow controllers (Unit Instruments, Ireland) with a constant total flow rate of 500 ml min^{-1} of ammonia and nitrogen gas mixtures

7.3.2.1 Sulfonephtalein Indicator

Bromocresol purple (BCP) is a cationic sulfonephtalein pH sensitive indicator which when immobilised in a sol-gel matrix exhibits an absorbance spectrum as is shown in figure 7 18, with a peak absorbance at 582 nm The ammonia detection mechanism is as previously mentioned for the situation of methyl red, the only difference being that the absorbance of the cationic indicator increases with increasing ammonia concentration

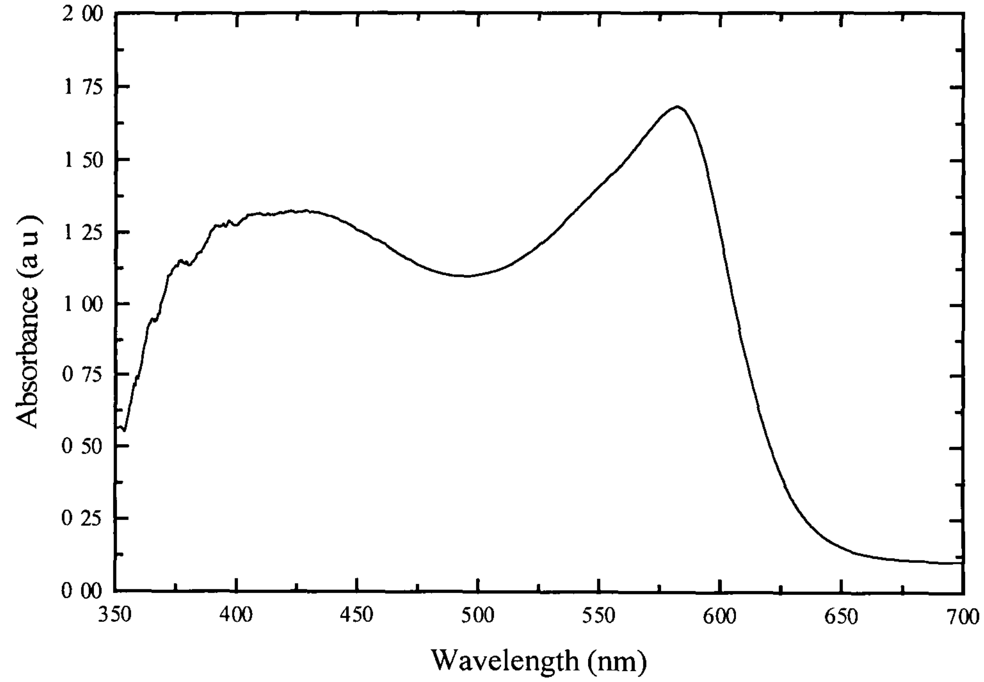

Figure 7.18 *Absorbance Spectrum of Bromocresol Purple in Sol-Gel Matrix*

Sensing layers are fabricated by initially dissolving the indicator in ethanol and mixing the resultant solution with pH1 water. The metal alkoxide precursor (tetraethylorthosilicate, $Si(OC_2H_5)_4$,TEOS) is then introduced and the entire mixture is stirred for 1 hour. The indicator-doped sol is then aged at 70°C for 17 hours. The sensing layers are deposited on the waveguides by dip-coating and dried at 70°C for 17 hours. Samples are then allowed to stabilise for 1 month prior to use.

Shown in figure 7.19 below is a response curve for device exposure to 100 ppm ammonia gas in nitrogen. It is immediately apparent from this response curve that the device response is quite slow with response times ($T_{90\%}$) of 21 minutes being observed upon exposure to ammonia while recovery times of greater than 200 minutes are not uncommon. It is thought that this is due to a strong interaction between the polar indicator dye and the polar silanol groups on the surface of the micro-porous sensing support matrix.

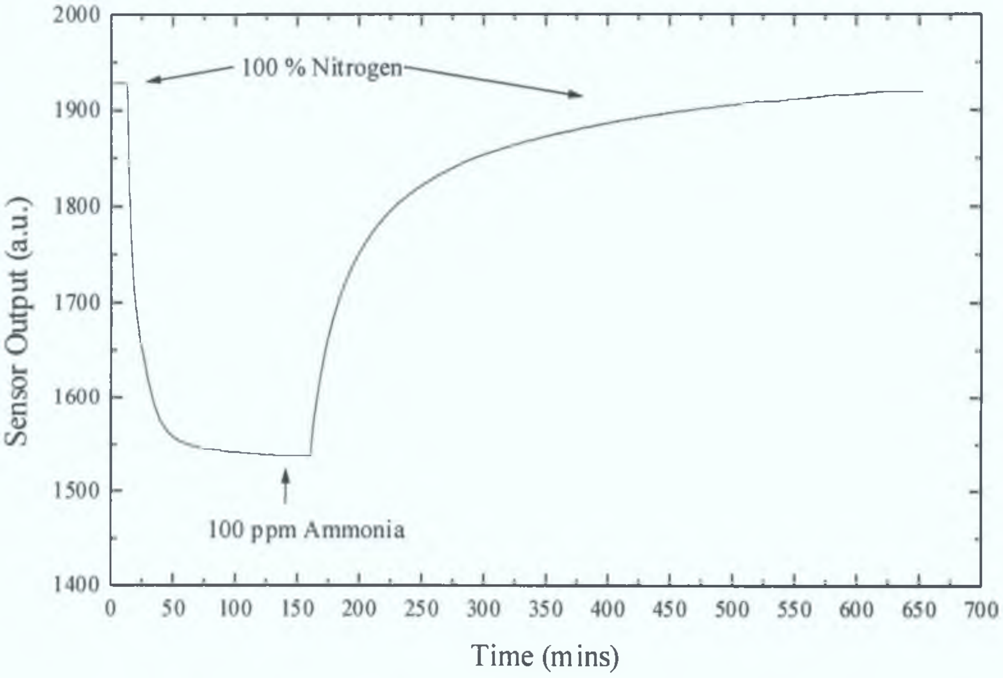

Figure 7.19 *Device Response to 100 ppm Ammonia in Nitrogen.*

The sensitivity of the device towards various concentrations of ammonia vapour may be seen in figure 7 20 It can be seen that as with the previous sulfonephtalein indicator employed, the device is responsive to the presence of low levels of ammonia gas A limit of detection of 0 3 ppm ammonia in nitrogen gas may be deduced, again this is comparable with the figure of 0 34 ppm for methyl red This indicates that the multimode device offers comparable performance to the low mode structure yet at a fraction of the cost

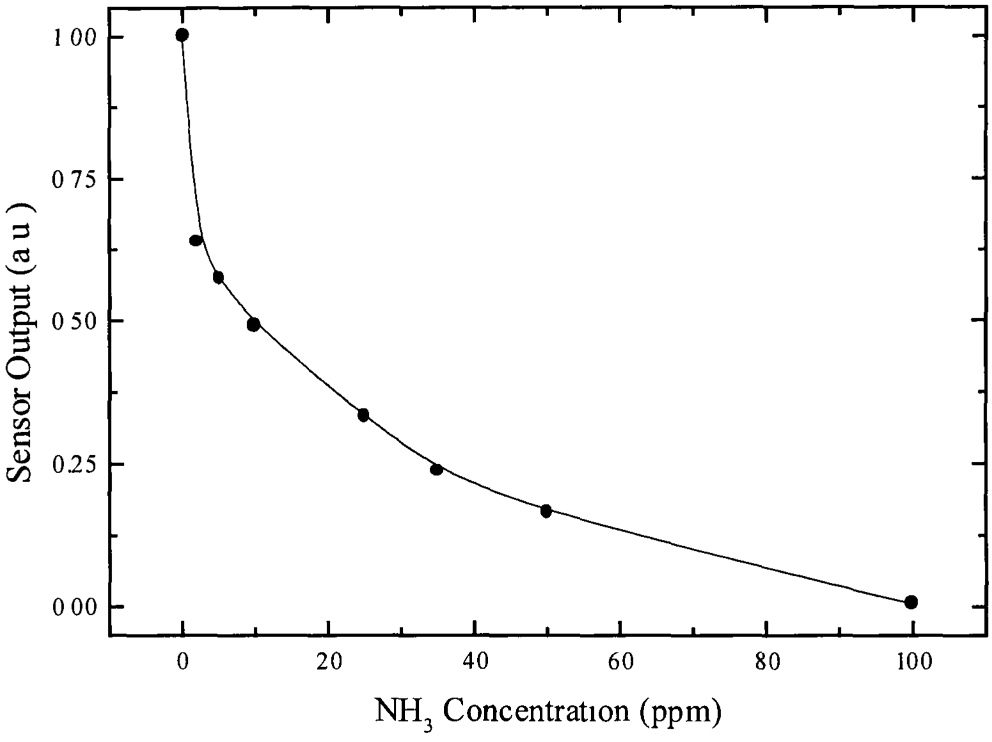

Figure 7.20 *Ammonia Response Calibration curve*

7.3.2.2 Polymethine Indicator

The polymethine dye employed in this section is a less polar indicator and hence should be less prone to interaction with the sensor membrane The dye, PM when immobilised in a sol-gel matrix exhibits an absorbance spectrum as is shown in figure 7 21 Peak absorbance occurs at 552 nm, which is compatible with the high power green LED described earlier The reversible ammonia detection mechanism is as previously mentioned with indicator absorbance increasing with higher ammonia levels

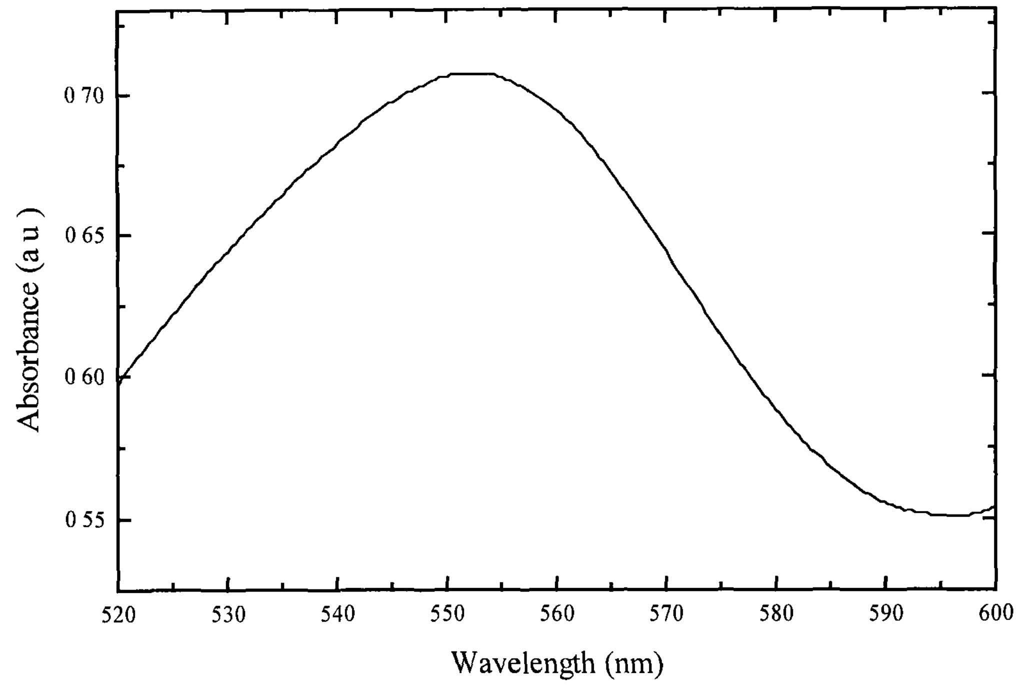

Figure 7.21 *Absorbance Spectrum of Polymethine Dye in Sol-Gel Matrix*

Sensing layers were fabricated by initially dissolving the indicator in ethanol and adding pH1 water The metal alkoxide precursor (TEOS) was then introduced and the entire mixture stirred for 1 hour, followed by aging at 70°C for 17 hours The liquid sol was then deposited on waveguides by dip-coating and the samples were dried at 70°C for 17 hours followed by 1 months stabilisation prior to use

The experimental configuration employed is identical to that illustrated in figure 7 16 The sensor was initially cyclically exposed to 100 ppm ammonia gas in nitrogen The sensor response is shown in figure 7 22 where is apparent that the device employing the polymethine dye exhibits much faster response times than that of the more polar sulfonephtalein indicator The response time ($T_{90\%}$) to the presence of 100 ppm ammonia is 1 minute, while the device recovery time is determined to be 3½ minutes

This may be attributed to the low polarity of the polymethine preventing strong interactions with the support matrix

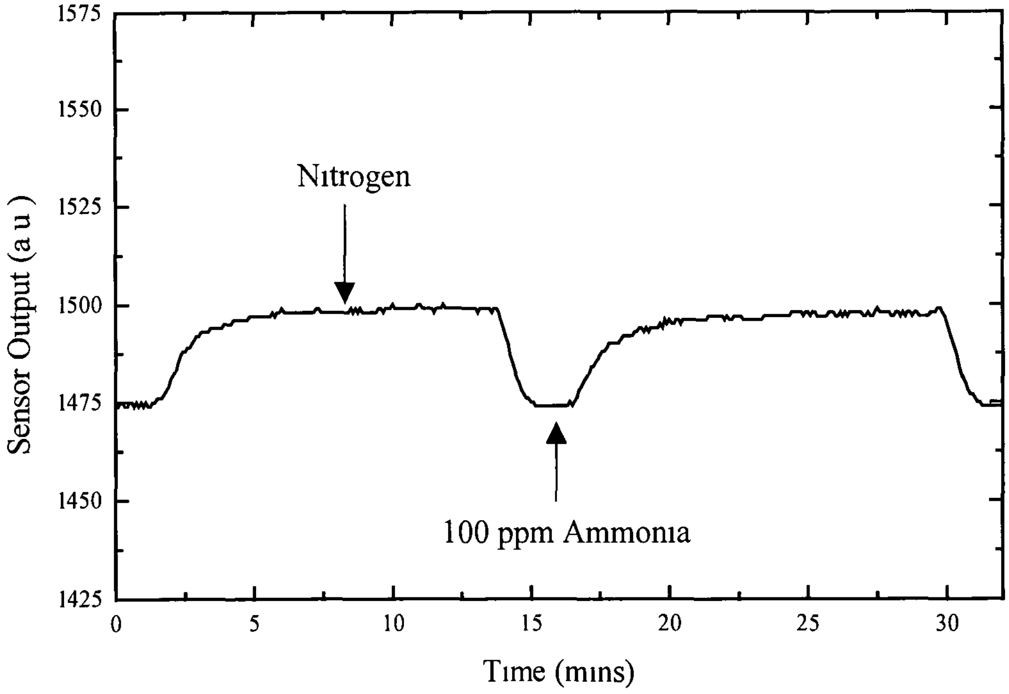

Figure 7.22 *Sensor Response to 100 ppm ammonia*

However, the polymethine indicator-doped sensor device is not without its drawbacks The indicator inherently has a lower sensitivity to ammonia than its more polar sulfonephtalein counterparts This is clearly illustrated in the calibration curve of figure 7 23 where it can be seen that there is an almost linear sensitivity response to the presence of gaseous ammonia in the concentration range 0 → 100 parts-per-million with a limit of detection of 2 ppm

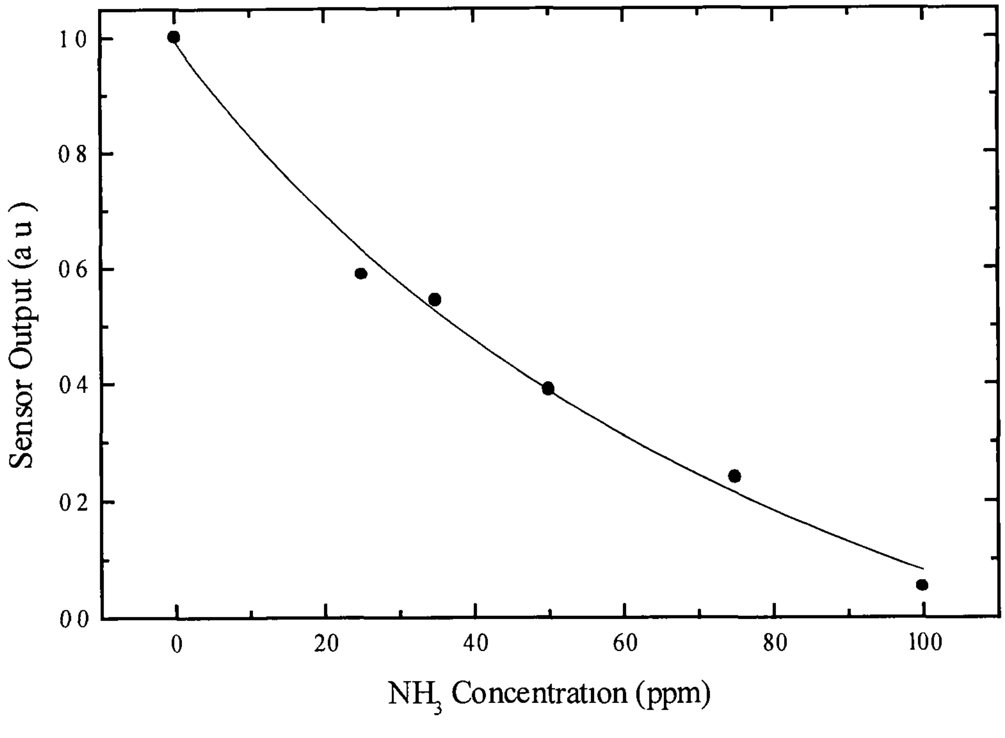

Figure 7.23 *Sensor Calibration curve*

7.3.3 Detection of Gaseous Carbon Dioxide

Detection of carbon dioxide is extremely important in a wide range of industries, from clinical applications such as breath by breath analysis, to the food industry where foodstuffs are packaged in carbon dioxide atmospheres to increase shelf lives

The conventional techniques used to determine carbon dioxide concentrations are based on infrared technology, carbon dioxide has an absorption band in the infrared, the magnitude of which varies depending on gas concentration Such devices are sensitive to the presence of carbon dioxide, but are quite costly and cumbersome The multimode waveguide platform presented here provides an alternative approach whereby an indicator with a carbon dioxide sensitive absorbance band may be used to modify the power in a guided mode

Optical detection of gas phase carbon dioxide using optical techniques requires the use of pH sensitive polar dyes and a moisture rich environment However, the use of polar dyes places a restriction on the range of possible matrices that can be used for immobilisation The support material must exhibit good solubility towards the indicator and must also retain sufficient moisture to facilitate the water-mediated sensor chemistry If the sensor membrane dries out it is not responsive to carbon dioxide

For liquid phase CO_2 detection the classical device requires a buffered, dye-doped layer of hydrophilic support material, such as a hydrogel[24] or moisture-rich sol-gel[25], to be maintained beneath a hydrophobic gas-permeable membrane, such as Teflon The buffer ensures that the dye is deprotonated in the initial state and the hydrophobic membrane prevents liquid from entering or escaping from the dye-doped layer However, the application of this configuration to gas phase sensing is limited by the need to maintain the moisture level in the sensitive membrane, as the application of dry gas will quickly render such sensor layer useless

The need for a moisture-rich environment has been overcome by employing an ion-pair aproach[26-31] to encapsulate highly polar, pH-dependent dyes into hydrophobic materials This methodology employs a phase transfer reagent to incorporate the polar dye into the support matrix During this procedure there is a significant quantity of moisture, in the form of water of crystallisation, encapsulated in the immobilisation matrix along with the dye

Sensing layers were fabricated by adding a solution of tetraoctyloxyammonium bromide (0 6 g) in methyltriethoxysilane (15 g) and dichloromethane (2 ml) to a stirred solution of cresol red (0 3 g) in water 10 g of this solution was added drop-wise to aqueous HCl solution (pH1, 4 0 g) After stirring for 1 hour tetraoctyloxyammonium hydroxide solution (2 5 ml) was added before thin films (~ 1 2 μm) were fabricated by dipcoating onto the unembossed face of the waveguiding structure These were dried overnight (70C) and left in ambient conditions for 1 week prior to use

Cresol red immobilised in a sol-gel matrix exhibits a carbon dioxide sensitive absorption band at 585 nm as shown in figure 6.24. This absorbance spectrum facilitates the use of the high power green LED described earlier.

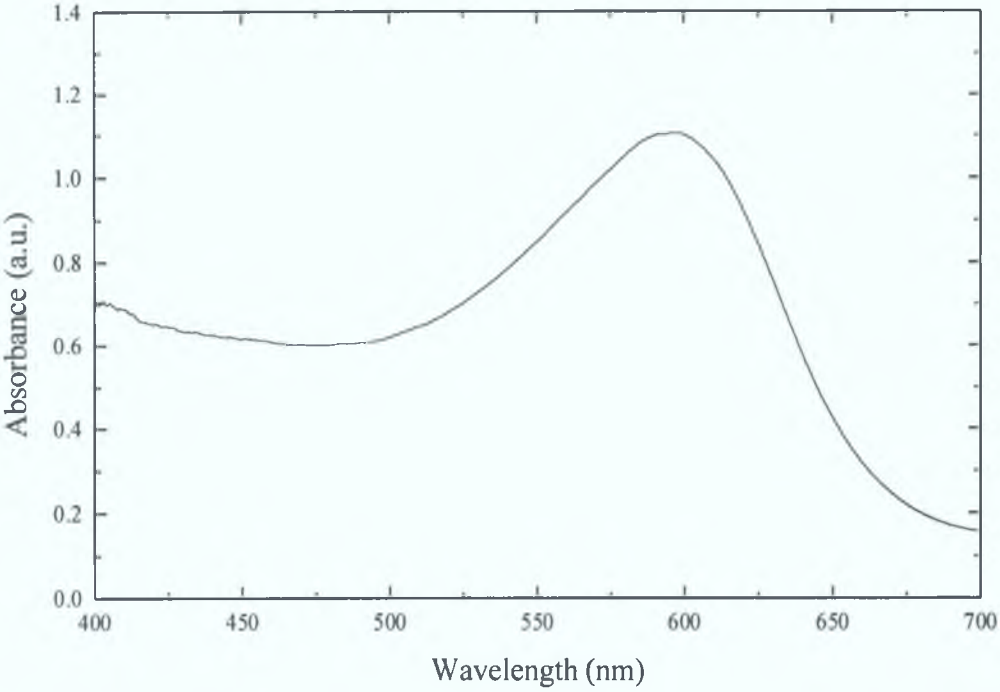

Figure 7.24 *Absorption Spectrum of Cresol Red-Doped Sol-Gel.*

The interaction of carbon dioxide with the immobilised indicator can be described as

$$Q^+D^-.xH_2O + CO_2 \rightarrow Q^+HCO_3^- + H^+D^-.(x-1)H_2O \qquad [7.7]$$

The carbon dioxide first diffuses through the sensor membrane and dissolves in the hydrous glass matrix in which the dye is immobilised forming carbonic acid, proton exchange occurs, resulting in a protonated form of the dye which exhibits a different absorbance spectrum to the unprotonated version.

Shown in figure 7.25 is the device response to 10 % carbon dioxide in nitrogen. It can be seen that the device response is both sensitive and reproducible with quick response and recovery times ($T_{90\%}$) of the order of 2 minutes.

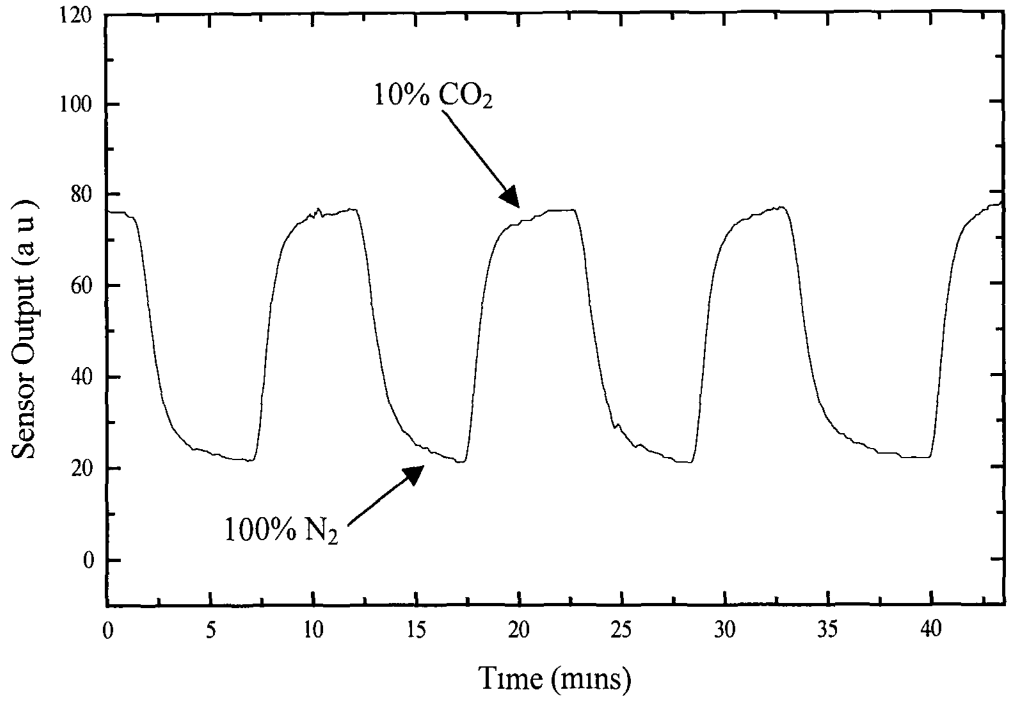

Figure 7.25 *Sensor response to 10% carbon dioxide*

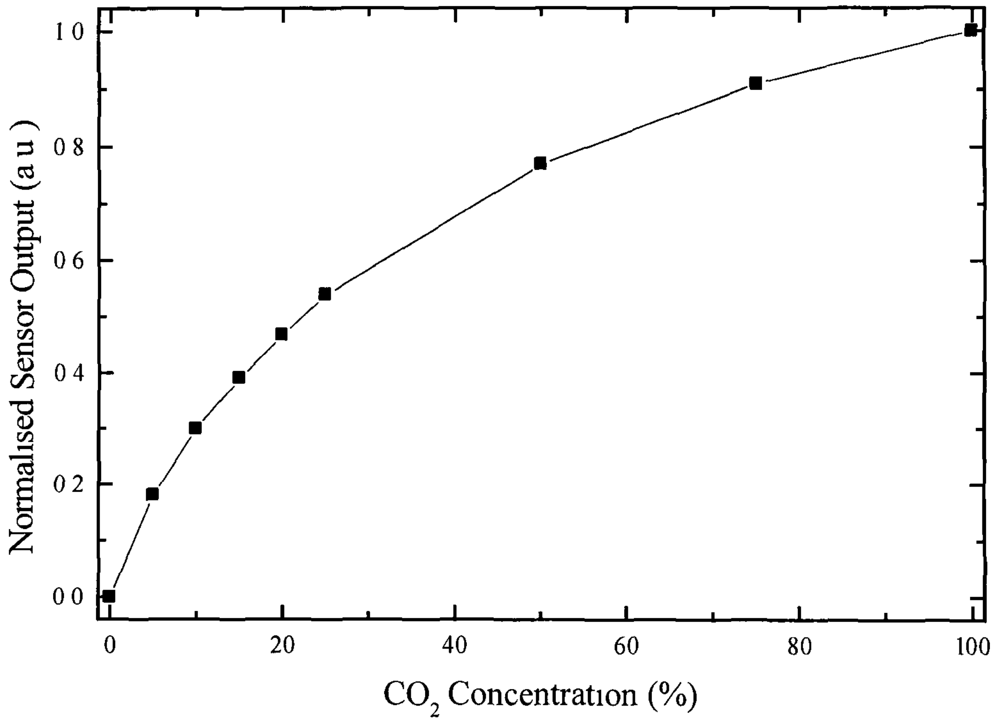

Figure 7.26 *Sensor Calibration curve*

The sensitivity of the device towards various concentrations of carbon dioxide is shown in figure 7.26 where it can be seen that the device exhibits high sensitivity to small carbon dioxide concentrations. A limit of detection of 0.1 % carbon dioxide in nitrogen gas was determined for the structure. This demonstrates that this optical configuration provides adequate sensitivity for many applications ranging from analysis of food packaging to breath-by-breath analysis.

7.3.4 Summary

A multimode waveguide platform for absorbance-based sensing has been presented. The entire device is fabricated using state of the art sol-gel technology with a straightforward, easy to fabricate design. Due to the multimodal nature of the waveguide, which relaxed the coupling conditions of the device, it was possible to employ LED light sources an therefore reduce device costs.

The structure performance was demonstrated by application to the detection of both gaseous ammonia and carbon dioxide. Detection of ammonia was demonstrated using two separate sensing layers. The first sensing layer employed a sulfonephtalein pH sensitive indicator immobilised in a sol-gel matrix. The device was sensitive to the presence of ammonia, with a limit of detection of 0.3 parts per million in nitrogen gas. However, due to the polarity of the dye and its affinity to the sensor membrane the response was extremely slow, with detection times of greater than 20 minutes and recovery times of well over 3 hours being observed. The second sensing layer provided less sensitive but more rapid ammonia detection. The dye utilised was a polymethine dye, again immobilised in a sol-gel matrix. The device only provided a limit of detection of 2 parts ammonia gas per million parts nitrogen. However, it exhibited significantly faster response times than its sulfonephtalein counterpart, with detection times of 1 minute and recovery times of 3.5 minutes being observed. Hence, two ammonia sensitive devices were developed which could satisfy different industrial requirements. Should the requirements be to monitor over long-term the ammonia concentration in a given environment where accuracy rather than response time is the most important issue then a sensor device employing bromocresol purple as the sensing indicator could be deployed However, if the emphasis is on an alarm type indicator where response times are crucial then the second sensing layer could be employed

The versatility of the device was further illustrated by the application of the device to the detection of carbon dioxide where it was found that the by employing a specially-prepared sensing layer, the device could detect levels of carbon dioxide in nitrogen of as little as 0 1%

7.4 Cross Sensitivity and Thermal Response

Optical chemical sensor devices employing pH-sensitive indicator dyes as sensing reagents are known to exhibit a cross sensitivity to a range of acidic and basic gases including ammonia, carbon dioxide and sulphur dioxide The effect and magnitude of this cross sensitivity was beyond the scope of the research reported in this thesis although it is understood that it is an important issue Therefore, it is imperative that future work on the development of these sensors for commercialisation should include a study on device cross-sensitivity and possible solutions

All sensing experiments reported in this thesis were carried out at ambient laboratory conditions It is expected that changes in environmental conditions, such as temperature and humidity will affect the device response An investigation into these effects was not carried out during the course of the research presented in this thesis It is therefore recommended that future work on the development of these sensors should include an in-depth study of device performance over a range of environmental conditions, and also possible techniques to control device temperature

7.5 Conclusion

In summary, two sol-gel-derived waveguide-based absorbance sensor platforms have been presented The devices employed grating coupling to launch light into guided modes and then utilised either the evanescent wave absorbance or direct absorbance sensing technique to detect for a target analyte Table 7 1 summarises the sensing results and problems encountered for each sensor reported in this chapter It may also be seen from this summary table that both alarm type and dosimeter of sensor requirements, discussed in section 7 2 2, could be satisfied using the configurations described here

<table>
<tr><th colspan="6">Low Mode Waveguide Structure</th></tr>
<tr><th>Waveguide t, n</th><th>Grating Period</th><th>Target Analyte</th><th>Sensing Reagent</th><th>LOD, Response Time</th><th>Problems Encountered</th></tr>
<tr><td>350 nm, 1 6</td><td>833 nm</td><td>NH_3</td><td>Methyl Red</td><td>0 3 ppm,
> 20 mins</td><td>Response Time,
Configuration,
In-Coupling</td></tr>
<tr><td>350 nm, 1 6</td><td>833 nm</td><td>NH_3</td><td>Calixarene</td><td>3 7 ppm,
> 10 mins</td><td>Response Time,
LOD,
Configuration,
In-Coupling</td></tr>
<tr><th colspan="6">Multimode Waveguide Structure</th></tr>
<tr><th>Waveguide t, n</th><th>Grating Period</th><th>Target Analyte</th><th>Sensing Reagent</th><th>LOD, Response Time</th><th>Problems Encountered</th></tr>
<tr><td>1 mm, 1 51</td><td>833 nm</td><td>NH_3</td><td>BCP</td><td>0 34ppm,
> 20 mins</td><td>Response Time</td></tr>
<tr><td>1 mm, 1 51</td><td>833 nm</td><td>NH_3</td><td>PM</td><td>2 ppm,
3 5 mins</td><td>LOD</td></tr>
<tr><td>1 mm, 1 51</td><td>833 nm</td><td>CO_2</td><td>Cresol Red</td><td>0 1%,
2 mins</td><td>Response Time</td></tr>
</table>

Table 7.1 *Summary of the waveguide sensor configurations investigated*

The first device discussed consisted of a low-mode sol-gel-derived planar waveguide which exhibited extremely angular dependent coupling conditions and required the use of a laser or laser diode source The device was applied to the detection of ammonia gas with limited success The platform exhibited a number of configuration-based and mechanical-based limitations which led to the necessity to develop an alternative design

The second platform presented consisted of a multimode waveguide structure which was LED compatible Focused LED light was used to launch light into multiple guided modes, each of which interrogated (directly or evanescently) the sensing layer The device was applied to the detection of gaseous ammonia and exhibited comparable performance to the supposedly more sensitive low mode structure As a further proof of the versatility of the device, it was successfully applied to the detection of gaseous carbon dioxide, yielding a limit of detection of 0 1% It is envisaged that the next step in this research would involve the optimisation of this platform and application to the detection of a wide range of target analytes

References

1 MacCraith B B , Ruddy V , Potter C **'Optical Waveguide Sensor using Evanescent Excitation of a Fluorescent Dye in a Sol-Gel Glass'**, Electronics Letters, 1991, Vol 14, No 27, pp 1247-1248

2 Arnold M A , Ostler T J **'Fibre Optic Ammonia Gas Sensing Probe'**, Analytical Chemistry, 1986, Vol 58, pp 1137-1140

3 Caglar P , Narayanaswamy R **'Ammonia-Sensitive Fibre Optic Probe Utilising an Immobilised Spectrophotometric indicator'**, Analyst, 1987, Vol 112, pp 1285-1288

4 Blue R , Stewart G **'Fibre Optic Evanescent pH Sensing with Dye Doped Sol-Gel Films'**, International Journal of Optoelectronics, 1995, Vol 10, pp 211-222

5 Abdelghani A , Chovelon J M , Jaffrezic-Renault N , Lacroix M , gagnaire H , Veillas C , Berkova B , Chomat M , Matejec V **'Optical Fibre Sensor Coated with Porous Silica Layers for Gas and Chemical Vapour Detection'**, Sensors and Actuators B, 1997, Vol 44, pp 495-498

6 Grady T , Butler T , MacCraith B D , Diamond D , McKervey M A **'Optical Sensor for Gaseous Ammonia with Tuneable Sensitivity'**, Analyst, 1997, Vol 122, pp 803-806

7 Trinkel M , Trettnak W , Reininger F , Benes R , O'Leary P , Wolfbeis O S **'Study of the Performance of an Optochemical Sensor for Ammonia'**, Analytica Chimica Acta, 1996, Vol 320, pp 235-243

8 Werner T , Klimant I , Wolfbeis O S '**Ammonia-Sensitive Polymer Matrix Employing Immobilised Indicator Ion Pairs**', Analyst, 1995, Vol 120, pp 1627-1631

9 Toth K , Nagy G , Lan B T T , Jeney J , Choquette S J '**Planar Waveguide Ion-Selective Sensors**', Analytica Chimica Acta, 1997, Vol 353, pp 1-10

10 Lee J L , Saavedra S S '**Evanescent sensing in doped Sol-Gel Glass Films**', Analytica Chimica Acta, 1994, Vol 285, pp 265-169

11 Yang L , Saavedra S S , Armstrong N R '**Sol-Gel Based Planar Waveguide Sensor for Gaseous Iodine**', Analytical Chemistry, 1996, Vol 68, pp 1834-1841

12 Brandenburg A , Edelhauser R , Werner T , He H , Wolfbeis O S '**Ammonia Detection via Integrated Optical Evanescent Wave Sensors**', Mikrochimica Acta, 1995, Vol 121, pp 95-105

13 Weiss M N , Srivastava R , Lo P , Groger H '**Polymer Optical Waveguide Ammonia Sensors**', Environmental Monitoring and Instrumentation, 1996, Vol 8, pp 32-37

14 Wiesmann R , Muller L , Klein R , Neyer A '**Low Cost polymer-Optical Ammonia Sensor**', Proceedings 7th European Conference On Integrated Optics, 1995, Sensors and Microsystems, pp 453-456

15 Lukosz W '**Integrated Optical Chemical and Direct Biochemical Sensors**', Sensors and Actuators B, 1995, Vol 29, pp 37-50

16 Mills A , Wild L , Chang Q '**Plastic Colourimetric Film Sensors for Gaseous Ammonia**', Mikrochimica Acta, 1995, Vol 121, pp 225-236

17 Sadoka Y , Sakai Y , Yamada M **'Optical Properties of Sulfonephtalein Dyes Entrapped within Polymer Matrices for Quantification of Ammonia Vapour and Humidity in Air'**, Journal of Material Chemistry, 1993, Vol 3, No 8, pp 877-881

18 Preininger C , Mohr G J **'Fluorosensors for Ammonia using Rhodamines Immobilised in Plasticised Poly(Vinyl Chloride) and in Sol-Gel; A Comparative Study'**, Analytica Chimica Acta, 1997, Vol 342, pp 207-213

19 Bishop E **'Indicators'**, Pergamon Press, 1972, Oxford

20 McCarrick M , Harris S J , Diamond D **'Assessment of a Chromogenic Calix[4]arene for the Rapid Colorimetric Detection of Trimethylamine'**, Journal of Material Chemistry, 1994, Vol 4, No 2, pp 217-221

21 Landl M , Simon P , Kvasnik F **'New Polymethine Dyes as Sensing Reagents for Ammonia Sensors'**, Sensors and Actuators B, 1998, Vol 51, pp 114-120

22 Malins C , Landl M , Simon P , MacCraith B D **'Fibre Optic Ammonia Sensing Employing Near Infrared Dyes'**, Sensors and Actuators B, 1998, Vol 51, pp 359-367

23 Malins C , MacCraith B D **'Dye-Doped Organically Modified Silica Glass for Fluorescence-Based Carbon Dioxide Gas Detection'**, Analyst, 1998, Vol 123, pp 2373-2376

24 Mills A , Chang Q , McMurray N **'Equilibrium Studies on Colorimetric Plastic Film Sensors for Carbon Dioxide'**, Analytical Chemistry, 1992, Vol 64, pp 1383-1389

25 Mills A , Chang Q **'Tuning Colorimetric and Fluorimetric Gas Sensors for Carbon Dioxide'**, Analytica Chimica Acta, 1994, Vol 285, No 1-2, pp 113-123

26 Mills A , Chang Q **'Fluorescence Plastic Thin-Film Sensor for Carbon Dioxide'**, Analyst, 1993, Vol 118, No 7, pp 839-843

27 Mills A , Chang Q **'Colorimetric Polymer Film Sensors for Dissolved Carbon Dioxide'**, Sensors and Actuators B, 1994, Vol 21, pp 83-89

28 Mills A , Lepre A , Wild L **'Breath-by-Breath Measurement of Carbon Dioxide using a Plastic Film Optical Sensor'**, Sensors and Actuators B, 1997, Vol 38-39, pp 419-425

29 Mills A , Monaf L **'Thin Plastic Film Colorimetric Sensors for Carbon Dioxide: Effect of Plasticizer on Response'**, Analyst, 1996, Vol 121, No 4, pp 535-540

30 Weigl B H , Wolfbeis O S **'New Hydrophobic Materials for Optical Carbon Dioxide Sensors based on Ion-Pairing'**, Analytica Chimica Acta, 1995, Vol 302, No 2-3, pp 249-254

31 Weigl B H , Wolfbeis O S **'Sensitivity Studies on Optical Carbon Dioxide Sensors based on Ion-Pairing'**, Sensors and Actuators B, 1995, Vol 28, pp 151-156

Chapter 8 Waveguide Sensor Platform for Fluorescence

8.1 Introduction

In this chapter a novel generic configuration for fluorescence-based optical sensors employing multimode waveguides is presented The analyte sensitive fluorescence emitted from a dye-doped sol-gel film coated upon the waveguide surface is efficiently coupled to guided modes in the waveguide The guided mode intensity is measured upon emergence from the end-face of the waveguide A large fraction of the emitted fluorescence is captured by the planar waveguide whereas only a very small amount of the excitation light is captured due to scattering Such a mechanism results in the angular separation of the excitation light and fluorescence emission thus enabling operation without the use of optical filters in the configuration

The key processes of fluorescence and fluorescence quenching-based sensing are briefly discussed The generic sensor configuration, principle of operation and characterisation are detailed The sensor is then applied towards the sensing of oxygen using a ruthenium doped sol-gel thin film which exhibits excellent response to gaseous oxygen

8.2 Introduction to Fluorescence

The term "fluorescence" was first coined by Sir George Stokes in the 19th century and refers to the phenomenon in which absorption of light of a given wavelength by a molecule is followed by the emission of light at longer wavelengths[1-4] The separation between the absorbed wavelength and the emitted wavelength is known as the Stokes shift Fluorescence techniques may be used for sensing applications and are in many ways superior to absorbance-based techniques due to higher sensitivity and selectivity In the following section the theory of fluorescence is explained in more detail

Every electron in a molecule carries a spin angular momentum with a spin quantum number, s = 1/2 The electron may be either spin-up ↑ or spin-down ↓ in nature The total spin angular momentum possessed by a many-electron atom or molecule is represented by the total spin quantum number, S, which is defined as the vector sum of all the individual contributions from each electron Two electrons each possessing s = 1/2 may be present with their spins parallel or opposed If the spins are opposed the total spin quantum number, S, is 0 and the electrons are said to be paired If the electron spins are parallel, the total quantum number, S, is 1 The spin multiplicity, that is the number of states in the presence of an applied magnetic field, is given by 2S + 1 A molecule with all electrons spin-paired possesses S = 0 and a spin multiplicity of 1 Such an electronic state is referred to as a singlet state A triplet state has a total spin quantum number of 1 and a spin multiplicity of 3

An electron in a molecule may be promoted to an excited state by interaction with light The excited state may be either singlet or triplet in nature Shown in figure 8 1 is an example of a simplified energy level diagram for the absorption and emission of light The ground state is defined as E_0 E_1 is defined as a triplet excited state, E_2 is defined as a singlet excited state, and E_3 is defined as the initial excited state

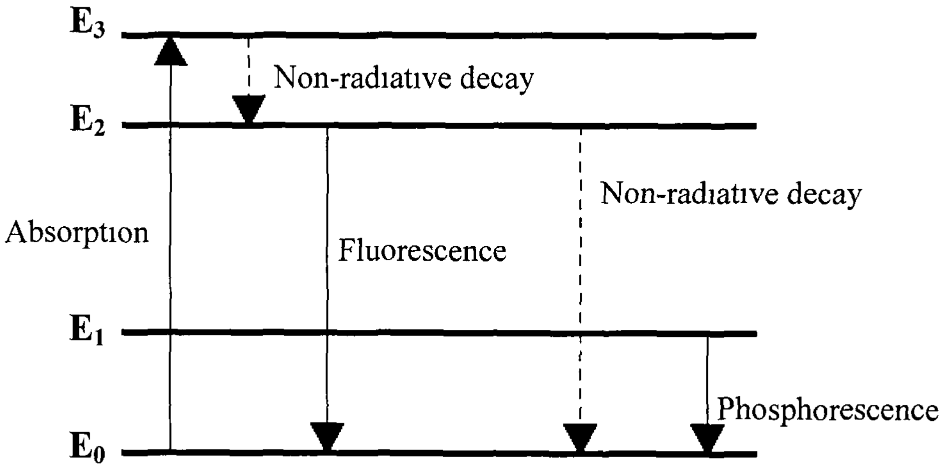

Figure 8.1 *Absorption and Emission Processes*

Excitation of a molecule that possesses a ground state energy level, E_0, by absorption of an incoming photon, can raise the molecule to an excited state, E_3. The absorbed energy may be released either radiatively or non-radiatively. If there is a small energy level separation between the excited states E_3 and E_2 then the electron tends to decay non-radiatively to E_2.

Fluorescence is the radiative emission resulting in de-excitation of a singlet state (E_2) to a singlet ground state. Such transitions are quantum mechanically allowed, with emission rates as high as 10^8 per second, resulting in fluorescence lifetimes of approximately 10 ns. Phosphorescence, emission from a triplet state excited electron (E_1) to a singlet ground state (E_0) is also a possibility. Transitions between states of different multiplicity are quantum mechanically forbidden, but in some molecules are weakly allowed. This happens when the molecule contains a heavy atom which, because of its strong spin - orbit interaction, can reverse the relative orientations of pairs of electrons. Emission rates are small and hence lifetimes are long.

In either the case of fluorescence or phosphorescence the emitted photons have energies given by

$$h\upsilon = \Delta E \qquad [8.1]$$

where h is Planck's constant 6.6256×10^{-34} J.s, υ is the frequency of the emitted light and ΔE is the separation of the energy levels participating in the process.

8.3 Fluorescence Quenching as a Sensing Mechanism

Fluorescence quenching describes any process that results in the non-radiative loss of energy from a molecule in an excited state[1,3,4]. Fluorescence quenching may be used as sensing technique for the detection of a wide range of analytes. If the analyte to be detected has a quenching effect on the fluorescence emission from some reagent, then by monitoring the extent of the fluorescence quenching it is possible to deduce the concentration of quencher present

Fluorescence quenching may be static or dynamic Static quenching results from the formation of a non-fluorescent complex between the fluorophore and quencher Dynamic quenching, on the other hand, results from the interaction of the excited fluorophore with a free molecule and causes de-excitation without formation of a complex Therefore, dynamic quenching is collisional in nature and thus requires close contact of molecules, is dependent on the concentration of the quenching molecule, and the rate at which the quencher can diffuse to the excited molecule An expression which fully describes a generic fluorescence quenching-based sensor will now be derived

After excitation by an incident pulse of light molecules in a fluorophore will subsequently relax back to the ground state with a rate constant K given by

$$K = K_e + K_i + K_t\,[A] \qquad [8\ 2]$$

where K_e is the rate constant for emission of a photon, K_i is the rate constant for internal conversion of the excitation energy, K_t is the rate constant for transfer of energy to the quenching agent and [A] is the concentration of quencher molecules

An important parameter, which quantifies the efficiency of radiative emission, is known as the fluorescence quantum yield, Q Q is defined as the ratio of the numbers of photons emitted by the fluorophore to the number of excitation photons absorbed and may be expressed as

$$Q = \frac{K_e}{K_e + K_i + K_t\,[A]} \qquad [8\ 3]$$

If fluorescence is the only possible mechanism for relaxation of the molecule back to its ground state then K_i and K_t are zero and thus $K = K_e$ resulting in a fluorescence quantum yield of one However, this is rarely the case due to internal conversion of the excited energy (K_i)

Q_0, the quantum yield in the absence of a quencher, is described by the equation below

$$Q_0 = \frac{K_e}{K_e + K_i}$$ [8 4]

A parameter Q_A, the quantum yield in the presence of a quencher concentration [A], is defined as

$$Q_A = \frac{K_e}{K_e + K_i + K_t\,[A]}$$ [8 5]

The ratio of the quantum yield in the absence of a quencher to the quantum yield in the presence of a quencher of concentration [A] may then be expressed as

$$\frac{Q_0}{Q_A} = \frac{K_e + K_i + K_t\,[A]}{K_e + K_i} = 1 + a\,K_t[A]$$ [8 6]

where $a = (K_e + K_i)^{-1}$

Equation 8 6 is known as the Stern-Volmer equation and may be rewritten in the more familiar expression

$$\frac{I_0}{I_A} = 1 + a\,K_t\,[A]$$ [8 7]

where I_0 is the fluorescence intensity in the absence of a quencher, I_A is the fluorescence intensity in the presence of a quencher of concentration [A], $a\,K_t$ is the Stern-Volmer quenching constant

The Stern-Volmer relationship that is described by equation 8 7 is linear in nature A graphical illustration is shown in figure 8 2 where it can be seen that it is possible to determine the concentration of quencher present in a system simply by obtaining the relevant Stern-Volmer quenching constant and experimentally determining the intensity ratio I_0/I_A

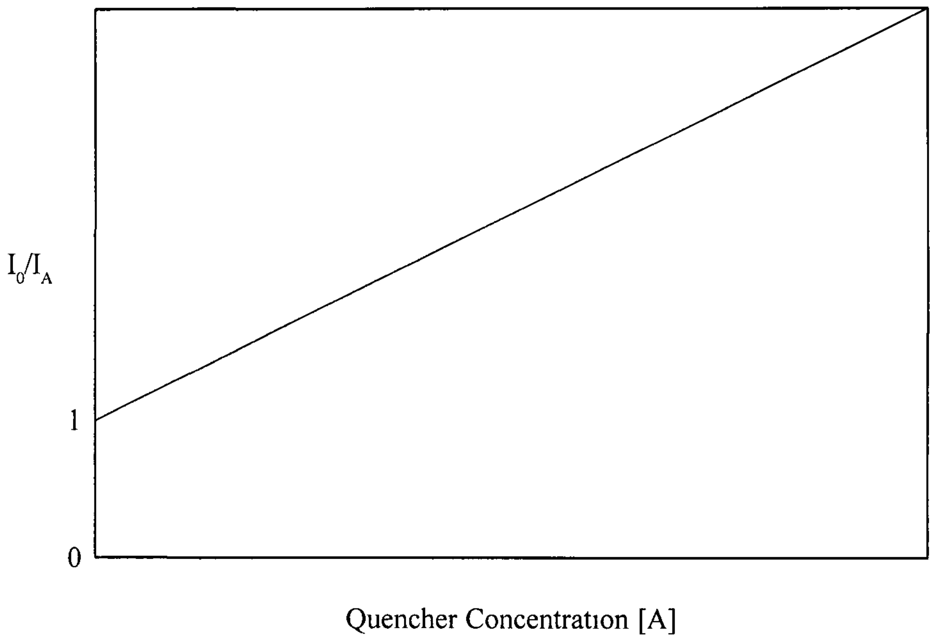

Figure 8.2 *Theoretical Stern-Volmer Plot*

8.4 Generic Fluorescence-Based Sensor

8.4.1 Sensor Configuration

The generic sensor configuration is illustrated in figure 8 3 The device consists of a multimode waveguide (typically a microscope slide, refractive index 1 515), one side of which is coated with a sol-gel thin film in which an analyte-sensitive fluorescent reagent is entrapped

The generic nature of the device allows for the detection of a wide range of analytes simply by utilising different sensing layer configurations and by careful choice of the immobilised fluorescent reagent so that it is quenched by the target analyte

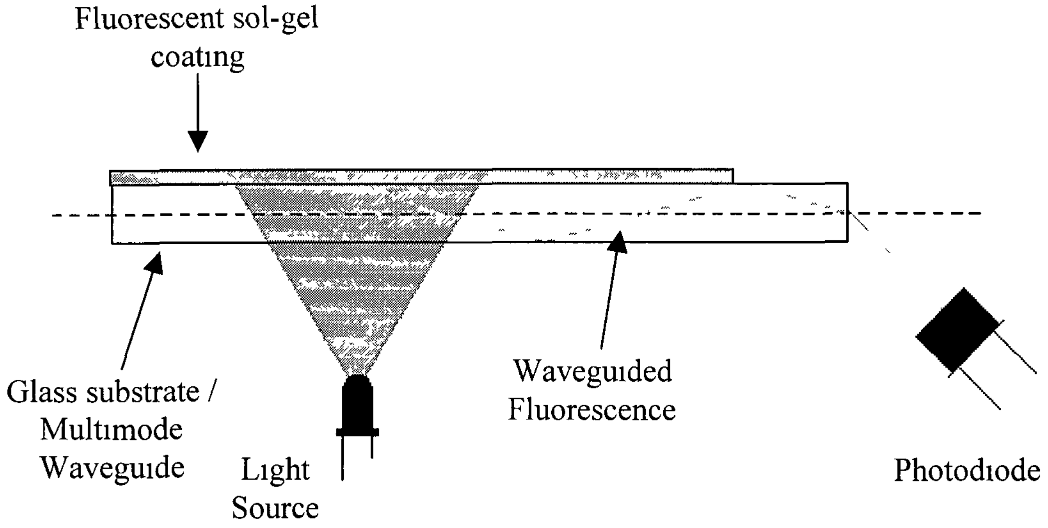

Figure 8.3 *Schematic diagram of generic sensor configuration*

8.4.2 Principle of Operation

Fluorophores which are situated at or within a close distance (one wavelength) of an interface, constituting a discontinuity in refractive index emit the greater part of their fluorescence into the medium with a higher refractive index[5-9] The angular distribution of the emission from such a surface-bound molecule differs significantly from that of the emission of a free molecule in a homogeneous medium For molecules situated at or near refractive-index discontinuities the emission maximum lies at the angle of total internal reflection (the critical angle) of the two media, with a significant part of the radiation being emitted at angles above the critical angle (so-called evanescent modes) If the medium below the interface is a waveguiding structure then if the wavevector of the emitted fluorescence coincides with the evanescent fields of guided modes then coupling of a large proportion of the emitted fluorescence into the modes of the waveguide can occur

In the configuration presented in this thesis an LED light source is used to excite fluorescent molecules located in a sol-gel-derived thin film which has been coated onto the surface of a multimode planar waveguide The maximum emission of these surface-bound fluorophores occurs in a downward direction at the critical angle of the two media with a substantial portion of the emitted radiation also occuring above the critical angle Therefore, the emitted fluorescence can be coupled into guided modes within the planar waveguide, due to the overlap of the emitted fluorescence with the evanescent fields of the guided modes Since most of the emitted fluorescence occurs at the critical angle, it is logical to suggest that the fluorescence is preferentially coupled into the higher order modes which occur around the critical angle The modes then propagate along the waveguide where upon emergence from the end-face they are detected using a photodiode Since the guided modes are high order it is beneficial to detect the emerging signal at an angle to the end-face since this would help reduce noise

If fluorescence quenching of the fluorophores occur, then the amount of emitted fluorescence decreases and the amount of captured fluorescence decreases accordingly Thus manifesting itself in a change in the signal detected at the waveguide end-face

A full theoretical treatment of this work is not presented in this thesis However, work is currently being carried out in the Optical Sensor Group to fully describe the observed phenomenon

8.4.3 Device Characterisation

The fluorescence signal emerging from the end-face of the waveguide is found to exhibit a strong angular dependence, whereas the signal due to scattering of the excitation source is almost constant over all output angles This is illustrated in figure 8 4 It is immediately evident from this plot that detection of the emerging fluorescence at the angle of maximum emission provides enhanced signal to noise performance over conventional detection of the entire end-face output

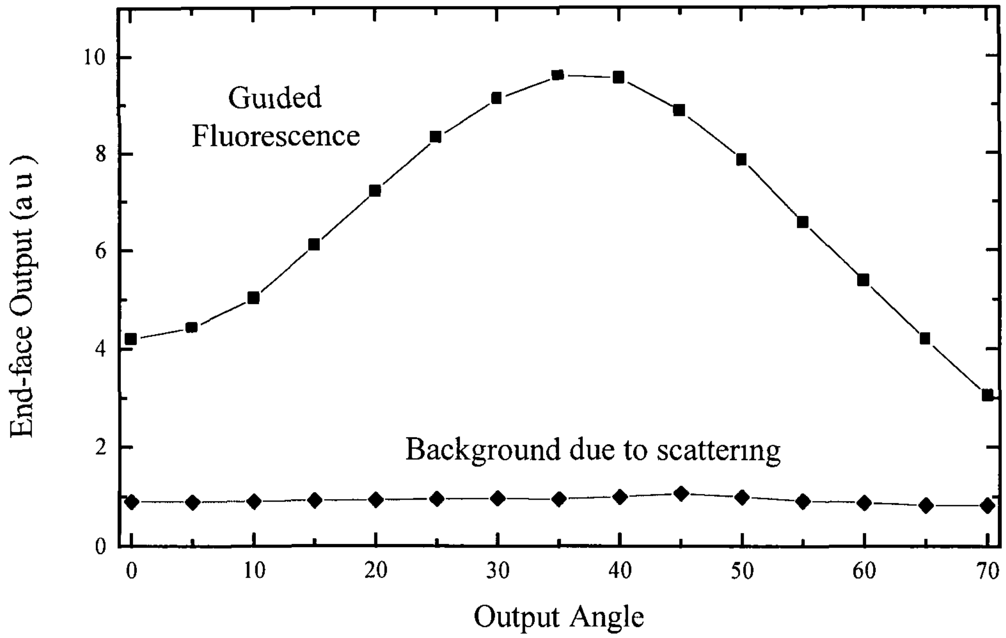

Figure 8.4 *Schematic diagram of generic sensor configuration*

This is further illustrated by measuring the spectrum of the emerging light over a wide range of angles The fluorophore employed in this situation is a ruthenium complex compound that has an absorption maximum at 450 nm and is excitable by a blue LED (central emission 450 nm) The resultant emission is centred at 610 nm Acquisition of the spectra was performed using a microspectrometer (S2000, Ocean Optics, USA), the collecting fibre (Core 200 μm) of which was positioned at the end-face of the waveguide as illustrated in figure 8 5

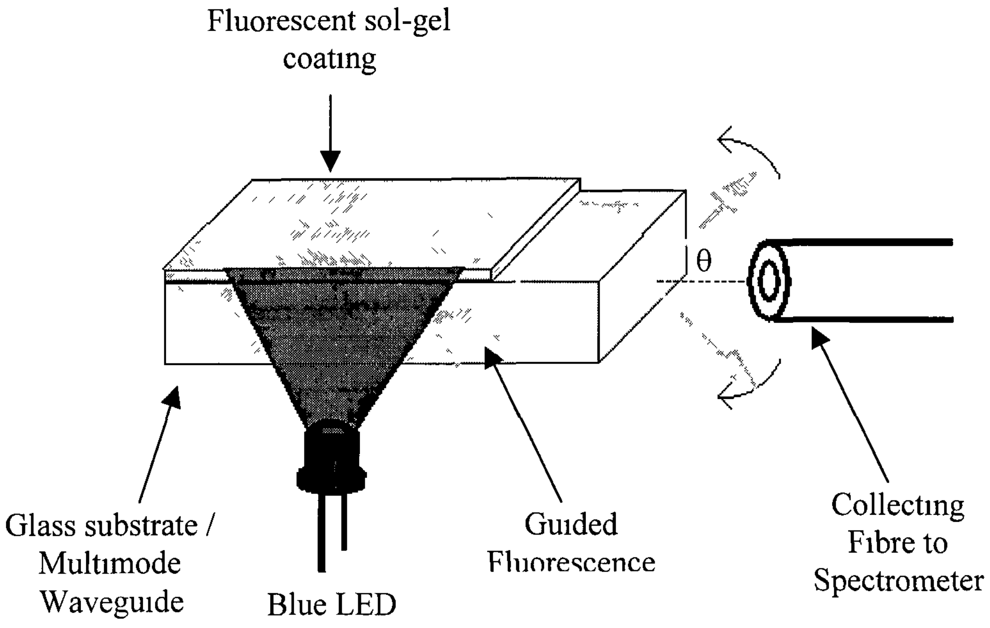

Figure 8.5 *Schematic diagram for determination of output spectrum*

The spectra of the emerging signal for a wide range of detection angles are presented in figure 8 6 It can be clearly seen that at a detection angle of θ = 0° the fluorescence and excitation cannot be distinguished from the background levels While this is partly due to the low capture efficiency of the collecting fibre, it also tends to imply that sensor performance at a detection angle of θ = 0° is not optimal It is also evident from figure 8 06 that as the detection angle increases, so to does the measured fluorescence intensity Such an observation is consistent with the selective coupling into higher order modes of the fluorescence This trend continues until an angle is reached above which the emerging fluorescence begins to decrease The angle of maximum ratio is determined by the properties of the thin sensing layer It is evident that at this detection angle there is a high level of signal to noise without the need for optical filters

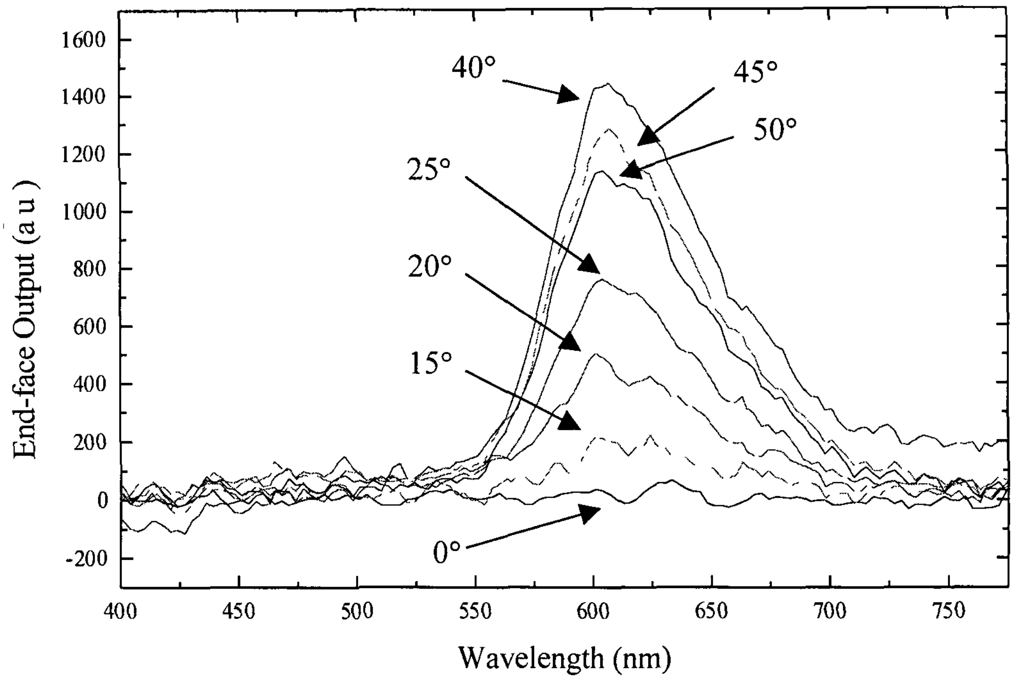

Figure 8.6 *Spectrum of end-face output for range of detection angles*

8.4.4 Effect of Refractive Index and Thickness of Sensing Layer

The end-face profile of the sensor device is dependent on the properties of the sol-gel-derived thin film In this section the effect of refractive index and thickness are investigated The aim of this study was to determine optimum sensing layer characteristics and the optimum angle of detection

Fluorophore-doped sol-gel-derived thin films with a range of refractive indices may be fabricated by mixing commercially available titania and silica-based precursors (Liquicoat, Lauder Chemicals, UK) The relative amounts of the two precursors define the refractive index in accordance with figure 8 7 The thm films were deposited on the multimode waveguides ($n_{waveguide}$ = 1 515) at a dip-speed of 2 8 mm sec^{-1} and dried at 100 °C for 10 minutes

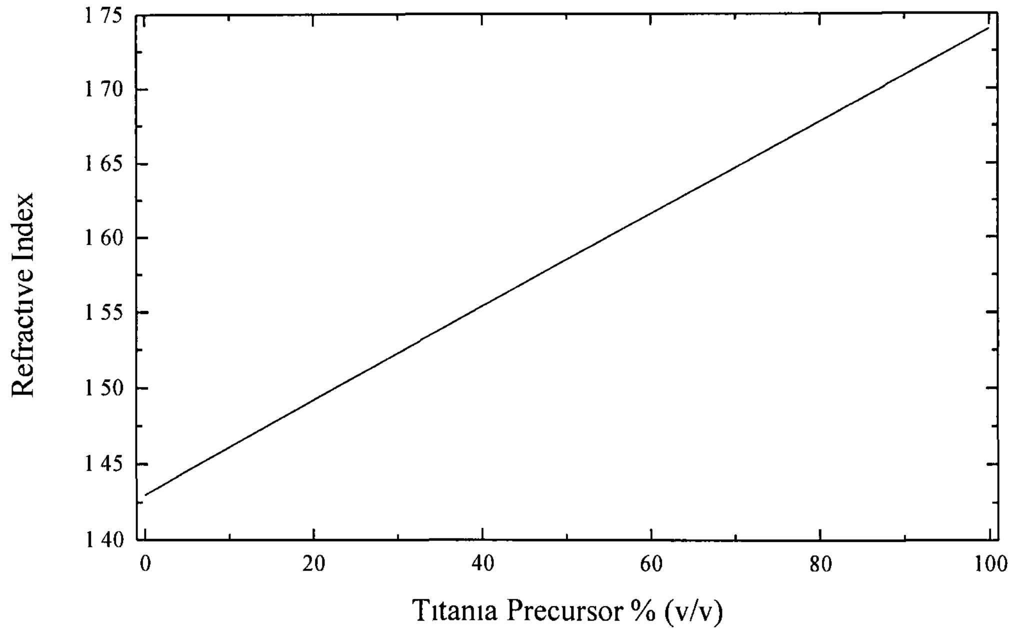

Figure 8.7 *Calibration curve for liquicoat-derived thin films*[8]

The angular distributions of light from the waveguide end-face are presented in figure 8 9 for a range of sensing layer refractive indices The angular spectra were determined by employing a silicon photodiode (Hamamatsu, UK) which was rotated with respect to the end-face of the planar waveguide as illustrated in figure 8 8

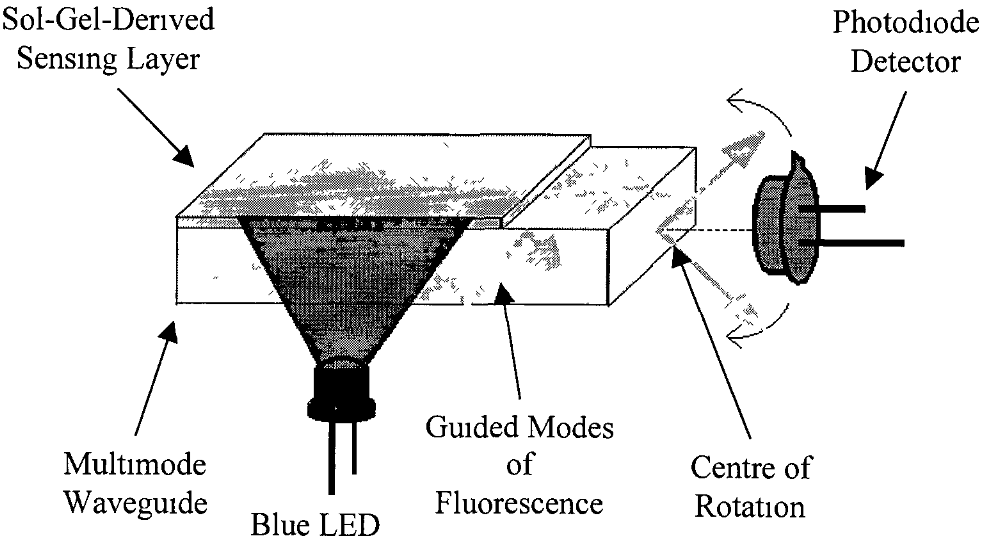

Figure 8.8 *Configuration for Determination of Angular Profile*

A number of observations can be made from the presented data Firstly, the angle of maximum emission from the waveguide decreases with increasing refractive index of the coating This is consistent with the theory, which indicates that optimum capture occurs at the critical angle, which is a function of the refractive index of the fluorescing layer Secondly, the intensity of this maximum output also decreases with increasing film refractive index Furthermore, the shape of the curves changes as the refractive index is varied At lower refractive indices, the peak becomes sharper, forming a well-defined maximum As the index matching condition between coating and substrate is approached ($n_{coating} = n_{waveguide}$), it can be seen that the angular dependence of the end-face output decreases Thus, a low refractive index coating seems to be the optimum choice for enhancing capture and angular dependence and thus increasing sensitivity Therefore, sensing layers fabricated from pure silica, which had a refractive index of 1 43 were employed These sensing layers exhibited peak fluorescence output at 37 5°

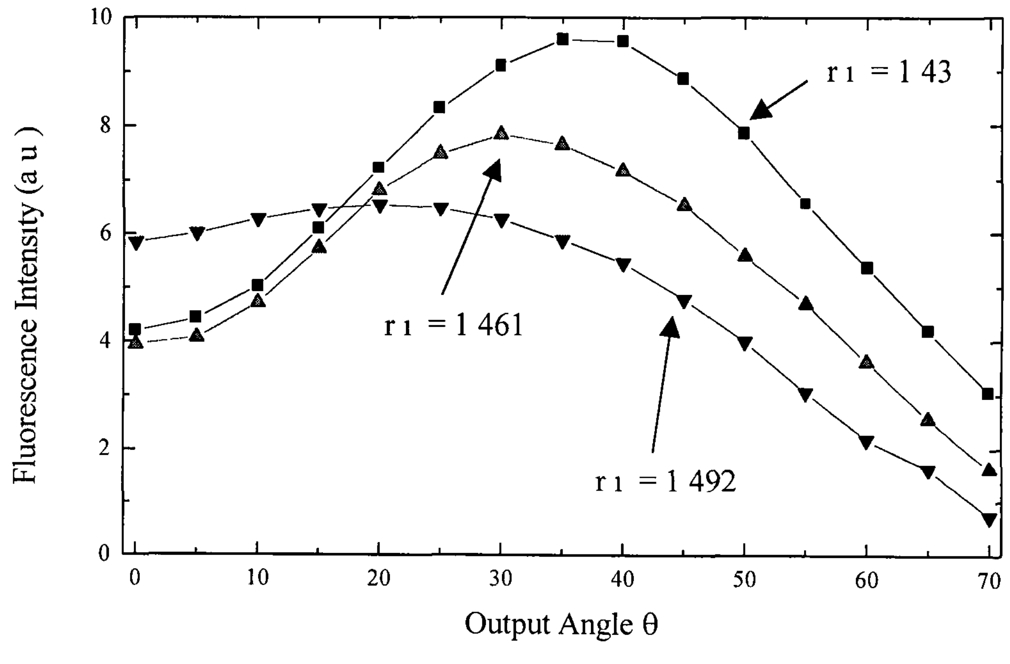

Figure 8.9 *Angular end-face output for a range of sensing layer refractive indices*

Two films of different thickness but the same refractive index were examined to investigate the effect of film thickness on the end-face output The films were fabricated from a pure silica precursor doped with a ruthenium fluorophore dip-coated onto the multimode waveguide speeds of 2 8 mm sec^{-1} and 1 mm sec^{-1} which yielded thicknesses of approximately 580 nm and 380 nm with the same refractive index of 1 43

The dependence of the profile of the end-face output on sensing layer thickness is shown in figure 8 10 It can be seen that as expected, the thickness of the sensing layer has a negligible effect on the position of the optimum detection angle However, the thickness of the sensing layer has a substantial effect on the intensity of the end-face output As the thickness of the sensing layer increases so too does the output intensity This is to be expected, since as the layer thickness increases there are more fluorophore molecules present resulting in increased levels of fluorescence and hence a larger amount of captured fluorescence

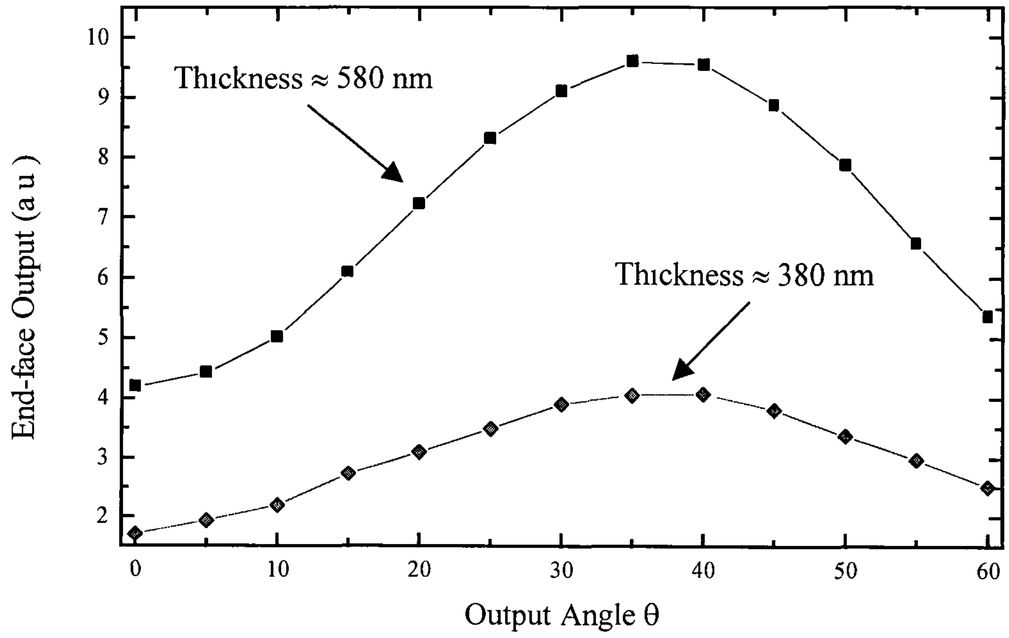

Figure 8.10 *Angular end-face output for different sensing layer thicknesses*

This observation suggests that the thicker the sensing layer the more efficient the sensor device due to increased signal levels This, however, is not always a valid assumption In optical gas sensors the thicker the sensing layer the longer the time required for the analyte to diffuse into the matrix and reach the sensing reagent Consequently, the response time of the sensor device increases Hence, a compromise between signal level and response time is required It was decided for the purpose of oxygen sensing that sol-gel-derived sensing layers of refractive index 1 43 and thickness of approximately 580 nm, corresponding to a dip-speed of 2 8 mm sec^{-1} provided a large enough signal with a rapid response time and therefore would be employed A detection angle of 37 5°, as derived from figure 8 09 was utilised

8.5 Application to Oxygen Sensing

8.5.1 Introduction to Oxygen sensing

The ability to accurately determine oxygen concentration is a crucial requirement in many industrial applications For example, in the mining industry knowledge and control of the oxygen levels in tunnels is crucial to the safety of workers Dry ambient air contains 20 9% oxygen by volume Should this level drop below 19 5% then breathing difficulties occur which may result in impaired co-ordination, unconsciousness, coma and death Therefore any oxygen sensor must be capable of detecting signal changes of 1% and less Oxygen detection is also important in a number of chemical and clinical analysis, and oxygen-sensing devices have also been exploited for monitoring the course of biochemical reactions during which oxygen is produced or consumed The conventional method for determination of oxygen concentration employs the amperometric Clark-type electrode which is illustrated in figure 8 11

The Clark electrode consists of an anode, cathode and an electrolyte Partial pressures of oxygen are determined by measuring the current flow between the electrodes At the cathode, the incoming oxygen is reduced to hydroxyl ions which in turn oxidise the metal anode according to the following equations

$$O_2 + 2H_2O + 4e^- \rightarrow 4OH^- \tag{8 8}$$

$$2Pb + 4OH^- \rightarrow 2PbO + 2H_2O + 4e^- \tag{8 9}$$

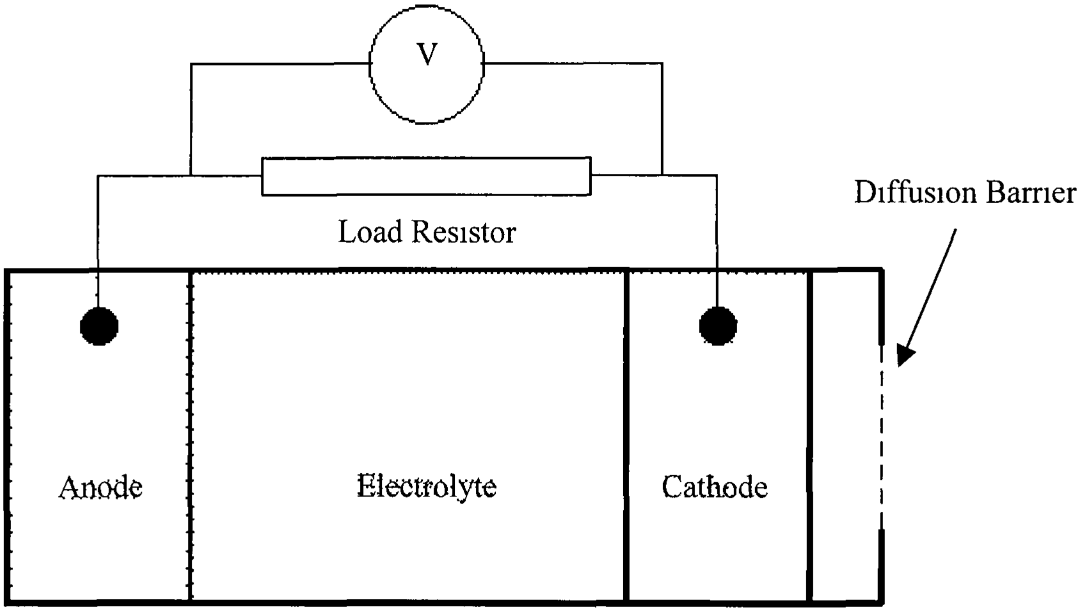

Figure 8.11 *Clark electrode*

The current produced is related to the rate of consumption of oxygen Such a device while providing an effective method for oxygen detection, is not without its disadvantages

1 Oxygen is irreversibly consumed during the detection as can be seen from the equations above Therefore, the device actually depletes the oxygen concentration of the sample being analysed

2 The signal from a typical cell is slightly non-linear

3 Acidic gases can produce false results due to their absorption by the electrolyte which allows the flux of oxygen to the electrode to increase

Optical detection of oxygen may be carried out by the fluorescence quenching technique described earlier in this chapter The most common oxygen sensitive fluorophores employed are the ruthenium family of compounds[11] which typically have absorption maxima at 450 nm, with oxygen-sensitive fluorescence centered at 610 nm The entire absorption and emission spectrum of such a compound is shown in figure 8 12 below

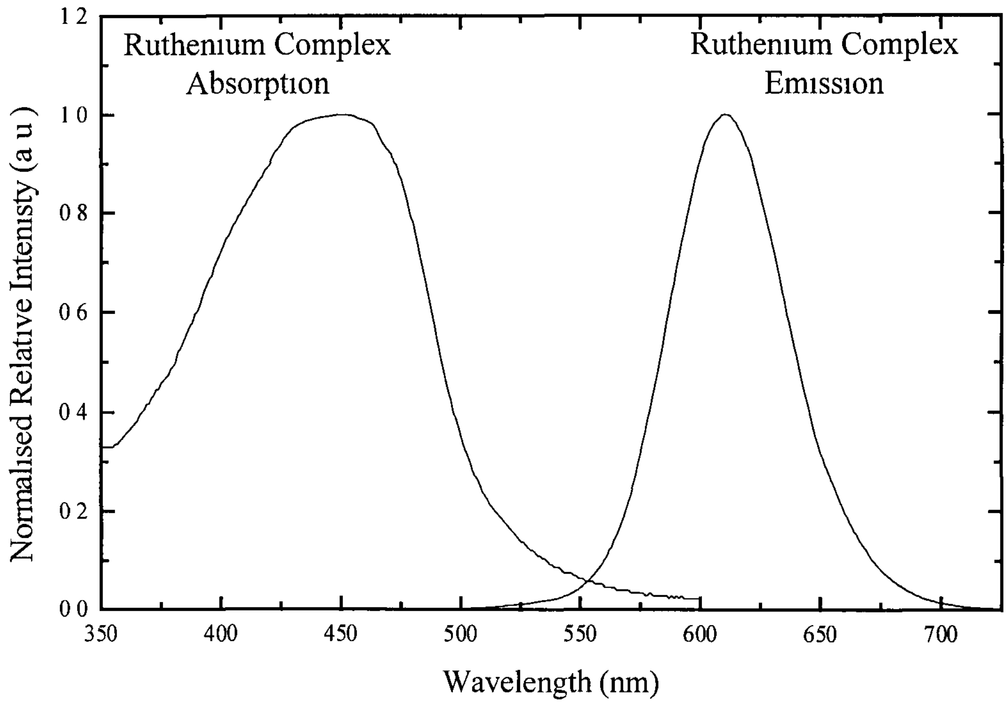

Figure 8.12 *Absorption and emission spectrum of a typical ruthenium compound*

The intensity of the fluorescence emitted from a typical ruthenium compound is quenched by oxygen in accordance with the Stern-Volmer equation, which was discussed in section 8 3

$$\frac{I_0}{I} = 1 + K_{SV}pO_2 \qquad [8\ 10]$$

where I is the fluorescence intensity in the presence of oxygen, I_0 is the fluorescence intensity in the absence of oxygen, K_{sv} is the Stern-Volmer constant and pO_2 is the partial pressure of oxygen Therefore, by monitoring the fluorescent intensity emitted by the sensing layer and coupled into the waveguide it is possible to determine the concentration of oxygen in the environment surrounding the sensor device

8.5.2 Oxygen Sensor Fabrication

Oxygen sensitive fluorescent sol-gel sensing layers[12,13] were fabricated by mixing a silicon alkoxide precursor (Ethyltriethoxysilane, $C_2H_5(C_2H_5O)_3Si$, ETEOS) with water, ethanol and hydrochloric acid, which acts as a catalyst The water was kept at pH1 and the R value (the ratio of water to silicon alkoxide precursor) at 2 The ruthenium complex, rutheniumII-tris (4,7-diphenyl-1,10-phenantroline) was added to the precursor solution, and stirred for 1 hour The typical concentration of ruthenium complex used was 20,000 ppm with respect to the precursor solution After stirring, the sol is stored at 70 °C for 5 hours to promote hydrolysis and condensation polymerisation Thin sensing layers were then dip-coated in a draught-free environment onto a single side of the multimode planar waveguides The samples were dried at 70 °C for 17 hours and left to stabilise at room temperature for 1 month prior to use These sensing layers had a refractive index of 1 43 and a thickness of 580 nm

8.5.3 Oxygen Sensor Characterisation

A schematic diagram of the experimental system employed to measure the oxygen-quenched fluorescence is shown in figure 8 13 The sol-gel-derived sensing layers employed in the device had a refractive index of 1 43 and therefore in accordance with figure 8 09 a silicon photodiode detector was positioned at the optimum detection angle of 37 5° to the plane of the waveguide Dedicated lock-in circuitry was used to measure the emerging fluorescence A custom-built flow-cell was attached to the sensor device and precise mixtures of oxygen and nitrogen gases were passed into the gas chamber using mass flow controllers (Unit Instruments, Ireland) which were controlled using a labVIEW© virtual control panel

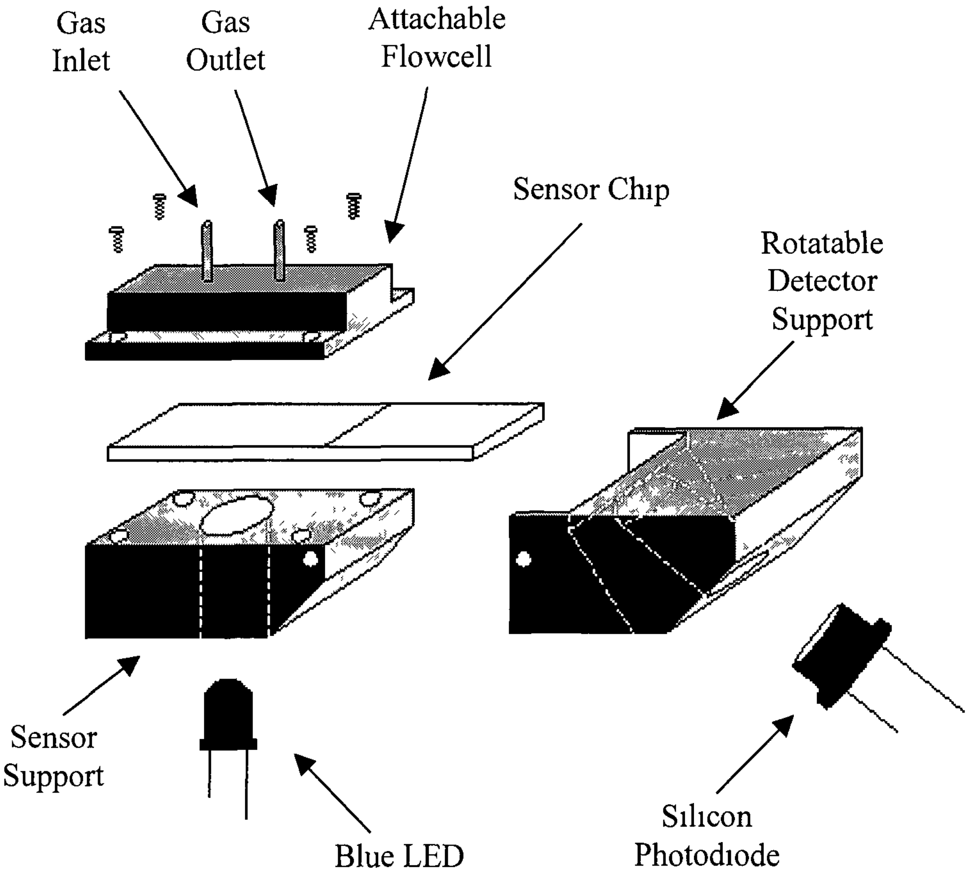

Figure 8.13 *Experimental set-up for optical oxygen sensing*

The light source employed to induce fluorescence of the ruthenium doped sol-gel layer was a high power blue light emitting diode (DCL Components, UK) the emission spectrum of which peaks at 450 nm as shown in figure 8 14 This light source is ideal for use in the oxygen sensor due to its large overlap with the absorption range of the ruthenium complex

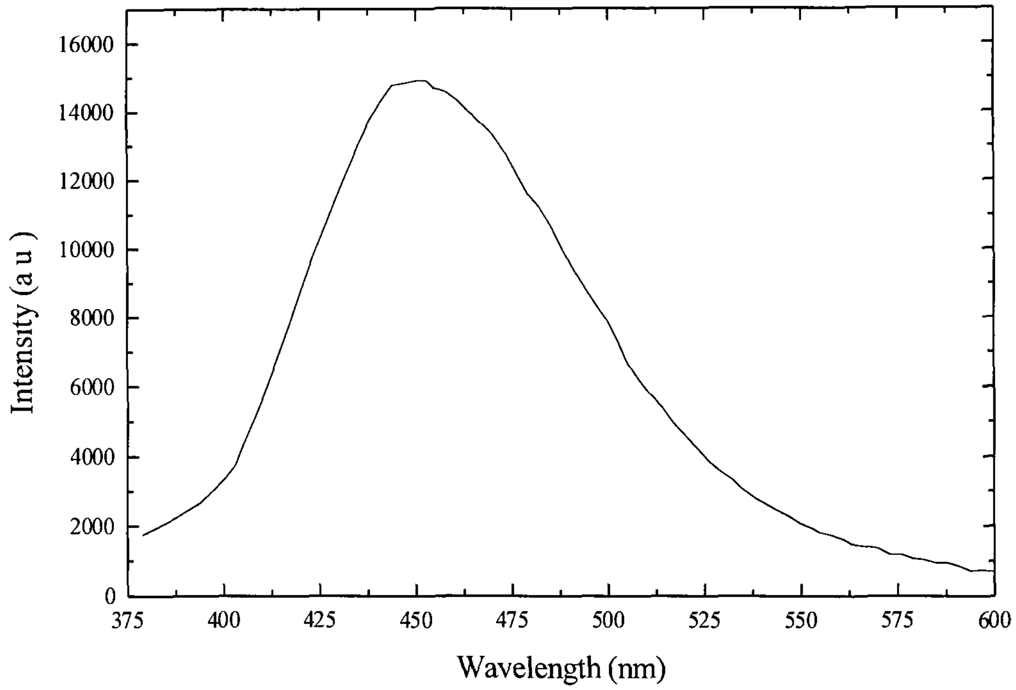

Figure 8.14 *Emission Spectrum of high power blue LED*

The sensor was exposed to alternate environments of 100% oxygen and 100% nitrogen and the output of the waveguide monitored A typical response curve is shown in figure 8 15 It can be seen from this plot that the fluorescence is quenched dramatically but reversibly in the presence of oxygen gas It is also evident from this plot that the signal to noise ratio is extremely high despite the absence of optical filters to help discriminate between excitation and emission radiation

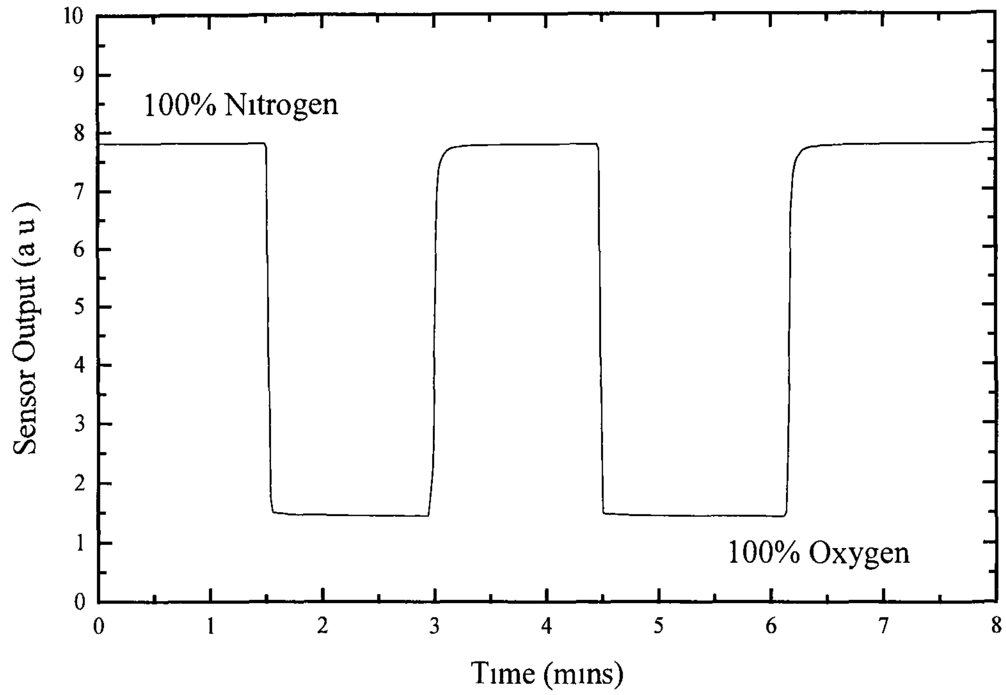

Figure 8.15 *Response of Sensor to 100% N_2 and 100% O_2 gas*

The response of the sensor to oxygen concentrations ranging from 0% to 100% in increments of 10% is shown in figure 8 16 It may be seen that the device sensitivity is highest at low oxygen concentrations Such behaviour has been investigated thoroughly in the literature[ref] and can be attributed to the sensing layer properties A Stern-Volmer plot was constructed from the presented data and is shown in figure 8 17, it can be seen that this curve is in agreement with the theoretical plot shown previously in figure 8 2

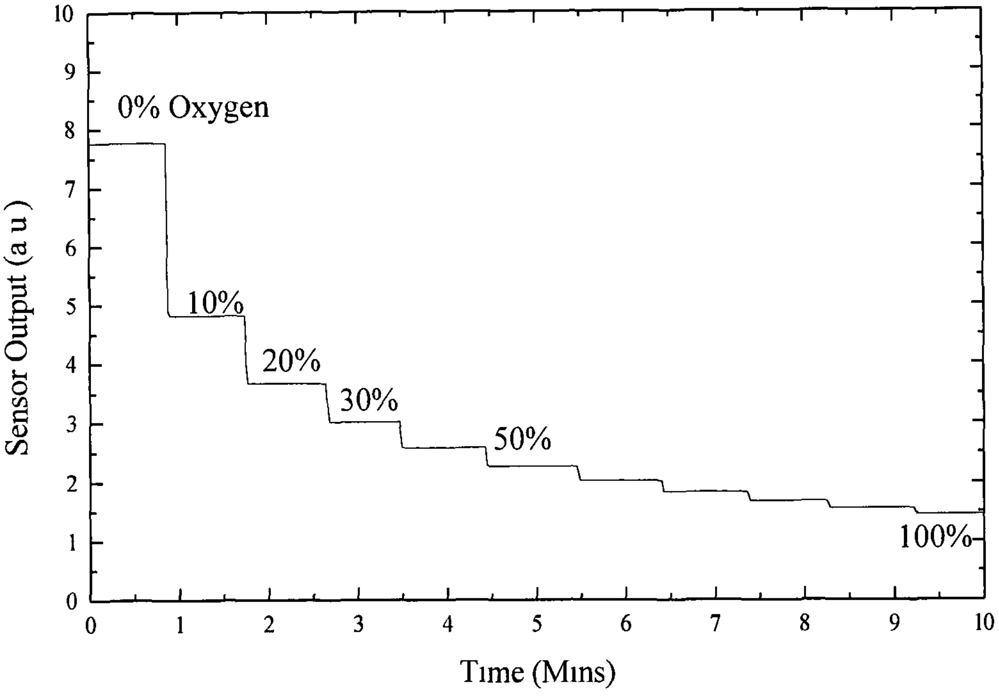

Figure 8.16 *Calibration response curve of sensor to varying concentrations of* O_2 *gas*

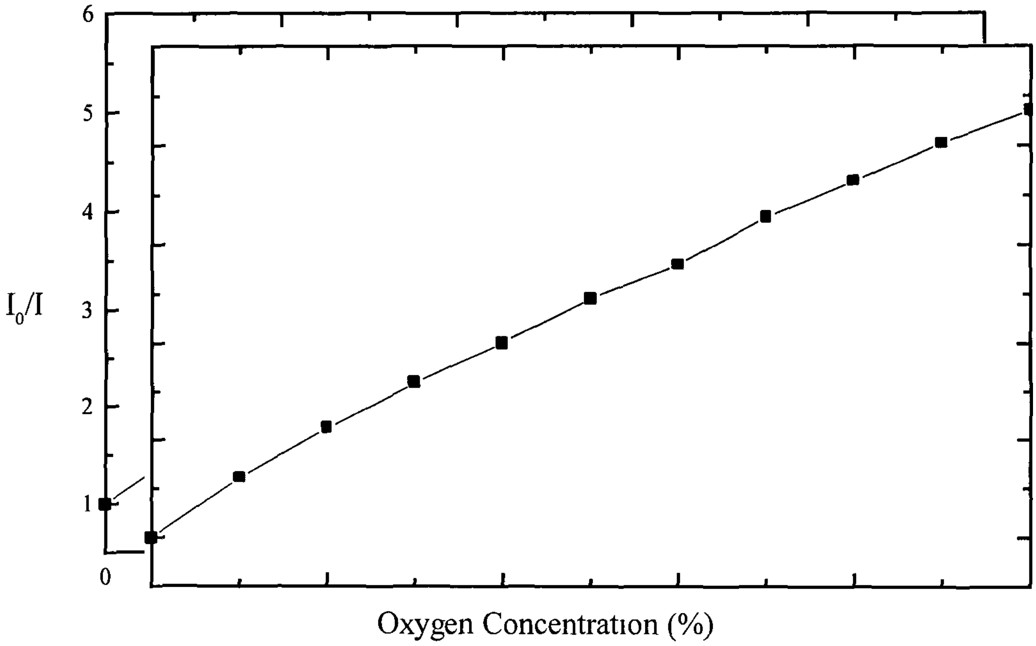

Figure 8.17 *Stern-Volmer plot for sensor*

Device response times upon exposure to and removal of gaseous oxygen were determined to be less than 1 second for a 90% signal change These response times comprise the inherent response time of the sensor (governed primarily by the time required by the analyte to diffuse into the sensor membrane and interact with the sensing reagent), the filling time for the gas flow-cell and the adjustment time of the mass flow controllers Finally, 0 027 % oxygen in nitrogen carrier gas was determined to be the device limit of detection Such a limit of detection is extremely favourable when compared to the requirements discussed in section 8 5 1 (ability to differentiate between 20 9% and 19 5%)

8.6 Conclusion

In conclusion, this chapter reports the development of a generic fluorescence sensor platform which could be applied towards the detection of both gaseous and aqueous phase chemicals The theory of fluorescence and fluorescence quenching, the key processes involved, were described in detail The configuration and operating principle of such a generic sensor device were detailed, with emphasis placed on the importance of tuning the sensor layer refractive index and detection angle

The sensor has been applied to the detection of gaseous oxygen and has been shown to exhibit an extremely rapid and large response to the presence of oxygen The high level of repeatability, good reversibility, rapid response times and a high signal-to-noise ratio despite the absence of optical filters in the configuration indicate that the device performance is comparable with that of other optical sensor configurations[14-17] yet is considerably less costly to produce

References

1 Lakowicz J R '**Principles of Fluorescence Spectroscopy**', 1983, Plenum Press, New York

2 Guilbault G G '**Practical Fluorescence, Theory, Methods and Techniques**', Marcel Dekker Inc , New York

3 McEvoy A K '**Development of an Optical Sol-Gel-Based Dissolved Oxygen Sensor**', PhD Thesis, 1996, Dublin City University, Ireland

4 O'Keeffe D G '**Development of Fibre Optic Evanescent Wave Fluorescence-Based Sensors**', PhD Thesis, 1995, Dublin City University, Ireland

5 Marcuse D '**Launching Light into Fiber Cores from Sources Located in the Cladding**', Journal of Lightwave Technology, 1988, Vol 6, No 8, pp 1273-1279

6 Lukosz W , Kunz R E '**Light Emission by Magnetic and Electric Dipoles Close to a Planar Interface I Total radiated power**', Journal of the Optical Society of America, 1977, Vol 12, pp 1607-1614

7 Enderlein J , Ruckstuhl T , Seeger S '**Highly Efficient Optical Detection of Surface-Generated Fluorescence**', Applied Optics, 1999, Vol 38, No 4, pp 724-732

8 Apel O , Marowsky G '**Waveguide Coupling at Supercritical Angles**', European Quantum Electronics Conference, 1998, Poster presentation, Glasgow, Scotland

9 Lippitsch M E , Draxler S , Kieslinger D **'Luminescence Lifetime-Based Sensing: New Materials, New Devices'**, Sensors and Actuators B, 1997, Vol 38-39, pp 96-102

10 Sheridan F 'KKK', M Sc Thesis, 199*, Dublin City University, Ireland

11 Kiernan P **'Oxygen Sensitivity of Ruthenium-Doped Sol-Gel-Derived Silica Films'**, M Sc Thesis, 1994, Dublin City University, Ireland

12 McDonagh C , MacCraith B D , McEvoy A K **'Tailoring of Sol-Gel Films for Optical Sensing of Oxygen in Gas and Aqueous Phase'**, Analytical Chemistry, 1998, Vol 70, No 1, pp 45-50

13 Lavin P **'Optimisation of Ormosil Thin Films for Sensor Applications'**, M Sc Thesis, 1997, Dublin City University, Ireland

14 Wolfbeis O S **'Fiber Optic Chemical Sensors and Biosensors'**, CRC Press, Boco Raton, FL, 1991, Vol 1

15 MacCraith B D , O'Keeffe G , McDonagh C , McEvoy A K **'LED-Based Fibre Optic Oxygen Sensors Using Sol-Gel Coating'**, Electronics Letters, 1994, Vol 30, No 11, pp 888-889

16 McEvoy A K , McDonagh C , MacCraith B D **'Dissolved Oxygen Sensor Based on Fluorescence Quenching of Oxygen-Sensitive Ruthenium Complexes Immobilised in Sol-Gel-Derived Porous Silica Coatings'**, Analyst, 1996, Vol 121, pp 785-788

17 Gouin J F , MacCraith B D , McEvoy A K , McDonagh C **'Humidity Insensitive Gas-Phase Optical Oxygen Sensor'**, Paper in preparation

Chapter 9 Development of SPR-Based Fibre Optic Biosensor

9.1 Introduction

The work presented in this chapter is unrelated to any work previously described in this thesis It was undertaken as part of a collaborative project between the schools of Physical, Chemical and Biological sciences at Dublin City University The aim of the project was to produce an optical-based biosensor that is capable of monitoring the 'real-time' interaction between biomolecules

Biomolecular interaction analysis describes the study of the interaction between a pair of biomolecules that express an affinity for each other The technique of biomolecular interaction may be used to detect for a target analyte, by incorporating a biomolecule that exhibits an affinity for it, into a sensor structure It can be also be used to determine the kinetics of how the two molecules interact

There currently exist a number of optical-based biosensing techniques The most common configurations typically employ either a grating coupler / waveguide configuration[1] that monitors the effective refractive index of a guided mode upon exposure to biomolecules, or a fluorescence-based waveguide device in which a target analyte-sensitive biomolecule is immobilised upon the waveguide surface[2,3] In the waveguide devices the guided mode evanescent field extends up to one wavelength into the medium above the waveguide surface The target molecule, which is labelled with a fluorophore, can specifically bind to the immobilised biomolecule and is effectively captured on the surface of the planar waveguide The labelled fluorophore is excited by the evanescent field of the guided mode and monitoring of the resultant fluorescence intensity allows for the determination of target analyte concentration and its affinity to the immobilised biomolecule Such a sensor device is indirect in nature in that it is not the target analyte that is being detected rather the attached fluorophore Also, such a configuration does not lend itself favourably to the real-time analysis of the biomolecular interaction, and hence a substantial amount of information such as binding mechanisms and association and dissociation rates of the target analyte and immobilised biomolecule can not be determined using this configuration

There exists an obvious need for a sensor capable of monitoring biomolecular interactions in 'real-time' Such a sensor would provide information on the target analyte concentration within the analysed sample However, in addition it could also provide a great deal of information about the actual interaction event such as the strength of the binding interactions, the binding mechanism and the speed with which affinity pairs bind and dissociate In a typical configuration, the 'real-time' biomolecular interaction analysis involves the immobilisation of one constituent of an affinity pair onto the sensor surface and continuous monitoring of surface mass changes upon exposure to a solution containing the other constituent[4] The majority of optical biosensors capable of 'real-time' biomolecular interaction analysis can be described as generic evanescent wave-based mass sensors whereby, an evanescent field of a guided mode probes refractive index changes within its penetration depth The changes in refractive index may then be related to mass changes, and the target analyte concentration determined

A common biosensing approach employing the evanescent wave technique is that of surface plasmon resonance (SPR) based sensors[5-7] The principle of SPR is outlined in more detail in section 9 2, however it will be briefly outlined here If a high refractive index medium (e g a glass slide) is surrounded a lower refractive index medium (e g aqueous sample), upon total internal reflection, the evanescent field of incident radiation extends a distance into the lower refractive index medium Let us now apply a thin (~50 nm) metal layer to the surface of the high refractive index layer At a specific angle of incidence, the evanescent wave can resonate with a surface plasmon[8] (i e free oscillating electrons) in the metal resulting in the transfer of energy This causes absorption of the light and a minimum in the intensity of the reflected light is observed The angular position of the resonance is sensitive to changes in the refractive index at the metal surface Hence, a plot of the resonance shift against time allows changes in the refractive index (as introduced by the increased mass near the sensor surface due to binding biomolecules) within the penetration depth of the evanescent field to be monitored This type of angular-dependent SPR is generated using monochromatic light, it is also possible to use polychromatic light and generate wavelength-dependent SPR

Currently there are several commercially available evanescent field-based SPR biosensors BIAcore AB (Uppsala, Sweden) are probably the industry leaders and have released a number of angular-dependent SPR-based biosensors (BIAcore 1000/2000/3000^{TM}) which are fully automated and consist of a disposable sensor chip, an optical detection unit, an integrated microfluidic cartridge, an autosampler, method programming and control software This configuration is capable of 'real-time' analysis and is widely employed in lab-based situations However, due to the large dimensions of the device, high cost (>£60,000), requirement for clean samples and the planar geometry of the sensor chip, it is not compatible with use in the field or in on-line configurations To this end BIAcore have also developed a wavelength-dependent SPR-based probe configuration that employs a polychromatic source with a gold-coated fibre optic configuration This arrangement enables dipstick-type analysis However, it is severely limited by non-'real-time' data acquisition and high cost (>£30,000) Therefore, there is an obvious need for a low cost dip-stick style sensor probe for on-line or field applications that is capable of accurately monitoring in 'real-time' biomolecular interactions

In this chapter, a polychromatic SPR-based fibre optic biosensor capable of monitoring in ‘real-time’ biomolecular interactions is presented The sensor is a low cost (<£5,000) yet sensitive device that is easy to fabricate Sensor construction, data processing and calibration techniques are presented As a proof of principle the sensor is then applied to the monitoring of the well-understood biomolecular interaction between protein A and its corresponding antibody rabbit IgG Finally, the device is then employed to rapidly determine red blood cell concentrations in solution All work reported in this chapter was carried out in collaboration with Dr John Quinn (School of Biological sciences) and Dr Shane O’Neill (School of Chemical Sciences), both of whom were postgraduate students at the time

9.2 Surface Plasmon Resonance

9.2.1 Angular-Dependent and Wavelength-Dependent Surface Plasmon Resonance

Surface plasmon resonance has its foundations in one of the basic principles of optics, that of total internal reflectance Consider two dielectric materials with refractive indices n_f and n_d respectively Total reflection of incident radiation occurs above a critical angle, theta, when $n_f > n_d$ At the same time, an evanescent electromagnetic wave propogates away from the interface Surface Plasmon Resonance (SPR) occurs when a thin conducting film is placed at the interface between the two optical media as shown in figure 9 1

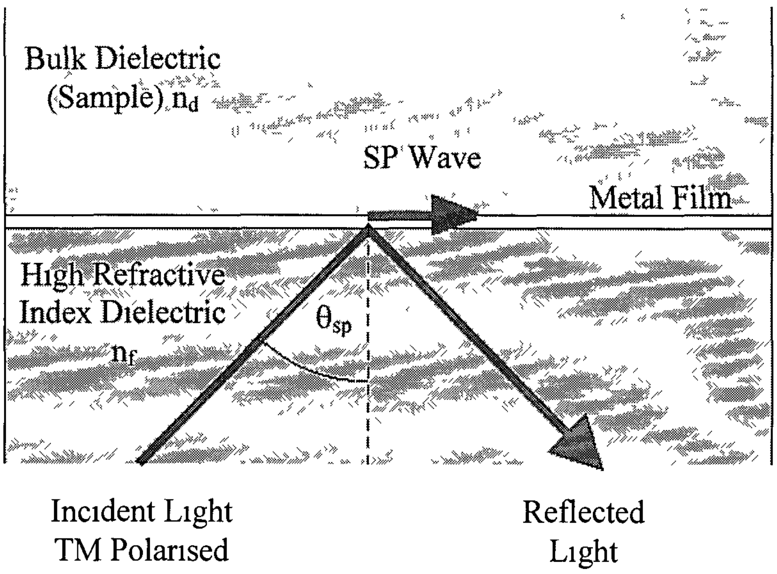

Figure 9.1 *Surface Plasmon Resonance*

At a specific incident angle, greater than the TIR angle, the surface plasmons (oscillating electrons at the edges of the metal) in the conducting film resonantly couple with the light because their frequencies match Since energy is absorbed in this resonance, the reflected intensity, I, shows a drop at the angle where SPR is occurring, as shown in the figure 9 2

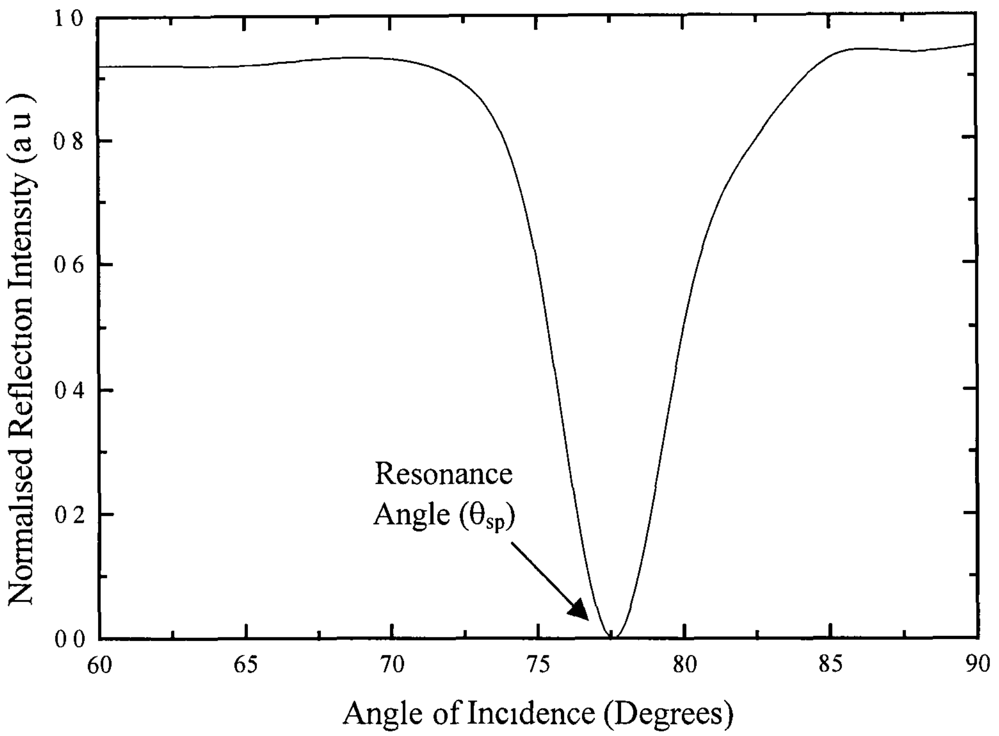

Figure 9.2 *Typical Theoretical Angular-Dependent SPR Spectrum*

Mathematically, the electric field of the surface plasmon wave propagating in the z-direction may be expressed as

$$E_x(x,z,t) = E_x^0(x)\exp(it\omega - ik_z z) \qquad [9\ 1]$$

where ω is the angular frequency and k_z is the SPR propagation constant along the z-direction which may be written as

$$k_z = k_z' + ik_z'' \qquad [9\ 2]$$

The SPR propagation constant depends on a number of parameters such as the free-space wavenumber (k_0), the complex permittivities of the metal and the dielectric (ε_m, ε_d), and may also be expressed as

$$k_z = k_0\left(\frac{\varepsilon_m \varepsilon_d}{\varepsilon_m + \varepsilon_d}\right)^{\frac{1}{2}} \qquad [9\ 3]$$

At the resonance angle θ_{sp}, the real component of the SPR propagation constant matches that of the incident beam along the z-direction, $k_0 n_f \sin\theta_{sp}$

$$k_z = k_0 n_f \sin\theta_{sp} \qquad [9\ 4]$$

where n_f is the refractive index of the high index medium Hence, it can be seen that these two equations describe fully how the phenomenon of surface plasmon resonance may be employed as a sensing mechanism The permittivity of the metal film and the refractive index of the high index medium are constant values, therefore, any change in the refractive index of the dielectric being sensed results in a shift in the angular resonance spectrum Therefore, by measuring SPR resonance parameters such as coupling angle, θ_{sp}, full width at half maximum, $\Delta\theta$, and the reflected light intensity, R_{min}) it is possible to determine the complex refractive index of the dielectric[9-11]

It is important to note that only TM polarised radiation contributes to the SPR effect This is due to this particular polarisation having an electric field oscillating in the plane normal to the plane that contains the metal film

It is also possible to generate surface plasmon resonance by combining polychromatic light and waveguides, such as optical fibres[12-14] The fibre optic accommodates multiple guided modes propagating at a range of angles wavelength If a part of the cladding of the fibre optic is removed and replaced with a thin metal film as shown in figure 9 3, then there are a range of wavelengths incident upon the core - metal film interface at a spread of angles The dielectric function (ε) of the metal is wavelength dependent, and hence for a given refractive index above the metal film, there exists a wavelength at which coupling between the incident light and surface plasmons can occur This manifests itself as a dip in the emerging wavelength spectrum at the specific resonance wavelength If the refractive index of the medium being sensed changes then so to does the wavelength at which resonance occurs Figure 9 4 shows a typical wavelength-dependent SPR spectrum

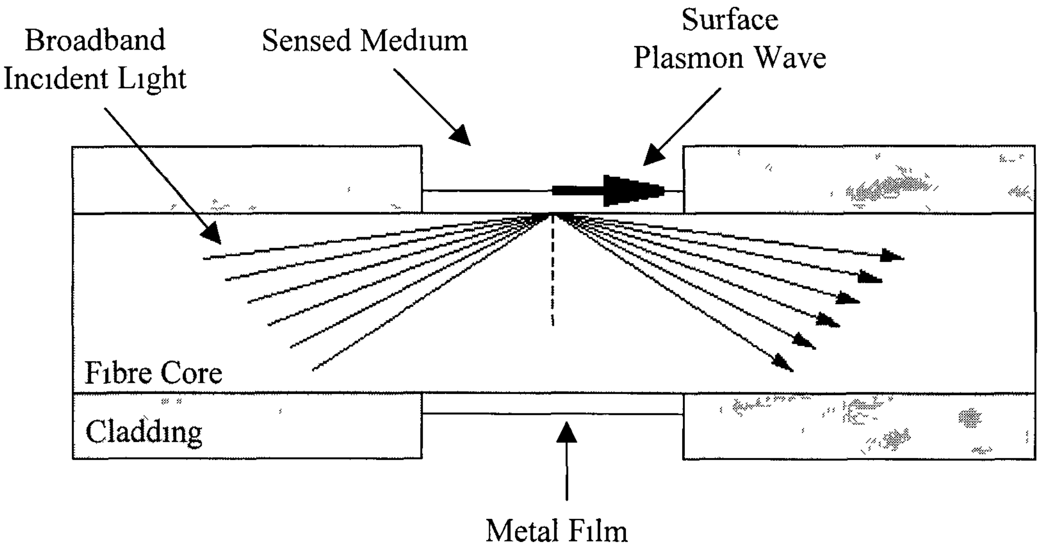

Figure 9.3 *Wavelength-Dependent SPR Configuration*

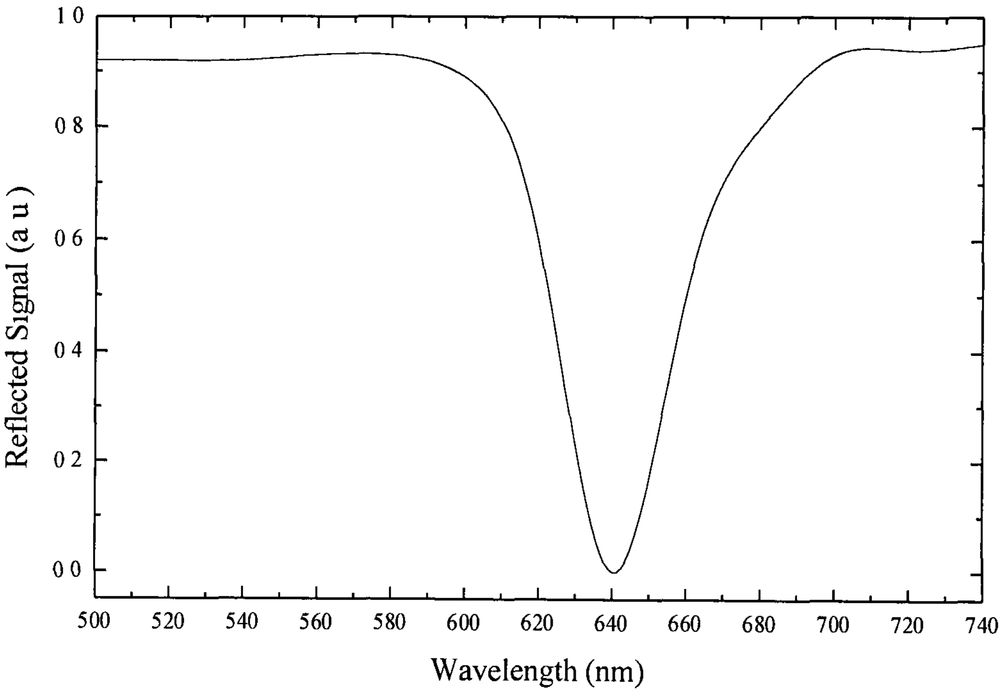

Figure 9.4 *Typical Wavelength-Dependent SPR Spectrum*

However, it should be noted that due to the nature of the broadband sources the systems cannot achieve better than 50 % attenuation since the white light used is usually unpolarised and the fibres used are large diameter fibres, which cannot maintain polarisation states

9.2.2 Choice of Metal Thin Film

In order for a metal to be applicable to surface plasmon resonance it must have conduction band electrons which are capable of resonating with radiation in the visible and near-infrared region of the spectrum[15] The main reason for this is the wide array of optical sources and detectors which function in this spectral range

There are a number of metallic elements that satisfy this initial requirement including gold, silver, gold, copper and aluminium In theory, it is possible to employ any of these metals in SPR applications However, in practise only gold or silver layers are utilised The main reason for this is the tendency of oxides and sulfide films to form on the surface of other elements which adversely affect SPR Another requirement demanded by SPR is that the metal must be compatible with the chemistries needed to perform assays Specifically, the chemical attachment of antibodies or other binding molecules to the metal surface must not impair the resonance

9.3 Fibre Optic-Based SPR Sensor

9.3.1 Sensor Construction and Operation

The main components of the sensor system are a tungsten halogen lamp (LS-1, 360 - 2000 nm), a fibre reflection probe (R200, 200 μm core), a miniature UV-VIS spectrometer (S2000), all of which were purchased from the same supplier (Ocean Optics, USA), an in-house fabricated fibre connector to couple from the fibre reflection probe to the CM5 probe, laptop computer and a gold-coated fibre optic probe (CM5

Probe, BIAcore, Sweden). The entire sensor device configuration is clearly illustrated in figure 9.5.

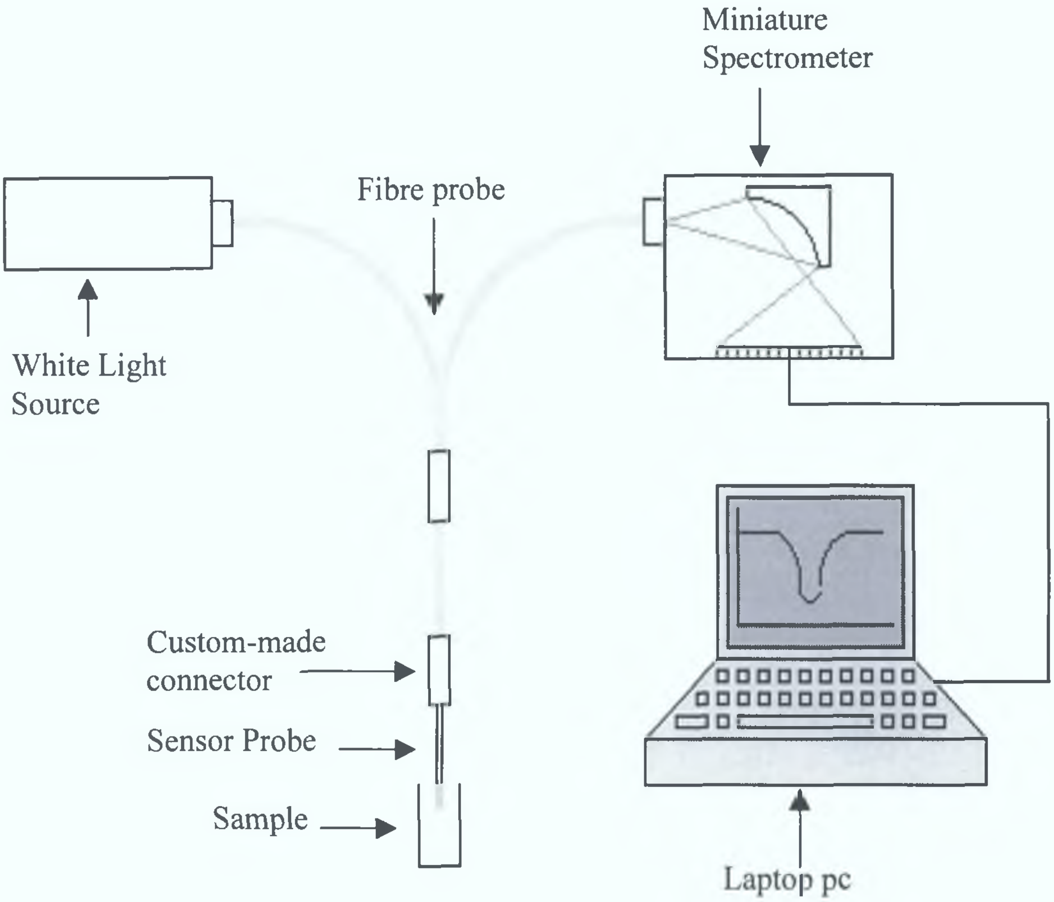

Figure 9.5 *Sensor configuration.*

White light from the tungsten halogen lamp is launched into the reflection probe and multiple modes propagate along the fibre probe. The propagating radiation is then coupled into the sensing element (CM5 Probe) which consisted of a gold-coated (1 cm in length, 50 nm thickness) optical fibre with a gold mirror deposited at the tip. A three-dimensional matrix (carboxymethylated dextran hydrogel) is deposited onto the gold surface by employing an alkanethiol self-assembled monolayer[16]. The purpose of this structure is to increase device sensitivity by facilitating the immobilisation of a large amount of biomolecules close to the metal film. Upon exposure to the other constituent of the biomolecular interaction there will be a large mass change close to the metal surface due to binding of the pair, which in turn leads to a refractive index change, which produces a shift in the SPR spectrum The sensing element is illustrated in figure 9 6 All interactions between evanescent fields and surface plasmons take place along the gold-coated sensing element and are performed at ambient temperatures and humidities The light is then reflected back along the probe via a mirror coated on the sensor element tip and the encoded signal is coupled to a miniature spectrometer A spectrum is generated and the resultant data is relayed to the laptop computer where a custom-written LabVIEW program finds the spectral shift of the reflectance minimum and generates a 'real-time' interaction curve

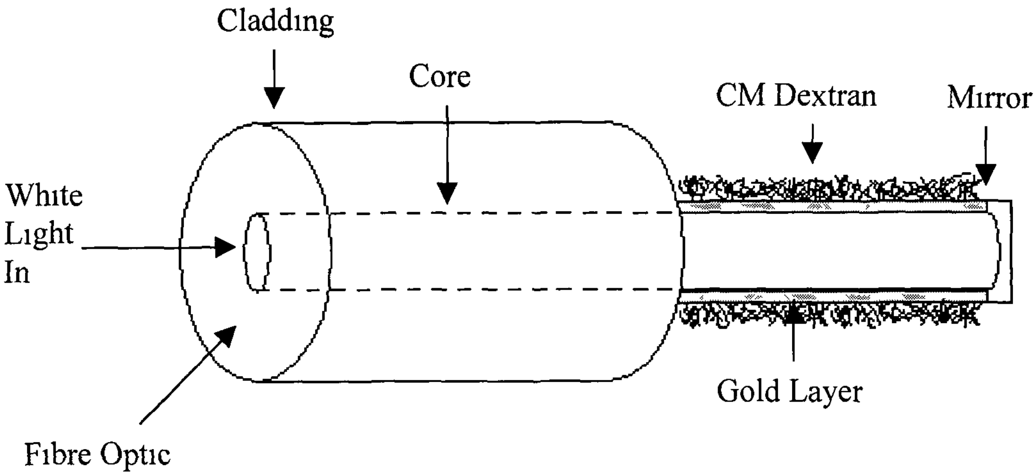

Figure 9.6 *Sensor element*

9.3.2 Data Acquisition, Processing and Display

A LabVIEW program consisting of a virtual control panel to allow user control is the method employed for data acquisition, processing and acquisition The program was written by Dr Shane O'Neill of the School of Chemical Sciences at Dublin City University Acquisition is performed using a National Instruments Daq – 700 PCMCIA I/O card

The output control panel is illustrated in figure 9 7 On the left hand side of the display are the experiment controls, which are used to define the polynomial order used in the data fitting routine, to save a reference spectrum and to save the actual resonance spectrum The right hand side of the panel contains four graphical displays, which are monitored throughout the experiment The graphical display marked 1 in the diagram is the intensity profile of the reflected light from the sensor device The observed dip in the signal is the SPR minimum Section 2 of the output display panel is the generated fitted resonance spectrum, which has been referenced against the absolute reflected intensity of the halogen light source in the absence of SPR Section 3 is a close up view of the resonance minimum, while section 4 is an example of a 'real-time' interaction curve In graphical display number 4 the x-axis is time in seconds while the y-axis is the position of the resonance minimum which will hereafter be referred to as response in arbitrary units (a u)

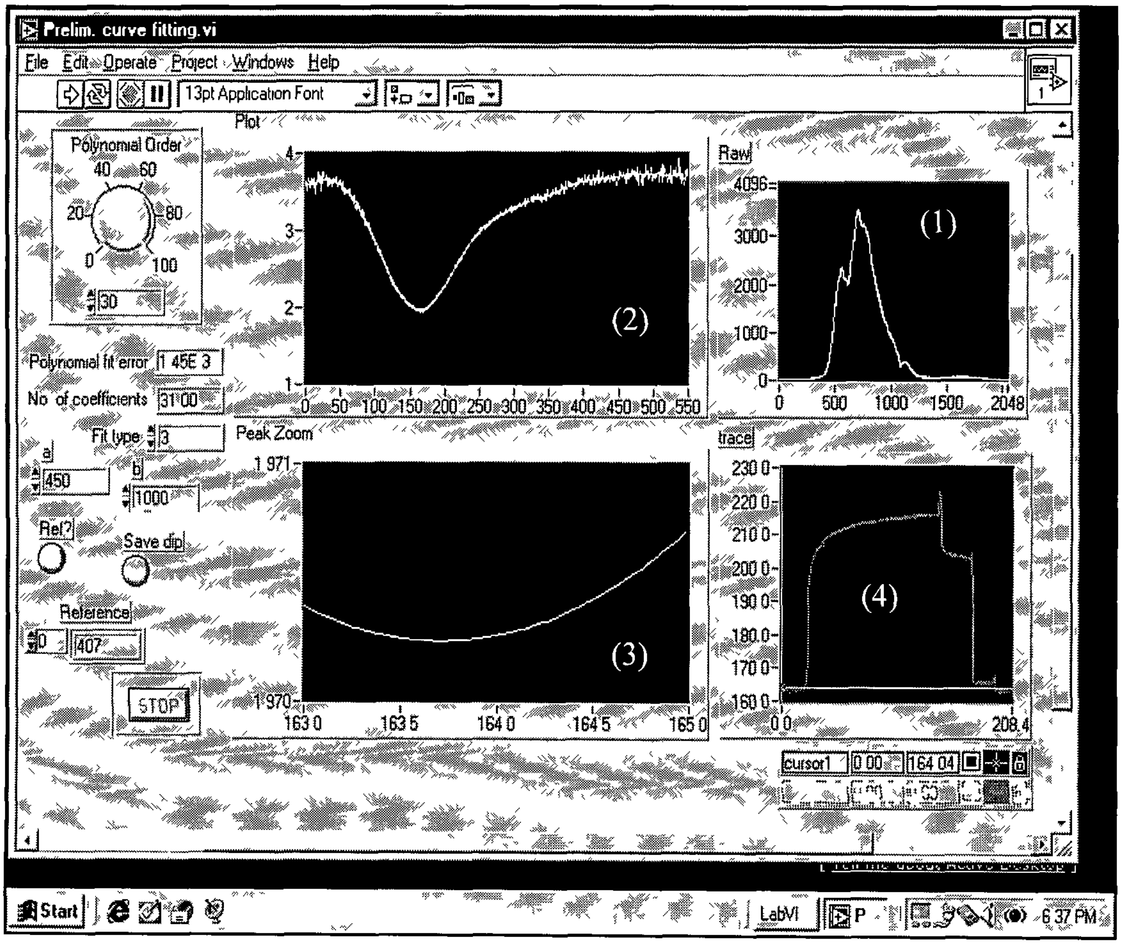

Polynomial Order 30

Polynomial fit error 1 45E 3

No of coefficients 31 00

Fit type 3

a 450

b 1000

Reference 0 407

cursor1 0 00 164 04

Figure 9.7 *LabVIEW virtual control panel and data display*

The resonance minimum as seen on the y-axis of display 4 was determined by fitting the spectrum with a 30th order polynomial and then using the Peak-Find algorithm supplied by LabVIEW This routine is performed every 0 4 seconds and thus a 'real-time' plot of the sensor response could be obtained and viewed on the display panel It was also possible to store the complete interaction curve as an ASCII file for analysis In addition, an option to save and store the resonance spectra at any point during the analysis was incorporated

9.4 Sensor Calibration

The sensing mechanism employed in this sensor is a wavelength shift in the resonance condition which is induced by a change in the refractive index surrounding the probe Therefore, prior to using this sensor configuration to detect for biological components it was necessary to calibrate the device response to different refractive indices The sensor probe was immersed in glycerol water solutions and the resultant shift of the resonance minima as a function of refractive index was measured The refractive indices of the calibration solutions were previously determined using an Abbe refractometer (Milton Roy Tabletop Refractometer 3L) and are presented in figure 9 8 This was then used to calibrate the fibre optic SPR sensor response

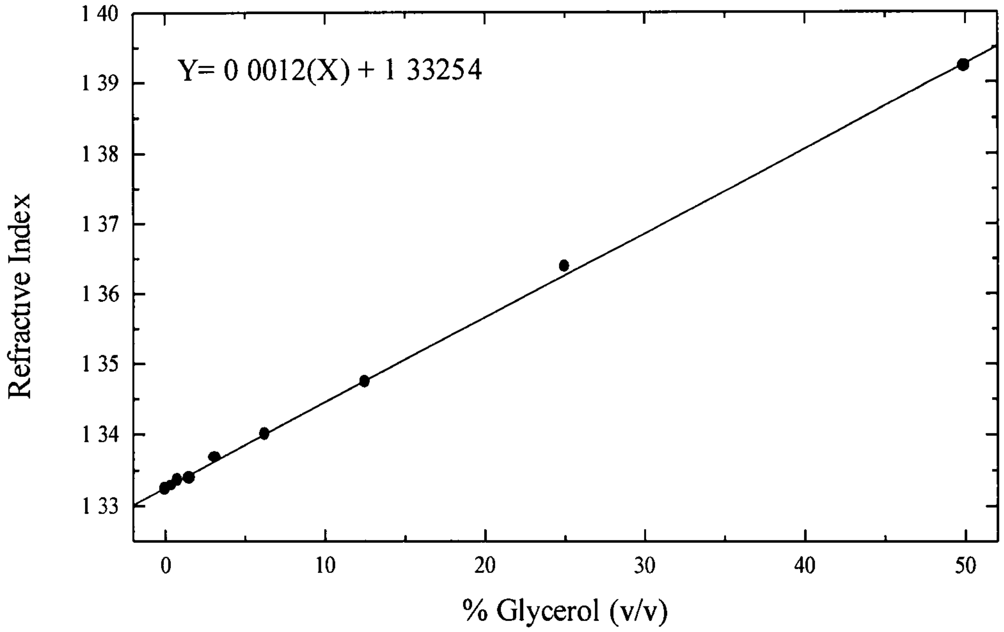

Figure 9.8 *Refractive index of glycerol water solutions*

Figure 9 9 shows the sensor response to glycerol water solutions with increasing glycerol concentrations from 5% to 50% in 5% increments The sensor element was immersed in the solutions for one minute at a time and the resulting resonance spectrum was recorded It can be seen that the resonance minimum shifts to higher wavelengths with increasing refractive index as predicted by theory

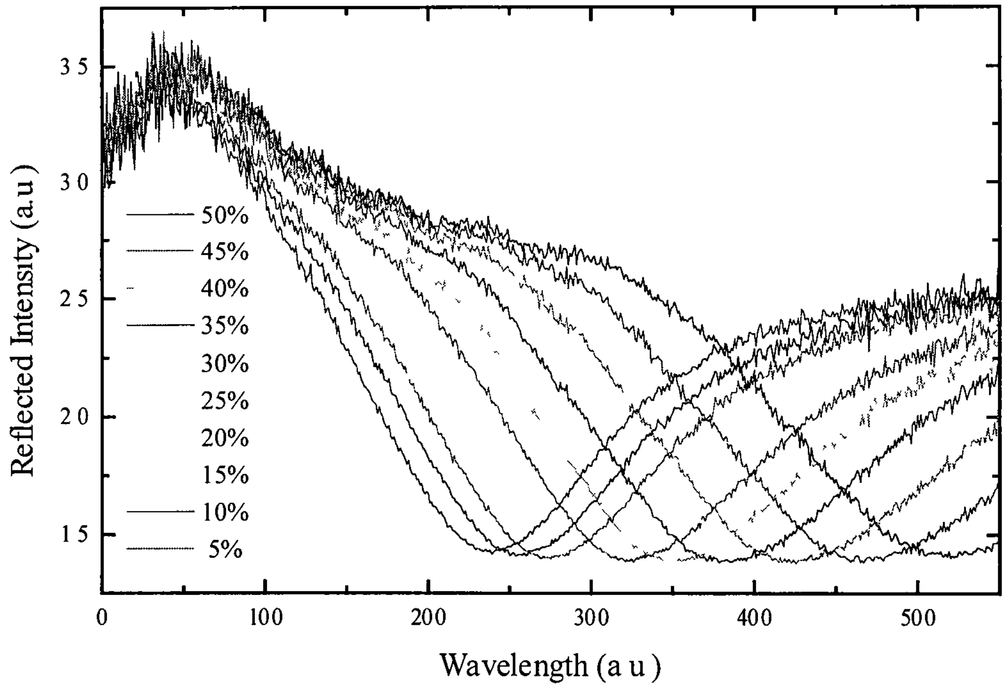

Figure 9.9 *Resonance spectra for glycerol water solutions ranging from 5% to 50% glycerol content*

The position of the resonance minima is related non-linearly to the refractive index of the glycerol water solutions and was determined by plotting the respective refractive indices against the shifts in the resonance minima obtained from the sensor device The resulting calibration curve is shown in figure 9 10 where it may be seen that the sensor response is non-linear and shows a slight increase in sensitivity at higher refractive indices The range of the sensor extends from a refractive index of 1 33 to 1 39 with a maximum achievable resolution of approximately 1 x 10^{-4} at the high sensitivity end

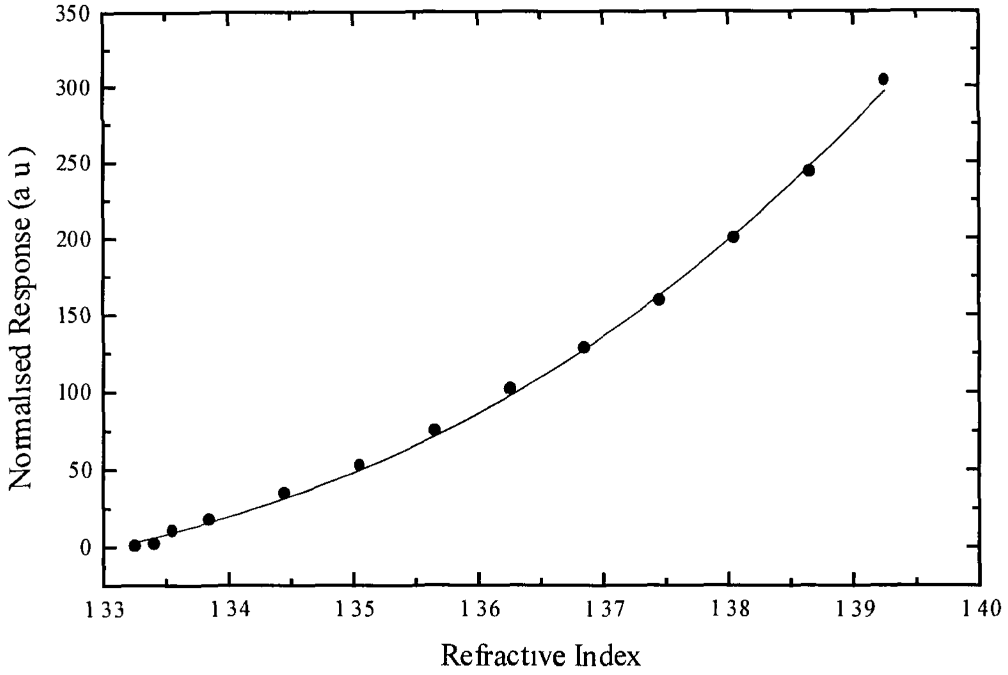

Figure 9.10 *Calibration curve of sensor response Vs refractive index*

9.5 Detection of Biomolecules

9.5.1 Introduction

Some of the most common biomolecular pairs that express an affinity for each other are proteins and antibodies A protein is very simply a collection of amino acids while antibodies are serum proteins produced by B-lymphocytes in response to a foreign substance (e g antigen) Antibodies may be raised to almost all classes of substances including, proteins, polysaccharides, nucleic acids and complex particles such as pollens, infectious agents and cells

When an antibody is raised to a specific antigen it exhibits a high level of attraction towards the antigen and likes to attach itself to the antigen One of the most widely understood antigen - antibody interactions is that of rabbit IgG antibody and protein A

The rabbit IgG is produced by extracting blood from a rabbit, which is then allowed to clot and the liquid serum remaining is removed. This serum contains the IgG antibody.

It is possible to employ the proposed SPR sensor device as an affinity-based sensor[17,18]. As a proof of principle for the proposed biosensor the interaction between these two biomolecules was analysed. The sensing arrangement is described in detail in the following section. However, a brief introduction to the principle of operation is also be presented here. Protein A is immobilised onto the hydrogel matrix at the probe surface. Upon introduction of a solution containing rabbit IgG binding occurs between the pair. The sensing mechanism is shown in figure 9.11a. The binding in the hydrogel matrix produces a mass change within the evanescent field of the sensor probe which manifests itself as a change ion the refractive index about the probes, which in turn leads to a shift in the wavelength position of the resonance condition. By monitoring the shift of resonance position on exposure to the antibody and the temporal profile, it is possible to extract information about the binding mechanism and antibody concentration.

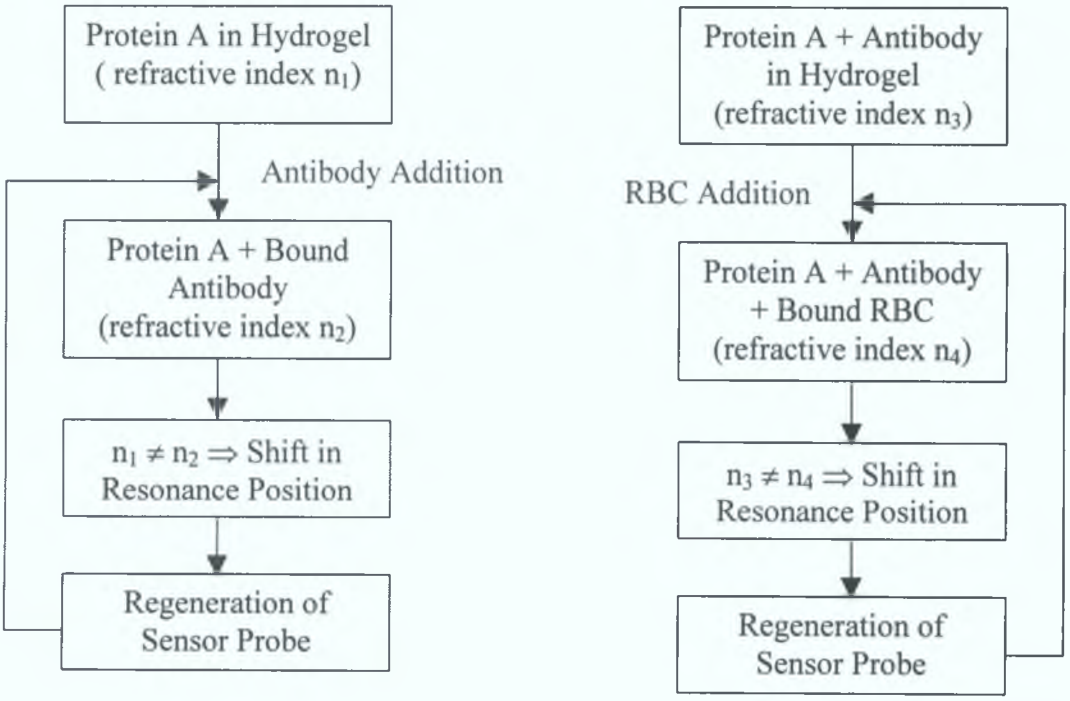

(a) (b)

Figure 9.11 *Detection Mechanism for (a) Antibody and (b) Red Blood Cells.*

The sensor was then applied to a realistic medical application, namely the determination of red blood cell (RBC) concentration in solution The principle of detection is similar to that employed for the determination of antibody concentration and is shown in figure 9 11b Protein A is immobilised on the sensor surface and a protein A-specific antibody is affinity captured This antibody, is not only specific to a single type of protein (A), but it is also exhibits an affinity with a single type of red blood cell (Group A) As a result, upon introduction of group A red blood cells in solution, there is binding between the Protein A - antibody structures and the blood cells Again, a mass change and hence a refractive index change near the probe surface is introduced which allows the target analyte concentration to be determined

9.5.2 Immobilisation of Protein A

The process of immobilising protein A on the hydrogel matrix is illustrated in figure 9 12 The sample was initially immersed in a phosphate buffered saline (PBS) solution, which provides for a neutral pH environment that does not destroy or degenerate the biomolecules The proteins in question are positively charged and hence in order for binding to occur, the hydrogel must be positively charged This was achieved by exposing it to an activation solution (1 1 mixture of 0 4 M N-ethyl-N'-(dimethylaminopropyl) carbodnmide (EDC) and 0 1 M N-hydroxysuccmimide (NHS) in ultrapure water for seven minutes) After hydrogel activation the probe was subsequently exposed to a protein A solution (50 µg/ml, in10 mM sodium acetate buffer, pH 4 3) for 11 minutes which allowed preconcentration of the positively charged protein onto the negative hydrogel This resulted in covalent coupling of the protein A to the activated surface The sensor was then immersed in PBS buffer for two minutes to remove any unbound proteins from the structure Upon removal of all unbound proteins it was necessary to block any free binding sites on the hydrogel to possible interferents by a process known as capping This is achieved by exposing the sensor probe to 1 M ethanolamine (pH8 5), which effectively neutralises the binding sites The sensor probe was then ready for use in the analysis of the biomolecular interaction between protein A and the protein A-specific antibody rabbit IgG

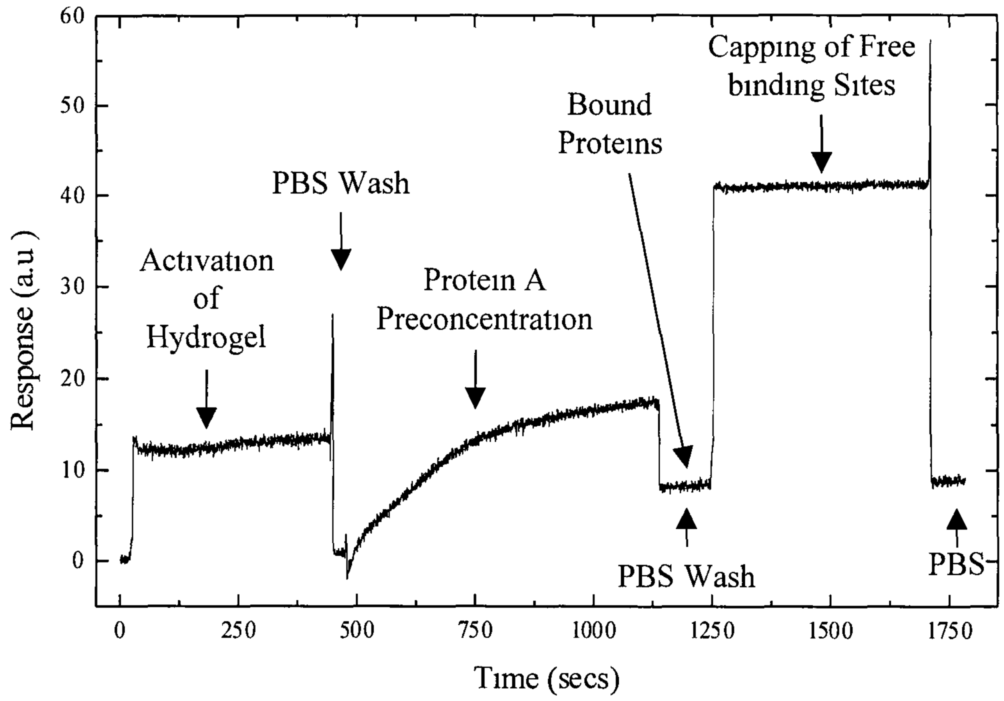

Figure 9.12 *Immobilisation of protein A onto hydrogel at sensor element surface*

9.5.3 Detection of Rabbit IgG Antibody

The protein A-coated sensing element was exposed to the varying concentrations of rabbit IgG antibody in PBS buffer solution for 2 minutes at room temperature, causing affinity binding of the respective biomolecules The interaction curves for a range of antibody concentrations are shown in figure 9 13 It can be seen that upon introduction of the antibody there is a significant shift in the surface plasmon resonance position (response) even for low concentration levels This shift is due to both bound and unbound antibody The absolute response due to bound antibody may be determined by a simple PBS exposure for thirty seconds to wash away any unbound antibody

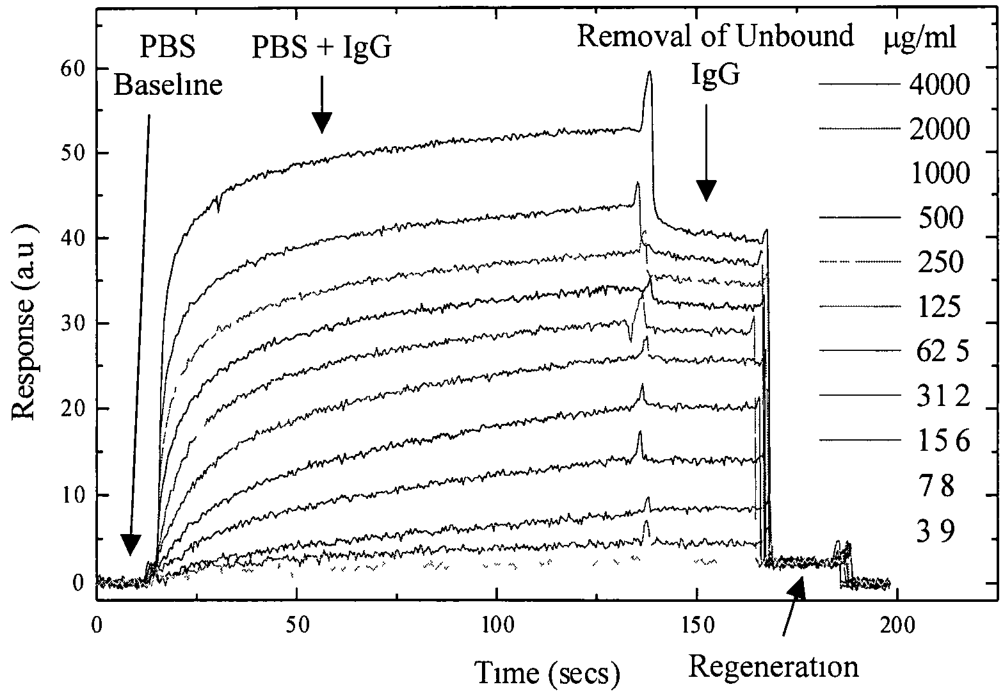

Figure 9.13 *Interaction curves for increasing concentrations of rabbit IgG antibody*

From the antibody binding response curves it was possible to construct a calibration curve as illustrated in figure 9 14 It can be seen that there is a sigmoidal shape to the data when antibody concentration is plotted on a log scale If we assume that the device response to low concentrations of rabbit IgG antibody is effectively linear, as shown in figure 9 15, then a limit of detection of 1 6 µg / ml for rabbit IgG can be deduced

Removal of bound antibody was achieved by exposing the probe to 20 mM HCl for thirty seconds and then to PBS It was observed that the sensor response returned to the initial baseline after each interaction, indicating complete removal of all bound antibody and therefore total regeneration of the surface This is an extremely desirable effect because it allows for repeated use of the same probe without degradation

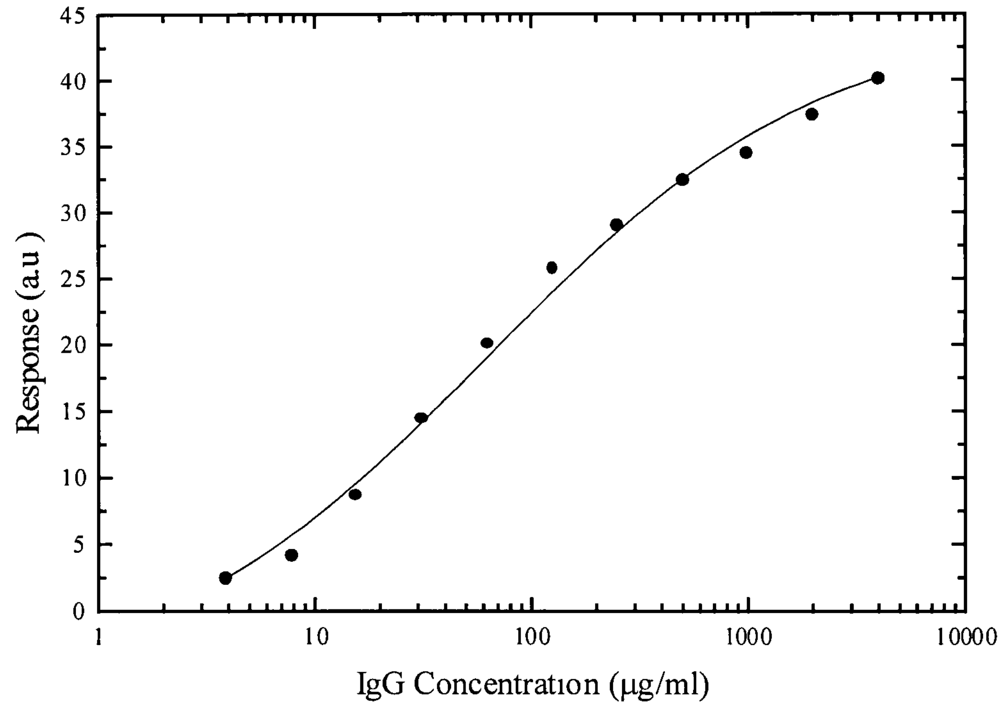

Figure 9.14 *Calibration curve for the interaction of rabbit IgG with a protein A*

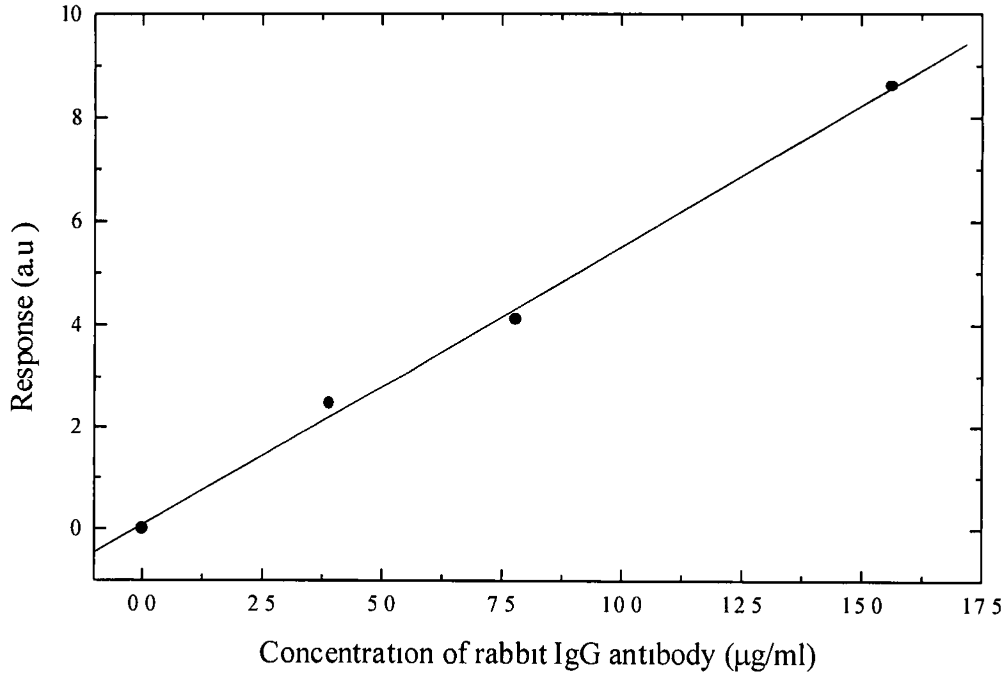

Figure 9.15 *Linear fit to calibration curve of low concentrations of rabbit IgG*

9.5.4 Detection of Red Blood Cells

Detection of group A red blood cell concentration was performed by covalently binding protein A to the sensor element as previously described An anti-A antibody (IgG_{2b}) which is specific only to protein A and group A RBC's was then bound to the protein by affinity-capture as per the mechanism described in the previous section Thus, the sensing probe consisted of a gold film with a hydrogel matrix upon which there were bound groups of protein A and anti-A antibody Upon exposure to type A RBC's in PBS solution, there is binding of the blood cells to the antibody which produces a localised change in the refractive index and thus a shift in the position of surface plasmon resonance A typical interaction curve for RBC detection is illustrated in figure 9 16

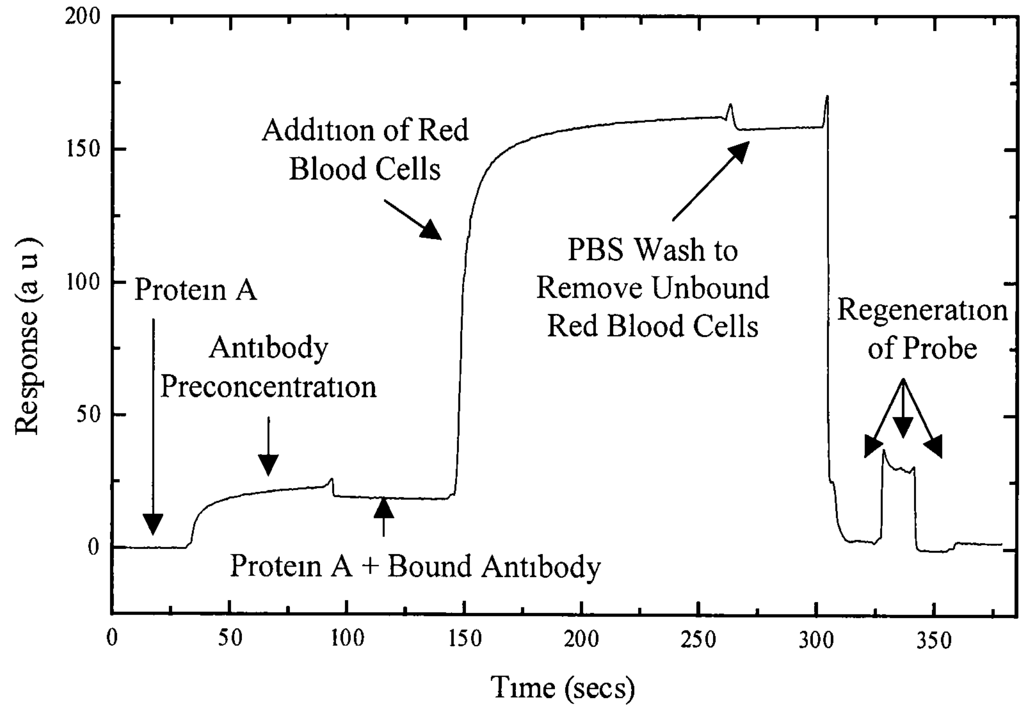

Figure 9.16 *Complete interaction curve for the detection of red blood cells*

It is possible to remove all bound antibody and red blood cells by exposing the probe sequentially to HCl, 0 1% Triton 100 in PBS, HCl and finally PBS This allows for complete regeneration of the sensor thus facilitating multiple use

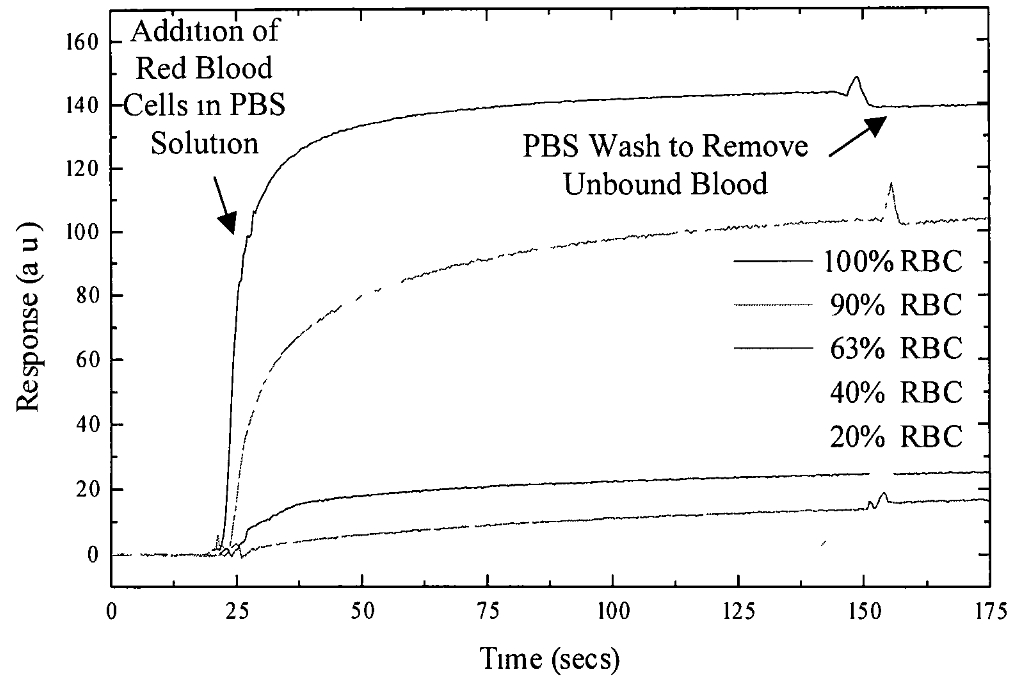

Figure 9.17 *Interaction curves for increasing red blood cell concentrations*

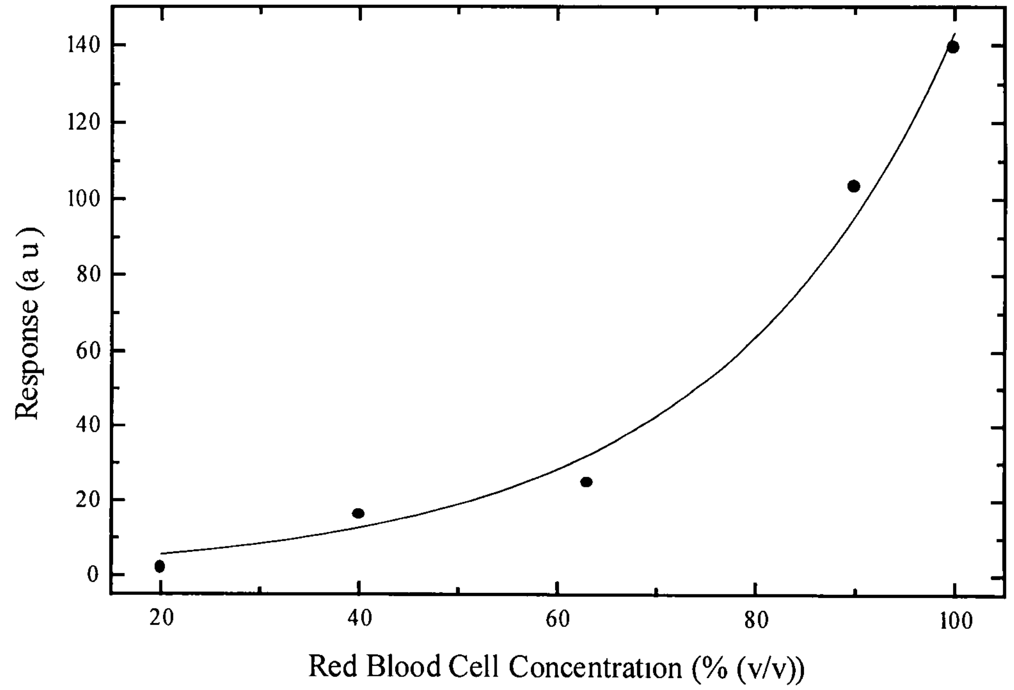

Figure 9.18 *Calibration curve for the detection of red blood cells*

Figure 9 17 shows the sensor response to a range of red blood cell concentrations in PBS It may be seen from this plot that the device exhibits higher sensitivity in the high concentration region From this data it is possible to construct a calibration curve as shown in figure 9 18 It can be seen that the relationship between device response and red blood cell concentration is approximately exponential in profile A limit of detection for red blood cell concentration in PBS solution of 4 5% (v/v) was determined

9.5.5 Non-Specific Binding

Non-specific binding of molecules to a functionalised biointerface is an undesireable process in biosensing and 'real-time' biomolecular interaction analysis of complex samples (e g serum, urine and milk) invariably suffer from non-specific binding Non-specific binding is the physisorption of sample components that do not possess specific interaction sites with the immobilised ligand and often results from an inherent hydrohobic or ionic character of the interfacial chemistry Generic transduction systems cannot discriminate between non-specifically adsorbed protein and specifically bound analyte Hence, the use of non-specific site blockers (e g bovine serum albumin), high ionic strength buffers, surfactants and spiking of samples with adsorbing molecules may be required

It was expected that there wouild be negligible non-specific binding in the sensor configuration presented here due to the high specificity of the components involved In order to determine the extent of non-specific binding of red blood cells to protein A which was not bound to red blood cell specific antibody, the protein A coated sensing element was exposed to 100 % (v/v) washed group A red blood cells for two minutes in the absence of anti-A IgG The interaction curve is illustrated in figure 9 19 It may be clearly seen from the graph that upon exposure to the red blood cells there is a change in the response of the device, due to bulk effects However, upon immersion in PBS buffer the response returns to the initial baseline Such observations indicate that the interaction of the group A red blood cells is highly specific, and they will bind only to anti-A materials and not to the immobilised protein A

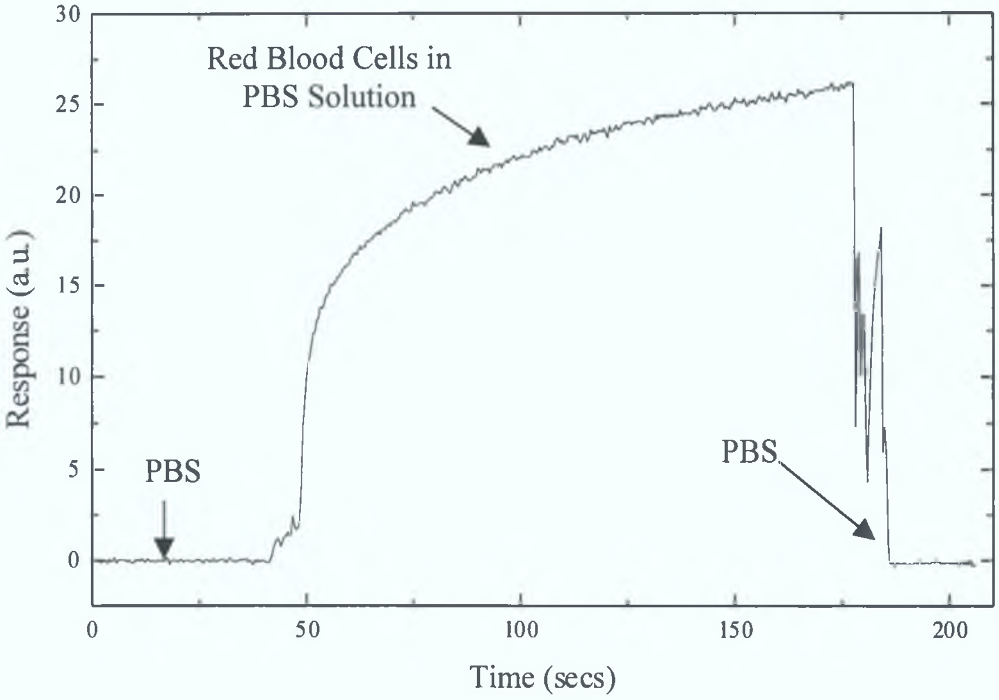

Figure 9.19 *Interaction curve of protein A and red blood cells in the absence of anti-A IgG.*

9.6 Conclusion

In this chapter a fibre optic-based SPR sensor capable of monitoring biomolecular interactions in 'real-time' was presented. The device, which is refractometric in nature, is low cost in nature, with all assembled components costing less than £5,000. This figure compares favourably with the cost of commercially available SPR probes (£30,000). However, the sensor configuration presented here has the added advantage of being able to monitor the interactions in 'real-time'. Thus, allowing for the analysis of the kinetics of interactions between biomolecules as well as target analyte concentration determination.

The sensor employs a gold-coated fibre optic probe into which white light is launched. Upon achievement of resonance conditions, energy is coupled into surface plasmons in the gold film and a dip in the reflected wavelength spectrum is observed The position of this dip exhibits a refractometric dependency and the device is capable of detecting refractive index changes of as low as 1 x 10^{-4}

As a proof of principle, the sensor was then successfully applied to the detection of both rabbit IgG antibody and group A red blood cells using a technique known as affinity capture The sensor was biologically engineered to be extremely target analyte-specific, with the result that the undesirable characteristic of non-specific binding of interferents to available sites was not observed

References

1 Nellen Ph M , Lukosz W **'Model Experiments with Integrated Optical Input Grating Couplers as Direct Immunosensors'**, Biosensors and Bioelectronics, 1991, Vol 6, pp 517-525

2 Zhou Y , Magill J , De La Rue R , Laybourn P **'Evanescent Fluorescence Immunoassays Performed with a Disposable Ion-Exchange Patterned Waveguide'**, Sensors and Actuators B, 1993, Vol 11, pp 245-250

3 Duveneck G , Pawlak M , Neuschafer D , Bar E , Budach W , Pieles U , Ehrat M **'Novel Bioaffinity Sensors for Trace Analysis Based on Luminescence Excitation by Planar Waveguides'**, Sensors and Actuators B, 1997, Vol 38-39, pp 88-95

4 Malmborg A-C , Michaelsson A , Ohlin M , Jansson B , Borrebaeck C A K **'Real-time Analysis of Antibody-Antigen Reaction Kinetics'**, Scandinavian Journal of Immunology, 1992, Vol 35, pp 643-650

5 Liedberg B , Nylander C , Lundstrom I **'Surface Plasmon Resonance for Gas Detection and Biosensing'**, Sensors and Actuators B, 1983, Vol 4, pp 299-304

6 Daniels P B , Deacon J K , Eddowes M J , Pedley D **'Surface Plasmon Resonance Applied to Immunosensing'**, Sensors and Actuators B, 1988, Vol 15, pp 11-17

7 Gent J , Lambreck P , Kreuwel H , Gerritsma G , Sudholter E , Reinhoudt D , Popma J L **'Optimisation of the Chemooptical Surface Plasmon Resonance Based Sensor'**, Applied Optics, 1990, Vol 29, pp 2843-2849

8 Raether H **'Surface Plasmons on Smooth and Rough Surfaces and on Gratings'**, 1988, Springer - Verlag, New York

9 Matsubaru K , Kawata S , Minami S **'Optical Chemical Sensor Based on Surface Plasmon Measurement'**, Applied Optics, 1988, Vol 27, pp 1160-1163

10 Kooyman R P H , Lenferink A T M , Eenink R G , Greve J **'Vibrating Mirror Surface Plasmon Resonance Immunosensor'**, Analytical Chemistry, 1991, Vol 63, pp 83-85

11 Yeatman E M **'Resolution and Sensitivity in Surface plasmon Microscopy and Sensing'**, Biosensors and Bioelectronics, 1996, Vol 33, No 6/7, pp 635-649

12 Ronot-Trioli C , Trouillet A , Veillas C , Gagnaire H **'Monochromatic Excitation of Surface plasmon Resonance in an Optical-Fibre refractive Index Sensor'**, Sensors and Actuators A, 1996, Vol 54, pp 589-593

13 Jorgenson R C , Yee S S **'A Fiber-Optic Chemical Sensor Based on Surface Plasmon Resonance'**, Sensors and Actuators B, 1993, Vol 12, pp 213-220

14 Jorgenson R C , Yee S S **'Control of the Dynamic Range and Sensitivity of a Surface Plasmon Resonance Based Fiber Optic Sensor'**, Sensors and Actuators A, 1994, Vol 43, pp 44-48

15 DeBrunn H E , Kooyman R P H , Greve J **'Choice of Metal and Wavelength for SPR Sensors: Some Considerations'**, Applied Optics, 1992, Vol 31, pp 440-442

16 Elender G , Kuhner M , Sackmann E **'Functionalisation of Si/SiO_2 and Glass Surfaces with Ultrathin Dextran Films and Deposition of Lipid Bilayers'**, Biosensors and Bioelectronics, 1996, Vol 11, No 6/7, pp 565-577

17 Fagerstam L G ,O'Shannessy D J **'Surface Plasmon resonance Detection in Affinity Technologies'**, Handbook of Affinity Chromatography, 1993, Vol 63, pp 229-252

18 Stenberg E , Persson B , Roos H , Urbaniczky C **'Quantitative Determination of Surface Concentration of Protein with Surface Plasmon Resonance using Radiolabeled Proteins'**, Journal of Colloid and Interface Science, 1991, Vol 143, No 2, pp 513-526

Chapter 10 Conclusion

The work presented in this thesis described the development of a number of evanescent wave-based sensor platforms for the detection of both chemical and biological target analytes The sensor platforms presented employed a range of sensing mechanisms such as analyte-sensitive absorption, fluorescence quenching and the refractometric technique of surface plasmon resonance

The sol-gel process, a simple and highly flexible process for the production of glassy materials, and the parameters that control the rates of the chemical reactions involved, were described It was illustrated how the sol-gel process may be employed to fabricate a wide range of glass components ranging from porous thin films, doped with an analyte-sensitive reagent for use as sensing layers, to integrated optic components such as planar waveguides and grating couplers, all of which may be incorporated into the platforms

Detailed theoretical analyses of the operation of planar waveguides and grating couplers were presented and the fabrication techniques employed to produce these components using sol-gel technology were then discussed The resultant integrated optic devices were then tested and characterised using a range of techniques, such as fourier transform infrared spectroscopy, atomic force, scanning tunnelling microscopy and diffraction studies and their physical and chemical characteristics were determined It was found that it was possible to fabricate high quality integrated optic components using low cost techniques such as dip coating and embossing The fabricated waveguides exhibited low losses and low surface roughness, while the embossed sol-gel-derived grating couplers closely matched the masters used to fabricate them and exhibited high coupling efficiencies despite the relatively simple technique employed for their fabrication

The fabricated grating coupler / planar waveguide platforms were then modelled using commercially available software The aim of which was to provide information on possible routes towards the optimisation of the grating coupling efficiency The software was used to monitor the effect of a wide range of system parameters, such as waveguide thickness, waveguide refractive index and grating groove depth upon the coupling efficiency of the grating coupler / planar waveguide structure

Two specific absorbance-based sensor platforms employing sol-gel technology, planar waveguides and grating couplers were proposed The first configuration employed a low-mode planar waveguide and a laser source The device was successfully applied to the detection of gaseous ammonia using a range of sensing layers However, due to the critical angular dependence of the resonance condition and the lack of mechanical stability of this device further development of this configuration was not continued A second platform was developed which had a relaxed resonance condition This configuration employed a multi-mode waveguide and focused LED light The device could simultaneously launch and support multiple guided modes and its generic nature was illustrated by the successful application to the detection of gaseous ammonia and carbon dioxide using a variety of sensing layers

A generic fluorescence-based sensor platform was also described The device employed the anisotropy of fluorescence emitted near an interface and the resultant evanescent capture of the emitted fluorescence by modes in a planar waveguide The device configuration and principle of operation were described and the effect of sensing layer properties on the device performance were discussed As a proof of principle the platform was applied to the detection of gaseous oxygen using an oxygen-sensitive fluorophore immobilised in a sol-gel-sensing layer It was seen that the device exhibited excellent response and reproducibility with a high signal to noise ratio despite the absence of optical filters

Finally, a sensor platform employing surface plasmon resonance and fibre optic technology was presented The theory of surface plasmon resonance (SPR) was discussed in detail, along with the factors governing the choice of metal layer A sensor probe configuration was presented and the principle of operation were described As a proof of principle the device was applied to the refractometric-based detection of a range of biological compounds

One possibility for future work involves identification of a new low temperature approach to the fabrication of sol-gel-derived planar waveguides A low temperature fabrication process would enable direct incorporation of the sensing reagent into the waveguide layer providing increased sensitivity due to increased interaction length and a simpler device configuration Possible approaches to such work could involve the use of photosensitive sol-gel materials which may be patterned by exposure to ultraviolet radiation, as was discussed in chapter 2

Similarly, work on improving the grating fabrication procedure needs to be investigated Direct writing of gratings into the waveguide core using the above-mentioned technique of photosensitive sol-gel materials should be investigated It is also necessary to investigate new improved grating embossing techniques for the production of grating couplers The use of chirped (aperiodic) grating couplers or diffractive optic elements (DOE's) to relax the resonance condition required to launch light into guided modes should also be addressed

There also exists the need for a detailed theoretical investigation of all sensor configurations This is necessary to optimise the geometry of the sensor platforms in order to enhance sensitivity and performance Application of each sensor platform to the detection of a wide range of target analytes would be advantageous since it could further prove the generic nature of the devices

Possible future work on the fluorescence-based sensor platform could involve modification of the device configuration so as to optimise fluorescence capture efficiency The application of the platform to the detection of a range of target analytes should also be addressed

An investigation into the cross sensitivity of each of the sensor devices presented in this thesis is also crucial The absorbance-based ammonia and carbon dioxide gas phase chemical sensors presented in this thesis employ pH-sensitive indicator dyes and as a result exhibit a certain amount of cross sensitivity to other gases which alter the pH of the indicator This cross sensitivity severely limits the possible applications of these sensors Therefore, the extent of the cross sensitivity must be determined by exposing each of the sensor devices and sensing layers to sample gases containing various levels of other acidic / basic gases This study would also be extremely beneficial in that it could provide information as to how overcome such a lack of device specificity The SPR-based biosensor presented in chapter 9 must also be further analysed for specificity This may be achieved by exposing the sensor probe to a range of biological entities which do not express an affinity with the bound biological reagent

Fouling of the devices due to chemical species absorbing on the sensing layer and also due to the evanescent field extending beyond the sensor layer into the surrounding media need to be investigated The former may be investigated by immersing the devices in a range of chemical environments and monitoring device performance upon exposure to the target analyte This study should provide information as to how to protect sensor devices from chemical fouling The latter type of fouling may be investigated by utilising guided modes with a range of penetration depths which are both confined to and extend beyond the sensing layer Device performance upon exposure to a known concentration of target analyte may then be used to determine the extent of fouling

The use of intensity referencing techniques must also be addressed In the current configurations there are no referencing mechanisms in operation This leads to degradation and uncertainty of device performance because fluctuations in the source intensity, for example, may manifest themselves as changes in device output There exists a range of referencing techniques which may be employed to counterbalance source fluctuations One of the easiest is to employ a beam-splitter to tap off a fraction of the incident radiation This signal may be then be used to remove source-based fluctuations in the sensor device output by employing a simple divider circuit In the case of the fluorescence-based systems, the use of fluorescence decay time instead of intensity overcomes many of these problems

Issues such as the thermal stability of the sensor devices have not been investigated in the course of the research presented in this thesis However, thermal stability is an extremely important for all sensor devices There is the need to measure the effect of temperature fluctuations on device performance Such a study is easily performed by mounting the sensor device upon a thermoelectric cooler (TEC) with thermistor-based temperature feedback to both control and alter the device temperature Analysis of the device properties for a range of thermal conditions would provide valuable information not only about the operating range for such sensors but also possible solutions to overcome thermal dependency

It is also necessary to investigate the effect of humidity upon device performance This study would require the use of an environmental chamber that can precisely control the relative humidity within the chamber The device response to a given gaseous concentration would then be determined for a range of humidities and correction factors may be used Again, such an investigation would be of crucial importance if commercialisation of such sensor devices is desired

List of Publications and Conference Presentations

Oral Presentations

1 **'Sol-gel based planar waveguide chemical sensors'**, Optical Engineering and Photonics Conference, 31st May 1996, Institute of Engineers of Ireland, Ballsbridge, Dublin 4

2 **'Planar Waveguide Sol-Gel Sensors'**, Institute of Physics Optical Group, 'Optical sensing and its applications', 13th Nov 1996, Dublin Institute of Technology, Kevin Street, Dublin 8

3 **'Sol-gel based chemical sensors'**, The Optical Engineering Society of Ireland, 'Lasers and Electro-optics '97', 6-7 June 1997, University College Galway, Co Galway

4 **'Fabrication of sol-gel based planar waveguide / grating coupler platforms for use as optical chemical sensors'**, Chemical, Biochemical and environmental fiber sensors IX, 16-18 June 1997, Munich, Germany

5 **'Optical waveguide chemical sensors using grating couplers'**, Conference on lasers and electro-optics (CLEO), 14-18 Sept 1998, Glasgow, Scotland

6 **'Sol-gel planar waveguide chemical sensors utilizing grating couplers'**, Chemical, Biochemical and environmental fiber sensors X, 02-05 Nov 1998, Boston, USA

7 **'Optical waveguide sensor system for oxygen and carbon dioxide in food packages'**, Chemical, Biochemical and environmental fiber sensors X, 02-05 Nov 1998, Boston, USA

Poster Presentations

1 **'Optical Waveguide Chemical Sensors Using Grating Coupling'**, Europt®ode IV, 29 March – 01 April 1998, Munster, Germany

Publications

1 **Doyle A**, MacCraith B D **'Fabrication of sol-gel based planar waveguide / grating coupler platforms for use as chemical sensors'**, SPIE Proceedings, Chemical, Biochemical, and Environmental Fiber Sensors IX, 1997, Vol 3105, pp 61-70

2 **Doyle A**, MacCraith B D **'Sol-gel planar waveguide chemical sensors utilizing grating couplers'**, SPIE Proceedings, Chemical, Biochemical, and Environmental Fiber Sensors X, 1998, Vol 3540, pp 136-145

3 Gouin J F, **Doyle A**, MacCraith B D **'Fluorescence capture by planar waveguides as platform for optical sensors'**, Electronics Letters, 1998, Vol 34, No 17, pp 1685-1686

4 Malms C, **Doyle A.**, MacCraith B D, Kvasnik F, Landl M, Simon P, Kalvoda L, Lukas R, Pufler K, Babusikalins I **'Personal Ammonia Sensor for Industrial Environments'**, J Environ Monit, 1999, Vol 1, pp 417-422

5 Quinn J G, O'Neill S, **Doyle A.**, McAtamney C, Diamond D, MacCraith B D, O'Kennedy R **'Development and Application of SPR-Based Biosensors for the Detection of Cell-ligand Interactions'**, Submitted to Applied Biochemistry

Appendix 1 Waveguide Theory

In wave optics, a mode may be characterised by its propagation constants, or more usually by its effective index n_{eff}. The plane wave propagation constant in the wave-normal direction is defined as k_0n_f, as shown in figure 1

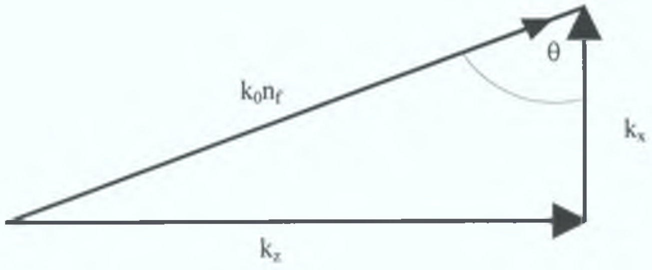

Figure 1 *Wave-vector diagram.*

where $k_0 = 2\pi/\lambda$ and λ is the light wavelength in free space. The relationship between the incident angle θ and the propagation constants along the x and z directions are

$$k_x = k_0 n_f \cos\theta \qquad [1]$$

$$k_z = k_0 n_f \sin\theta \qquad [2]$$

The effective index of a guided mode n_{eff} can be defined as

$$n_{eff} = n_f \sin\theta \qquad [3]$$

It follows that

$$k_z = k_0 n_{eff} \qquad [4]$$

The range of angles for guided modes is $\theta_c^s < \theta < 90°$, and this corresponds to an effective index range of $n_s < n_{eff} < n_f$.

Two of Maxwell's equations in isotropic, lossless dielectric medium are

$$\nabla \times \tilde{E} = -\mu_0 \frac{\partial \tilde{H}}{\partial t} \qquad [5]$$

and

$$\nabla \times \tilde{H} = \varepsilon_0 n^2 \frac{\partial \tilde{E}}{\partial t} \qquad [6]$$

where ε_0 and μ_0 are the dielectric permittivity and magnetic permeability of free space, respectively, and n is the refractive index In the orthogonal co-ordinate system (x, y, z), suppose that the plane wave propagates along the z direction with the propagation constant k_z The electromagnetic fields vary as

$$\tilde{E} = E(x,y)\ e^{j(\omega t - k_z z)} \qquad [7]$$

$$\tilde{H} = H(x,y)\ e^{j(\omega t - k_z z)} \qquad [8]$$

where the angular frequency $\omega = 2\pi c/\lambda$, and c is the light velocity in free space ($c = 1/\sqrt{(\varepsilon_0\mu_0)}$) In the step-index 2-D waveguide in figure 1, the electromagnetic fields are independent of y, Accordingly, since $\partial/\partial t = j\omega$, $\partial/\partial z = -jk_z$ and $\partial/\partial y = 0$, equations 5 and 6 yield two different modes with mutually orthogonal polarisation states One is the transverse electric (TE) mode, which consists of the field components E_y, H_x, and H_z The other is the transverse magnetic (TM) mode, which has components E_x, H_y, and E_z The field solutions and the boundary conditions at the interfaces $x = -d/2$ and $x = d/2$ lead to eigenvalue equations that determine the propagation characteristics of the TE and TM modes In this chapter only the transverse electric waveguide modes will be discussed in detail

For TE modes we use Maxwell's equation 5 to obtain an expression for the guidance condition

$$\nabla \times \tilde{E} = -\mu \frac{\partial \tilde{H}}{\partial t} = -\omega j \mu \, \tilde{H} \qquad [9]$$

The curl of the field can be expressed as

$$\left(\vec{\nabla} \times \vec{E}\right)_x = \left(\frac{\partial E_z}{\partial y} - \frac{\partial E_y}{\partial z}\right) \qquad [10]$$

$$\left(\vec{\nabla} \times \vec{E}\right)_y = \left(\frac{\partial E_x}{\partial z} - \frac{\partial E_z}{\partial x}\right) \qquad [11]$$

$$\left(\vec{\nabla} \times \vec{E}\right)_z = \left(\frac{\partial E_y}{\partial x} - \frac{\partial E_x}{\partial y}\right) \qquad [12]$$

However, since the electromagnetic fields are independent of y, equations 10 - 12 become

$$\left(\vec{\nabla} \times \vec{E}\right)_x = \left(-\frac{\partial E_y}{\partial z}\right) \qquad [13]$$

$$\left(\vec{\nabla} \times \vec{E}\right)_y = \left(\frac{\partial E_x}{\partial z} - \frac{\partial E_z}{\partial x}\right) \qquad [14]$$

$$\left(\vec{\nabla} \times \vec{E}\right)_z = \left(\frac{\partial E_y}{\partial x}\right) \qquad [15]$$

These equations can be further simplified because we know that for TE modes $E_z = 0$ and $\partial/\partial z = -jk_z$ Therefore equations 13 - 15 become

$$\left(\vec{\nabla}\times\vec{E}\right)_x = \left(jk_z E_y\right) \qquad [16]$$

$$\left(\vec{\nabla}\times\vec{E}\right)_y = \left(-jk_z E_x\right) \qquad [17]$$

$$\left(\vec{\nabla}\times\vec{E}\right)_z = \left(\frac{\partial E_y}{\partial x}\right) \qquad [18]$$

However, in equation 9 we have already that

$$\nabla\times\tilde{E} = -\mu\frac{\partial\tilde{H}}{\partial t} = -\omega j\mu\,\tilde{H} \qquad [19]$$

We can therefore equate the x, y and z components to their counterparts in equations 16 - 18 giving

$$jk_z E_y = -\mu j\omega H_x \qquad [20]$$

$$-jk_z E_x = -\mu j\omega H_y \qquad [21]$$

$$\frac{\partial E_y}{\partial x} = -\mu j\omega H_z \qquad [22]$$

Equation 22 implies that the tangential component of H may be obtained directly from the equation below,

$$H_z(x,z) = \frac{j}{\omega\mu}\frac{\partial}{\partial x}E_y(x,z) \qquad [23]$$

We now assume that the field distribution for TE modes decays exponentially in both the cover and substrate regions, and is oscillatory in the waveguide film region The fields are of the form

$$E_y(x,z)=E_c e^{-\alpha_c x}e^{-jk_z z} \qquad \text{- Cover} \qquad [24]$$

$$E_y(x,z)=E_f\cos(k_x x+\psi)e^{-jk_z z} \qquad \text{- Film} \qquad [25]$$

$$E_y(x,z)=E_s e^{-\alpha_s x}e^{-jk_z z} \qquad \text{- Substrate} \qquad [26]$$

where the transverse wavenumbers are defined by the appropriate dispersion relation in each region

$$\alpha_c=\sqrt{k_z^2-\omega^2\mu_c\varepsilon_c} \qquad [27]$$

$$\alpha_s=\sqrt{k_z^2-\omega^2\mu_s\varepsilon_s} \qquad [28]$$

$$k_x=\sqrt{\omega^2\mu_f\varepsilon_f-k_z^2} \qquad [29]$$

The constant ψ present in the field description for the waveguide film region represents the asymmetry of the structure Its relationship to the amplitude coefficients E_c, E_f and E_s is to be determined from the requirement of continuity of tangential **E** and **H** at $x = \pm d/2$

Equations 23 – 26 yield

$$H_z(x,z)=\frac{-j\alpha_c}{\omega\mu_c}E_c e^{-\alpha_c x}e^{-jk_z z} \qquad x>d/2 \qquad [30]$$

$$H_z(x,z)=\frac{-jk_x}{\omega\mu_f}E_f\sin(k_x x+\psi)e^{-jk_z z} \qquad |x|\le d/2 \qquad [31]$$

$$H_z(x,z) = \frac{j\alpha_s}{\omega\mu_s} E_s e^{-\alpha_s x} e^{-jk_z z} \qquad x < -d/2 \qquad [32]$$

Applying boundary conditions at x = d/2 (E_y, H_y (cover) = E_y, H_y (guide))yields

$$E_c e^{-\alpha_c (d/2)} = E_f \cos(k_x (d/2) + \psi) \qquad [33]$$

$$E_c e^{-\alpha_c (d/2)} = \frac{\mu_c k_x}{\mu_f \alpha_c} E_f \sin(k_x (d/2) + \psi) \qquad [34]$$

As the left-hand sides of these two equations are equal, we can equate the right hand sides as follows

$$\cos(k_x (d/2) + \psi) = \frac{\mu_c k_x}{\mu_f \alpha_c} \sin(k_x (d/2) + \psi) \qquad [35]$$

By manipulating this equation, one obtains the following equation

$$\tan(k_x (d/2) + \psi) = \frac{\mu_f \alpha_c}{\mu_c k_x} \qquad [36]$$

Applying boundary conditions at x = - d/2 yields

$$E_s e^{-\alpha_s (d/2)} = E_f \cos(-k_x (d/2) + \psi) \qquad [37]$$

$$E_s e^{-\alpha_s (d/2)} = \frac{-\mu_s k_x}{\mu_f \alpha_s} E_f \sin(-k_x (d/2) + \psi) \qquad [38]$$

We now equate equations 37 and 38 yielding

$$\cos(-k_x (d/2) + \psi) = \frac{-\mu_s k_x}{\mu_f \alpha_s} \sin(-k_x (d/2) + \psi) \qquad [39]$$

Further development of equation 39 gives

$$\tan\left(-k_x(d/2)+\psi\right)=\frac{-\mu_f\alpha_s}{\mu_s k_x} \qquad [40]$$

but we know that tan(-A) = -tan(A) Thus,

$$\tan\left(-k_x(d/2)+\psi\right)=-\tan\left(k_x(d/2)-\psi\right) \qquad [41]$$

and hence

$$\tan\left(k_x(d/2)-\psi\right)=\frac{\mu_f\alpha_s}{\mu_s k_x} \qquad [42]$$

Recall that tan(A) = tan(A ± nπ) where n is an integer Therefore, equations 36 and 42 can be rewritten as

$$\tan\left(k_x(d/2)+\psi \pm n\pi\right)=\frac{\mu_f\alpha_c}{\mu_c k_x} \qquad [43]$$

and

$$\tan\left(k_x(d/2)-\psi \pm m\pi\right)=\frac{\mu_f\alpha_s}{\mu_s k_x} \qquad [44]$$

By taking the inverse tan of both sides of equations 43 and 44 we obtain the following equations

$$k_x(d/2)+\psi=\tan^{-1}\left(\frac{\mu_f\alpha_c}{\mu_c k_x}\right)\mp n\pi \qquad [45]$$

and

$$k_x(d/2)-\psi=\tan^{-1}\left(\frac{\mu_f\alpha_s}{\mu_c k_x}\right)\mp m\pi \qquad [46]$$

Let us now define two components φ_c^{TE} and φ_s^{TE} as follows

$$\varphi_c^{TE}=2\tan^{-1}\left(\frac{\mu_f\alpha_c}{\mu_c k_x}\right) \qquad [47]$$

$$\varphi_s^{TE}=2\tan^{-1}\left(\frac{\mu_f\alpha_s}{\mu_s k_x}\right) \qquad [48]$$

The components φ_c^{TE} and φ_s^{TE} represent the phase shifts resulting from total internal reflection at the waveguide interfaces with both the cover and substrate regions We can use these components to write equations 45 and 46 in the form shown below

$$k_x(d/2)+\psi=\frac{1}{2}\varphi_c^{TE}\mp n\pi \qquad [49]$$

and

$$k_x(d/2)-\psi=\frac{1}{2}\varphi_s^{TE}\mp m\pi \qquad [50]$$

Treating these two equations as simultaneous equations and adding to eliminate ψ yields

$$2k_x d-\varphi_c^{TE}-\varphi_s^{TE}=2p\pi \qquad p=0,1, \qquad [51]$$

Equation 51 is the most general guidance condition for the TE modes of a slab waveguide and we will now attempt to further simplify We can then use the equation to obtain all the propagation characteristics of any specific mode supported by the waveguide

By direct substitution for k_x, φ_c^{TE}, φ_s^{TE}, α_c, and α_s one can rewrite the guidance condition in the form shown in equation 52

$$d\sqrt{\omega^2\mu_f\varepsilon_f - k_z^2} = p\pi + \tan^{-1}\left(\frac{\mu_f\sqrt{k_z^2-\omega^2\mu_c\varepsilon_c}}{\mu_c\sqrt{\omega^2\mu_f\varepsilon_f-k_z^2}}\right) + \tan^{-1}\left(\frac{\mu_f\sqrt{k_z^2-\omega^2\mu_s\varepsilon_s}}{\mu_s\sqrt{\omega^2\mu_f\varepsilon_f-k_z^2}}\right) \qquad [52]$$

but we also know that the wavevector in the z direction $k_z = \omega(\mu\varepsilon_{eff})^{1/2}$ Hence equation can be further simplified to the equation below

$$d\sqrt{\omega^2\mu_f\varepsilon_f - \omega^2\mu_f\varepsilon_{eff}} = p\pi + \tan^{-1}\left(\frac{\mu_f\sqrt{\omega^2\mu_f\varepsilon_{eff}-\omega^2\mu_c\varepsilon_c}}{\mu_c\sqrt{\omega^2\mu_f\varepsilon_f-\omega^2\mu_f\varepsilon_{eff}}}\right) + \tan^{-1}\left(\frac{\mu_f\sqrt{\omega^2\mu_f\varepsilon_{eff}-\omega^2\mu_s\varepsilon_s}}{\mu_s\sqrt{\omega^2\mu_f\varepsilon_f-\omega^2\mu_f\varepsilon_{eff}}}\right) \qquad [53]$$

We now make the valid assumption that all three regions are magnetically equivalent and therefore we can assume that all permeabilities are the same $\mu_c = \mu_f = \mu_s = \mu$ Therefore, equation 53 now becomes

$$d\omega\sqrt{\mu}\sqrt{\varepsilon_f - \varepsilon_{eff}} = p\pi + \tan^{-1}\left(\sqrt{\frac{\varepsilon_{eff}-\varepsilon_c}{\varepsilon_f-\varepsilon_{eff}}}\right) + \tan^{-1}\left(\sqrt{\frac{\varepsilon_{eff}-\varepsilon_s}{\varepsilon_f-\varepsilon_{eff}}}\right) \qquad [54]$$

Let us now define a parameter b, which is known as the normalised waveguide index

$$b = \frac{\varepsilon_{eff}-\varepsilon_s}{\varepsilon_f-\varepsilon_s} \qquad [55]$$

By manipulating equation 55 we find that

$$\frac{b}{1-b} = \frac{\varepsilon_{eff}-\varepsilon_s}{\varepsilon_f-\varepsilon_{eff}} \qquad [56]$$

and equation 3 56 can now be expressed as

$$d\omega\sqrt{\mu}\sqrt{\varepsilon_f - \varepsilon_{eff}} = p\pi + \tan^{-1}\left(\sqrt{\frac{\varepsilon_{eff} - \varepsilon_c}{\varepsilon_f - \varepsilon_{eff}}}\right) + \tan^{-1}\left(\sqrt{\frac{b}{1-b}}\right) \qquad [57]$$

We now also define a parameter a^{TE} that is a measure of the asymmetry of the waveguide (in this case of TE modes)

$$a^{TE} = \frac{\varepsilon_s - \varepsilon_c}{\varepsilon_f - \varepsilon_s} \qquad [58]$$

By combining 55 and 58 one finds that

$$\frac{b + a^{TE}}{1-b} = \frac{\varepsilon_{eff} - \varepsilon_c}{\varepsilon_f - \varepsilon_{eff}} \qquad [59]$$

Therefore equation 57 becomes

$$d\omega\sqrt{\mu}\sqrt{\varepsilon_f - \varepsilon_{eff}} = p\pi + \tan^{-1}\left(\sqrt{\frac{b + a^{TE}}{1-b}}\right) + \tan^{-1}\left(\sqrt{\frac{b}{1-b}}\right) \qquad [60]$$

Finally, we define a normalised frequency parameter V (the V number), which is a measure of how many modes a waveguide may support

$$V = k_0 d\sqrt{\frac{\varepsilon_f - \varepsilon_s}{\varepsilon_0}} \qquad [61]$$

We also know that $k_0 = \omega(\mu\varepsilon_0)^{1/2}$, and thus can write V in the form

$$V = d\omega\sqrt{\mu}\sqrt{\varepsilon_f - \varepsilon_s} \qquad [62]$$

Hence we find that

$$V\sqrt{1-b} = d\omega\sqrt{\mu}\sqrt{\varepsilon_f - \varepsilon_{eff}} \qquad [63]$$

Therefore, the guidance condition for TE modes in an asymmetric slab waveguide becomes

$$V\sqrt{1-b} = p\pi + \tan^{-1}\left(\sqrt{\frac{b+a^{TE}}{1-b}}\right) + \tan^{-1}\left(\sqrt{\frac{b}{1-b}}\right) \qquad [64]$$

Appendix 2 Ellipsometry

Ellipsometry is an optical technique routinely employed to determine the thickness of a film The technique involves measurement of the change of polarisation of an incident collimated beam of monochromatic light of known, controllable polarisation when it is obliquely reflected from a film surface

The state of polarisation of the incident and reflected beam may be described by the relative amplitude (amplitude ratio) and by the relative phase (phase difference) of their two orthogonal linearly-polarised components (p and s components) When the incident beam of monochromatic polarised light is reflected from the film surface, a change in the relative phases and the relative amplitudes of the p and s components will generally occur These changes determine two angles, Δ and Ψ which are related by

$$\rho = \tan\Psi a^{i\Delta} \qquad [1]$$

Where ρ is the ratio of the complex reflection coefficients r_p and r_s Ψ may have any angle between 0° and 90°, and Δ may have any angle between 0° and 360° The angles Δ and Ψ determine the thickness and refractive index of the sample

A typical ellipsometric configuration is illustrated in figure 1 The main components are a laser, polariser, analyser, compensator and detector In a typical measurement the incident-beam and reflected-beam are set at some desired angle of incidence with respect to the sample The polariser and analyser are alternately rotated until the intensity of the reflected beam is reduced to a minimum At this null condition the angles of the polariser and analyser are determined and converted by means of known equations into the polarisation parameters Δ and Ψ For a transparent film on a reflecting substrate, Δ and Ψ are functions of the angle of incidence, the wavelength of light, the refractive index of the ambient medium, substrate refractive index, sample thickness and sample refractive index Most of these parameters are known, and therefore software within the ellipsometer can determine sample thickness and refractive index

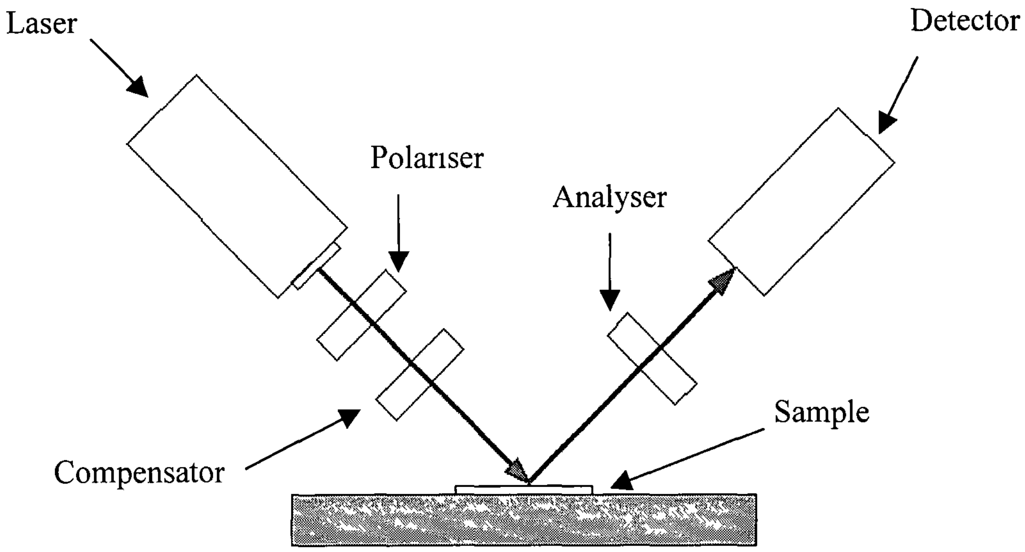

Figure 1 *Ellipsometry Setup*

However, it is important to note that Δ and Ψ are cyclical functions of film thickness, that is to say that when the optical path length of the light traversing the film reaches one wavelength (or 2,3, etc), Δ and Ψ are the same for no film at all Due to this cyclic behaviour an independent measure of thickness is needed Spectrophotometry is one such technique and is discussed in the following appendix

Appendix 3 Spectral Transmission

The thickness and refractive index of a thin film may be determined by measuring its transmission spectrum over the wavelength range 350 - 1200 nm The technique is based on the reflectance and transmission of light by a non-absorbing film coated onto a non-absorbing substrate as illustrated in figure 1

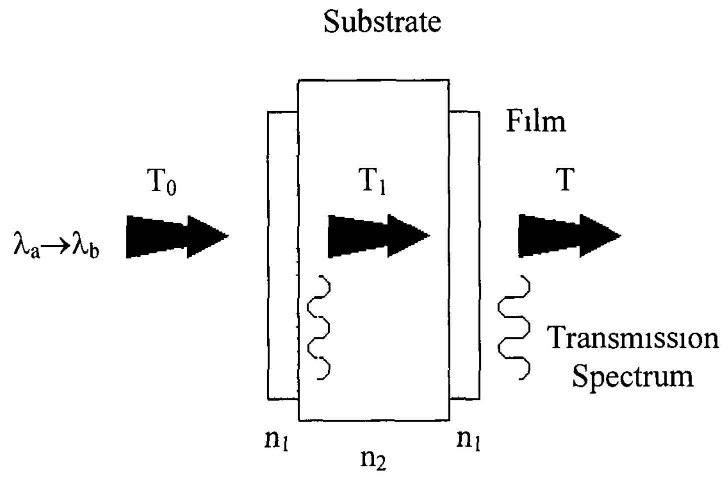

Figure 1 *Non-Absorbing Film on Substrate*

Upon encountering an interface, incident radiation is partially transmitted and partially reflected The total transmission or reflectance intensity may then be obtained by summing over all interfaces

Consider the case for a single film of thickness d and refractive index n_1 coated onto an infinite glass substrate of refractive index n_2 as is shown in figure 2

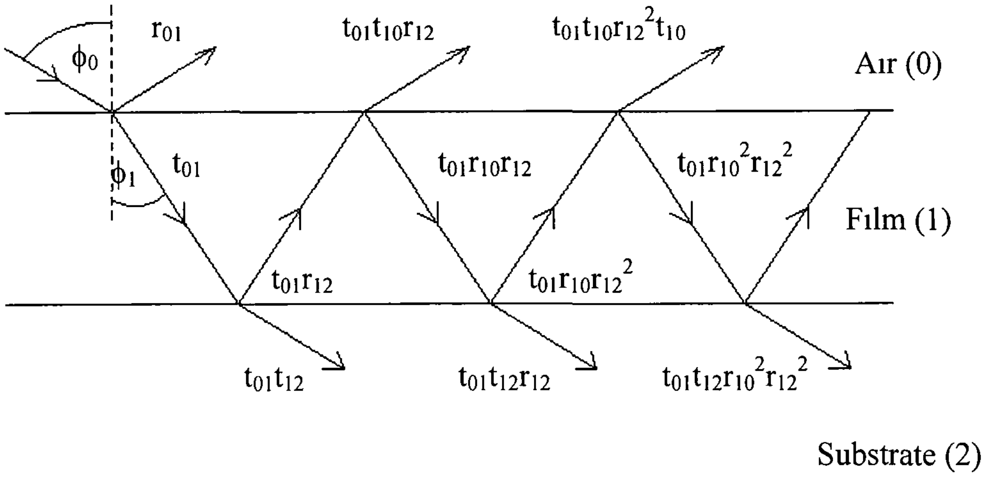

Figure 2 *Reflectance and Transmittance of Light from a Film Coated onto an Infinite Substrate*

The amplitudes of successive beams reflected from the glass substrate are represented by r_{01}, $t_{01}t_{10}r_{12}$, $t_{01}t_{10}r_{10}r_{12}^2$ The change in phase δ_1 of the beam in traversing the film is given by

$$\delta_1 = \frac{2\pi}{\lambda} n_1 d \, \mathrm{Cos}\phi_1 \qquad [1]$$

Therefore, the reflected amplitude is given by

$$R = r_{01} + t_{10}t_{01}r_{12}e^{-2i\delta_1} - t_{10}t_{01}r_{10}r_{12}^2e^{-4i\delta_1} + \qquad [2]$$

which may be rewritten as

$$R = r_{01} + \frac{t_{10}t_{01}e^{-2i\delta_1}}{1 + r_{01}r_{12}e^{-2i\delta_1}} \qquad [3]$$

Conservation of energy and Stokes law yields

$$R = \frac{r_{01} + r_{12} e^{-2i\delta_1}}{1 + r_{01} r_{12} e^{-2i\delta_1}} \qquad [4]$$

where R represents the total amplitude of the reflected beams The corresponding intensity is given by

$$R_{tot} = R\,R^{*} = \frac{r_{01}^{2} + r_{12}^{2} + 2 r_{01} r_{12}\ \mathrm{Cos}2\delta_1}{1 + r_{01}^{2} r_{12}^{2} + 2 r_{01} r_{12} \mathrm{Cos}2\delta_1} \qquad [5]$$

where for normal incidence

$$r_{01} = \frac{n_0 - n_1}{n_0 + n_1} \qquad [6]$$

$$r_{12} = \frac{n_1 - n_2}{n_1 + n_2} \qquad [7]$$

From equations 1 and 5, it can be seen that the maxima and minima of the reflectance curve occur at values of $n_1 d$ given by

$$n_1 d_1 = (2m + 1)\frac{\lambda}{4} \qquad [8]$$

$$n_1 d_1 = (2m + 2)\frac{\lambda}{4} \qquad [9]$$

If the film refractive index is greater than the refractive index of the substrate i e $n_1 > n_2$, the reflectances at these points are given by

$$R_{min} = \left(\frac{r_{01} + r_{12}}{1 + r_{01} r_{12}}\right)^{2} = \left(\frac{n_2 - n_0}{n_2 + n_0}\right)^{2} \qquad [10]$$

$$R_{max} = \left(\frac{r_{01} - r_{12}}{1 - r_{01} r_{12}} \right)^2 = \left(\frac{n_1^2 - n_0 n_2}{n_1^2 + n_0 n_2} \right)^2 \qquad [11]$$

The sum of the reflectance and transmittance must equal 1 Therefore, the light intensity transmitted into the glass substrate may be expressed as

$$T_{(1)min} = 1 - \left(\frac{n_1^2 - n_0 n_2}{n_1^2 + n_0 n_2} \right)^2 \qquad [12]$$

$$T_{(1)max} = 1 - \left(\frac{n_2 - n_0}{n_2 + n_0} \right)^2 \qquad [13]$$

At this stage, the light has traversed an air-film-glass path On exiting the slide the light undergoes the reverse path i e glass-film-air It can be shown from equations 12 and 13 that the analysis for these two paths are identical Therefore,

$$T_{min} = T_{(1)min}^2 = \left[1 - \left(\frac{n_1^2 - n_0 n_2}{n_1^2 + n_0 n_2} \right)^2 \right]^2 \qquad [14]$$

$$T_{max} = T_{(1)max}^2 = \frac{2n_2}{n_2^2 + 1} \qquad [15]$$

Therefore, it is possible to determine the refractive index of the film (n_1) by measuring the difference between the maximum and minimum transmission values as shown below

$$\Delta T = \frac{2n_2}{n_2^2 + 1} - \left[1 - \left(\frac{n_1^2 - n_0 n_2}{n_1^2 + n_0 n_2} \right)^2 \right]^2 \qquad [16]$$

Similarly for the case where the film refractive index is lower than the refractive index of the substrate

$$\Delta T = \left[1 - \left(\frac{n_1^2 - n_0 n_2}{n_1^2 + n_0 n_2} \right)^2 \right]^2 - \frac{2n_2}{n_2^2 + 1} \qquad [17]$$

It is also possible to determine the film thickness from the transmission spectra by measuring the position of the interference extrema The basic condition for interference fringes is

$$2nd = m\lambda \qquad [18]$$

From this it follows that the thickness is given by

$$d = \frac{\Delta m}{2n_c \left(\frac{1}{\lambda_1} - \frac{1}{\lambda_2} \right)} \qquad [19]$$

where Δm is the order of separation between the extrema and λ_1, λ_2 are the wavelengths at the extrema of interest

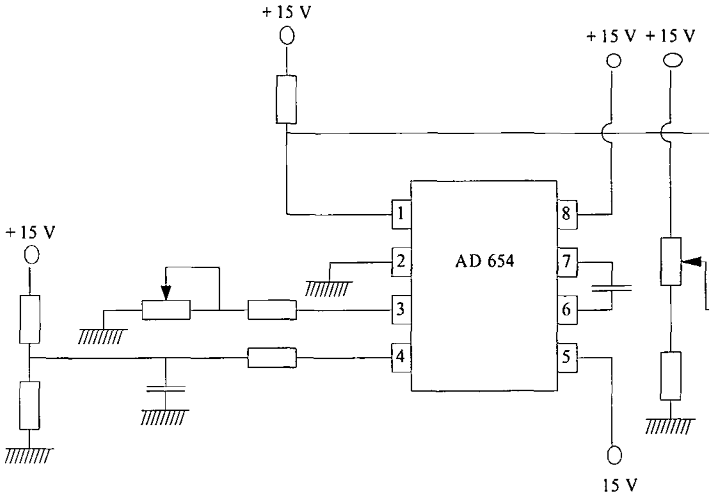
+ 15 V
+ 15 V
+ 15 V
+ 15 V
1
2
3
4
AD 654
8
7
6
5
15 V

Appendix 4 LED Driver Circuit

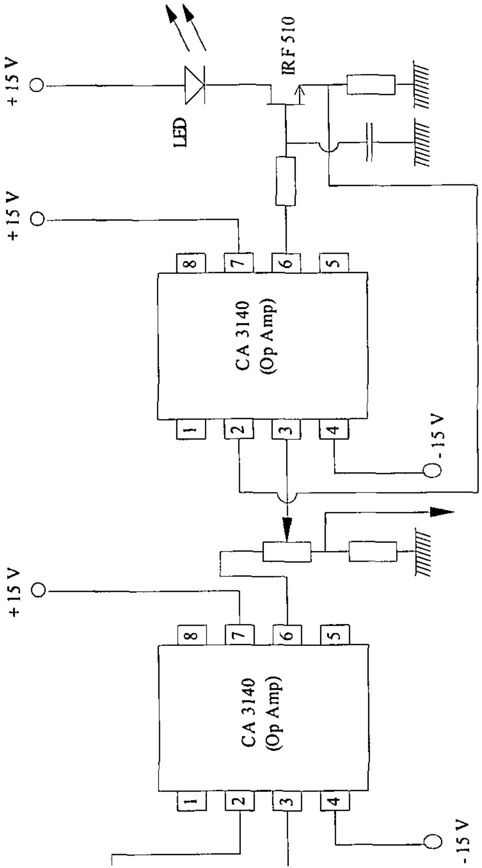

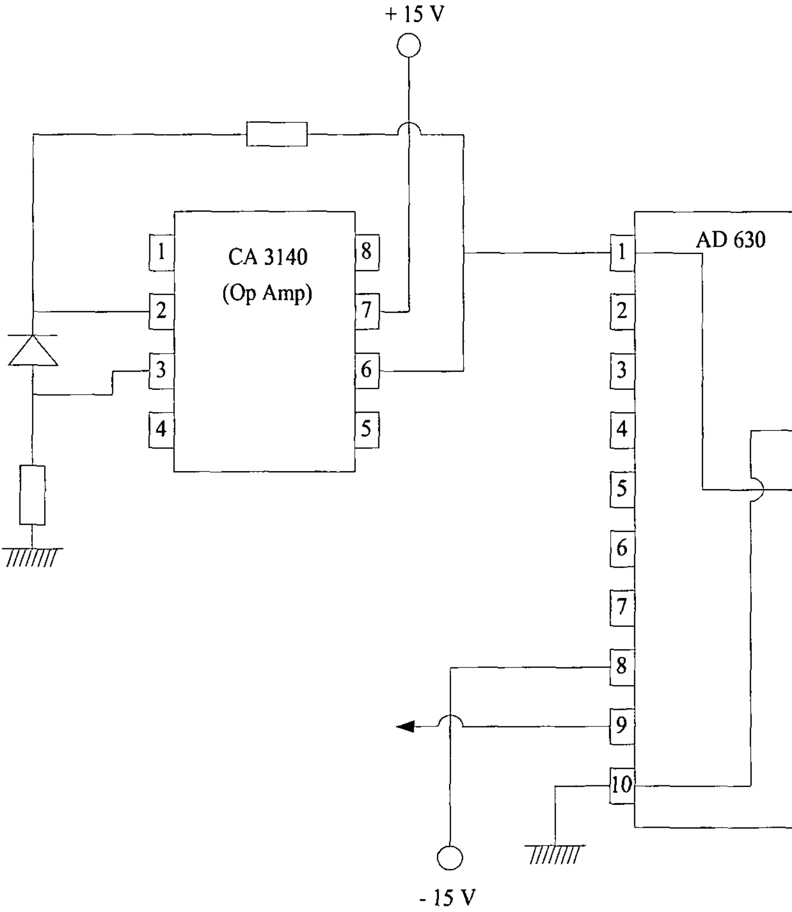
+ 15 V
CA 3140
(Op Amp)
1
2
3
4
8
7
6
5
AD 630
1
2
3
4
5
6
7
8
9
10
- 15 V

Appendix 5   Lock-In Detection Circuit